NUMERICAL SIMULATION OF IMPERFECT GAS FLOWS

by

John Murray Anderson, B. Eng.

Thesis submitted to the Faculty of Engineering,
the University of Glasgow, for the degree of Doctor of Philosophy.

August 1992

Chapter Three

Chapter Four

Chapter Five

Chapter Six

Chapter Seven

ACKNOWLEDGEMENTS

The author would like to thank Professor Bryan E. Richards, Mechan Professor of Aerospace Engineering, for supervising this project.

I would like to express my sincere gratitude to Professor Roderick A. McD. Galbraith, head of Aerospace Engineering, for his support and encouragement in the later stages of this work.

My thanks also extend to the academic and research staff of the Aerospace Engineering Department, many of whom have contributed either through discussion or by technical assistance to this work. I would particularly like to single out Dr Qin Ning and Dr Zhi Jian Wang for propounding much invaluable information regarding numerical aspects of this work. I would also like to acknowledge Miss Margaret Simpson and Mrs Emily Garman, secretaries to the Aerospace Engineering Department, who have provided invaluable secretarial assistance, and the advisory staff of the Computing Service Department for their assistance with computational matters.

This work has been supported financially by the Science and Engineering Research Council and British Aerospace plc under a CASE award, and latterly by the Science and Engineering Research Council and the Ministry of Defence under grant number GR/F 90035.

I am indebted to the many friends I have in Glasgow, and especially to Dr Fiona J. Watson and Miss Susannah Miles for proof-reading this document.

Finally, I would like to thank my family for their patience and understanding during the periods when progress in this work was slow. I would particularly like to express my appreciation of the support provided by my parents throughout the duration of this project.

DECLARATION

The research contained in this thesis was carried out independently by the author during the period from October 1987 to August 1992. No portion of this work has been submitted in support of any other degree or qualification at this or any other university or institute of learning.

J. Murray Anderson
August 1992.

ABSTRACT

This dissertation reports research into the thermochemical modelling of imperfect air with applications to computational fluid dynamics (CFD). The work is broadly separated into two topics; physical modelling of imperfect gases and numerical aspects of simulating the flow of such gases.

Various levels of physical modelling are considered. Primarily, state equation models for high temperature air in vibrational and chemical equilibrium are examined. The most popular techniques currently used for modelling the thermodynamic state of such gases are based on either look up tables or curve fits. Available curve fit data are therefore examined and used in the validation of more physically based methods.

A six species, three reaction, ionization free air state model is developed based on the solution of the laws of mass action to compute the flow chemistry. The calorically imperfect behaviour of the component species is modelled using both available curve fit data and statistical mechanics expressions, and it is concluded that species property curve fits are more appropriate for applications within the CFD environment. However, existing models based on this approach are limited by their inability to compute the derivative information required for the formation of the flux Jacobian and for the calculation of sonic speed. These limitations are overcome by developing innovative expressions for the required thermodynamic derivatives. Novel equations describing the frozen and equilibrium speeds of sound in a chemically reacting imperfect gas are also developed.

In order to apply any state model within the numerical solution of the flow equations, it is necessary to identify the correct dependent and independent variables. The nature of any model based on the solution of the laws of mass action requires that the equilibrium temperature is used as an independent variable. Techniques for inverting the state equations to give temperature as a dependent variable are therefore investigated, and a novel algorithm is developed based on a Newton-Raphson iteration for this inversion.

Many modern algorithms for the solution of hyperbolic and hyperbolic-parabolic systems of equations rely on mathematical properties associated with calorically perfect state equations. Algorithms developed on the basis of perfect gas behaviour must therefore be modified to account for thermal imperfections in high temperature air. The principal modifications identified here are the restructuring of the flux Jacobian to account for temperature variations of the ratio of specific heats, the nonhomogeneous nature of the flux vector with respect to the conserved variables and the lack of a closed form for the characteristic variables.

In order to illustrate the application of equilibrium gas models within the CFD environment, a solution of the quasi-one-dimensional Euler equations is presented for supersonic and hypersonic nozzle flows with and without a shock wave present. Particular attention is given to the characteristic treatment of boundary conditions, as this is an area in which perfect and equilibrium gas models require distinct treatments. The scheme used is a trapezoidal time/central space differenced one with added artificial dissipation.

In addition to modelling the thermodynamic state equations for reacting gases, some progress towards the modelling of translational nonequilibrium is described. Methods for evaluating the transport coefficients of air in chemical equilibrium are addressed. Chemically relaxing inviscid flows are also examined and techniques are proposed for the solution of such flow problems.

NOMENCLATURE

Roman Symbols:

A	nozzle cross sectional area (section 2.2)	m^2
	Jacobian matrix $\partial \mathbf{F}/\partial \mathbf{U}$ (section 3.1)	
$\tilde{A}$	transformed Jacobian matrix $M^{-1}AM$	
a_i	pressure curve fit coefficients (section 4.1)	
	species property curve fit coefficients (section 4.4)	
$a_{\mu i}$, $b_{\mu i}$, $c_{\mu i}$	species viscosity curve fit coefficients	
b_i	temperature curve fit coefficients	
c_e	equilibrium speed of sound	$m\ s^{-1}$
c_f	frozen speed of sound	$m\ s^{-1}$
c_i	mixture viscosity curve fit coefficients	
c_p	specific heat at constant pressure	$J\ kg^{-1}\ K^{-1}$
$\hat{c}_p$	molar heat at constant pressure	$J\ mol^{-1}\ K^{-1}$
c_v	specific heat at constant volume	$J\ kg^{-1}\ K^{-1}$
$\hat{c}_v$	molar heat at constant volume	$J\ mol^{-1}\ K^{-1}$
d_i	mixture thermal conductivity curve fit coefficients	
E	Total energy density	$J\ m^{-3}$
e	specific internal energy	$J\ kg^{-1}$
$\hat{e}$	molar internal energy	$J\ mol^{-1}$
$\hat{e}_f^0$	molar heat of formation at absolute zero	$J\ mol^{-1}$
$\hat{e}_R^0$	molar heat of reaction at absolute zero	$J\ mol^{-1}$
$\mathbf{F}$	inviscid flux vector	
$\mathbf{F}_v$	viscous flux vector	
f_1, f_2, f_3	component functions for pressure curve fits	
g_1, g_2, g_3	component functions for temperature curve fits	
g_i	degeneracy factor	
$\hat{g}^0$	standard state molar Gibbs free energy	$J\ mol^{-1}$
h	specific enthalpy	$J\ kg^{-1}$
h_o	specific total enthalpy	$J\ kg^{-1}$
$\hat{h}$	molar enthalpy	$J\ mol^{-1}$
$\hat{h}^{T0}$	molar enthalpy at $T_0 = 298.15$ K	$J\ mol^{-1}$
I	identity matrix	
K	equilibrium constant in terms of specific concentrations	
K_i	sonic speed curve fit coefficients	
K_p	equilibrium constant in terms of partial pressures	

k	coefficient of thermal conductivity (section 2.2)	$J\ m^{-1}\ s^{-1}\ K^{-1}$
	Boltzmann constant (section 4.4)	$1.380\ 62 \times 10^{-23}\ J\ K^{-1}$
k_b	backward reaction rate constant	
k_f	forward reaction rate constant	
L	transformation matrix $\partial \mathbf{V}/\partial \mathbf{W}$	
l_i	left eigenvectors of the Jacobian A	
M	transformation matrix $\partial \mathbf{U}/\partial \mathbf{V}$	
$\hat{M}$	molar mass	$kg\ mol^{-1}$
m	momentum density (section 3.1)	$kg\ m^{-2}\ s^{-1}$
	molecular weight (section 4.4)	u
Pr	Prandtl number $c_p\mu/k$	
p	static pressure	$N\ m^{-2}$
$\overline{p}$	locally normalized pressure	
p_i	partial pressure	$N\ m^{-2}$
p_0	standard state pressure	$101\ 325\ N\ m^{-2}$
Q	molecular partition function	
$\hat{R}$	molar gas constant	$8.314\ 4\ J\ mol^{-1}\ K^{-1}$
R_0	specific gas constant	$J\ kg^{-1}\ K^{-1}$
s	specific entropy	$J\ kg^{-1}\ K^{-1}$
$\hat{s}$	molar entropy	$J\ mol^{-1}\ K^{-1}$
$\hat{s}^0$	standard state molar entropy	$J\ mol^{-1}\ K^{-1}$
$\hat{s}^{T0}$	molar entropy at $T_0 = 298.15$ K	$J\ mol^{-1}\ K^{-1}$
T	temperature	K
T^*	reduced temperature	
T_c	critical temperature	K
t	temporal coordinate	s
$\mathbf{U}$	vector of conserved variables	
u	velocity	$m\ s^{-1}$
$\mathbf{V}$	vector of primitive variables	
$\mathbf{W}$	vector of characteristic variables	
w_i	characteristic variables	
x	spatial coordinate (section 2.2)	m
	mole fraction (section 4.3)	
x, y, z	independent variables in Grabau type curve fits	
X_s	species number s in reaction equation	

Greek Symbols:

α	mass fraction (section 4.3)	
	second order damping factor (section 5.4)	
γ	specific heat ratio	
$\bar{\gamma}$	enthalpy/internal energy ratio	
δ	differential operator, $\partial/\partial\rho$ or $\partial/\partial T$	
δ_{ij}	Kronecker delta	
ε	internal energy density = ρe	J m^{-3}
ε_0	Lennard-Jones potential parameter	J
η	specific concentration	mol kg^{-1}
η^*	specific concentration at equilibrium	mol kg^{-1}
η_N	specific concentration of oxygen nuclei	mol kg^{-1}
η_O	specific concentration of nitrogen nuclei	mol kg^{-1}
θ_i	characteristic temperature for electronic excitation	K
θ_r	characteristic temperature for rotational excitation	K
θ_v	characteristic temperature for vibrational excitation	K
ι	ionization parameter	J^2 kg^{-2} K^{-1}
κ	thermodynamic derivative $(\partial p/\partial\varepsilon)_\rho$	
Λ	matrix of eigenvalues	
λ	second coefficient of viscosity	kg m^{-1} s^{-1}
λ_i	eigenvalues of the Jacobian A	m s^{-1}
μ	first coefficient of viscosity	kg m^{-1} s^{-1}
μ_B	coefficient of bulk viscosity	kg m^{-1} s^{-1}
ν_N	coefficient of artificial viscosity	
ν'	reactant stoichiometric coefficients	
ν''	product stoichiometric coefficients	
ρ	mass density	kg m^{-3}
σ	symmetry factor (section 4.4)	
	collision cross section (section 6.3)	Å
ϕ	viscosity parameter	
ϕ_1, ϕ_2, ϕ_3	component functions for viscosity curve fits	
χ	thermodynamic derivative $(\partial p/\partial\rho)_\varepsilon$	J kg^{-1}
ψ_1, ψ_2, ψ_3	component functions for conductivity curve fits	
Ω	source vector	
$\tilde{\Omega}$	transformed source vector $M^{-1}\Omega$	
$\Omega^{(2,2)*}$	reduced collision integral for viscosity calculations	
$\dot{\omega}$	production rate	mol m^{-3} s^{-1}

Subscripts

c	equations of motion related to flow chemistry (section 2.2)
f	equations of motion related to fluid motion (section 2.2)
i	space index, $x = i \Delta x$ (section 5.4)
i, j, k	summation indices
r	reaction number
s	species number

Superscripts

n	time index, $t = n \Delta t$ (section 5.4)
*	equilibrium conditions (section 4.9)

Chapter One

INTRODUCTION

New concepts in launch vehicle design and ambitious space research projects have broadened interest in hypersonic aerodynamics over the last decade. In light of these programmes, this dissertation examines aspects of the modelling of air as a real gas and presents simulation techniques for hypersonic flows. This introductory chapter gives a brief historical perspective on the evolution of hypersonic flight, along with some notes on important projects currently under consideration. As a prelude to the detailed examination of hypersonic flows, the terms "hypersonic" and "real gas" are discussed. A brief overview of some numerical aspects of the project is then presented. Finally the thesis under investigation is presented and the scope of the current study is outlined. The chapter concludes by outlining the layout of the dissertation.

1.1 THE EVOLUTION OF HYPERSONIC FLIGHT.

Not only does successful hypersonic flight require an extremely powerful engine, but it also demands an understanding of the behaviour of air under abnormal conditions. Parallel developments in both propulsion and aerodynamics in the first half of the twentieth century have therefore contributed to the rapid advancement of hypersonics, from the first successful hypersonic projectile launched by R. H. Goddard on February 24, 1949, to the launch of the Space Shuttle Columbia on April 12, 1981. Recent applications demand better understanding of hypersonic aerodynamics for two reasons. Firstly, there is a trend towards the use of lifting surfaces on re-entry vehicles, to permit their safe return to a designated base. Secondly, proposed interplanetary and deep space missions involve high atmospheric entry speeds which must be reduced aerodynamically to safe landing velocities. Hypersonic aerodynamics therefore forms an important aspect of space research.

As early as 1687 Newton had recognized that sound propagates through air at a finite speed and proposed an expression for this, based on the elasticity of air. Unfortunately, he incorrectly assumed the propagation of sound to be an isothermal process, and it was not until 1816 that the French mathematician Laplace published the first correct expression for acoustic propagation, based on the isentropic compressibility of air.

The existence of a finite speed of sound led to the question of what would happen when an object travelled faster than that speed. Shock waves had by this time been recognized and Bernhard Riemann made the first attempts at their analysis in 1858. He, like Newton, made a fundamental error in his assumptions about the nature of the problem, and it was not until 1870 that the Scottish engineer William Rankine published the normal shock relations generally accepted today. These equations were rediscovered independently by the Frenchman Pierre Henry Hugoniot seventeen years later, and it is to these two men that the normal shock relations are generally ascribed. By 1910 the theoretical behaviour of normal shocks was capped by the application of the second law of thermodynamics to the problem by both Lord Rayleigh and G. I. Taylor. This established the direction of changes through a normal shock, precluding the existence of expansion shocks.

In 1893, the Swedish engineer Carl de Laval demonstrated the use of a convergent-divergent nozzle within a steam turbine to achieve exceptionally high rotation speeds. At the time, the supersonic nature of the flow in such nozzles was unproven, and it fell to Aurel Stodola to demonstrate its existence experimentally and substantiate the relationship between his experiments and normal shock theories in his book "Steam Turbines", published in 1903.

It is interesting to note that 1903 also saw the publication in Russia of a paper entitled "Investigations of Space by Means of Rockets" by Konstantine Tsiolkovsky. This represented the first practical suggestions that liquid fuelled rockets could be used as a propulsion system to investigate space. Unfortunately, the paper was too far ahead of its time - given that the first successful powered flight only took place in December of that year, under the control of Orville Wright. Tsiolkovsky was proposing flight at escape velocities at a time when the Wright brothers had achieved a mere 30 miles per hour.

Less than five years after the Wright brothers first flight, the German aerodynamicist Ludwig Prandtl was engaged in research into the theoretical nature of oblique expansion processes. Using photographic techniques pioneered by Ernst Mach, Prandtl, assisted by Theodor Meyer, produced some outstanding research on supersonic flows. It was in Meyer's doctoral dissertation in 1908 that the oblique expansion relations were first laid down, together with the basis for the understanding of oblique shock behaviour. By the end of the decade, the fundamentals of supersonic flow were understood. However, this field of research was still very much of academic interest, as there were few practical applications for such theories.

In 1909, the American engineer Robbert H. Goddard embarked upon a career which was to lead to the patenting of the world's first design for a liquid fuelled rocket

in 1914 and the subsequent publication of his paper "A Method of Reaching Extreme Altitudes" in 1919. It is the work of Goddard, together with that of Tsiolkovsky and later of the Austro-Hungarian engineer Hermann Oberth, which led to the development of a propulsion system ultimately capable of attaining hypersonic velocities. Despite the early visions of Tsiolkovsky, and the influential work of Oberth through his publication of "De Raket zu den Planetenraümen" (The Rocket into Interplanetary Space) in 1923, it was Goddard who first successfully launched a liquid fuelled rocket on March 16, 1926. It was also Goddard who first shot a liquid fuelled rocket through the sound barrier in 1935.

While the practicalities of using rocket power to attain escape velocities were being investigated in the mid 1920s, Prandtl, with his Swiss colleague Jacob Ackeret, and the English aerodynamicist Hermann Glauert, were independently considering the more immediate problem of establishing the effect of Mach number on propeller tips. The solution of this problem led to the publication of linearized theories on the behaviour of aerofoils in compressible flows. Another colleague of Prandtl's, Adolf Busemann, went on to present fully nonlinear solutions to supersonic flow problems using the method of characteristics. This analytic technique was used to design the first practical supersonic wind tunnels in the mid 1930s.

Rocket powered flight became a reality on September 30, 1929, when Fritz von Opel flew in a powered glider, propelled by a solid fuel rocket. German interest in rocketry was spurred by restrictions placed on her ability to perform artillery tests under the Treaty of Versailles, and the work of Oberth in the early 1930s was soon recognized for its military potential. A former assistant to Oberth, Wernher von Braun, became technical director of the rocket research centre at Peenemünde in northwest Germany in 1935, after such research for civilian purposes was forbidden by his government. Braun became responsible for the management of the A-4 rocket programme, later designated V-2 by the German Propaganda ministry. The first successful A-4 launch took place at Peenemünde during October 1942, by which time Germany was firmly established as world leader in rocket research.

At the end of the Second World War many of the German rocket scientists, including Braun, were moved to the United States, where they contributed both to the peaceful application of rocketry to space research and to its application to long range ballistic missiles. A high point in the fields of both rocket research and aerodynamics came on October 14, 1947, when Chuck Yeager in the rocket powered Bell X-1 became the first man to fly faster than the speed of sound. Further advances came quickly, with the first multistage rocket launch being accomplished on February 24,

1949. This experiment had the further distinction of producing the first successful hypersonic flight.

Under the auspices of the International Geophysical Year, an 18 month period from July 1957 to December 1958, several important events took place. Firstly, on October 4, 1957, the U.S.S.R. stamped its authority on space research by launching Sputnik 1, the first artificial satellite to orbit Earth. This was followed by nine more sputnik missions carrying out a number of experiments, including research into life support systems. Less than four months later, on January 31, 1958, under the direction of Braun, the U.S. successfully launched its first satellite, Explorer 1. In October of that year, the National Aeronautics and Space Administration was established in the U.S. with the express purpose of achieving parity with the Soviet space programme. A space race had begun between the two most powerful nations on Earth.

The 1960s represented the first peak in research into hypersonic flow. The Soviet Union at first confirmed its authority over the space race by launching Yuri Gagarin into orbit on April 12, 1961, and safely returning him to Earth. Alan B. Shepherd performed a slightly less ambitious sub orbital flight on May 5, after which President John F. Kennedy publicly committed the U.S. to landing a man on the moon by the end of the decade. Also about this time some practical propositions were being made towards the concept of a reusable orbital transfer vehicle, ideas which were later to evolve into the American Space Shuttle. The decade ended with the historic Apollo 11 mission, which landed Neil Armstrong and Edwin Aldrin on the surface of the moon, and returned them safely.

During the 1970s and '80s, launchings of artificial satellites became commonplace. However, waning public interest in manned space flight lead to the termination of the Apollo program after 17 missions. With the Soviet manned space program concentrating on maintaining support for their Salyut space station through the use of disposable launchers, the U.S. took a different approach and concentrated on the idea of a reusable launch vehicle. This led to the launch of the Space Shuttle Columbia on April 12, 1981. The Shuttle is unique in its ability to provide flight test data in the hypersonic regime.

The late 1980s have seen a resurgence in interest in hypersonic flight for several reasons. Increasing launch costs highlight the desire for a fully reusable space vehicle. The two-stage-to-orbit German Sänger project is an example of the use of current engine technology to achieve this. Also, advancing engine technology has led to the proposal of hybrid air breathing/rocket motor designs. These ideas have fuelled research into single-stage-to-orbit vehicles, such as the American NASP (National

Aerospace Plane) and British HOTOL (Horizontal Take-off and Landing). As far as manned space flight is concerned, it is likely that less ambitious projects will prevail, such as the European Space Agency's mini-shuttle Hermies.

Future aero-thermodynamic challenges are not restricted to the field of manned space flight. Such projects as the European Cassini/Huygens mission to land a planetary probe on Titan, or the Rosetta mission to collect and return cometary samples to Earth will call for detailed knowledge of the hypersonic behaviour of gas mixtures. Proposed Mars lander missions present similar problems. Furthermore, low Earth orbit satellites, such as the gravitational research satellite Aristoteles, require an understanding of the high speed rarefied gas flows they encounter, in order to effectively control aerodynamic drag.

The study of hypersonic flow is of continuing interest to a large number of practical research programmes. It is therefore important to detail exactly what is meant by the term hypersonic and establish the breadth of this field of study. A specific area of research can then be identified and investigated.

1.2 Definition of Hypersonic Real Gas Flows.

Unlike the clear demarcation between subsonic and supersonic flows, there is no single point beyond which a flow can be classified as hypersonic. Anderson (1986) defines hypersonic flow as "that regime where certain physical flow phenomena become progressively more important as the Mach number is increased to higher values". The lack of precision in this statement is compounded by the vagueness of the term "real gas". It is therefore important to qualify the various phenomena which fall into the category of hypersonic real gas flows.

1.2-a Hypersonic Flows.

There are various phenomena which occur within high Mach number flows which are present irrespective of the thermochemical model chosen to represent the gas. They exist because of the high speed of the flow and are generally present at Mach numbers above five. It is instructive to first look at these effects without reference to the modelling of the gas, although all such effects are influenced to some degree by the choice of gas model.

As flow speed increases above sonic, the bow shock formed ahead of a blunt body will steadily strengthen and move closer to the body. The resulting thin shock layer can be used to advantage in reducing the complexity of the problem, providing the Reynolds number of the flow is sufficiently high to prevent the shock and boundary

layers interacting. Examples of such theories relying on the thin shock layer in inviscid flows are Newtonian theory, modified Newtonian theory, Newtonian-Busemann theory and Maslen's thin shock-layer theory. It is emphasized that these theories give only approximate solutions based on the absence of viscosity and the nearness of the shock to the body.

Another inviscid phenomenon associated with hypersonic flows is the formation of an entropy layer on a body's surface. Due to the high curvature of the bow shock at the leading edge of an hypersonic projectile, large gradients in entropy can be set up normal to the direction of the flow. Although inviscid mechanisms are responsible for the formation of the entropy layer, its importance lies mainly with its influence on the viscous boundary layer. Through the vorticity associated with strong entropy gradients, a highly curved bow shock interacts with the growth and development of the viscous boundary layer, and it becomes difficult to separate viscous and inviscid regions of the flow.

It is not only through the entropy layer that viscous/inviscid interactions can take place. At the low Reynolds numbers often associated with re-entry problems, thick boundary layers tend to merge into the shock layer. This precludes any possibility of solving the viscous and inviscid portions of the flow separately. Even numerical solutions for merged shock/boundary layers are difficult because of the need to maintain a dissipative scheme for the correct capturing of shocks, without adversely affecting the resolution of strong shear layers.

1.2-b Real Gas Flows.

The term "real gas" is generally taken to describe any gas which does not have constant specific heats. Such gases require detailed modelling of their internal structure in order to correctly represent their behaviour. The internal structure of diatomic and monatomic gases will be discussed in section 2.1.

Caloric imperfections are the first real gas effects to become evident in any gas flow. These imperfections give rise to a temperature dependence for the specific heats of the gas so that internal energy is no longer linearly related to temperature. Calorically imperfect gases do, however, obey Boyle's law, so that pressure is a linear function of density at a fixed temperature. Gases which fail to obey Boyle's law are thermally imperfect. Thermal imperfections can come about because chemical activity changes the molar mass of the gas, or because of high density effects, where virial corrections are applied to the thermal state equation to account for the finite volume of individual atoms. Electrical excitation within a gas can be treated as a special case of

chemical activity, giving rise to complex caloric imperfections, eventually leading up to ionization.

The extreme velocities associated with hypersonic flight imply that the finite number of collisions required to excite some molecular processes take place over appreciable length scales. In such circumstances the affected processes must be modelled out of equilibrium. Such nonequilibrium modelling can lead to considerable difficulties with the different time scales associated with various processes. Also, nonequilibrium processes lead to spatial gradients in fluid properties which in turn give rise to diffusive effects. Heat and momentum transfer phenomena are consequences of translational nonequilibrium, and are implicit in many perfect gas models of fluid flow. However, chemical and vibrational rate processes are specific to real gas flows and form important research topics in their own right.

Low density effects give rise to some very specialized real gas problems. In situations where the Knudsen number (the ratio of the mean distance between molecules to a characteristic length of the boundaries) becomes large, free molecular flows result, and the continuum equations of motion no longer apply. Such flows carry their own solution techniques, often relying on stochastic models. In the same way that supersonic and hypersonic flows have an indistinct boundary, the transition from continuum to free molecular flows is not clearly defined. Transitional flows are an area of current interest to many researchers, because of their relevance to atmospheric entry problems.

Complex physical processes, such as radiative heat transfer, electrical and magnetic effects in ionized flows or nuclear activity are beyond the scope of the current research.

1.3 The Need for Hypersonic Flow Simulations.

Some distinctive attributes of the behaviour of gas mixtures under extreme conditions have been outlined in the preceding section. It is clear that only in a limited number of cases will there be analytic solutions to problems involving such gases. Those solutions that do exist are restricted to simple geometries or specific points in the flow, and therefore are of limited use in the practical design of lifting re-entry vehicles. However, such theoretical solutions that do exist are of immense importance to the understanding of physical phenomena which form the basis of all computational and experimental analysis.

It is recognized that the design of the U.S. Space Shuttle relied principally on data derived experimentally. However, while the four Shuttle orbiters remain the only

reusable manned spacecraft yet built, they no longer represent the state of the art in spacecraft design technology. During initial flight testing of the orbiter Columbia, several anomalies were observed regarding the preflight data. Most notably these were the required flap deflection for trim and severe heating rates measured on the lee surface of the orbiter (Young et al., 1981). These effects have subsequently been investigated using computationally based simulations (Maus et al., 1984) and the differences have been put down to real gas effects.

The primary reason for the incorrect flap angle and heating rate preflight predictions for the shuttle was the difficulty in experimentally simulating high altitude hypersonic flows in ground test facilities. Such high enthalpy facilities are very expensive to build and operate, and much care must be taken when extrapolating test results to full scale flows. Because of the complexity of the behaviour of gas mixtures such as air, uninterpretable results would come from such facilities unless they utilize simple gases such as monatomic-diatomic nitrogen mixtures. These may be less representative of actual conditions in the upper atmosphere. The short run times of many types of high enthalpy tunnel give rise to measurement difficulties, particularly for parameters such as heat transfer rate or skin friction. Also, in situations where densities are low and Mach numbers high, dynamic similarity of nonequilibrium flows can only be achieved on a full scale model, which implies flight testing. Clearly then, hypersonic wind tunnel test results require more care in their extrapolation to the full scale case than do the equivalent supersonic results.

The evolution of computational fluid dynamics (CFD) over the last two decades has provided an additional tool for the analysis of hypersonic flows. The simultaneous simulation of mass, length, time and temperature scales for complex geometries, such as the shuttle orbiter, is now a practical proposition, albeit for limited degrees of physical modelling. Increasing computing power, vectorization and parallelization of computer codes, and reductions in the cost of fast access memory all point towards CFD becoming more widely used in the design process over the next few years.

However, CFD is still limited in many respects. Early algorithms have been developed largely on a mathematical basis, and often rely on certain restrictive properties of the equation of state for a perfect gas. As a consequence, it is not always possible to extend some of the advanced modern high resolution shock capturing algorithms directly to incorporate even the simplest equilibrium air models. Much work remains to be done in the field of algorithm development.

It is unlikely that computational solutions will ever entirely replace experimental or theoretical work. Rather they will be used, as at present, to substantiate and facilitate

the analysis of experimental and flight test results. With the development of faster and more robust codes, increasing use will be made of such solutions within the design process. The field of hypersonics will probably see the biggest advantages from CFD, because the difficulties in deriving numerical solutions will be outweighed by the cost and complexity of deriving and analysing meaningful experimental results.

1.4 Some General Numerical Aspects of Flow Simulations.

The most distinctive feature of hypersonic flows is the presence of very strong shock waves. Shock waves are discussed in greater detail in section 3.3. The only solution to the Euler equations which satisfies shock inducing boundary conditions is a discontinuous one, representing an instantaneous adjustment of all molecular energy modes across the shock. The same is not true of the Navier-Stokes equations†, which can model the internal structure of weak shocks. Shock structures are, however, only important when the mean free path between molecules approaches the length scale of the boundary conditions. In most continuum flows shocks can therefore be treated as if they are discontinuities, and many numerical algorithms are developed on this basis.

There are two basic techniques for modelling shock waves within a numerical scheme. These are shock fitting and shock capturing. Shock fitting techniques rely on a prior knowledge of the position and strength of shock waves. The jump in conditions across the shock are established from the Rankine-Hugoniot relations, and the shock is treated as a boundary to the flow. This has the advantage of concentrating the solution process in the field of interest (ie between the bow shock and the body), but is limited by the need to compute the location of the shock and the jump in conditions across it. The advantages of shock fitting techniques are gradually being eroded by the development of high resolution shock capturing algorithms. These rely on modelling the shock as part of the solution, and require no advance knowledge of shock position. Shock capturing schemes can successfully deal with embedded shocks, which are common in hypersonic flows over complex geometries.

The method chosen to discretize the equations of motion has a significant effect upon the validity and accuracy of their numerical solution. It also affects the speed of convergence to a steady state. Treating time derivatives and space derivatives

---

† The term *Navier-Stokes equations* is taken to refer to the full set of conservation equations for a fluid, including the mass and energy conservation laws, rather than the momentum conservation equations alone.

separately, there are two classes of techniques for differencing each of these terms: implicit or explicit time differencing and central or upwind space differencing. Discretization of the equations of motion is dealt with in section 3.2.

1.5 THE SCOPE OF THIS STUDY.

The general objective of this work is to investigate and implement improved physical models for air within the CFD environment. It is not yet possible to include every degree of realism within a numerical simulation, and it is therefore the purpose of this section to highlight those particular aspects of the task which fall within the scope of this study.

This research concentrates primarily on modelling the equations of state for inviscid equilibrium air at moderate densities. Principally, the effects of calorific and thermal imperfections in the state equations are addressed, and only continuum flows are considered. The modifications to existing implicit algorithms required for the implementation of equilibrium gas models are then examined.

To illustrate the use of these state equation models, they are applied to a one dimensional test case. The scheme used is trapezoidal time differenced, central space differenced (Beam and Warming, 1976) with Jameson (Jameson et al., 1981) type artificial dissipation.

Some progress towards steady state nonequilibrium modelling, both in terms of rotational and translational nonequilibrium and in chemical nonequilibrium, has also been made. Perhaps of most immediate importance to hypersonic flow is the modelling of the translational nonequilibrium, as this effect leads directly to the transport properties of the flow, and is responsible for surface shear stresses and heat transfer rates. Fast methods for computing the transport coefficients for gas mixtures are therefore desirable.

The emphasis throughout this dissertation is placed on physical modelling rather than algorithm development. Numerical aspects are vital because of the modifications to the basic equations brought about by changing the physics of a flow, but it is not the purpose of this thesis to evolve revolutionary techniques for the solution of these equations. Rather, existing numerical methods are picked upon and modifications are presented to allow their application to more physical problems. Further improvements in efficiency of the solution process will always be possible by developing better numerical techniques.

1.6 THE STRUCTURE OF THE DISSERTATION.

There are two aspects to the research presented in this dissertation. These are the physical modelling of the gas and the numerical representation of these models. As mentioned in section 1.5, priority is given to improving the physical modelling in CFD codes, and emphasis is placed on that aspect. Chapter two therefore presents detailed background information on the behaviour of imperfect gases, expanding on information introduced in section 1.2. Chapter three continues by providing the background for numerical modelling.

Chapters four and five form the core of the thesis, as they present the development and implementation of fast equilibrium models for inviscid flows. The relative merits of different techniques are discussed in these chapters.

Progress towards nonequilibrium modelling, both in terms of Navier-Stokes type simulations, and vibrational and chemical nonequilibrium problems, is discussed in chapter six.

Chapter seven concludes the dissertation by restating what has been achieved and putting forward recommendations on the use of the techniques developed. Future research directions are also discussed in this chapter.

Chapter Two

PHYSICAL GAS DYNAMICS

This chapter describes the fundamental equations on which subsequent work is based. A microscopic account of the internal structure of gases is given first, followed by a description of the equations of motion for viscous and inviscid gases. The similarities between these equations and the equivalent perfect gas equations are discussed. The effects of chemical activity within the gas are considered, and the equations describing both nonequilibrium and equilibrium chemical reactions are presented. Finally, the equations of state are discussed and the departures from perfect gas behaviour highlighted.

2.1 THE INTERNAL STRUCTURE OF GASES.

The imperfect behaviour of gases at high temperature is principally due to the excitation of internal energy modes inactive at lower temperatures. For this reason, a qualitative understanding of the internal structure of gases such as air is important.

Air at low temperatures is normally considered to be a mixture of 78% diatomic nitrogen, 21% diatomic oxygen and 1% argon. Other gases, such as ozone, carbon dioxide, nitrogen dioxide, sulphur dioxide and water vapour are present in varying degrees at different altitudes, but, with the exception of water vapour, the concentrations of these species are never more than 0.1%. In the upper reaches of the stratosphere, where continuum hypersonic flows are likely to be encountered during reentry, the oxygen concentration can fall to about 15% and nitrogen concentration can vary between 70% and 80%, according to altitude. At any altitude, the principal reactions therefore involve nitrogen and oxygen in some form. Air can then be considered to be a mixture of monatomic and diatomic non polar gases.

A monatomic gas can only store energy through the translational motion and electronic excitation of its component atoms. Such a gas can be visualized as consisting of fast moving point masses which interact through an electrostatic potential. When two atoms come sufficiently close for their respective potentials to interact, an exchange of energy takes place, and their translational or electronic modes change state. The way in which the potential is modelled therefore dictates many aspects of the gas behaviour. Examples of commonly used models are the rigid sphere, square well, Lennard-Jones and Buckingham potentials illustrated in Figure 2.1.

If two atoms collide and disperse energy in the process, they may form a chemical bond. This bond is created because of the potential well[†] illustrated in Figure 2.1. The molecule so formed has both rotational and vibrational energy storage modes in addition to translational and electronic modes. Furthermore, if vibrational energy levels are low, the potential well may be approximated by either rigid rotator or harmonic oscillator models.

In the perfect gas model of air, the gas is represented by a uniform mixture of rigid rotating diatomic molecules, which interact according to the rigid sphere model. Vibrational and electronic modes are not present and the translational and rotational modes are assumed to be fully excited so that internal energy is a linear function of temperature. This model is illustrated in Figure 2.2a. Perfect gas descriptions of air are valid from about 200 K up to 600 K, and are characterized by having constant specific heats.

Above 600 K vibrational excitation becomes significant, and the rigid rotator model must be replaced by an harmonic oscillator. Further increases in temperature, up to 1000 K, lead to electronic excitation and chemical activity, in which case harmonic oscillator models must be supplemented by dissociation models or replaced by more representative potentials, such as the Lennard-Jones (6-12) potential. Figure 2.2b illustrates a vibrationally and electronically excited gas.

To excite rotational or translational energy modes, only a small number of molecular collisions are required. However, at the continuum level, spatial gradients in these forms of internal energy lead to the transport of mass, momentum and energy. These effects are accounted for through the transport coefficients, and will be discussed in greater detail in chapter six. Vibrational and chemical excitation require significantly more collisions, and therefore take longer to relax back to an equilibrium state after being perturbed. If the flow speed is very high, these relaxation processes can therefore take place over considerable spatial distances. Chemical and vibrational relaxation processes must be accounted for if internal energy exchanges in hypersonic flows are to be correctly modelled.

2.2 THE CONSERVATION LAWS FOR MASS, MOMENTUM AND ENERGY.

The equations of motion for a chemically reacting real gas can be derived from a continuum point of view by applying the fundamental principles of mass, momentum and energy conservation to a moving fluid element (Liepmann and Roshko, 1957). Applying these principles at an atomic level results in a more involved analysis leading

[†]If energy is removed during the collision process, the colliding atoms may be left with insufficient energy to overcome this potential well and therefore become bonded.

to the same equations (Vincenti and Kruger, 1965). The following sections present the equations describing the motion of viscous and inviscid fluids in chemical equilibrium. These equations are then simplified to one dimensional flows.

2.2-a Viscous Equations.

The conservation laws for mass, momentum and energy in the absence of body forces can be written using the summation convention as:

$$\frac{\partial \rho}{\partial t} + \frac{\partial \rho u_j}{\partial x_j} = 0 \tag{2.1}$$

$$\frac{\partial \rho u_i}{\partial t} + \frac{\partial \rho u_i u_j}{\partial x_j} + \frac{\partial p}{\partial x_i} = \frac{\partial}{\partial x_j}\left[\mu\left(\frac{\partial u_i}{\partial x_j} + \frac{\partial u_j}{\partial x_i}\right)\right] + \frac{\partial}{\partial x_i}\left[\lambda \frac{\partial u_k}{\partial x_k}\right] \tag{2.2}$$

$$\frac{\partial}{\partial t}\left[\rho\left(e + \frac{u^2}{2}\right)\right] + \frac{\partial}{\partial x_j}\left[\rho u_j\left(e + \frac{p}{\rho} + \frac{u^2}{2}\right)\right] = \frac{\partial}{\partial x_j}\left[u_k \mu\left(\frac{\partial u_j}{\partial x_k} + \frac{\partial u_k}{\partial x_j}\right) + u_j \lambda \frac{\partial u_k}{\partial x_k}\right] + \frac{\partial}{\partial x_j}\left(k \frac{\partial T}{\partial x_j}\right) \tag{2.3}$$

The above equations can be expressed in vector form as:

$$\frac{\partial \mathbf{U}_f}{\partial t} + \frac{\partial \mathbf{F}_{fj}}{\partial x_j} = \frac{\partial \mathbf{F}_{fvj}}{\partial x_j} \tag{2.4}$$

where:

$$\mathbf{U}_f = \begin{bmatrix} \rho \\ \rho u_i \\ \rho\left(e + \frac{u^2}{2}\right) \end{bmatrix} \tag{2.5}$$

$$\mathbf{F}_{fj} = \begin{bmatrix} \rho u_j \\ \rho u_i u_j + \delta_{ij} p \\ \rho u_j\left(e + \frac{p}{\rho} + \frac{u^2}{2}\right) \end{bmatrix} \tag{2.6}$$

$$\mathbf{F}_{fvj} = \begin{bmatrix} 0 \\ \mu\left(\frac{\partial u_i}{\partial x_j} + \frac{\partial u_j}{\partial x_i}\right) + \delta_{ij}\lambda \frac{\partial u_k}{\partial x_k} \\ u_k \mu\left(\frac{\partial u_j}{\partial x_k} + \frac{\partial u_k}{\partial x_j}\right) + u_j \lambda \frac{\partial u_k}{\partial x_k} + k \frac{\partial T}{\partial x_j} \end{bmatrix} \tag{2.7}$$

The transport coefficients, μ, λ and k, appearing in the these equations are discussed in chapter six.

2.2-b Inviscid Equations.

The inviscid equations can easily be obtained from Eqs. (2.4) by setting the transport coefficients to zero. This eliminates the viscous flux vector, and so the equations of motion become:

$$\frac{\partial \mathbf{U}_f}{\partial t} + \frac{\partial \mathbf{F}_{fj}}{\partial x_j} = \mathbf{0} \tag{2.8}$$

with $\mathbf{U}_f$ and $\mathbf{F}_{fj}$ defined by Eqs. (2.5) and (2.6).

The quasi-one-dimensional equations of motion are obtained from Eqs. (2.8) by replacing the j = 1 and j = 2 derivatives with a source term representing area changes in those directions, as follows:

$$\frac{\partial \mathbf{U}_f}{\partial t} + \frac{\partial \mathbf{F}_f}{\partial x} = \Omega_f \tag{2.9}$$

where:

$$\mathbf{U}_f = \begin{bmatrix} \rho \\ \rho u \\ \rho\left(e + \frac{u^2}{2}\right) \end{bmatrix} \tag{2.10}$$

$$\mathbf{F}_f = \begin{bmatrix} \rho u \\ \rho u^2 + p \\ \rho u\left(e + \frac{p}{\rho} + \frac{u^2}{2}\right) \end{bmatrix} \tag{2.11}$$

$$\Omega_f = -\begin{bmatrix} \rho u \\ \rho u^2 \\ \rho u\left(e + \frac{p}{\rho} + \frac{u^2}{2}\right) \end{bmatrix} \frac{d}{dx} \ln A \tag{2.12}$$

Both the viscous equations, Eqs. (2.4), and the inviscid equations, Eqs. (2.8), can be derived purely from conservation principles. No reference to the composition of the gas is necessary, and they therefore apply equally well to perfect gases and chemically reacting gases.

The principal differences between perfect and real gas models lie in two areas. Firstly, additional equations must be introduced to represent the chemical behaviour of a reacting gas. The form of these additional equations depends on whether or not the chemistry is modelled in equilibrium. Secondly, the state equations describing the thermodynamic behaviour of the gas differ considerably, depending on the gas model chosen.

2.3 THE CONSERVATION LAWS FOR COMPONENT SPECIES.

In situations where chemical reactions are out of equilibrium, conservation equations are introduced to describe the internal production of component species. For viscous flows, these equations are further complicated by additional mass diffusion terms. However, nonequilibrium aspects of this work address either translational or chemical relaxation, and therefore only the species production rate equations for inviscid flows are required. These equations are:

$$\frac{\partial \rho \eta_s}{\partial t} + \frac{\partial \rho u_j \eta_s}{\partial x_j} = \dot{\omega} \tag{2.13}$$

where the subscript s represents each species present in the gas mixture. Equations (2.13) can be written in vector form, similar to Eq. (2.4) as:

$$\frac{\partial \mathbf{U}_c}{\partial t} + \frac{\partial \mathbf{F}_{cj}}{\partial x_j} = \Omega_c \tag{2.14}$$

where:

$$\mathbf{U}_c = \left[\rho \eta_s\right] \tag{2.15}$$

$$\mathbf{F}_{cj} = \left[\rho u_j \eta_s\right] \tag{2.16}$$

$$\Omega_c = \left[\dot{\omega}_s\right] \tag{2.17}$$

Equations (2.13) are not fully independent, but are related to the global mass conservation equation. One species production rate equation can be replaced by the algebraic relation:

$$\sum_s \hat{M}_s \eta_s = 1 \tag{2.18}$$

Furthermore, if the gas is composed of more than one element, nuclear conservation equations can be used to eliminate an additional production rate equation, reducing the number of independent rate equations to (s-2).

The full set of equations representing an inviscid chemical nonequilibrium flow may be written by combining Eq. (2.8) with Eq. (2.14) to give:

$$\frac{\partial \mathbf{U}}{\partial t} + \frac{\partial \mathbf{F}_j}{\partial x_j} = \Omega \tag{2.19}$$

where:

$$\mathbf{U} = \begin{bmatrix} \mathbf{U}_f \\ \mathbf{U}_c \end{bmatrix} \tag{2.20}$$

$$\mathbf{F} = \begin{bmatrix} \mathbf{F}_f \\ \mathbf{F}_c \end{bmatrix} \tag{2.21}$$

$$\Omega = \begin{bmatrix} 0 \\ \Omega_c \end{bmatrix}. \tag{2.22}$$

2.4 THE LAW OF MASS ACTION.

If the chemical production rates are small in relation to the flux terms, they may be set to zero and Eqs. (2.13) become redundant. This is the frozen flow limit, where the chemical composition is fixed at its initial condition. The gas chemistry in this case does not need to be computed.

The opposite extreme arises when the chemical production rates are large relative to the flux terms. In this case, chemical reactions proceed comparatively quickly and so remain always in equilibrium. Again the production rate equations become redundant. However, the gas composition is not now fixed at its initial condition, but must be computed from equilibrium considerations.

The specific concentrations of the component species in equilibrium can be found from the law of mass action in the form:

$$\frac{\prod_s (\eta_s)^{\nu''_{sr}}}{\prod_s (\eta_s)^{\nu'_{sr}}} = K_r \tag{2.23}$$

where the stoichiometric coefficients, ν'_{sr} and ν''_{sr}, are found by writing the reaction equations as:

$$\sum_s \nu'_{sr} X_s \leftrightarrow \sum_s \nu''_{sr} X_s \,. \tag{2.24}$$

The equilibrium constants in terms of the specific concentrations are given by:

$$K_r = \left(\frac{p_0}{\rho \hat{R} T}\right)^{\sum_s (\nu''_{sr} - \nu'_{sr})} K_{pr} . \qquad (2.25)$$

Finally, the equilibrium constants in terms of partial pressures can be related to the thermodynamic state of the gas through the Gibbs free energy at the standard state (Kuo, 1986):

$$K_{pr} = \exp\left(-\frac{\Delta \hat{g}_r^0}{\hat{R}T}\right). \qquad (2.26)$$

Equations (2.23) represent r equations for the s unknown species, and there are therefore a further (s-r) equations required to complete the chemical description of the gas. These follow from the nuclear conservation equations expressing the fact that the total number of atomic nuclei remains constant.

2.5 EQUATIONS OF STATE.

The equations of motion represented by Eq. (2.4), Eq. (2.8) or Eq. (2.19) are not fully determined until the thermodynamic state equations are defined. Two state equations are generally required to describe a gas, although perfect gas models often combine these into a single equation of state. A caloric equation is required to relate internal energy to temperature and a thermal equation is necessary to relate temperature to pressure and density. In their generic form, the state equations may be written as follows.

Caloric equation of state: $$e = e(T, \eta_s) . \qquad (2.27)$$

Thermal equation of state: $$p = p(\rho, T, \eta_s) . \qquad (2.28)$$

At high temperatures and low densities, where the mean free path is sufficiently large for the finite volume of atoms and molecules to be considered negligible, air can be modelled as a chemically reacting mixture of thermally perfect component species. In this case the state equations take the form:

$$e = \sum_s \eta_s \hat{e}_s(T) \qquad (2.29)$$

$$p = \sum_s \eta_s \hat{R} \rho T . \qquad (2.30)$$

If the gas remains in chemical equilibrium, its composition can be expressed as a function of density and temperature only, and Eqs. (2.27) and (2.28) can be reduced to:

$$e = e(\rho, T) \tag{2.31}$$

$$p = p(\rho, T) . \tag{2.32}$$

Techniques for modelling Eqs. (2.31) and (2.32) are the subjects of chapter four.

If a gas is thermally perfect, the specific gas constant is independent of the state of the gas, and Eq. (2.30) reduces to:

$$p = R_0 \rho T \tag{2.33}$$

Furthermore, if the gas is also calorically perfect, its specific heats are independent of the state of the gas, and Eq. (2.29) reduces to:

$$e = c_v T \tag{2.34}$$

Equations (2.33) and (2.34) can then be combined to give the simple relation:

$$p = (\gamma - 1)\rho e \tag{2.35}$$

High temperature air deviates from perfect gas behaviour because the assumptions on which Eqs. (2.33) and (2.34) are based cease to be valid. Firstly, vibrational excitation of the diatomic species causes an increase in the heat capacity of the gas and caloric imperfections become evident. Secondly, chemical reactions change the molar mass of the gas and its specific gas constant changes, introducing thermal imperfections.

Chapter Three

COMPUTATIONAL GAS DYNAMICS

The equations of motion presented in chapter two form a set of nonlinear partial differential equations describing the flow field. There is a limited number of analytic solutions to these equations, even when perfect gas behaviour is assumed. For chemically active imperfect gas mixtures and generalized boundary conditions, analytic solutions become intractable. In such situations, numerical solutions must be sought. It is therefore important to highlight the mathematical aspects of these equations pertinent to developing numerical algorithms for their solution.

The following analysis concentrates on mixtures of thermally perfect gases in chemical equilibrium. Transport phenomena are neglected.

3.1 THE MATHEMATICAL CHARACTER OF THE FLOW EQUATIONS.

The viscous conservation laws expressed by Eqs. (2.4) form an hybrid system of parabolic-hyperbolic second order partial differential equations (Hirsch, 1989b). Eliminating the diffusive terms by setting the transport coefficients to zero leads to the unsteady Euler equations, Eqs. (2.8), which are a set of purely hyperbolic first order partial differential equations. The unsteady Euler equations therefore exhibit the wave like properties associated with hyperbolic convection equations.

The analysis of the Euler equations for an equilibrium reacting gas is more involved than for perfect gases, because of the complexity of the state equations. In general, it is not possible to find simple expressions for Eqs. (2.31) and (2.32), so the generic form of these equations must be retained.

3.1-a Linearization of the Equations of Motion.

The system of equations under investigation are the quasi-one-dimensional Euler equations for equilibrium air, represented by Eqs. (2.9). These can be written in a linearized form by expressing the flux vector **F** in terms of the solution vector **U**. Dropping the subscript f from Eqs. (2.9), on the understanding that no chemical relaxation equations are required, the form of these equations becomes:

$$\frac{\partial \mathbf{U}}{\partial t} + A\frac{\partial \mathbf{U}}{\partial x} = \Omega \qquad (3.1)$$

where:
$$A = \frac{\partial \mathbf{F}}{\partial \mathbf{U}} . \tag{3.2}$$

Equation (3.2) is evaluated in appendix one to give:

$$A = \begin{bmatrix} 0 & 1 & 0 \\ \chi - (2-\kappa)\frac{u^2}{2} & (2-\kappa)u & \kappa \\ (\chi + \kappa\frac{u^2}{2} - h_o)u & h_o - \kappa u^2 & (1+\kappa)u \end{bmatrix} \tag{3.3}$$

where:
$$h_o = h + \frac{u^2}{2} . \tag{3.4}$$

In deriving the Jacobian, the thermal state equation is assumed to be a function of mass density and internal energy density, such that:

$$p = p(\rho, \varepsilon) \tag{3.5}$$

The choice of dependent variables in this equation is largely subjective, and alternatives are discussed in section 5.2. With the state equation written in the form of Eq. (3.5), the thermodynamic derivatives appearing in the Jacobian matrix are:

$$\chi = \left(\frac{\partial p}{\partial \rho}\right)_\varepsilon = \left(\frac{\partial p}{\partial \rho}\right)_e + \frac{e}{\rho}\left(\frac{\partial p}{\partial e}\right)_\rho \tag{3.6}$$

$$\kappa = \left(\frac{\partial p}{\partial \varepsilon}\right)_\rho = \frac{1}{\rho}\left(\frac{\partial p}{\partial e}\right)_\rho \tag{3.7}$$

3.1-b Variable Transformations and the Compatibility Relations.

In order to establish the hyperbolic nature of Eqs. (3.1) for a general equation of state, it is necessary to show that the eigenvalues of the Jacobian A are all real. This is most easily shown if the equations are first transformed into primitive variables. Defining the vector of primitive variables **V** as:

$$\mathbf{V} = \begin{bmatrix} \rho \\ u \\ p \end{bmatrix} = \begin{bmatrix} \rho \\ m/\rho \\ p(\rho, E) \end{bmatrix} \tag{3.8}$$

The Jacobian of the transformation between conserved and primitive variables is given by:

$$M^{-1} = \frac{\partial \mathbf{V}}{\partial \mathbf{U}} \tag{3.9}$$

Evaluating this gives:

$$M^{-1} = \begin{bmatrix} 1 & 0 & 0 \\ -\frac{u}{\rho} & \frac{1}{\rho} & 0 \\ \chi + \kappa\frac{u^2}{2} & -u\kappa & \kappa \end{bmatrix} \tag{3.10}$$

which is inverted to give:

$$M = \begin{bmatrix} 1 & 0 & 0 \\ u & \rho & 0 \\ \frac{u^2}{2} - \frac{\chi}{\kappa} & \rho u & \frac{1}{\kappa} \end{bmatrix}. \tag{3.11}$$

Equations (3.1) can now be written in terms of the primitive variables as:

$$\frac{\partial \mathbf{V}}{\partial t} + \tilde{A}\frac{\partial \mathbf{V}}{\partial x} = \tilde{\Omega} \tag{3.12}$$

where:

$$\tilde{A} = M^{-1}AM = \begin{bmatrix} u & \rho & 0 \\ 0 & u & \frac{1}{\rho} \\ 0 & \chi + \kappa h & u \end{bmatrix} \tag{3.13}$$

$$\tilde{\Omega} = M^{-1}\Omega = -\begin{bmatrix} \rho u \\ 0 \\ \rho u(\chi + \kappa h) \end{bmatrix} \frac{d}{dx} \ln A \,. \tag{3.14}$$

The group $\chi + \kappa h$ can be identified as the equilibrium speed of sound as follows. Firstly, the second law of thermodynamics can be expressed in the form:

$$\rho T ds = d\varepsilon - h\, d\rho \tag{3.15}$$

from which:

$$\left(\frac{\partial \varepsilon}{\partial \rho}\right)_s = h \,. \tag{3.16}$$

Secondly, differentiating Eq. (3.5) with respect to density while holding entropy constant, the equilibrium speed of sound is given by:

$$\left(\frac{\partial p}{\partial \rho}\right)_s = \left(\frac{\partial p}{\partial \rho}\right)_\varepsilon + \left(\frac{\partial p}{\partial \varepsilon}\right)_\rho \left(\frac{\partial \varepsilon}{\partial \rho}\right)_s . \tag{3.17}$$

Hence, from the definitions of χ and κ, Eqs. (3.6) and (3.7):

$$c_e^2 = \chi + \kappa h \tag{3.18}$$

Equations (3.12) can now be decoupled by diagonalizing the $\tilde{A}$ matrix. The eigenvalues of $\tilde{A}$ are first found from:

$$\left| \tilde{A} - I\lambda \right| = 0 \tag{3.19}$$

which gives:

$$\lambda_1 = u \tag{3.20}$$

$$\lambda_2 = u + c_e \tag{3.21}$$

$$\lambda_3 = u - c_e . \tag{3.22}$$

These eigenvalues are all real and therefore, because Jacobians A and $\tilde{A}$ are similar, Eqs. (3.1) are hyperbolic. $\tilde{A}$ can now be diagonalized by computing a transformation based on its left eigenvectors:

$$l_1^T = \left(1 \quad 0 \quad -\frac{1}{c_e^2} \right) \tag{3.23}$$

$$l_2^T = \left(0 \quad 1 \quad \frac{1}{\rho c_e} \right) \tag{3.24}$$

$$l_3^T = \left(0 \quad 1 \quad -\frac{1}{\rho c_e} \right) \tag{3.25}$$

The transformation matrix takes the form:

$$L^{-1} = \frac{\partial W}{\partial V} \tag{3.26}$$

where:
$$L^{-1} = \begin{bmatrix} 1 & 0 & -\frac{1}{c_e^2} \\ 0 & 1 & \frac{1}{\rho c_e} \\ 0 & 1 & -\frac{1}{\rho c_e} \end{bmatrix} \tag{3.27}$$

Inverting Eq. (3.27) gives:

$$L = \begin{bmatrix} 1 & \frac{\rho}{2c_e} & -\frac{\rho}{2c_e} \\ 0 & \frac{1}{2} & \frac{1}{2} \\ 0 & \frac{\rho c_e}{2} & -\frac{\rho c_e}{2} \end{bmatrix}. \tag{3.28}$$

Finally, Eqs. (3.1) can be written:

$$\frac{\partial W}{\partial t} + \Lambda \frac{\partial W}{\partial x} = L^{-1}\tilde{\Omega} \tag{3.29}$$

where:
$$\Lambda = L^{-1}\tilde{A}L = \begin{bmatrix} u & 0 & 0 \\ 0 & u+c_e & 0 \\ 0 & 0 & u-c_e \end{bmatrix} \tag{3.30}$$

and:
$$L^{-1}\tilde{\Omega} = \begin{bmatrix} 0 \\ -uc_e \\ uc_e \end{bmatrix} \frac{d}{dx} \ln A \, . \tag{3.31}$$

Equations (3.29) are the compatibility relations for an equilibrium reacting gas. They form a set of three independent wave equations describing the propagation of the characteristic variables w_1, w_2 and w_3 at wave speeds u, $u+c_e$ and $u-c_e$ respectively. They differ from the equivalent perfect gas equations only in the formulation of the speed of sound.

3.1-c A Comment on the Characteristic Variables.

For a general equilibrium gas with state equation described by Eq. (3.5), variations in internal energy density can be expressed as:

$$d\varepsilon = \frac{1}{\kappa} dp - \frac{\chi}{\kappa} d\rho \, . \tag{3.32}$$

The second law of thermodynamics expressed by Eq. (3.15) can then be invoked to establish the relationship:

$$d\rho - \frac{dp}{c_e^2} = -\frac{\kappa\rho T}{c_e^2} ds \ . \tag{3.33}$$

From Eqs. (3.26), dw_1 is identified as:

$$dw_1 = d\rho - \frac{dp}{c_e^2} \ . \tag{3.34}$$

The first component of the compatibility relations, Eqs. (3.29), describes the propagation of the property w_1 throughout the flow field, such that:

$$\frac{\partial w_1}{\partial t} + u \frac{\partial w_1}{\partial x} = 0 \ . \tag{3.35}$$

Combining Eqs. (3.33) to (3.35) leads to:

$$\frac{\partial s}{\partial t} + u \frac{\partial s}{\partial x} = 0 \ . \tag{3.36}$$

This equation describes the convection of entropy along path lines and so the first of the compatibility relations expresses the fact that for any equilibrium inviscid gas flow, entropy is conserved. In this respect, perfect and equilibrium gas flows are identical.

From Eq. (3.33), for an isentropic process in an equilibrium gas:

$$dp = c_e^2 \, d\rho \ . \tag{3.37}$$

The second and third components of Eqs. (3.26) can then be written as:

$$dw_2 = du + \frac{c_e}{\rho} d\rho \tag{3.38}$$

$$dw_3 = du - \frac{c_e}{\rho} d\rho \ . \tag{3.39}$$

Integrating these equations gives:

$$w_2 = u + \int \frac{c_e}{\rho} d\rho \tag{3.40}$$

$$w_3 = u - \int \frac{c_e}{\rho} d\rho \ . \tag{3.41}$$

For an isentropic perfect gas flow, sonic speed can be expressed as a function of density only. Equations (3.40) and (3.41) can then be integrated to give closed forms for the characteristic variables. This is, however, no longer the case for an equilibrium gas, where in general:

$$c_e = c_e(\rho, \varepsilon) \tag{3.42}$$

Closed forms for the characteristic variables do not therefore exist. Numerical integration schemes and boundary treatments which rely on such closed form equations for the characteristics must therefore be reformulated before being applied to an equilibrium gas. Characteristic boundary treatments are discussed in section 5.5.

3.2 DISCRETIZATION OF THE EQUATIONS OF MOTION.

In order to compute a numerical solution for Eqs. (2.4), (2.8) or (2.9), they must first be approximated by a set of algebraic equations. Computational techniques can then be used to solve these equations. The techniques available for reducing the equations of motion to a form in which they can be solved numerically are discussed in this section.

Discontinuities within the flow field are correctly captured only if the equations of motion are discretized in their conservative form, given by Eqs. (2.4) for viscous fluids and Eq. (2.8) for inviscid fluids. No attempt has been made to solve the viscous equations here and consequently only solution techniques for the Euler equations have been investigated.

Steady state solutions for the Euler equations are generally achieved through a time marching approach, principally because the steady state Euler equations are hybrid hyperbolic-elliptic equations at subsonic speeds, which are difficult to solve. Time dependent terms are therefore retained and used to develop iterative numerical algorithms which afford steady state solutions.

3.2-a Temporal Discretization.

Two families of techniques for discretizing the time derivatives in Eqs. (2.8) can be identified. Explicit methods relate unknown variables at a given time step to known variables from previous time steps only. Each grid point can therefore be advanced forward in time independently of its neighbours. Implicit methods, on the other hand, simultaneously advance every grid point, and are therefore more complex than their explicit counterparts.

Explicit methods are widely used in solving both the viscous and inviscid equations, because of their numerical simplicity and their suitability for vectorization on modern computers. Historically, explicit techniques such as Lax-Wendroff and MacCormack schemes were developed at an early stage (MacCormack, 1969). However, these early schemes are based on combined space and time differencing,

which can lead to time step dependence for the steady state solution (Qin, 1987). Stable explicit schemes with independent time integration, based on Runge-Kutta time stepping schemes, can be defined (Jameson et al., 1981) which circumvent both the time step dependence problems and some of the restrictive stability requirements of earlier schemes.

Implicit techniques involve more computation per time step, because large matrix inversions are required to advance solutions. However, the stability characteristics of such schemes are greatly improved over explicit methods, with allowable time steps being restricted only by accuracy requirements (Beam and Warming, 1976). Implicit schemes are of great importance within chemically reacting flow simulations, because the stiffness associated with fast reactions can impose an unacceptably short time step on an explicit algorithm (Oran and Boris, 1987).

3.2-b Spatial Discretization.

The form of discretization applied to the time derivatives appearing in Eqs. (2.8) dictates the allowable time step and the time accuracy of a numerical algorithm. The fidelity of the converged solution, however, is largely governed by the treatment of spatial terms. As with the time derivatives, there are two broad classes of technique which can be applied to discretize these terms - central differencing and upwind differencing.

Central differencing is the more straight forward technique to apply. The MacCormack, Jameson and Beam-Warming schemes referenced earlier are all examples of centrally differenced schemes. However, central difference schemes lack dissipation, and therefore give rise to large oscillations at discontinuities in the flow field. This occurs because a centrally based scheme tries to represent derivatives near shock waves using information on both sides of the shock - a representation which is clearly invalid if the shock is a true discontinuity in the flow field. The success of centrally based schemes in capturing shock waves depends on the construction of artificial dissipation terms which damp oscillations (Jameson et al. 1981). However, these additional viscous terms tend to smear shock waves over several grid points, turning them into steep gradients rather than discontinuities. A degree of numerical experiment is therefore required to establish the best compromise between damping oscillations and smearing the shock.

Upwind schemes utilize the hyperbolic nature of the equations of motion to construct dissipative algorithms (Wang, 1990). Such schemes correctly account for the wave like behaviour of the flow. Crisp resolution of shocks is achieved at the expense of greater complexity of the numerical algorithms. In order to construct stable

upwind schemes, flux terms must be separated into forward and backward propagating components and the appropriate directional differencing applied to each component. Flux splitting followed by differencing leads to flux-vector split schemes (Anderson et al., 1985). Flux differencing followed by splitting forms an alternative approach known as flux-difference splitting. The schemes described by Roe (1981), Osher and Solomon (1982) and Osher and Chakravarthy (1983) fall into this category.

3.3 SHOCK WAVES.

In the absence of second order viscous terms, entropy is conserved throughout the flow field, according to Eq. (3.36). No physical mechanism exists within the gas model to generate entropy. Mathematically, shocks appearing in solutions to the Euler equations must be represented by true discontinuities, with the states on either side of the discontinuity being related by the Rankine-Hugoniot equations. The principal difficulty with numerical shock capturing schemes is in correctly representing this discontinuity. Furthermore, there is no mathematical reason why expansion shocks cannot exist within an inviscid flow, despite their obvious physical impossibility.

The transformation relations defined by Eqs. (3.10) and (3.27) can be applied to the viscous equations, Eqs. (2.4), to give, in an analogous fashion to the derivation of Eq. (3.36):

$$\frac{\partial s}{\partial t} + u\frac{\partial s}{\partial x} = \frac{2\mu+\lambda}{\rho T}\left(\frac{\partial u}{\partial x}\right)^2 + \frac{1}{\rho T}\frac{\partial}{\partial x}\left(k\frac{\partial T}{\partial x}\right). \qquad (3.43)$$

Equation (3.43) describes the convection of entropy along path lines in a viscous flow, and is valid at every point in the flow field. Most importantly, this equation provides the mechanism by which entropy can be produced within the fluid, and therefore permits solutions including shock waves of finite thickness. However, for most continuum flows of engineering interest, shock wave thicknesses are of the order of 10^{-6} m, and can only be resolved on exceptionally fine grids. Shocks in viscous flows can therefore be treated numerically as discontinuities.

Chapter Four

EQUILIBRIUM AIR MODELS

This chapter presents techniques for modelling the equilibrium thermochemical properties of air. The types of available model are split into two families; data base models and physical models. These are illustrated in Figure 4.1. It can be seen that both families of techniques subdivide into two classes. Anderson (1989) gives a review of these techniques, and includes a discussion of their application to an existing perfect gas Euler code.

The first section of the chapter examines the family of data base models, giving information on both lookup tables and curve fitting techniques. This section comprises mainly of review material and it details the two important sets of curve fits used later in this dissertation.

The substance of this chapter concerns the development of a fast computational module for the calculation of equilibrium state properties. This module is based on the works of Prabhu and Erickson (1988) and Poll and Hodgson (1988), extending the techniques presented by those authors to include the calculation of derivative information required to form the flux Jacobian and to calculate sonic speeds. The air model chosen is at present restricted to six species and three reactions and is therefore simpler than the ionized air models chosen by the above authors, but extension to more complex chemistry is possible. Differences between the air models leads to a modification in the low temperature treatment of air, which is also discussed in this chapter.

The equilibrium air module falls into the class of simplified physical model, and relies on the solution of the law of mass action to compute the chemical state of the gas. Simplifications over the full statistical mechanics model of air come about through the use of curve fits for the thermodynamic properties of the component species. Anderson (1992) reports the original development of these routines.

4.1 CURVE FITTING TECHNIQUES AND DATA BASE MODELS.

In chapter two, the equations of state were discussed and it was indicated that for a gas everywhere in local thermochemical equilibrium any one state variable is a function only of two independent variables. The most important state equations from the point of view of CFD calculations are those relating pressure and temperature, which appear

in the flux terms of both the Euler and Navier-Stokes equations, to density and internal energy, which appear in the vector of conserved variables.

Tabulated data relating these variables have been available for a number of years (Mansen and Hodge, 1961; Hilsenrath and Klein, 1965). Such data are based on accurate evaluation of statistical mechanics expressions combined with carefully executed experimental work. FORTRAN programs have been developed (Lomax and Inouye, 1964) using these data to construct lookup tables for coefficients of interpolation functions. These programs require extensive data bases to represent the complex behaviour of air at high temperature, and are therefore quite demanding on memory resources. Also, only limited information is available from such a data base, since only the variables tabulated can be retrieved. While this is not necessarily a limitation during the time dependent solution of a fluid flow problem, is does limit the amount of thermodynamic and chemical data which can be extracted from the final converged solution.

The principal disadvantage of data base techniques is the amount of information required to provide sufficient accuracy. Over 10 000 tabulated values, equivalent to 78 Kbytes for 8 byte single precision calculations, may be required for each state relationship. Also, programs such as NASA-Ames RGAS which rely on the lookup of cubic coefficients for interpolation functions are too cumbersome and slow to be efficiently implemented in CFD codes (Srinivasan et al., 1987a).

Curve fitting techniques are closely related to the data base methods described above. They may be regarded as coming from the same family of techniques, but are characterized by the small number of data points necessary to represent the interpolation curves, and the sophisticated nature of these curves. Amongst the earliest attempts at applying this approach to air thermochemistry is the work of Grabau (1959). The success of this approach is exemplified by its adoption by Tannehill and Mugge (1974) and subsequently by Srinivasan et al. (1987a) to produce accurate and convenient curve fits for air thermodynamic properties. Both these sets of curve fits have been used in applications within this dissertation, and are now summarized briefly.

4.1-a Grabau Type Transition Functions.

The concept originally proposed by Grabau was to use a discrete set of smooth curves, linked by carefully constructed transition functions, to represent the thermodynamic behaviour of air. The general form of the Grabau type transition function is:

$$z(x,y) = f_1(x,y) + \frac{f_2(x,y) - f_1(x,y)}{1 \pm \exp(f_3(x,y))} \qquad (4.1)$$

16 Coefficient Curve Fits	24 Coefficient Curve fits
$p = p(e,\rho)$, $c_e = c_e(e,\rho)$	$p = p(e,\rho)$, $c_e = c_e(e,\rho)$
$T = T(e,\rho)$	$T = T(e,\rho)$, $s = s(e,\rho)$
$h = h(p,\rho)$, $T = T(p,\rho)$	$h = h(p,\rho)$, $T = T(p,\rho)$
	$\rho = \rho(p,s)$, $c_e = c_e(p,s)$
	$e = e(p,s)$

Table 4.1 Available Curve Fits for Equilibrium Air Properties.

where $f_1(x,y)$ and $f_2(x,y)$ are polynomial functions between which a smooth transition is required. The sign in front of the exponential term in Eq. (4.1) dictates whether the transition is odd or even. If this sign is positive, the transition will be odd and contain an inflection point, as shown in Figure 4.2a, and if the sign is negative, the transition will be even and contain no inflection, as in Figure 4.2b. The coefficients of $f_3(x,y)$ determine the rate of the transition between $f_1(x,y)$ and $f_2(x,y)$.

Tannehill and Mugge developed sixteen coefficient curve fits based on transition functions of the above form. The curve fits developed by Srinivasan et al. are similar in form, but improved smoothness is achieved through the use of twenty-four coefficients. Table 4.1 gives the properties to which these curves were fitted. The curves of particular interest in developing CFD codes are:

$$p = p(\rho,e) \tag{4.2}$$

$$c_e = c_e(\rho,e). \tag{4.3}$$

An estimate of temperature as a function of both mass density and specific internal energy is necessary for the application of some physical models of equilibrium air to CFD codes. It is also therefore important to have data for the curves:

$$T = T(\rho,e). \tag{4.4}$$

For both the sixteen and twenty-four coefficient curve fits, the thermal state equation, Eq. (4.2), is expressed in terms of the enthalpy/internal energy ratio $\bar{\gamma}$:

$$p = (\bar{\gamma} - 1)\,\rho\, e\,. \tag{4.5}$$

Grabau type curve fits are developed for $\bar{\gamma}$, expressed in terms of base ten logarithms of density and internal energy:

$$\bar{\gamma}(y,z) = f_1(y,z) + \frac{f_2(y,z) - f_1(y,z)}{1 \pm \exp(f_3(y,z))} \tag{4.6}$$

where:

$$y = \log_{10}(\rho/\rho_0) \tag{4.7}$$

$$z = \log_{10}(e/e_0). \tag{4.8}$$

The calorific state equation, Eq. (4.4), is expressed directly as curve fits for the base ten logarithm of temperature:

$$\log_{10}(T/T_0) = g_1(y,z) + \frac{g_2(y,z) - g_1(y,z)}{1 \pm \exp(g_3(y,z))} \tag{4.9}$$

where:

$$x = \log_{10}(p/p_0) \tag{4.10}$$

$$y = \log_{10}(\rho/\rho_0) \tag{4.11}$$

$$z = x - y\,. \tag{4.12}$$

To evaluate x in Eq. (4.10), pressure is first calculated using Eq. (4.6) for $\bar{\gamma}$ in Eq. (4.5).

4.1-b Sixteen Coefficient Curve Fits.

For the sixteen coefficient curve fits the interpolation and transition functions for $\bar{\gamma}$ in Eq. (4.6) are defined as follows:

$$f_1(y,z) = a_1 + a_2y + a_3z + a_4yz + a_5y^2 + a_6z^2 + a_7yz^2 + a_8z^3 \tag{4.13}$$

$$f_2(y,z) - f_1(y,z) = a_9 + a_{10}y + a_{11}z + a_{12}yz \tag{4.14}$$

$$f_3(y,z) = (a_{13} + a_{14}y)(z + a_{15}y + a_{16}) \tag{4.15}$$

where y and z are given by Eqs. (4.7) and (4.8) respectively.

The temperature curve fit functions for Eq. (4.9) are given by:

$$g_1(y,z) = b_1 + b_2y + b_3z + b_4yz + b_5z^2 + b_6y^2 + b_7y^2z + b_8yz^2 \tag{4.16}$$

$$g_2(y,z) - g_1(y,z) = b_9 + b_{10}y + b_{11}z + b_{12}yz + b_{13}z^2 \tag{4.17}$$

$$g_3(y,z) = (b_{14}y + b_{15})(z + b_{16}) \tag{4.18}$$

with y and z defined by Eqs. (4.11) and (4.12) respectively.

To evaluate the sonic speed, the isentropic density derivative of Eq. (4.5) can be formed. This is done in appendix two, with the following result:

$$c_e^2 = e\left[(\bar{\gamma} - 1)\left(\bar{\gamma} + \left(\frac{\partial\bar{\gamma}}{\partial \ln e}\right)_\rho \right) + \left(\frac{\partial\bar{\gamma}}{\partial \ln \rho}\right)_e \right]. \tag{4.19}$$

This expression is formulated in terms of derivatives of Eq. (4.6). As such, discontinuities and a lack of smoothness in these curves mean Eq. (4.19) is not

accurate if used directly. For the sixteen coefficient curve fits, correction coefficients are introduced to improve their accuracy. The sonic speed curve fits become:

$$c_e^2 = e\left[K_1 + (\bar{\gamma} - 1)\left(\bar{\gamma} + K_2\left(\frac{\partial\bar{\gamma}}{\partial \ln e}\right)_\rho\right) + K_3\left(\frac{\partial\bar{\gamma}}{\partial \ln \rho}\right)_e\right]. \qquad (4.20)$$

The coefficients a_1 to a_{16}, b_1 to b_{16} and K_1 to K_3 are given in Tables A3.1 and A3.2, appendix three. For this set of curves, all transitions are odd and the signs before the exponential terms in Eqs. (4.6) and (4.9) are always positive.

4.1-c Twenty-Four Coefficient Curve Fits.

The following interpolation and transition functions define the twenty-four coefficient curve fits for $\bar{\gamma}$ in Eq. (4.6):

$$f_1(y,z) = a_1 + a_2y + a_3z + a_4yz + a_5y^2 + a_6z^2 + a_7y^2z + a_8yz^2 + a_9y^3 + a_{10}z^3 \qquad (4.21)$$

$$f_2(y,z) - f_1(y,z) = a_{11} + a_{12}y + a_{13}z + a_{14}yz + a_{15}y^2 + a_{16}z^2 + a_{17}y^2z + a_{18}yz^2 + a_{19}y^3 + a_{20}z^3 \qquad (4.22)$$

$$f_3(y,z) = a_{21} + a_{22}y + a_{23}z + a_{24}yz \qquad (4.23)$$

with y and z again being given by Eqs. (4.7) and (4.8).

The temperature curve fit functions in this case become:

$$g_1(y,z) = b_1 + b_2y + b_3z + b_4yz + b_5y^2 + b_6z^2 + b_7y^2z + b_8yz^2 + b_9y^3 + b_{10}z^3 \qquad (4.24)$$

$$g_2(y,z) - g_1(y,z) = b_{11} + b_{12}y + b_{13}z + b_{14}yz + b_{15}y^2 + b_{16}z^2 + b_{17}y^2z + b_{18}yz^2 + b_{19}y^3 + b_{20}z^3 \qquad (4.25)$$

$$g_3(y,z) = b_{21} + b_{22}y + b_{23}z + b_{24}yz \qquad (4.26)$$

with y and z defined from Eqs. (4.11) and (4.12) respectively.

These curve fits are regarded as being sufficiently smooth at their junctions to permit the application of Eq. (4.19) directly to compute the speed of sound. Furthermore although the temperature curve fits are all still odd transitions, the $\bar{\gamma}$ curves now include an even function, and so the coefficients a_1 to a_{24} in Table A3.3, appendix three, are supplemented with the sign of the exponential term appearing in Eq. (4.6). The coefficients b_1 to b_{24} appear in Table A3.4.

The two sets of curve fits presented above have specific advantages and disadvantages which dictate the application to which they may be put. Firstly, both sets of curve fits lack any form of physical input. Whilst the chosen form of the curves is based on sound physical reasoning, the polynomial coefficients are derived purely on a mathematical basis, and indeed the choice of junction points between curves or how many coefficients to retain in any one curve is quite subjective. Unlike the physically based models presented later, only one thermodynamic variable is available from each curve, and therefore only very limited information can be gained with the curves presented here. Secondly, it is not possible to have one continuous curve representing the full range of possible densities and internal energies, and so there are inevitable discontinuities in the derivatives at junctions. These discontinuities cause noticeable inaccuracies in the derivative information used to calculate sonic speed.

Figures 4.3a and 4.3b illustrate the pressure curve fits, for densities in the range 1.225×10^{-6} kg m^{-3} to 122.5 kg m^{-3}. Similar plots for the same density range are produced for the temperature curve fits and shown in Figures 4.4a and 4.4b. The sonic speed data are plotted in Figures 4.5a and 4.5b and this clearly illustrates the problems in continuity with the derivatives appearing in Eq. (4.19).

The speed of execution of the routines which evaluate the different curve fits will be discussed in relation to the physical techniques outlined next.

4.2 PHYSICALLY BASED TECHNIQUES.

The most fundamental technique for relating state variables in an equilibrium gas is to apply the results of statistical mechanical calculations, together with accurately measured data on the properties of the component species, to the gas mixture. Such an approach allows any gas mixture to be modelled, providing the assumption of equilibrium thermochemistry is valid. However, by the nature of the algebra involved in solving the large numbers of highly nonlinear equations associated with the law of mass action, and the complexity of the partition functions for electrically excited gases at high temperatures, such an approach is impractical within a time dependent CFD code. Alternative techniques are discussed by Balakrishnan et al. (1983). In particular, free energy minimization procedures have been adopted (Gordon and McBride, 1971) to develop large and versatile programs, such as the NASA-Lewis CEC72 and TRAN76 codes. These programs are considerably more versatile than the NASA RGAS program mentioned earlier, and can deal with combusting hydrocarbon mixtures as well as high temperature air. However, the cumbersome nature of the free

energy minimization technique led to the development of fast methods for calculating equilibrium compositions in the late sixties (Erickson et al., 1966). These techniques have been further refined to deal specifically with equilibrium air mixtures (Prabhu and Erickson, 1988; Poll and Hodgson, 1988).

The application of these fast techniques to state calculations within CFD codes still requires some research. The remainder of this chapter discusses the development of a state calculation module based on a restricted chemical model of air, which includes routines for computing important thermodynamic derivatives.

4.3 THE CHEMICAL COMPONENTS.

The model chosen to represent air involves the following six species: diatomic oxygen O_2, diatomic nitrogen N_2, monatomic oxygen O, nitric oxide NO, monatomic nitrogen N and argon Ar. All ionized species and trace species such as carbon dioxide, water vapour and ozone are ignored. Table 4.2 gives the atomic weights of these species, together with their low temperature concentrations.

Argon is treated as an inert gas, and does not participate in any reactions. It does, however, make a contribution to the internal energy of the gas mixture which must be accounted for. The reactions which take place between the above species are:

$$O_2 + X \leftrightarrow 2O + X \qquad \Delta\hat{e}_R{}^0 = 493.566 \text{ kJ mol}^{-1} \quad (4.27)$$

$$N_2 + O_2 \leftrightarrow 2NO \qquad \Delta\hat{e}_R{}^0 = 181.342 \text{ kJ mol}^{-1} \quad (4.28)$$

$$N_2 + X \leftrightarrow 2N + X \qquad \Delta\hat{e}_R{}^0 = 941.636 \text{ kJ mol}^{-1}. \quad (4.29)$$

			Proportions at T = 273.15 K	
Species Number	Species	Molar Mass $\hat{M}$ (kg mol^{-1})	Mole Fraction x	Mass Fraction α
1	O_2	0.031999	0.2095	0.2314
2	N_2	0.028013	0.7809	0.7553
3	O	0.015999	0.0000	0.0000
4	NO	0.030006	0.0000	0.0000
5	N	0.014007	0.0000	0.0000
6	Ar	0.039948	0.0096	0.0133
Molar Mass of Air at 273.15 K = $\Sigma(x_i\hat{M}_i)$ = 0.028963 kg mol^{-1}				

Table 4.2 Low Temperature Composition of Air.

In these reactions, species X represents a catalytic body which is present only to act as an energy source for the reaction. For example, diatomic oxygen cannot spontaneously decompose into oxygen atoms - a catalyst must collide with the molecule and supply sufficient energy to break the atomic bond. This catalytic body may be any atom or molecule present in the mixture and, for an equilibrium calculation, is of little significance. It is, however, vitally important in nonequilibrium calculations, where different catalysts yield different reaction rates. The $\Delta\hat{e}_R{}^0$ above are the heats of reaction at absolute zero for the three reactions.

4.4 THERMODYNAMIC PROPERTIES OF THE COMPONENT SPECIES.

Consideration is being given to developing an equilibrium air thermochemical model suitable for atmospheric reentry problems. The hypersonic velocities associated with such problems are most likely to be encountered at high altitudes. Figure 4.6 shows a velocity altitude map for the space shuttle STS-1 flight reentry. From this it can be seen that the hypersonic portion of that flight took place mainly in the upper layers of the atmosphere. These are regions of very low density and pressure - of the order of 10^{-4} kg m^{-3} and 10^{-2} kN m^{-2} respectively at 65 km altitude. As a consequence, the component species of the gas can be assumed to be thermally perfect and no viral corrections are required (Poll and Hodgson, 1988).

Two techniques have been investigated for calculating the species thermodynamic properties. Firstly, the direct evaluation of partition functions associated with the internal energy modes of atoms and molecules has been implemented. This is potentially the most versatile method, as it does not restrict the gas mixture to particular components. However, the complex functions describing the electronic behaviour of a species give rise to large computing times. Compromises can be made by neglecting some of the high order electronic terms, but significant loss in accuracy at high temperatures then results.

The second, and preferred, technique for calculating the species properties relies on fitting polynomial curves to statistically calculated data. This has the advantage of improving the accuracy of the calculations, at the expense of some generality.

4.4-a Direct Calculation of Species Properties from Partition Functions.

Energy contributions due to the different modes within an atom or molecule can be evaluated from their partition functions using the relations (Vincenti and Kruger, 1965):

$$\hat{e} = \hat{R}\, T^2 \frac{\partial}{\partial T} \ln Q + \hat{e}_f^0 \tag{4.30}$$

$$\hat{c}_v = \left(\frac{\partial \hat{e}}{\partial T}\right)_\rho \tag{4.31}$$

where $\hat{e}$ is the molar internal energy, $\hat{c}_v$ is the molar heat at constant volume and Q is the statistically evaluated partition function. The partition function for each species can be broken down into components representing the individual energy modes within the atom or molecule, which yield expressions of the form (Mayer and Mayer, 1940):

$$Q_{translational} = V\left(\frac{2\pi mkT}{h^2}\right)^{3/2} \tag{4.32}$$

$$Q_{electronic} = \sum_{i\geq 0} g_i\, e^{-\theta_i/T} \tag{4.33}$$

$$Q_{rotational} = \frac{1}{\sigma}\left(\frac{T}{\theta_r}\right) \tag{4.34}$$

$$Q_{vibrational} = \frac{1}{1 - e^{-\theta_v/T}}. \tag{4.35}$$

In Eq. (4.34), σ is a symmetry factor and is one for heteronuclear molecules and two for homonuclear molecules. Rotational and vibrational contributions can apply only to the diatomic species. These partition functions give the molar heats and internal energies for diatomic species in the form:

$$\hat{c}_v = \hat{R}\left[\frac{3}{2} + \frac{1}{\left(\sum_i g_i\, e^{-\theta_i/T}\right)^2} \sum_{i>j}\sum_j \left(g_i \frac{\theta_i}{T} - g_j \frac{\theta_j}{T}\right)^2 e^{-(\theta_i+\theta_j)/T} + 1 + \left(\frac{\theta_v/T}{e^{\theta_v/2T} - e^{-\theta_v/2T}}\right)^2\right] \tag{4.36}$$

$$\hat{e} = \hat{R}T\left[\frac{3}{2} + \frac{1}{\sum_i g_i\, e^{-\theta_i/T}} \sum_i g_i \frac{\theta_i}{T} e^{-\theta_i/T} + 1 + \frac{\theta_v/T}{e^{\theta_v/T} - 1}\right] + \hat{e}_f^0. \tag{4.37}$$

It is noted that the above expressions are based on an harmonic oscillator model of the vibrational modes, and no account is taken of coupling effects between the rotation and vibration in diatomic molecules. Contributions due to electronic excitation are in an open ended form, and it is desirable only to consider those terms in the series which

Species	θ_1 (K)	θ_2 (K)	g_0	g_1	g_2	σ	θ_r (K)	θ_v (K)	$\hat{e}_f^0$ (kJ mol^{-1})
O_2	11 390		3	2		2	2.1	2 270	0.0
N_2			1			2	2.9	3 390	0.0
O	228	326	5	3	1				246.783
NO	174		2	2		1	2.5	2 740	90.671
N			4						470.818
Ar			1						0.0

Table 4.3 Statistical Constants for the Main Chemical Components of Air.

contribute significantly to $\hat{c}_v$ or $\hat{e}$. From a practical point of view, it is necessary to limit the number of terms in this series to avoid lengthy computing times for $\hat{c}_v$. Table 4.3 presents the data used to calculate $\hat{c}_v$ and $\hat{e}$ for the six species in Table 4.2 (Moore, 1949, et seq).

To give the desired computational speed, a maximum of three terms (including the constant term g_0) are retained in the electronic partition functions. High temperature electronic effects, anharmonic effects and coupling effects are therefore neglected. This leads to errors at temperatures above 6000 K, particularly notable in the molar heat variations. Figure 4.7a presents the distribution of molar heat calculated from Eq. (4.36) for 200 K to 6000 K. Monatomic gases are observed to have $\hat{c}_v$ equal to $3/2\ \hat{R}$ ($\approx$ 12.5 J mol^{-1} K^{-1}) at 200 K and diatomic gases have $\hat{c}_v$ equal to $5/2\ \hat{R}$ ($\approx$ 20.8 J mol^{-1} K^{-1}). At this temperature rotation is fully excited in diatomic molecules, and there is some small electronic contribution, notably in species containing oxygen. Vibrational modes excite at temperatures between 400 K and 2000 K, giving a smooth rise in $\hat{c}_v$ up to about 29.1 J mol^{-1} K^{-1} for diatomic species. Departures from this value are due to electronic effects, most notable in O_2. Corresponding data for $\hat{e}$ are presented in Figure 4.8a.

4.4-b Polynomial Curve Fits for the Species Properties.

It was pointed out earlier that the statistical mechanics approach described above is potentially more accurate, but this has to be traded against increased computing times. Applying a curve fit to detailed calculations of the species properties allows a fast close approximation to them, which can extend the range of the model at no additional computational expense. This is the approach adopted by Prabhu and Erickson (1988), and the curve fits presented in that reference are used here. Additional curve fits are presented by Park (1990), but these are formulated in terms of the total number density

and as such are not suited to an equilibrium calculation, unless it is based on an iterative quasi-nonequilibrium method.

A fifth order polynomial in T is fitted to data for $\hat{c}_p$ and the required properties are calculated as follows. It is first noted that $\hat{c}_p$ is a function of temperature only so that:

$$\hat{c}_p(T) = \left(\frac{\partial \hat{h}}{\partial T}\right)_p = \hat{R} \sum_{j=1}^{5} a_j T^{j-1} . \tag{4.38}$$

The differential relationships:

$$d\hat{h} = \hat{c}_p(T)\, dT \tag{4.39}$$

$$d\hat{s} = \hat{c}_p(T) \frac{dT}{T} - \hat{R} \frac{dp}{p} \tag{4.40}$$

lead to:

$$\begin{aligned} \hat{h} &= \int_{T0}^{T} \hat{c}_p(T)\, dT + \hat{h}^{T0} \\ &= \hat{R}\left[\sum_{j=1}^{5} \frac{a_j}{j} T^j + a_6 \right] \end{aligned} \tag{4.41}$$

and:

$$\begin{aligned} \hat{s}^0 &= \int_{T0}^{T} \frac{\hat{c}_p(T)}{T} dT + \hat{s}^{T0} \\ &= \hat{R}\left[a_1 \ln T + \sum_{j=2}^{5} \frac{a_j}{j-1} T^{j-1} + a_7 \right]. \end{aligned} \tag{4.42}$$

Data are available for curve fits in this form for temperatures in the range 200 K to 15 000 K, and are presented in Table A3.7, appendix three. At temperatures at or below about 300 K, the statistical mechanics approach with the data presented in Table 4.3 will yield more accurate results, down to temperatures approaching θ_r (generally of the order of 3 K for the gases considered). However, such low temperatures are very unlikely to be encountered in trans-atmospheric flight, and will be associated with thermal imperfections in the species behaviour which invalidate the present method. The curve fit approach is therefore adopted as it is more efficient at high temperatures. Figure 4.7b is provided for comparison with the statistical data on $\hat{c}_v$ in the range 200 K to 6 000 K. Figure 4.8b presents the data for $\hat{e}$ throughout this temperature range and compares with the statistical calculation in Figure 4.8a.

The molar heats $\hat{c}_v$ are plotted throughout the range 200 to 15 000 K in Figure 4.9 using the curve fit data, from which it is observed that the neglect of high temperature terms in the electronic partition functions has a pronounced effect on both monatomic and diatomic species characteristics. Diatomic species are further influenced by both coupling and anharmonic effects, therefore the simplified statistical expressions cannot be considered valid at temperatures above about 8 000 K.

4.5 EQUILIBRIUM SPECIES CONCENTRATIONS.

The method used for calculating the equilibrium species concentrations is a modified version of that presented by Prabhu and Erickson (1988). The chemical equilibrium equations, corresponding to Eqs. (4.27) to (4.29) are combined with mass conservation equations to give a non-linear set of algebraic equations for the equilibrium concentrations.

The equilibrium equations associated with the three reactions under consideration are as follows:

$$K_{p1} = \frac{(p_3/p_0)^2}{(p_1/p_0)} \tag{4.43}$$

$$K_{p2} = \frac{(p_4/p_0)^2}{(p_1/p_0)(p_2/p_0)} \tag{4.44}$$

$$K_{p3} = \frac{(p_5/p_0)^2}{(p_2/p_0)} . \tag{4.45}$$

The p_i represent the partial pressures of each species i (see Table 4.2) and the K_{p_j} are the equilibrium constants for reactions one to three, evaluated at standard state pressure $p_0 = 101\ 325\ N\ m^{-2}$. It is more convenient to work in mole mass ratios η_i rather than partial pressures, so the relation:

$$p_i = \eta_i \rho \hat{R} T \tag{4.46}$$

is applied to give:

$$\frac{\eta_3^2}{\eta_1} = \frac{p_0}{\rho \hat{R} T} K_{p1} = K_1 \tag{4.47}$$

$$\frac{\eta_4^2}{\eta_1 \eta_2} = K_{p2} = K_2 \tag{4.48}$$

$$\frac{\eta_5^2}{\eta_2} = \frac{p_0}{\rho \hat{R} T} K_{p3} = K_3 . \tag{4.49}$$

The K_{p_j} are related to the species properties through the Gibbs free energy in the standard state:

$$\Delta \hat{g}_j^0 = -\hat{R}\, T \ln K_{p_j} . \tag{4.50}$$

If the reactions are written in the form:

$$\sum_{i=1}^{N} \nu_{ij}' X_i \leftrightarrow \sum_{i=1}^{N} \nu_{ij}'' X_i \tag{4.51}$$

then the free energy change $\Delta \hat{g}_j^0$ will be given by (see Kuo, 1986):

$$\Delta \hat{g}_j^0 = \sum_i \nu_{ij}'' \hat{g}_i^0 - \sum_i \nu_{ij}' \hat{g}_i^0 . \tag{4.52}$$

The $\hat{g}_i^0$ represent the standard state free energy for species i and can be evaluated from the species properties already presented:

$$\hat{g}_i^0 = \hat{h}_i - T \hat{s}_i^0 . \tag{4.53}$$

For any given temperature and density, Eqs. (4.47) to (4.49) provide three equations for the five unknown mole mass ratios η_i. As already stated, argon is considered to be inert in this case and so η_6 has a fixed value corresponding to the low temperature concentration of the species:

$$\eta_6 = \eta_{Ar} . \tag{4.54}$$

Two further equations are required before the problem is fully defined. These follow from the nuclear conservation equations, relating the number of oxygen and nitrogen nuclei under any condition to their low temperature concentrations:

$$2\eta_1 + \eta_3 + \eta_4 = \eta_O \tag{4.55}$$

$$2\eta_2 + \eta_4 + \eta_5 = \eta_N . \tag{4.56}$$

These six equations, Eqs. (4.47) to (4.49) and (4.54) to (4.56), can be combined and solved to yield the mole mass ratios, or specific concentrations, of the species at any temperature and density.

4.6 Low Temperature Considerations.

In the solution of the six equilibrium equations, the ratio $K_2/(K_1K_3)$ occurs frequently, and care is therefore required at low temperatures, where the concentrations of

monatomic nitrogen and oxygen tend to zero. This results in a division by zero error when K_1 or K_3 is smaller than a machine representable number. This problem is circumvented by assuming that if the natural log of K_{p3} is less than -100, reaction three does not take place and similarly if the natural log of K_{p1} is less than -100 then reaction one does not occur. Figure 4.10 shows the temperature variation of the reaction constants between 200 K and 1 500 K. From this it can be deduced that below about 530 K neither reaction one nor reaction three can be simulated and below 1 000 K only reaction three cannot be simulated. There are therefore three cases to be considered.

4.6-a Very low temperature: ln K_{p1} < -100, T < 530 K.

In this case reactions one and three do not occur. Mole mass ratios for O and N are correspondingly set to zero, and the remaining mole mass ratios are calculated from the equilibrium balance of reaction two.

Assumption:
$$\eta_3 = 0 \tag{4.57}$$
$$\eta_5 = 0\,, \tag{4.58}$$

equilibrium:
$$\frac{\eta_4^2}{\eta_1\eta_2} = K_2\,, \tag{4.59}$$

nuclear conservation:
$$2\eta_1 + \eta_4 = \eta_O \tag{4.60}$$
$$2\eta_2 + \eta_4 = \eta_N \tag{4.61}$$
$$\eta_6 = \eta_{Ar}\,. \tag{4.62}$$

4.6-b Low temperature: ln K_{p3} < -100, T < 1 000 K.

Reaction one now leads to some oxygen dissociation, and the assumption of negligible monatomic oxygen is no longer considered valid. Nitrogen dissociation has not yet begun.

Assumption:
$$\eta_5 = 0\,, \tag{4.63}$$

equilibrium:
$$\frac{\eta_3^2}{\eta_1} = K_1 \tag{4.64}$$
$$\frac{\eta_4^2}{\eta_1\eta_2} = K_2\,, \tag{4.65}$$

nuclear conservation:

$$2\eta_1 + \eta_3 + \eta_4 = \eta_O \tag{4.66}$$

$$2\eta_2 + \eta_4 = \eta_N \tag{4.67}$$

$$\eta_6 = \eta_{Ar}\,. \tag{4.68}$$

4.6-c High temperature: T > 1 000 K

All three reactions are important and so the full solution for the six unknown mole mass ratios is required.

Equilibrium:

$$\frac{\eta_3^2}{\eta_1} = K_1 \tag{4.69}$$

$$\frac{\eta_4^2}{\eta_1\eta_2} = K_2 \tag{4.70}$$

$$\frac{\eta_5^2}{\eta_2} = K_3\,, \tag{4.71}$$

nuclear conservation:

$$2\eta_1 + \eta_3 + \eta_4 = \eta_O \tag{4.72}$$

$$2\eta_2 + \eta_4 + \eta_5 = \eta_N \tag{4.73}$$

$$\eta_6 = \eta_{Ar}\,. \tag{4.74}$$

4.7 SOLUTION OF THE EQUILIBRIUM EQUATIONS.

The solution of the equilibrium equations for the very low temperature case is a straight forward non-iterative process. Equations (4.59), (4.60) and (4.61) are combined to give:

$$\eta_4 = -\left\{ \frac{(\eta_N + \eta_O) + \left[(\eta_N^2 + \eta_O^2) + (16/K_2 - 2)\eta_N\eta_O\right]^{1/2}}{2\,(4/K_2 - 1)} \right\}. \tag{4.75}$$

Mole mass ratios for the remaining unknown species follow from Eqs. (4.60) and (4.61):

$$\eta_1 = 1/2(\eta_O - \eta_4) \tag{4.76}$$

$$\eta_2 = 1/2(\eta_N - \eta_4)\,. \tag{4.77}$$

For the higher temperature models, it is not possible to solve the problem analytically, as above. Instead a fourth order polynomial in η_3 is solved using a Newton-Raphson iteration. This polynomial takes the form:

$$\sum_{j=0}^{4} b_j \eta_3^j = 0 \tag{4.78}$$

where:

$$b_0 = 2K_1\eta_O^2 \tag{4.79}$$

$$b_1 = (K_eK_3 - 4)K_1\eta_O \tag{4.80}$$

$$b_2 = 2K_1 - K_eK_3K_1 - 8\eta_O - K_2(\eta_N - \eta_O) \tag{4.81}$$

$$b_3 = 8 - K_2 - 2K_eK_3 \tag{4.82}$$

$$b_4 = (8 - 2K_2)/K_1 \tag{4.83}$$

and:

$$K_1K_3K_e^2 = K_2 \,. \tag{4.84}$$

The above coefficients relate to the high temperature model of air. In the low temperature case, the same polynomial is solved, but the coefficients are modified because the product K_3K_e must be set to zero.

An initial guessed value of η_3 is calculated by assuming η_5 is zero and that η_2 can be approximated by:

$$\eta_2 = \frac{\eta_N}{2} \,. \tag{4.85}$$

This leads to the equations:

$$2\eta_1 + \eta_3 + \eta_4' = \eta_O \tag{4.86}$$

$$\eta_1 = \frac{\eta_3^2}{K_1} \tag{4.87}$$

$$\frac{\eta_4'}{\eta_3} = \left(\frac{\eta_N K_2}{2K_1}\right)^{1/2} \,. \tag{4.88}$$

where η_4' is an approximate value of η_4. This initial guess is very good for the low temperature model where Eq. (4.85) is a close approximation. However, at higher temperatures, η_5 starts to become significant and the guess is consequently less accurate. However, it is observed that three iterations of a Newton-Raphson scheme is sufficient to provide a converged solution for η_3 in Eq. (4.78), even at high temperatures. From Eqs. (4.86) to (4.88), the initial value of η_3 is given by:

$$\eta_3{}^1 = \left[\left\{ \frac{K_1}{4} + \left(\frac{\eta_N K_1 K_2}{32} \right)^{1/2} \right\}^2 + \frac{K_1 \eta_O}{2} \right]^{1/2} - \left\{ \frac{K_1}{4} + \left(\frac{\eta_N K_1 K_2}{32} \right)^{1/2} \right\} . \quad (4.89)$$

Equation (4.78) is now solved in three iterations by the following Newton-Raphson algorithm:

$$f(\eta_3{}^n) = \sum_{j=0}^{4} b_j (\eta_3{}^n)^j \quad (4.90)$$

$$f'(\eta_3{}^n) = \sum_{j=1}^{4} j b_j (\eta_3{}^n)^{j-1} \quad (4.91)$$

$$\eta_3{}^{n+1} = \eta_3{}^n - \frac{f(\eta_3{}^n)}{f'(\eta_3{}^n)} . \quad (4.92)$$

Having achieved a converged solution for η_3, the remaining unknown mole mass ratios follow algebraically. For the low temperature model, the unknowns are:

$$\eta_5 = 0 \quad (4.93)$$

$$\eta_4 = \eta_O - \eta_3 - \frac{2}{K_1} \eta_3{}^2 \quad (4.94)$$

$$\eta_2 = \frac{1}{2}(\eta_N - \eta_4) \quad (4.95)$$

$$\eta_1 = \frac{1}{2}(\eta_O - \eta_3 - \eta_4) \quad (4.96)$$

$$\eta_6 = \eta_{Ar} . \quad (4.97)$$

For the high temperature model, they are:

$$\eta_5 = \frac{\eta_O - \eta_3 - \frac{2}{K_1} \eta_3{}^2}{K_c \eta_3} \quad (4.98)$$

$$\eta_4 = K_c \eta_3 \eta_5 \quad (4.99)$$

$$\eta_2 = \frac{1}{2}(\eta_N - \eta_4 - \eta_5) \quad (4.100)$$

$$\eta_1 = \frac{1}{2}(\eta_O - \eta_3 - \eta_4) \quad (4.101)$$

$$\eta_6 = \eta_{Ar} . \quad (4.102)$$

Figures 4.11a to 4.11c illustrate the chemical composititon of air as calculated using the above method at densities of 1.225×10^{-4} kg m^{-3}, 1.225 kg m^{-3} and 122.5 kg m^{-3}. These are plots of mole fractions against temperature in the range 200 K to 15 000 K. The relationship between the mole fractions and mole mass ratios is:

$$x_i = \frac{\eta_i}{\sum_{j=1}^{6} \eta_j} . \qquad (4.103)$$

With the chemical properties of the gas mixture now known, it is possible to calculate the associated thermodynamic properties.

4.8 THERMODYNAMIC PROPERTIES OF THE MIXTURE.

Having calculated the equilibrium chemical properties of the mixture for a given temperature and density, it is possible to compute the mixture thermodynamic properties. Of particular importance are the pressure and internal energy, but any thermodynamic variable can be calculated from the available information. The specific concentration of the mixture is given by:

$$\eta = \sum_{i=1}^{6} \eta_i . \qquad (4.104)$$

Pressure can then be found from the thermal state equation in the form:

$$p = \hat{R}\, \eta\, \rho\, T . \qquad (4.105)$$

Specific enthalpy is given by:

$$h = \sum_{i=1}^{6} \hat{h}_i\, \eta_i \qquad (4.106)$$

and specific internal energy follows from:

$$e = h - \hat{R}\, \eta\, T . \qquad (4.107)$$

The calculation of the mixture entropy is more complex. Returning to the differential form of the second law of thermodynamics, for a single species i:

$$T\, ds_i = dh_i - \frac{dp_i}{\rho} \qquad (4.108)$$

or, since $s_i = \eta_i \hat{s}_i$, $p_i = \hat{R}\eta_i\rho T$ and $dh_i = \eta_i \hat{c}_{pi} dT$:

$$d\hat{s}_i = \hat{c}_{pi} \frac{dT}{T} - \hat{R} \frac{dp_i}{p_i} . \qquad (4.109)$$

Integrating this expression then gives:

$$\hat{s}_i = \int_{T_0}^{T} \frac{\hat{c}_p}{T} dT \; - \; \hat{R} \int_{p_0}^{p_i} \frac{1}{p_i} dp_i \; + \; \hat{s}_i^{T_0} . \qquad (4.110)$$

The first and last terms on the right hand side of this equation are recognised from Eq. (4.42) to be the standard state entropy at $p_i = p_0$. Equation (4.110) therefore becomes:

$$\hat{s}_i = \hat{s}_i^0 - \hat{R} \ln \frac{p_i}{p_0} . \tag{4.111}$$

The mixture specific entropy will be the summation of the species entropies multiplied by their respective concentrations:

$$s = \sum_i \eta_i \hat{s}_i$$

$$s = \sum_i \left(\eta_i \hat{s}_i^0 - \hat{R} \eta_i \ln \frac{p_i}{p} - \hat{R} \eta_i \ln \frac{p}{p_0} \right)$$

$$s = - \hat{R} \eta \ln \frac{p}{p_0} + \sum_i \eta_i \left(\hat{s}_i^0 - \hat{R} \ln \frac{p_i}{p} \right) . \tag{4.112}$$

The partial pressures can be written in terms of mole mass ratios through an application of the thermal state equation, Eq. (4.105):

$$\ln \frac{p_i}{p} = \ln \frac{\hat{R} \eta_i \rho T}{\hat{R} \eta \rho T} = \ln \eta_i - \ln \eta . \tag{4.113}$$

		Enthalpy (x 10^6 J kg^{-1})			Entropy (x 10^3 J kg^{-1} K^{-1})		
Density (kg m^{-3})	Temp. (K)	Mollier Chart	Calculated Value	Difference	Mollier Chart	Calculated Value	Difference
12.88	1000	1.0470	1.0535	0.0065	7.1185	7.1277	0.0092
	2000	2.2673	2.2928	0.0255	7.7526	7.7800	0.0274
	3000	3.7001	3.7344	0.0343	8.2137	8.2435	0.0298
	6000	10.226	10.325	0.099	9.4530	9.4843	0.0313
	8000	16.083	16.101	0.018	10.182	10.176	0.006
	12000	32.907	32.735	0.172	11.715	11.698	0.017
0.1288	1000	1.0470	1.0535	0.0065	8.4299	8.4544	0.0245
	2000	2.2751	2.2956	0.0205	9.0783	9.1082	0.0299
	3000	4.0543	4.0785	0.0242	9.6605	9.6910	0.0305
	6000	13.407	13.542	0.135	11.514	11.572	0.058
	8000	30.939	30.862	0.075	13.790	13.782	0.008
1.288x10^{-4}	1000	1.0470	1.0535	0.0065	10.404	10.445	0.041
	2000	2.3617	2.3900	0.0283	11.096	11.147	0.051
	3000	6.9514	7.0344	0.0830	12.753	12.818	0.065

Table 4.4 Validation Data from Royal Aeronautical Society Mollier Charts.

Equation (4.112) can now be expressed in terms of total pressure and mole mass ratios, reproducing the result presented by Prabhu and Erickson (1988):

$$s = - \hat{R} \eta \ln \frac{p}{\eta p_0} + \sum_i \eta_i \left(\hat{s}_i^0 - \hat{R} \ln \eta_i \right) . \qquad (4.114)$$

The Gibbs free energy can also be calculated for the mixture:

$$g = h - Ts . \qquad (4.115)$$

Figure 4.12 illustrates the application of these equations to compute an enthalpy-entropy diagram. Lines of constant temperature and constant density are plotted against calculated values of enthalpy and entropy. The resulting chart has been compared with Mollier chart data published by the Royal Aeronautical Society (1962) and gives good agreement, as shown by the results in Table 4.4. It is noted, however, that the flattening of the chart in Figure 4.12 at high enthalpies and entropies is due to the mixture becoming fully dissociated and no further chemical changes taking place. This region of the chart is inaccurate, because of the lack of an ionization model. It is, however, useful to have an approximate prediction of conditions in this region, even without ionization modelled, in case the method should be used by a CFD code which allows accurate modelling within the general flow field, but where one or two points lie outside the valid enthalpy-entropy range.

A useful indication of when ionization is likely to become important is to evaluate the product of enthalpy and entropy and compare this to the parameter:

$$\iota = h s > 9.2 \times 10^6 \, J^2 \, kg^{-2} \, K^{-1} . \qquad (4.116)$$

4.9 Equilibrium and Frozen Speeds of Sound.

In an equilibrium flow calculation, it is important to be able to correctly evaluate the propagation speed of acoustic waves, particularly if a flux vector splitting or flux difference splitting technique is being used to discretize the fluid equations. Also, the frozen speed of sound[†] is important in nonequilibrium problems, and it is desirable to have a method for calculating this parameter at the equilibrium condition.

[†] In a purely equilibrium calculation, the frozen speed of sound is meaningless. If, however, account is taken of nonequilibrium effects, then high frequency components of an acoustic wave will propagate into the equilibrium free stream at the frozen speed of sound, and this becomes an important parameter. Also, the ratio of the frozen to equilibrium speed of sound gives an indication of how much an acoustic wave will distort due to nonequilibrium effects.

The equilibrium and frozen speeds of sound are given by the expressions:

$$c_e^2 = \left(\frac{\partial p}{\partial \rho}\right)_{s,\eta=\eta^*} \tag{4.117}$$

$$c_f^2 = \left(\frac{\partial p}{\partial \rho}\right)_{s,\eta} . \tag{4.118}$$

The constraints $\eta = \eta^*$ or η = constant must be imposed on the pressure derivative as well as the familiar constraint on entropy being constant because in a nonequilibrium gas, any thermodynamic variable is a function of not only any two other state variables, but also the chemical state of the gas. Imposing these constraints therefore leads to unique values for the pressure derivative, one of which permits an infinitely fast adjustment of the chemical state of the gas (c_e) and the other of which permits no chemical changes (c_f). The two propagation speeds therefore lie at extreme ends of the range of speeds at which a sound wave may propagate in a nonequilibrium gas.

Considering an equilibrium chemically reacting gas, the first and second laws of thermodynamics lead to the relation:

$$T\,ds = de - \frac{p}{\rho^2}\,d\rho . \tag{4.119}$$

This is equally valid for perfect, frozen or equilibrium gas models. In terms of specific enthalpy, this expression is:

$$T\,ds = dh - \frac{1}{\rho}\,dp . \tag{4.120}$$

The enthalpy of the reacting gas mixture has already been expressed as a function of temperature and the chemical state of the gas, Eq. (4.106). That is:

$$h = h\,(T, \eta_i) . \tag{4.121}$$

Differentiating this gives:

$$dh = (h)_T\,dT + \sum_{i=1}^{6} (h)_{\eta_i}\,d\eta_i \tag{4.122}$$

where:

$$(h)_T = \left(\frac{\partial h}{\partial T}\right)_{\eta_i} \tag{4.123}$$

$$(h)_{\eta_i} = \left(\frac{\partial h}{\partial \eta_i}\right)_{T,\eta_{j\neq i}} . \tag{4.124}$$

Furthermore, the species mole mass ratios in equilibrium are functions only of temperature and density:

$$\eta_i = \eta_i (\rho, T) \tag{4.125}$$

$$d\eta_i = (\eta_i)_\rho \, d\rho + (\eta_i)_T \, dT \tag{4.126}$$

where:

$$(\eta_i)_\rho = \left(\frac{\partial \eta_i}{\partial \rho}\right)_T \tag{4.127}$$

$$(\eta_i)_T = \left(\frac{\partial \eta_i}{\partial T}\right)_\rho . \tag{4.128}$$

The thermal state equation for a chemically reacting gas can be written:

$$p = \hat{R} \sum_{i=1}^{6} \eta_i \, \rho \, T \tag{4.129}$$

which in differential form becomes:

$$dp = \hat{R} \left(\sum_{i=1}^{6} \eta_i \, \rho \, dT + \sum_{i=1}^{6} \eta_i \, T \, d\rho + \rho \, T \sum_{i=1}^{6} d\eta_i \right). \tag{4.130}$$

Putting Eq. (4.126) into Eq. (4.130) yields:

$$dT = \frac{1}{\left[\eta + T \sum_i (\eta_i)_T\right]} \frac{dp}{\hat{R}\rho} - \frac{\left[\eta + \rho \sum_i (\eta_i)_\rho\right]}{\left[\eta + T \sum_i (\eta_i)_T\right]} \frac{T \, d\rho}{\rho} . \tag{4.131}$$

Substituting Eq. (4.126) into Eq. (4.122) gives:

$$dh = \left[(h)_T + \sum_i (h)_{\eta_i} (\eta_i)_T\right] dT + \left[\sum_i (h)_{\eta_i} (\eta_i)_\rho\right] d\rho . \tag{4.132}$$

Now putting Eq. (4.131) into Eq. (4.132), then applying the resulting expression for dh to the Tds equation in the form of Eq. (4.120) gives an expression for ds as a function of dp and dρ:

$$\left[\eta + T \sum_i (\eta_i)_T\right] T \, ds = \left\{\frac{1}{\hat{R}\rho}\left[(h)_T + \sum_i (h)_{\eta_i}(\eta_i)_T\right] - \frac{1}{\rho}\left[\eta + T \sum_i (\eta_i)_T\right]\right\} dp -$$

$$\left\{\frac{T}{\rho}\left[(h)_T + \sum_i (h)_{\eta_i}(\eta_i)_T\right]\left[\eta + \rho \sum_i (\eta_i)_\rho\right] -\right.$$

$$\left.\left[\sum_i (h)_{\eta_i}(\eta_i)_\rho\right]\left[\eta + T \sum_i (\eta_i)_T\right]\right\} d\rho . \tag{4.133}$$

The equilibrium speed of sound is now given by setting ds in Eq. (4.133) to zero:

$$\left(\frac{\partial p}{\partial \rho}\right)_{s,\eta_i=\eta_i^*} = \frac{\hat{R}T\left[(h)_T + \sum_i (h)_{\eta_i}(\eta_i)_T\right]\left[\eta + \rho\sum_i(\eta_i)_\rho\right]}{\left[(h)_T + \sum_i(h)_{\eta_i}(\eta_i)_T\right] - \hat{R}\left[\eta + T\sum_i(\eta_i)_T\right]} -$$

$$\frac{\hat{R}\rho\left[\sum_i(h)_{\eta_i}(\eta_i)_\rho\right]\left[\eta + T\sum_i(\eta_i)_T\right]}{\left[(h)_T + \sum_i(h)_{\eta_i}(\eta_i)_T\right] - \hat{R}\left[\eta + T\sum_i(\eta_i)_T\right]} . \qquad (4.134)$$

Equation (4.134) gives c^2 for an equilibrium gas. If the gas is frozen in any chemical state, the derivatives $(\eta_i)_T$ and $(\eta_i)_\rho$ will be zero, since no change in the chemistry of the gas can occur. Equation (4.134) then reduces to:

$$\left(\frac{\partial p}{\partial \rho}\right)_{s,\eta_i} = \frac{\hat{R}\eta T(h)_T}{(h)_T - \hat{R}\eta} \qquad (4.135)$$

which is c^2 in a frozen gas.

Furthermore, it is interesting to note that the product $\hat{R}\eta$ is the specific gas constant, R, and from Eq. (4.123), $(h)_T$ is the specific heat, c_p, for a chemically inert gas. If Eq. (4.134) is simplified to the perfect gas case, the result is therefore:

$$\left(\frac{\partial p}{\partial \rho}\right)_{s,\eta_i} = \frac{c_p}{c_p - R} RT = \gamma RT . \qquad (4.136)$$

This is the familiar result for a nonreacting perfect gas.

Once the chemical composition of the gas has been calculated, it is necessary to calculate the thermodynamic derivatives appearing in Eq. (4.134). The mixture enthalpy is given by Eq. (4.106). With the species molar enthalpies from Eq. (4.41), this can be differentiated directly to give $(h)_T$:

$$(h)_T = \hat{R}\sum_{i=1}^{6}\eta_i\left(\sum_{j=1}^{5} a_{ij}\,T^{j-1}\right) . \qquad (4.137)$$

Similarly $(h)_{\eta_i}$ is given by:

$$(h)_{\eta_i} = \hat{R}\left(\sum_{j=1}^{5}\frac{a_{ij}}{j}\,T^{j-1} + a_{i6}\right) . \qquad (4.138)$$

Calculation of the derivatives $(\eta_i)_T$ and $(\eta_i)_\rho$ is less straight forward. In the very low temperature case, where the η_i are explicit functions of the equilibrium coefficient

K_2 the derivatives are given by the differential forms of Eqs. (4.57) to (4.61), which lead to:

$$\delta\eta_4 = \frac{2\eta_1\eta_2}{4\eta_4 + K_2(\eta_1 + \eta_2)}\delta K_2 \tag{4.139}$$

$$\delta\eta_1 = -\frac{1}{2}\delta\eta_4 \tag{4.140}$$

$$\delta\eta_2 = -\frac{1}{2}\delta\eta_4 \tag{4.141}$$

$$\delta\eta_3 = 0 \tag{4.142}$$

$$\delta\eta_5 = 0 \tag{4.143}$$

where δ represents either $\partial/\partial\rho$ or $\partial/\partial T$.

The equations representing the low temperature model, Eqs. (4.63) to (4.67), can be written in differential form as:

$$2\eta_3\delta\eta_3 = K_1\delta\eta_1 + \eta_1\delta K_1 \tag{4.144}$$

$$2\eta_4\delta\eta_4 = K_2\eta_1\delta\eta_2 + K_2\eta_2\delta\eta_1 + \eta_1\eta_2\delta K_2 \tag{4.145}$$

$$2\delta\eta_1 + \delta\eta_3 + \delta\eta_4 = 0 \tag{4.146}$$

$$2\delta\eta_2 + \delta\eta_4 = 0\,. \tag{4.147}$$

This is a set of linear algebraic equations in the unknown chemical derivatives $\delta\eta_i$, which can be solved analytically to give:

$$\delta\eta_4 = \frac{\eta_1\eta_2\delta K_2 - \frac{\eta_1\eta_2}{2\eta_3}(K_1\delta K_2 - K_2\delta K_1)}{4\eta_4 + K_2(\eta_1 + \eta_2) + K_2\frac{\eta_2}{\eta_3} + \frac{1}{4}K_1K_2\frac{\eta_1}{\eta_3}} \tag{4.148}$$

$$\delta\eta_3 = \frac{2\eta_1\delta K_1 - K_1\delta\eta_4}{4\eta_3 + K_1} \tag{4.149}$$

$$\delta\eta_2 = -\frac{1}{2}\delta\eta_4 \tag{4.150}$$

$$\delta\eta_1 = -\frac{1}{2}(\delta\eta_3 + \delta\eta_4) \tag{4.151}$$

$$\delta\eta_5 = 0\,. \tag{4.152}$$

Unlike the low temperature models, in the high temperature case chemical derivatives must be found from the fourth order polynomial Eq. (4.78). Implicit differentiation of this equation leads to expressions for $(\eta_3)_T$ and $(\eta_3)_\rho$:

$$\delta\eta_3 = -\frac{\sum_{j=0}^{4} \delta b_j \eta_3^j}{\sum_{j=1}^{4} j b_j \eta_3^{j-1}} \quad . \tag{4.153}$$

The b_j are the coefficients in Eq. (4.78) and δb_j represent the temperature or density derivatives of these coefficients. The derivatives of these coefficients are found by differentiating Eqs. (4.79) to (4.83):

$$\delta b_0 = 2\eta_O^2 \delta K_1 \tag{4.154}$$

$$\delta b_1 = (K_e K_3 - 4)\eta_O \delta K_1 + K_1 K_e \eta_O \delta K_3 + K_1 K_3 \eta_O \delta K_e \tag{4.155}$$

$$\delta b_2 = 2\delta K_1 - (\eta_N - \eta_O)\delta K_2 - K_3 K_e \delta K_1 - K_1 K_e \delta K_3 - K_1 K_3 \delta K_e \tag{4.156}$$

$$\delta b_3 = -\delta K_2 - 2K_3 \delta K_e - 2K_e \delta K_3 \tag{4.157}$$

$$\delta b_4 = (-b_4 \delta K_1 - 2\delta K_2)/K_1 \, . \tag{4.158}$$

Having found $\delta\eta_3$ from the above expressions, the remaining chemical derivatives follow from Eqs. (4.98) to (4.101) in differential form:

$$\delta\eta_5 = \frac{2\eta_3}{K_1^2 K_e}\delta K_1 - \left(\frac{\eta_5}{\eta_3} + \frac{4}{K_1 K_e} + \frac{1}{K_e \eta_3}\right)\delta\eta_3 - \frac{\eta_5}{K_e}\delta K_e \tag{4.159}$$

$$\delta\eta_4 = \eta_3\eta_5\delta K_e + K_e\eta_5\delta\eta_3 + K_e\eta_3\delta\eta_5 \tag{4.160}$$

$$\delta\eta_2 = -\frac{1}{2}(\delta\eta_4 + \delta\eta_5) \tag{4.161}$$

$$\delta\eta_1 = -\frac{1}{2}(\delta\eta_3 + \delta\eta_4) \, . \tag{4.162}$$

In order to evaluate the above expressions for the chemical derivatives η_i, a knowledge of the derivatives of the equilibrium constants K_j is required. These are found from Eqs. (4.50) and (4.84). From (4.84):

$$\delta K_e = \frac{K_e}{2K_2}\left[\, \delta K_2 - K_3 K_e^2 \, \delta K_1 - K_1 K_e^2 \, \delta K_3 \,\right] . \tag{4.163}$$

From Eqs. (4.47) to (4.50):

$$K_1 = \exp\left[\frac{\hat{g}_1^0}{\hat{R}T} - 2\,\frac{\hat{g}_3^0}{\hat{R}T} + \ln\frac{p_0}{\rho\hat{R}T} \right] \tag{4.164}$$

$$K_2 = \exp\left[\frac{\hat{g}_1^0}{\hat{R}T} + \frac{\hat{g}_2^0}{\hat{R}T} - 2\,\frac{\hat{g}_4^0}{\hat{R}T} \right] \tag{4.165}$$

$$K_3 = \exp\left[\frac{\hat{g}_2^0}{\hat{R}T} - 2\,\frac{\hat{g}_5^0}{\hat{R}T} + \ln\frac{p_0}{\rho\hat{R}T} \right] . \tag{4.166}$$

Differentiating these equations will lead to expressions involving the derivatives of the Gibbs free energies, defined according to Eq. (4.53). As the standard state free energies are a function only of temperature, their density derivatives are all zero. The temperature derivatives can be found most easily by replacing the enthalpy and entropy in Eq. (4.53) by Eqs. (4.41) and (4.42), giving:

$$\hat{g}^0 = \int_{T0}^{T} \hat{c}_p\,dT + \hat{h}_f^{T0} - T\int_{T0}^{T} \frac{\hat{c}_p}{T}\,dT - T\,\hat{s}^{T0} \tag{4.167}$$

$$\frac{\partial}{\partial T}\left(\frac{\hat{g}^0}{\hat{R}\,T}\right) = \frac{\hat{c}_p}{\hat{R}\,T} - \frac{1}{\hat{R}\,T^2}\int_{T0}^{T} \hat{c}_p\,dT - \frac{\hat{h}_f^{T0}}{\hat{R}\,T^2} - \frac{\hat{c}_p}{\hat{R}\,T} \tag{4.168}$$

$$\frac{\partial}{\partial T}\left(\frac{\hat{g}^0}{\hat{R}\,T}\right) = -\frac{\hat{h}}{\hat{R}\,T^2} . \tag{4.169}$$

Utilising Eq. (4.169) for the five active species, and differentiating Eqs. (4.164) to (4.166) with respect to temperature or density leads to:

$$\frac{\partial K_1}{\partial T} = \frac{K_1}{T}\left[2\,\frac{\hat{h}_3}{\hat{R}T} - \frac{\hat{h}_1}{\hat{R}T} - 1 \right] \tag{4.170}$$

$$\frac{\partial K_2}{\partial T} = \frac{K_2}{T}\left[2\,\frac{\hat{h}_4}{\hat{R}T} - \frac{\hat{h}_2}{\hat{R}T} - \frac{\hat{h}_1}{\hat{R}T} \right] \tag{4.171}$$

$$\frac{\partial K_3}{\partial T} = \frac{K_3}{T}\left[2\,\frac{\hat{h}_5}{\hat{R}T} - \frac{\hat{h}_2}{\hat{R}T} - 1 \right] \tag{4.172}$$

$$\frac{\partial K_1}{\partial \rho} = -\frac{K_1}{\rho} \tag{4.173}$$

$$\frac{\partial K_2}{\partial \rho} = 0 \tag{4.174}$$

$$\frac{\partial K_3}{\partial \rho} = -\frac{K_3}{\rho} \quad . \tag{4.175}$$

All the chemical and thermodynamic derivatives appearing in Eq. (4.134) can now be calculated for each of the three air models, and it is therefore possible to compute the equilibrium speed of sound.

Equilibrium and frozen speed of sound variations with temperature are illustrated in Figures 4.13a to 4.13c, for three different densities. These show solutions of Eqs. (4.134) and (4.135). For comparison, the perfect gas, $\gamma = 1.4$, solution is also shown. It is noted that the low density case (Figure 4.13a) exhibits perfect gas-like behaviour at high temperatures. This is because the diatomic species become fully dissociated at these temperatures and no further chemical changes take place. This behaviour would be significantly modified if the presence of ionization were modelled.

It is also interesting to note that the fully dissociated gas behaves like a perfect gas with $R = 571.4$ J kg^{-1} K^{-1} and $\gamma = 1.40$. This specific gas constant corresponds to that expected from the low temperature data in Table 4.2. However, the value of γ for a fully monatomic gas would be expected to be 5/3 or 1.67. The departure from this value is explained by the high temperature behaviour of monatomic nitrogen, illustrated in Figure 4.9. It is seen that the molar heat of nitrogen increases by about 8.5 J mol^{-1} K^{-1} due to electronic contributions to the partition function. As this species composes over 78% of the gas, this causes the ratio of specific heats to fall significantly.

The ratio of sonic speeds, c_f/c_e, is plotted in Figure 4.14. These curves show where the derivative terms in Eq. (4.134) are large, corresponding to the two peaks. These are the points of maximum dissociation rate (with respect to temperature) firstly for oxygen and then for nitrogen. It is possible that flight conditions giving sonic speed ratios at or near these points in large sections of the flow field will require to be modelled out of equilibrium.

4.10 VALIDATION.

The scheme presented here has been validated against the twenty-four coefficient curve fits presented earlier and the Royal Aeronautical Society Mollier charts. For temperatures in the range 200 K to 15 000 K and densities from 1.225×10^{-6} kg m^{-3} to 1.225×10^{2} kg m^{-3} the equilibrium speed of sound, pressure and specific internal energy were calculated using the method presented here. The specified density and calculated internal energy were then applied to the curve fits to compute comparative values of pressure and equilibrium sonic speed. The data were then

	Mean	Max.	Min.	Std. Dev.
16 Coefficient Pressure	9.51	28.4	2.4	3.138
24 Coefficient Pressure	11.97	29.4	8.4	2.325
16 Coefficient Temperature	46.77	76.4	35.4	5.586
24 Coefficient Temperature	51.62	104.4	44.4	5.599
16 Coefficient Sonic Speed	52.41	77.2	41.2	3.867
24 Coefficient Sonic Speed	56.82	86.2	47.2	3.610
State Calculation without Sonic Speed	80.42	108.4	37.4	8.032
State Calculation with Sonic Speed	107.9	146.4	51.2	10.76

Table 4.5 Comparison Between Execution Times for Curve Fit Calculations and Thermochemical State Calculations, in microseconds.

nondimensionalized consistently and plotted in Figures 4.15 and 4.16. In these figures, continuous lines represent the results of the current scheme, and crosses correspond to curve fit data.

From Figure 4.15 it is clear that there is excellent agreement between the calculated and curve fit pressure data. There is some departure of the two methods at low densities and high energies, because of the presence of ionization data in the curve fits.

A significant advantage of this scheme over the curve fits is evident from Figure 4.16. The calculated sonic speed data are smooth and continuous throughout the applied temperature range. The curve fit data, because it relies on differentiating sets of discontinuous curves, cannot match this smoothness, and significant errors are apparent at junctions between curves - most noticeable at lower densities. Again the lack of an ionization model in the present scheme accounts for the low density, high energy departures noted in Figure 4.16, but otherwise agreement is very good.

Table 4.5 gives the results of comparing the execution speeds for routines evaluating both sets of curve fits presented in Section 4.1 and the thermochemical state calculation technique. Computation times (in microseconds) are given for state calculations both with and without associated sonic speed calculations.

Chapter Five

IMPLEMENTATION OF EQUILIBRIUM AIR MODELS IN THE CFD ENVIRONMENT

In chapter four, the types of model available for computing the thermochemical state of equilibrium high temperature air were discussed and an air model was developed based on the solution of the laws of mass action. However, no reference was made as to how this model could be used in the numerical solution of the equations of motion. The problems associated with implementing equilibrium air models within CFD codes are therefore addressed in this chapter.

To illustrate the application of these techniques, the solution of a quasi-one-dimensional inviscid nozzle problem is presented. The specific differences between the perfect and real gas numerical routines for solving this problem lie in two areas; the formation of the implicit operator for the chosen scheme and the application of boundary conditions. In chapter three, it was pointed out that for a general real gas, the characteristic variables cannot be integrated to give simple closed forms for the Riemann invariants. This can lead to difficulties when including real gas effects in some of the modern high resolution schemes. However, progress is being made in this direction (Abgrall, 1991; Glaister, 1988; Grossman and Walters, 1989; Liou et al., 1990; Suresh and Liou, 1991; Vinokur and Montagne, 1990). The scheme used here is an implicit time, central space differenced one (Beam and Warming, 1976) with added artificial dissipation (Jameson et al., 1981). This scheme is chosen for its numerical simplicity. The principal difficulties encountered are therefore with the implementation of the equilibrium gas dynamics, rather than the numerical analysis. The experience gained with developing the implicit operator for this scheme can be extrapolated to more advanced algorithms, which are discussed as a topic for future research in chapter seven.

5.1 INVERSION OF THE STATE EQUATIONS.

The method for calculating the equilibrium thermochemical state of the gas mixture presented in chapter four has been formulated on the basis that the independent variables are the fluid density and temperature. Mass density was chosen primarily because it is one of the conserved fluid variables, as well as a principal thermodynamic variable. Pressure could be used as an alternative to mass density, but such a formulation would be less useful in solving fluid flow problems. Ideally, the second

independent variable would be specific internal energy, as this relates closely to the conserved total energy density:

$$E = \rho\left(e + \frac{u^2}{2}\right). \tag{5.1}$$

However, it is not possible to use this variable because each component species carries its own internal energy, and the mixture internal energy can only be determined once the composition of the gas is known. Moreover, since the gas is in thermal equilibrium, each component must have the same temperature, irrespective of the gas composition. Temperature therefore makes an essential second choice as independent variable.

As a consequence of using mass density and temperature to specify the state of the system, a problem arises when relating a given mixture internal energy to an unknown temperature. The only way of achieving this is through an iterative numerical scheme (Anderson, 1989). This puts a limitation on the application of such models within a time dependent CFD code, as the inversion process must be repeated at every grid point, and therefore leads to a large amount of time spent calculating numerous variables, many of which are not explicitly required by the solution algorithm.

Three inversion schemes have been considered. These were a linear point iterative scheme, a superlinear Regula falsi method and a quadratic Newton-Raphson scheme (Fröberg, 1985). The first scheme was restricted by its slow convergence rate and was immediately discounted on that point. The second two methods were limited by their need for an accurate initial guess of temperature corresponding to the known internal energy. The choice between these techniques was based on the fact that, for the Newton-Raphson scheme, the chemical state of the gas needed to be calculated at only one point during the iteration. The Regula falsi technique required the chemistry to be analysed at an additional point on the temperature scale in order to calculate

	Mean	Max.	Min.	Std. Dev.
Time Per Iteration, x 10^{-6} s				
Regula falsi	156.3	184.9	100.2	10.91
Newton Raphson	138.5	162.4	79.2	10.76
Number of Iterations, $\Delta T < 0.1$ K				
Regula falsi	3.332	5.0	2.0	0.8590
Newton Raphson	2.891	4.0	1.0	0.5936

Table 5.1 Comparison Between Execution Times for Regula falsi and Newton-Raphson inversion of the Thermodynamic State Equations.

derivative information, and also required a more accurate initial guess. This offset the reduced computational effort required because none of the thermochemical derivatives needed to be calculated. In addition, the Regula falsi method, being only superlinear, did not exhibit as fast a convergence rate as the quadratic Newton-Raphson scheme.

Details of the execution speeds of the Regula falsi and Newton-Raphson techniques are given in Table 5.1, from which it can be seen that the Regula falsi method not only required more time per iteration, but also required more iterations to converge to a desired temperature tolerance. The final choice of a Newton-Raphson scheme was therefore made.

The scheme is summarised as follows:

$$T^0 = T_{estimate}\,(\rho, e) \tag{5.2}$$

$$e^n = e^n\,(\rho, T^n) \tag{5.3}$$

$$\left(\frac{\partial e^n}{\partial T}\right)_\rho = \left(\frac{\partial}{\partial T} e^n(\rho, T^n)\right)_\rho \tag{5.4}$$

$$T^{n+1} = T^n - \frac{e^n - e}{(\partial e^n/\partial T)_\rho} \tag{5.5}$$

Details of the calculation of internal energy as a function of mass density and temperature have already been presented in section 4.8. The energy derivative follows from the chemical state of the gas in a manner similar to that presented in section 4.9 for the derivatives appearing in the acoustic equations. Internal energy is a function of temperature and the chemical state of the gas, in an analogous fashion to Eq. (4.121):

$$e = e\,(T, \eta_i)\,. \tag{5.6}$$

Then:
$$\left(\frac{\partial e}{\partial T}\right)_{\eta_i=\eta_i^*} = (e)_T + \sum_i (e)_{\eta_i}(\eta_i)_T \tag{5.7}$$

where:
$$(e)_T = \left(\frac{\partial e}{\partial T}\right)_{\eta_i} \tag{5.8}$$

$$(e)_{\eta_i} = \left(\frac{\partial e}{\partial \eta_i}\right)_{T,\eta_{j\neq i}} \tag{5.9}$$

$$(\eta_i)_T = \left(\frac{\partial \eta_i}{\partial T}\right). \tag{5.10}$$

It is noted that the above derivatives are evaluated with mass density constant, so the chemical state of the system is a function of temperature only, according to Eq. (5.4). Enthalpy and internal energy are related through:

$$e = h - \hat{R}\,\eta\,T \tag{5.11}$$

$$(e)_T = (h)_T - \hat{R}\,\eta \tag{5.12}$$

$$(e)_{\eta_i} = (h)_{\eta_i} - \hat{R}\,T\,(\eta)_{\eta_i}\,. \tag{5.13}$$

In the above expressions $(h)_T$ and $(h)_{\eta_i}$ can be found from Eqs. (4.137) and (4.138). The derivative $(\eta)_{\eta_i}$ is found from Eq. (4.104):

$$(\eta)_{\eta_i} = \sum_j^6 \left(\frac{\partial \eta_j}{\partial \eta_i}\right) = 1 \tag{5.14}$$

Equation (5.13) now reduces to:

$$(e)_{\eta_i} = (h)_{\eta_i} - \hat{R}\,T \tag{5.15}$$

Calculation of the chemical derivatives $(\eta_i)_T$ in Eq. (5.7) has already been discussed in section 4.9.

In order to initiate the iterative inversion of the scheme using this method, an accurate initial estimate of temperature is required. The most efficient way of doing this is to use the sixteen coefficient curve fits presented in section 4.1-b.

Figures 5.1 and 5.2 illustrate the results of calculating the equilibrium pressure and sonic speed from given specific internal energy and mass density. Temperature appears in this calculation only as an intermediate variable, but is plotted in Figure 5.3 for direct comparison with Figures 4.4a and 4.4b. A maximum of three iterations are required in the inversion process at low temperatures to achieve a converged solution to within 0.01 K. However, because the curve fits include the effects of ionization, up to five iterations are required at higher temperatures. The curve fits do not provide a good estimate to the solution of the state equation model under these conditions because the gas models from which the two methods are derived are not directly equivalent. As can be seen by comparing Figures 5.1 and 5.2 with Figures 4.3 and 4.5, this technique provides improved smoothness and continuity throughout the valid range of densities and internal energies over that provided by the equivalent curve fits.

5.2 CALCULATION OF THE χ AND κ DERIVATIVES.

The two thermodynamic derivatives χ and κ form the link between the thermochemical and dynamic behaviour of an equilibrium gas. They are the real gas counterparts of the ratio of specific heats, γ, in a perfect gas model. They were defined in chapter three as:

$$\chi = \left(\frac{\partial p}{\partial \rho}\right)_{\varepsilon} \tag{5.16}$$

$$\kappa = \left(\frac{\partial p}{\partial \varepsilon}\right)_{\rho} . \tag{5.17}$$

The choice of these particular derivatives is not unique. For example, Table 5.2 lists the choice of derivatives used by various authors. This list is by no means exhaustive, but serves to illustrate that any orthogonal pair of derivatives on a thermodynamic surface can be chosen.

The choice of derivative is largely dictated by the form of the state equation. However, in this case it is possible to obtain any pair of derivatives, and the choice of χ and κ is made because of the simplicity of the resulting acoustic equation.

The derivatives are given by (see appendix four):

$$\kappa = \frac{\hat{R}\left[\eta + T\sum_i (\eta_i)_T\right]}{\left[(h)_T + \sum_i (h)_{\eta_i}(\eta_i)_T\right] - \hat{R}\left[\eta + T\sum_i (\eta_i)_T\right]} \tag{5.18}$$

	Thermodynamic Surface	Thermodynamic Derivatives
Vinokur and Montagné (1990) Abgrall (1991)	$p(\rho, \varepsilon)$	$(\partial p/\partial \rho)_{\varepsilon}$ $(\partial p/\partial \varepsilon)_{\rho}$
Liou et al. (1990)	$\gamma(\rho, e)$ $\gamma = h/e$	$(\partial \gamma/\partial \rho)_{e}$ $(\partial \gamma/\partial e)_{\rho}$
Suresh and Liou (1991) Glaister (1988)	$p(\rho, e)$	$(\partial p/\partial \rho)_{e}$ $(\partial p/\partial e)_{\rho}$
Grossman and Walters (1989)	$p(\tau, e)$ $\tau = 1/\rho$	$(\partial p/\partial \tau)_{e}$ $(\partial p/\partial e)_{\tau}$

Table 5.2 Thermodynamic Derivatives Chosen by Various Authors to Represent the Behaviour of Equilibrium Air.

$$\chi = \frac{\hat{R}T\left[(h)_T + \sum_i (h)_{\eta_i}(\eta_i)_T\right]\left[\eta + \rho\sum_i(\eta_i)_\rho\right]}{\left[(h)_T + \sum_i(h)_{\eta_i}(\eta_i)_T\right] - \hat{R}\left[\eta + T\sum_i(\eta_i)_T\right]} -$$

$$\frac{\hat{R}\left[h + \rho\sum_i(h)_{\eta_i}(\eta_i)_\rho\right]\left[\eta + T\sum_i(\eta_i)_T\right]}{\left[(h)_T + \sum_i(h)_{\eta_i}(\eta_i)_T\right] - \hat{R}\left[\eta + T\sum_i(\eta_i)_T\right]} . \qquad (5.19)$$

For a perfect gas, these expressions reduce to:

$$\kappa = \frac{R_0}{c_p - R_0} = \gamma - 1 \qquad (5.20)$$

$$\chi = \frac{R_0(c_pT - h)}{c_p - R_0} = 0 \qquad (5.21)$$

The behaviour of the thermodynamic derivatives is illustrated in Figures 5.4a and 5.4b. From these figures, κ can be seen to have a low temperature value of 0.4 and χ to be zero, corresponding to Eqs. (5.20) and (5.21). As temperature increases, κ remains constant up to about 400 K, illustrating that the gas is behaving perfectly in this region. Between 400 K and 2000 K, vibrational excitation dominates the behaviour of the gas and caloric imperfections are evident. This corresponds to the increase in molar heat for the three diatomic molecules (see Figure 4.9) and the associated decrease in κ. Chemical changes in the gas start to become important at about 1500 K. Since the chemical composition of the gas is density dependent, curves depicting the behaviour of both χ and κ diverge for different densities above this temperature, illustrating the thermally imperfect nature of air at these temperatures.

The first minimum in the κ curves (and associated maximum in the χ curves) corresponds to the point of maximum dissociation rate, with respect to temperature, of diatomic oxygen. It also corresponds to the first maximum in the ratio of sonic speeds in Figure 4.14. The second minimum corresponds to the maximum dissociation rate of diatomic nitrogen. Small changes in temperature at these points will lead to large chemical changes in the gas. Rapid changes in temperature around these points may therefore lead to nonequilibrium chemical behaviour. The maximum value of κ between these regions represents a chemically more stable temperature.

At high temperatures, the diatomic species become dissociated and the chemical composition of the gas tends towards fully monatomic oxygen and nitrogen, together with a small amount of argon. These species are, however, electrically excited, although not ionized in this model; therefore the molar heats at constant volume are larger than at low temperatures. This results in κ returning to a value slightly greater

than 0.4, rather than 0.67 predicted for a monatomic gas with no internal structure (Vincenti and Kruger, 1965).

The large negative value of χ at high temperatures can be interpreted as follows. Despite the fact that the gas mixture at these temperatures is behaving perfectly in the sense that its specific heats and chemical composition are nearly constant, large amounts of energy have been absorbed both by the internal modes of the atoms and the decomposition of the diatomic species. The specific enthalpy of the mixture is therefore considerably more than would be expected according to the perfect gas relationship:

$$h = c_p T . \tag{5.22}$$

Equation (5.22) can therefore be replaced by an expression of the form:

$$h_{actual} = c_p T + \Delta h . \tag{5.23}$$

The increment in enthalpy can be related to the thermodynamic derivatives through:

$$\Delta h = - \frac{\chi}{\kappa} . \tag{5.24}$$

The ratio $-\chi/\kappa$ is therefore interpreted as representing the enthalpy of the mixture absorbed by internal modes of the atoms and molecules and by the dissociation of molecules.

5.3 THE QUASI-ONE-DIMENSIONAL NOZZLE PROBLEM.

In order to illustrate the application of the preceding state equation models to a fluid dynamic problem, the computational solution to the quasi-one-dimensional nozzle problem with equilibrium inviscid air has been generated. Practical applications for such a solution are limited because nonequilibrium effects, particularly diffusive effects, influence the behaviour of air in hypervelocity nozzles. Additionally, nozzle problems are more closely associated with propulsion applications, where combusting hydrocarbon chemistry is important. Even within hypersonic test facilities utilizing such nozzles, the gases used are unlikely to be as complex as the air mixture presented here.

This test case has been selected primarily because it forms a bench mark for testing most computational algorithms. The authors mentioned in Table 5.2 use a one-dimensional analysis to develop their algorithms, and use either a quasi-one-dimensional nozzle problem or a shock tube problem to illustrate this. The solution to the one-dimensional Euler equations contains the essential aspects of the convective

behaviour of high speed air flow. This problem does not require time accurate algorithms, and is ideally suited to rigorous testing of boundary condition algorithms. Furthermore, exact solutions can be generated for nozzle problems, if somewhat tediously, using Mollier chart data.

The nozzle shape chosen here is described by the equation:

$$A = \exp\left(\sum_{i=1}^{n} c_i \, x^i\right) \tag{5.25}$$

where x is the spatial coordinate and the coefficients c_i determine the area distribution through the nozzle. These coefficients are chosen to satisfy prescribed inlet, throat and exhaust conditions.

5.4 DISCRETIZATION OF THE EQUATIONS OF MOTION.

For a quasi-one-dimensional nozzle problem, conservation principles lead to the following formulation:

$$\frac{\partial \mathbf{U}}{\partial t} + \frac{\partial \mathbf{F}}{\partial x} = \Omega \tag{5.26}$$

$$\mathbf{U} = \begin{bmatrix} \rho \\ \rho u \\ \rho\left(e + \frac{u^2}{2}\right) \end{bmatrix} = \begin{bmatrix} \rho \\ m \\ E \end{bmatrix} \tag{5.27}$$

$$\mathbf{F} = \begin{bmatrix} \rho u \\ \rho u^2 + p \\ \rho u\left(e + \frac{u^2}{2} + \frac{p}{\rho}\right) \end{bmatrix} = \begin{bmatrix} m \\ \frac{m^2}{\rho} + p \\ \frac{m}{\rho}(E + p) \end{bmatrix} \tag{5.28}$$

$$\Omega = -\begin{bmatrix} \rho u \\ \rho u^2 \\ \rho u\left(e + \frac{u^2}{2} + \frac{p}{\rho}\right) \end{bmatrix} \frac{d}{dx} \ln A = -\begin{bmatrix} m \\ \frac{m^2}{\rho} \\ \frac{m}{\rho}(E + p) \end{bmatrix} \frac{d}{dx} \ln A \, . \tag{5.29}$$

This set of nonlinear partial differential equations is closed by an algebraic state equation in the form:

$$p = p(\rho, e) \, . \tag{5.30}$$

Techniques for modelling this equation have been discussed in previous sections.

5.4-a Numerical Discretization.

In order to solve Eq. (5.26) numerically, it is discretized using an implicit (trapezoidal) time, central space scheme (Beam and Warming, 1976). Centrally differenced schemes suffer from a lack of dissipation (Wang, 1990) and therefore require the addition of an artificial dissipation term to maintain stability and smooth shock profiles. The success of such schemes lies in the careful construction of the numerical viscosity which provides this dissipation.

Adding a second order viscous term to Eq. (5.26) gives:

$$\frac{\partial \mathbf{U}}{\partial t} + \frac{\partial \mathbf{F}}{\partial x} = \Omega + \frac{\partial}{\partial x}\left(\nu_N \frac{\partial \mathbf{U}}{\partial x}\right). \tag{5.31}$$

Trapezoidal time differencing takes the form:

$$\frac{\Delta \mathbf{U}}{\Delta t} = \frac{1}{2}\left(\frac{\partial \mathbf{U}^n}{\partial t} + \frac{\partial \mathbf{U}^{n+1}}{\partial t}\right) \tag{5.32}$$

where:
$$\Delta \mathbf{U} = \mathbf{U}^{n+1} - \mathbf{U}^n. \tag{5.33}$$

Using Eq. (5.31) in Eq. (5.32) and expanding terms at time n+1 in a Taylor series about time step n gives (see appendix five):

$$\left[\frac{\mathrm{I}}{\Delta t} - \frac{1}{2}\frac{\partial \Omega}{\partial \mathbf{U}} + \frac{1}{2}\frac{\partial}{\partial x}\frac{\partial \mathbf{F}}{\partial \mathbf{U}} \cdot - \frac{\mathrm{I}}{2}\frac{\partial^2}{\partial x^2}\nu_N \cdot\right]^n \Delta \mathbf{U}$$

$$= \left[- \frac{\partial \mathbf{F}}{\partial x} + \Omega + \frac{\partial}{\partial x}\left(\nu_N \frac{\partial \mathbf{U}}{\partial x}\right)\right]^n + O(\Delta t^2) \tag{5.34}$$

Time accuracy is not required from this expression, and so the algorithm can be simplified by treating the source term explicitly, and assuming the numerical viscosity is locally constant. This reduces Eq. (5.34) to:

$$\left[\frac{\mathrm{I}}{\Delta t} + \frac{1}{2}\frac{\partial}{\partial x}\frac{\partial \mathbf{F}}{\partial \mathbf{U}} \cdot - \frac{\nu_N}{2}\,\mathrm{I}\,\frac{\partial^2}{\partial x^2} \cdot\right]^n \Delta \mathbf{U}$$

$$= \left[- \frac{\partial \mathbf{F}}{\partial x} + \Omega + \frac{\partial}{\partial x}\left(\nu_N \frac{\partial \mathbf{U}}{\partial x}\right)\right]^n + O(\Delta t^2) \tag{5.35}$$

In their original paper, Beam and Warming mention simplifications to this expression in the case where **F** is an homogeneous function of degree one in **U**. In appendix six, it is shown that this is true only when the functional form of the state equation satisfies:

$$p(\rho, e) = \frac{p(\lambda\rho, e)}{\lambda} \tag{5.36}$$

for some constant λ. This implies that pressure must be linearly related to density for the homogeneity condition to hold. For such a linear relationship to hold, the derivative $(\partial p/\partial \rho)_e$ must be constant. In the case of a perfect gas, this is easily shown to be true. However, for chemically reacting air, Figure 5.5 illustrates that this is untrue, especially at high internal energies. Equation (5.35) has therefore been derived without applying the homogeneous property to the flux vector.

Centrally differencing the spatial derivatives in Eq. (5.35) leads to the fully discretized equations:

$$\left[-\frac{A_{i-1}}{4\Delta x} - \frac{\nu_{N_i}}{2\Delta x^2} \right]^n \Delta \mathbf{U}_{i-1} + \left[\frac{1}{\Delta t} + \frac{\nu_{N_i}}{\Delta x^2} \right]^n \Delta \mathbf{U}_i + \left[\frac{A_{i+1}}{4\Delta x} - \frac{\nu_{N_i}}{2\Delta x^2} \right]^n \Delta \mathbf{U}_{i+1}$$

$$= -\frac{\mathbf{F}^n_{i+1}}{2\Delta x} + \frac{\mathbf{F}^n_{i-1}}{2\Delta x} + \Omega^n_i + \nu_{N_{i+1/2}} \frac{\mathbf{U}^n_{i+1} - \mathbf{U}^n_i}{\Delta x^2} - \nu_{N_{i-1/2}} \frac{\mathbf{U}^n_i - \mathbf{U}^n_{i-1}}{\Delta x^2} + O(\Delta t^2, \Delta x^2) \tag{5.37}$$

where:
$$\nu_{N_{i+1/2}} = \frac{1}{2}\left(\nu_{N_{i+1}} + \nu_{N_i}\right) . \tag{5.38}$$

This is a set of N-2 linear algebraic equations for N unknown values of $\Delta\mathbf{U}$ at time step n. The additional two equations for $\Delta\mathbf{U}$ at i=1 and i=N follow from the boundary conditions discussed later.

5.4-b Artificial Dissipation.

The numerical viscosity, ν_N, appearing in Eq. (5.37) is based on the model proposed by Jameson et al. (1981). It is desirable to have relatively high second order dissipation at or near shocks, where truncation errors resulting from central differencing compound to produce oscillations, but maintain the second order accuracy of the scheme by minimalizing the dissipative terms in smooth regions of the flow. Jameson et al. found that their scheme did not converge to a truly steady state unless a fourth order damping term was included in the algorithm. This has not been found necessary here, and only the second order damping term in Eq. (5.37) is required.

The magnitude of the damping term is related to the locally normalized pressure derivative as follows:

$$\nu_N = \alpha \frac{\partial \bar{p}}{\partial x^2} \Delta x^2 \tag{5.39}$$

where α is a variable parameter allowing some degree of control over the strength of the damping term. Discretization of Eq. (5.39) gives:

$$\nu_{N_i} = \alpha \frac{p_{i+1} - 2p_i + p_{i-1}}{p_{i+1} + 2p_i + p_{i-1}}. \tag{5.40}$$

5.5 BOUNDARY CONDITIONS.

At a boundary there is an exchange of information between the system and its surroundings. The direction in which that information travels is dictated by the behaviour of the characteristics of the equations of motion, and whether the mass flux through the boundary is positive (inflow) or negative (outflow). There are four possible boundary conditions to be considered in a one-dimensional flow: subsonic inflow, supersonic inflow, subsonic outflow and supersonic outflow. Figures 5.6a and 5.6b indicate the direction of propagation of information at each type of boundary. These follow from the propagation directions of the characteristic variables in Eqs. (3.29).

Numerous schemes are available for computing boundary conditions. The simplest of these is to extrapolate the correct number of primitive variables from the interior of the flow to establish the numerical conditions, and impose physical boundary conditions on those remaining. The choice of which primitive variables are extrapolated at any type of boundary influences the stability of the algorithm. For example, at a subsonic outflow boundary, specifying pressure and extrapolating density and velocity leads to a stable algorithm, but specifying either density or velocity and extrapolating pressure and the remaining variable leads to problems.

Which variables can and cannot be extrapolated at any type of boundary is dictated by the characteristic behaviour at that boundary. Physical boundary conditions are dictated by information propagating along incoming characteristics, and numerical conditions by the outgoing characteristics. It therefore makes sense to apply boundary conditions directly in terms of the characteristic variables. However, in the case of a thermally imperfect gas, analytic expressions for the characteristic variables cannot be found, so a direct extrapolation of these variables cannot be implemented. Two other techniques have been investigated for getting round this problem. The first relies on the solution of the appropriate compatibility relations at the boundary, and the second is based on the extrapolation of time differences of the characteristics.

All boundary conditions have been treated explicitly in this case. That is to say, at each time step, the interior points are all updated implicitly using Eq. (5.37) with fixed

values of $\Delta \mathbf{U}$ at i = 1 and i = N, then the boundary points are updated using one of the three above techniques.

Hirsch (1989b) discusses extrapolation techniques for establishing numerical boundary conditions, and includes the extrapolation of time differences of the characteristics as a feasible approach. This treatment is conceptually straight forward and therefore easy to implement. However, no evaluation of the effectiveness of this extrapolation is made in the above reference, and several deficiencies are noted here.

5.5-a Subsonic Characteristic Boundary Conditions.

From Figure 5.6a, it can be seen that for a subsonic problem two of the characteristics run in the direction of flow and one against. The two forward running characteristics represent the convection of entropy and the propagation of pressure disturbances in the direction of flow. The backward running characteristic represents the propagation of information against the flow, and is present because the flow is subsonic. When there is a transition to supersonic flow, this backward running characteristic changes direction, and the nature of the flow is therefore modified.

The presence of a backward running characteristic allows information to propagate from the system out into the surroundings through an inflow boundary, and similarly form the surroundings into the system at an outflow. It is therefore necessary to apply one numerical and two physical boundary conditions at an inflow, and two numerical and one physical boundary conditions at an outflow.

Physical boundary conditions at inlet are applied through a specified density and pressure:

$$\Delta p_1 = p_{inlet} - p_1 \tag{5.41}$$

$$\Delta \rho_1 = \rho_{inlet} - \rho_1 \tag{5.42}$$

The compatibility relations, Eqs. (3.29), describing the propagation of the characteristics are:

$$\frac{\partial w_1}{\partial t} + u \frac{\partial w_1}{\partial x} = 0 \tag{5.43}$$

$$\frac{\partial w_2}{\partial t} + (u + c_e) \frac{\partial w_2}{\partial x} = -u c_e \frac{d}{dx} \ln A \tag{5.44}$$

$$\frac{\partial w_3}{\partial t} + (u - c_e) \frac{\partial w_3}{\partial x} = u c_e \frac{d}{dx} \ln A \, . \tag{5.45}$$

At an inflow boundary, the numerical boundary condition can be established by discretizing Eq. (5.45) using forward spatial differences. This differencing will be stable because w_3 propagates out of the system, $(u - c_e)$ is negative and the differencing is upwind. First order forward differencing of w_3 and explicit time differencing leads to:

$$\Delta(w_3)_1 = u_1 c_{e_1} \left[\frac{d}{dx} \ln A\right]_1 \Delta t - (u_1 - c_{e_1}) \left[(u_2 - u_1) - \frac{(p_2 - p_1)}{\rho_1 c_{e_1}}\right] \frac{\Delta t}{\Delta x} . \tag{5.46}$$

The unknown primitive variable is computed from:

$$\Delta u_1 = \Delta(w_3)_1 + \frac{\Delta p_1}{\rho_1 c_{e_1}} \tag{5.47}$$

and the transformation matrix M given by Eq. (3.11) is used to compute the required $\Delta \mathbf{U}$ at the inlet:

$$\Delta \mathbf{U} = M \, \Delta \mathbf{V} . \tag{5.48}$$

A similar technique is applied at the outflow boundary, where Eqs. (5.43) and (5.44) are discretized to establish the numerical boundary conditions and exhaust pressure is imposed physically:

$$\Delta p_N = p_{exhaust} - p_N \tag{5.49}$$

$$\Delta(w_1)_N = - u_N \left[(\rho_N - \rho_{N-1}) - \frac{(p_N - p_{N-1})}{c_{e_N}^2}\right] \frac{\Delta t}{\Delta x} \tag{5.50}$$

$$\Delta(w_2)_N = - u_N c_{e_N} \left[\frac{d}{dx} \ln A\right]_N \Delta t - (u_N + c_{e_N}) \left[(u_N - u_{N-1}) + \frac{(p_N - p_{N-1})}{\rho_N c_{e_N}}\right] \frac{\Delta t}{\Delta x} \tag{5.51}$$

$$\Delta \rho_N = \Delta(w_1)_N + \frac{\Delta p_N}{c_{e_N}^2} \tag{5.52}$$

$$\Delta u_N = \Delta(w_2)_N - \frac{\Delta p_N}{\rho_N c_{e_N}} . \tag{5.53}$$

Equation (5.48) is then applied at the exhaust to compute the conserved variables. Spatial differencing of Eqs. (5.43) and (5.44) is now backward because the outgoing

characteristics are running forwards. This differencing is still therefore upwind and stable.

The second technique for implementing boundary conditions on the characteristic variables relies on the first order extrapolation of time differences of the characteristic variables. Equations (5.41) and (5.42) are again used to compute density and pressure at the inlet, but the characteristic extrapolation now takes the form:

$$\Delta(w3)_1 = 2\Delta(w3)_2 - \Delta(w3)_3 \,. \tag{5.54}$$

The inlet velocity then follows from Eq. (5.47).

At a subsonic exhaust, Eq. (5.49) gives the exhaust pressure, then the density and velocity follow from Eqs. (5.52) and (5.53) with the right running characteristics extrapolated according to:

$$\Delta(w1)_N = 2\Delta(w1)_{N-1} - \Delta(w1)_{N-2} \tag{5.55}$$

$$\Delta(w2)_N = 2\Delta(w2)_{N-1} - \Delta(w2)_{N-2} \,. \tag{5.56}$$

The required conserved variables at either the inlet or exhaust follow from Eq. (5.48).

5.5-b Supersonic Characteristic Boundary Conditions.

The application of supersonic boundary conditions is more straight forward than the equivalent subsonic case. This is primarily because all the characteristics run in the same direction in this case. There is therefore no choice about the physical or numerical boundary conditions. Figure 5.6b illustrates why all the boundary conditions at a supersonic inflow must be physical, and all those at a supersonic outflow must be numerical.

Inflow boundary conditions need not refer to characteristic information in any way. They are applied through known values of the three primitive variables at the boundary:

$$\Delta\rho_1 = \rho_{inlet} - \rho_1 \tag{5.57}$$

$$\Delta u_1 = u_{inlet} - u_1 \tag{5.58}$$

$$\Delta p_1 = p_{inlet} - p_1 \,. \tag{5.59}$$

These boundary conditions can be further simplified if the initial conditions set the primitive variables to their correct values. The implicit solution for interior values does not effect the boundary values, so Eqs. (5.57) to (5.59), combined with the transformation to conserved variables, Eq. (5.48), lead to:

$$\Delta U_1 = 0 \,. \tag{5.60}$$

To numerically establish the outflow boundary conditions, Eqs. (5.43) to (5.45) are all discretized using backward differences:

$$\Delta(w_1)_N = - u_N \left[(\rho_N - \rho_{N-1}) - \frac{(p_N - p_{N-1})}{c_{e_N}^2} \right] \frac{\Delta t}{\Delta x} \tag{5.61}$$

$$\Delta(w_2)_N = - u_N c_{e_N} \left[\frac{d}{dx} \ln A \right]_N \Delta t - (u_N + c_{e_N}) \left[(u_N - u_{N-1}) + \frac{(p_N - p_{N-1})}{\rho_N c_{e_N}} \right] \frac{\Delta t}{\Delta x} \tag{5.62}$$

$$\Delta(w_3)_N = u_N c_{e_N} \left[\frac{d}{dx} \ln A \right]_N \Delta t - (u_N - c_{e_N}) \left[(u_N - u_{N-1}) - \frac{(p_N - p_{N-1})}{\rho_N c_{e_N}} \right] \frac{\Delta t}{\Delta x} \,. \tag{5.63}$$

The conserved variables can then be computed by the direct transformation:

$$\Delta \mathbf{U} = (\mathrm{ML})\, \Delta \mathbf{W} \tag{5.64}$$

The alternative extrapolation of time differences of the characteristics for numerical boundary conditions leads to outflow boundary conditions, Eqs. (5.61) to (5.63), being replaced by:

$$\Delta(w_1)_N = 2\Delta(w_1)_{N-1} - \Delta(w_1)_{N-2} \tag{5.65}$$

$$\Delta(w_2)_N = 2\Delta(w_2)_{N-1} - \Delta(w_2)_{N-2} \tag{5.66}$$

$$\Delta(w_3)_N = 2\Delta(w_3)_{N-1} - \Delta(w_3)_{N-2} \,. \tag{5.67}$$

5.5-c Evaluation of Boundary Treatments - Supersonic Exhaust.

The three boundary treatments examined in detail are as follows:

1) first order extrapolation of the primitive variables,
2) solution of the characteristic equations using first order upwind differencing,
3) first order extrapolation of time differences of the characteristic variables.

For the supersonic exhaust case, no shock is present in the flow and so the artificial dissipation can be set quite low. This prevents any numerically induced oscillations at the boundaries from being too heavily damped and therefore shows up any errors induced by reflections at these points.

The test case considered for this analysis is a low speed, high temperature one. The nozzle geometry is specified through an equation of the form (see appendix seven):

$$A(x) = \exp\left(\sum_{i=0}^{3} c_i \, x^i\right). \tag{5.68}$$

The throat and exhaust locations are taken to be $x_t = 0.25$ m and $x_e = 1.00$ m, and the radii at these points are $r_t = 5$ mm and $r_e = 5.05$ mm. These values give the coefficients of Eq. (5.68) as:

$c_0 = -9.443\,797$, $c_1 = -0.070\,758\ m^{-1}$,
$c_2 = 0.176\,895\ m^{-2}$, $c_3 = -0.094\,344\ m^{-3}$.

The geometry of this nozzle is illustrated in Figure 5.7.

Stagnation conditions are selected such that the gas behaves thermally perfectly within the nozzle. An inlet static temperature of 1760 K gives an expansion through the nozzle in the region where κ is a function only of temperature and not of density (see Fig. 5.4a). The stagnation conditions at the inlet are:

pressure $p_0 = 69\,576.0\ N\ m^{-2}$,
density $\rho_0 = 0.123\,26\ kg\ m^{-3}$,
enthalpy $h_0 = 2.233\,8 \times 10^6\ J\ kg^{-1}$,
entropy $s = 9\,064.2\ J\ kg^{-1}\ K^{-1}$.

The molar mass of the gas, and hence the specific gas constant, is constant through the length of the nozzle:

molar mass $\hat{M} = 0.028\,962\ kg\ mol^{-1}$,
specific gas constant $R = 287.08\ J\ kg^{-1}\ K^{-1}$.

The boundary conditions are completely defined by the static density and pressure at the subsonic inlet corresponding to the above stagnation conditions. These are:

static pressure $p = 42\,159.0\ N\ m^{-2}$,
static density $\rho = 0.082\,432\ kg\ m^{-3}$.

The initial conditions for the solution of Eqs. (5.37) were generated from an exact perfect gas solution to the nozzle geometry using the following conditions:

stagnation pressure $p_0 = 70\,345.0\ N\ m^{-2}$,
stagnation density $\rho_0 = 0.122\,50\ kg\ m^{-3}$,
ratio of specific heats $\gamma = 1.333$.

The differences between the different boundary treatments lie in three areas: the computational effort required to implement the technique, the convergence rate for the iterative solution of Eq. (5.37) and the accuracy of the converged solution at the boundary. From the point of view of computational effort, linear extrapolation of the primitive variables is the most attractive technique, requiring only transformation between conserved and primitive variables at the exhaust and the first two interior points. However, this technique does give rise to small oscillations at the exhaust boundary, when compared to the solution generated by implementing Eqs. (5.61) to

	i = N	i = N-1	i = N-2	i = N-3	$\log_{10}(\Delta\rho)$
x/x_0	1.00	0.99	0.98	0.97	
A/A_t	1.010 00	1.010 00	1.009 98	1.009 96	
Mach Number:					
B. C. Type 1	1.155 9	1.155 8	1.155 8	1.155 5	-5.64
difference		0.000 3	0.000 0	0.000 2	
B. C. Type 2	1.155 9	1.155 9	1.155 7	1.155 5	-6.09
difference		0.000 0	0.000 2	0.000 2	
B. C. Type 3	1.155 8	1.156 0	1.155 7	1.155 6	-5.67
difference		-0.000 2	0.000 3	0.000 1	

Table 5.3 Supersonic Exhaust Conditions, 3000 iterations at CFL = 0.98.

(5.63). Also small reflections caused by this boundary condition do not escape from the system as quickly as for either characteristic based method, and the convergence rate with the same interior scheme, illustrated in Figure 5.8, is slightly slower.

The solution of the compatibility relations at the boundary, being the most physically based of the three techniques considered, does not give rise to oscillations, and gives the fastest convergence rate, since excess energy can escape the system correctly and without reflection. Furthermore, the penalty for this in terms of computational effort is only marginally greater than for the above case.

Linear extrapolation of time differences of the characteristic variables has not been found to be an effective treatment for several reasons. The computational effort required is higher than the other two techniques because of the need to transform between conserved, primitive and characteristic variables at the boundary and the first two interior points. Also the convergence rate is only marginally better than for extrapolation of the primitive variables and oscillations are more pronounced than either of the other techniques.

Table 5.3 presents Mach number details at the exhaust for the three different boundary treatments. Oscillations appear to be most pronounced in this variable, but are also present in other thermodynamic variables, such as total enthalpy, internal energy and temperature. The degree of reflection present with each boundary treatment can be assessed from the differences between Mach numbers at consecutive points. These differences show the oscillatory nature of the solutions for types one and three boundary treatments, when compared with the solution of the compatibility relations at the boundary.

Figures 5.9a to 5.9d illustrate the variation of Mach number, pressure, enthalpy and temperature through the nozzle for a supersonic exhaust. For comparison, perfect gas solutions generated with the same stagnation pressure, density and enthalpy are also plotted, with a constant ratio of specific heats fixed by the stagnation conditions as:

$$\gamma = \frac{1}{1 - \frac{p_0}{\rho_0 h_0}} = 1.338 \qquad (5.69)$$

For the moderate test conditions presented here, there is only a marginal difference between the equilibrium gas and perfect gas solutions. The most noticeable difference appears in the temperature variation. It can be seen that the perfect gas model gives an over expansion of the gas, when compared to the vibrationally excited solution. Perfect gas Mach numbers are slightly higher than the equivalent equilibrium gas case. Similarly the perfect gas solution expands to lower pressure, enthalpy and significantly lower temperature.

The above results can be explained in the following manner. As the gas expands and the temperature falls, the energy stored internally by vibrational excitation is released and goes into translational excitation of the molecules. This keeps the temperature of the gas higher than in the perfect gas case. At the same time, the specific heats are decreasing and offsetting the effects of increased temperatures on the static enthalpy. The combination of increased temperature and decreased specific heats do not exactly compensate each other, and the result is a static enthalpy slightly greater than the perfect gas prediction. Given that the total enthalpy is the same in both cases, less enthalpy is available to accelerate the flow through the nozzle, and so the expansion is less than predicted by a perfect gas analysis.

5.5-d Evaluation of Boundary Treatments - Subsonic Exhaust.

In order to generate a shock within the nozzle, an exhaust pressure is imposed, and subsonic exhaust boundary conditions are implemented. The same three boundary treatments are examined in this case as for the supersonic case, and the same nozzle geometry and inlet stagnation conditions are used. The static pressure imposed at the exhaust is:

pressure $p = 44\,000.0 \text{ N m}^{-2}$

This pressure gives rise to a stationary shock located at x = 0.71 m. Initial conditions are generated from the same perfect gas solution as before, only with a shock induced at x = 0.75 m.

	i = N	i = N-1	i = N-2	i = N-3	$\log_{10}(\Delta\rho)$
x/x_0	1.00	0.99	0.98	0.97	
A/A_t	1.010 00	1.010 00	1.009 98	1.009 96	
Mach Number:					
B. C. Type 1	0.862 84	0.863 01	0.863 01	0.863 34	-5.78
difference		0.000 17	0.000 00	0.000 33	
B. C. Type 2	0.862 87	0.863 05	0.863 02	0.863 36	-5.84
difference		0.000 18	-0.000 03	0.000 34	
B. C. Type 3	0.862 90	0.863 04	0.863 04	0.863 36	-5.85
difference		0.000 14	0.000 00	0.000 32	

Table 5.4 Subsonic Exhaust Conditions, 3000 iterations at CFL = 0.98.

In order to prevent excessive oscillations developing at the shock in this case, the second order damping factor is increased from $\alpha = 0.01$ to $\alpha = 0.1$. Unfortunately, this also damps oscillations at the exhaust boundary, making conclusions about the performance of the different boundary treatments less easy to draw. Additionally, the presence of a shock gives rise to some lightly damped oscillations in the subsonic part of the flow, further confusing the picture at the exhaust. The addition of this artificial dissipation tends to smear the shock over several grid points (in this case the shock is spread over five cells). Application of high resolution techniques, rather than the central differencing used here, could solve these problems, with the latest techniques having been shown to capture shocks with at most one interior point (Suresh and Liou, 1991).

Table 5.4 gives Mach number data at the subsonic exhaust and Figure 5.10 illustrates the convergence histories for the three types of boundary condition. From this, similar conclusions can be drawn as in the supersonic case. That is to say, the solution of the compatibility relations at the exhaust boundary is again the most successful technique, although the advantages are more marginal in this case. Particularly, both characteristic techniques yield similar degrees of oscillation and convergence rates, but the lower computational effort required to implement Eqs. (5.50) and (5.51) rather than Eqs. (5.55) and (5.56) give this technique the advantage.

Figures 5.11a to 5.11d give the variation of the thermodynamic variables through the nozzle, compared with a perfect gas solution with the same stagnation conditions and shock location. Upstream of the shock, identical behaviour to the supersonic case is observed, as expected. However, the strength of the shock is influenced by the presence of internal gas modes, with the equilibrium shock being slightly weaker than

the perfect gas prediction. This is clearly seen in the Mach number plots, where Mach number ahead of the shock is less than the perfect gas prediction, and beyond the shock slightly greater. However, the effect is most noticeable in the temperature jump across the shock, where the equilibrium gas gives a jump of 98.5 K compared with 116.9 K for the perfect gas between the same x locations (x = 0.69 and x = 0.74). The shock strength is weaker because the vibrational modes of the gas are capable of further excitation, and therefore less energy goes into increasing the temperature across the shock.

5.6 HYPERSONIC EXPANSION NOZZLE.

A more demanding test of the state equation model presented in chapter four is an hypersonic expansion nozzle. In this case, the gas is expanded from very high temperature reservoir conditions up to hypersonic Mach numbers. A nozzle geometry specified by Eq. (5.68) is again used, with throat and exhaust locations at x = 0.1 m and x = 1.0 m respectively, and radii of 5 mm and 182.7 mm at these points. The coefficients of Eq. (5.68) therefore become:

$c_0 = -9.165\,624$ $\qquad$ $c_1 = -5.923\,050\ m^{-1}$

$c_2 = 32.576\,774\ m^{-2}$ $\qquad$ $c_3 = -19.743\,499\ m^{-3}$

This gives the nozzle geometry shown in Fig 5.12.

The stagnation conditions for this test are chosen to give an expansion through a region of thermally imperfect gas behaviour, and no exhaust pressure is imposed, so no shock is present. The reservoir conditions are:

pressure $\quad p_0 = 25.167 \times 10^6\ N\ m^{-2}$,

density $\quad \rho_0 = 6.425\ kg\ m^{-3}$,

enthalpy $\quad h_0 = 25.164 \times 10^6\ J\ kg^{-1}$,

entropy $\quad s = 11310.0\ J\ kg^{-1}\ K^{-1}$,

temperature $\quad T_0 = 9434.8\ K$.

The perfect gas solution used for comparison is generated with the same stagnation conditions, but with the molar mass of the gas held constant and equal to its stagnation value. Thus:

molar mass $\quad \hat{M} = 0.020\,026\ kg\ mol^{-1}$,

specific gas constant $\quad R = 415.18\ J\ kg^{-1}\ K^{-1}$,

ratio of specific heats $\quad \gamma = 1.184$

Figures 5.13a to 5.13c illustrate the variation of Mach number, enthalpy and temperature through the nozzle for both perfect and equilibrium gas expansions. A Mollier chart solution is also presented to validate the equilibrium calculation. As for

the supersonic test cases presented in section 5.5, the most noticeable difference between perfect and equilibrium gas solutions is in the temperature prediction. The perfect gas model over-predicts the expansion, giving exhaust temperatures of 1 860 K compared to the equilibrium solution of 2 710 K. This over-prediction of temperature drop is in part caused by the incorrect modelling of internal energy modes, as was the case with the supersonic nozzle discussed earlier. At the stagnation condition for the equilibrium gas case, a significant proportion of the internal energy is stored by modes not present at lower temperatures, whereas for the perfect gas model, the same number of excited modes is present at all temperatures. The equivalent γ for the perfect gas calculation has been chosen according to Eq. (5.69) to give the same stagnation enthalpy, pressure and density as in the equilibrium gas case, and the difference between the internal structures of the two gas models is evident only in the values of the thermodynamic derivatives at stagnation. Particularly, the value of κ for the equilibrium model at stagnation, which should equate to $(\gamma - 1)$ in the absence of a complex internal structure, is lower than the value required to simulate the same conditions with a perfect gas: 0.135 as opposed to 0.184. The difference in the thermodynamic derivatives is a consequence of the distribution of internal energy among modes (notably electronic and vibrational) which have a complex temperature dependence in the equilibrium gas case.

In addition to considering the effects of internal modes on the expansion of the gas, chemical changes must also be accounted for, since substantial internal energy exchanges occur because of the recombination of monatomic species. Figure 5.14a shows the calculated chemical distribution along the nozzle, and Figures 5.14b to 5.14d give the variation of molar mass and derivatives χ and κ. The ability to compute this data illustrates an advantage of the present state equation modelling over the curve fitting techniques presented at the start of chapter four. From Figure 5.14a it is seen that nitrogen recombination is present throughout the high temperature regions of the nozzle, from inlet up to about $x = 0.6$, and oxygen recombination becomes significant from $x = 0.5$ onwards. A major chemical change within the gas is evident between $x = 0.5$ and $x = 0.6$. Furthermore, the variations of the thermodynamic derivatives exhibit turning points at $x = 0.58$, indicating that a change in the behaviour of the gas takes place around this point. These effects manifest themselves most clearly in the Mach number plots, where the equilibrium calculation is initially less than the perfect gas prediction, but displays a sudden steepening at the point where the derivatives χ and κ start increasing. Upwind of this point, nitrogen recombination is the dominant reaction from the thermodynamic point of view, and downwind oxygen recombination is more significant. Comparing the results in Figures 5.13c and 5.14c

with the temperature dependence of κ illustrated in Figure 5.4a shows that the peak value of κ corresponds to the ridge separating oxygen and nitrogen dissociation reactions.

The enthalpy plot (Figure 5.13b) shows the equilibrium calculation slightly lower than the perfect gas prediction, mainly because of the presence of the enthalpy of formation for the monatomic species in Eqs. (4.27) to (4.29) - despite the higher temperatures associated with the equilibrium calculation, some of the available enthalpy goes into dissociating diatomic species, and the static enthalpy of the gas remains lower than the perfect gas prediction.

Chapter Six

NONEQUILIBRIUM THERMOCHEMICAL MODELLING

Chapter four presented techniques for modelling the thermochemical state of air under equilibrium conditions. Chapter five discussed the implementation of these models within a computational algorithm for the solution of inviscid flow problems. Together, those chapters describe a successful and versatile method for solving chemically reacting, fully equilibrium air flow problems. However, while such techniques can provide more accurate and detailed solutions to high enthalpy flow problems than are possible using perfect gas theory, their applicability is limited. Most notably, the assumption that all the internal molecular modes remain in equilibrium must be questioned.

Several important phenomena occur because the equilibrium assumption breaks down at an atomic level. Among the most significant of these effects are transport phenomena, which are a consequence of the excitation of rotational and translational energy modes during a collision process. They give rise to viscosity and heat conduction in a gas where momentum and temperature gradients exist, and mass diffusion where a chemical imbalance is present. Such nonequilibrium effects are accounted for within continuum derivations of the conservation equations by including shear stress and heat conduction terms within the model. State equation models must then be supplemented by suitable models for the viscous and heat transfer coefficients.

Rotational and translational energy modes reach equilibrium within a very small number of collisions, under normal circumstances. For this reason, they are not of great significance unless there are strong gradients present in the flow, such as near solid surfaces or within shock waves and strong shear layers. Conversely, vibrational modes and chemical reactions require more significant numbers of collisions to adjust to equilibrium, and therefore may remain out of equilibrium, or even frozen, throughout large areas of the flow. The effects of chemical and vibrational relaxation are exaggerated by high flow speeds associated with hypersonic flight, and are of great significance where they impinge upon a body surface, where catalysis may give rise to unexpectedly high heat transfer rates.

Aspects of the modelling of both transport and chemical nonequilibrium effects have been investigated and are presented in this chapter as topics for future research.

6.1 TRANSLATIONAL AND ROTATIONAL RELAXATION IN CHEMICAL EQUILIBRIUM.

The random translational motion of gas molecules results in the diffusion of mass, momentum and energy along gradients in these properties. If the gas remains in chemical equilibrium, mass diffusion is continuously balanced by chemical reactions. This diffusional process is therefore of no consequence within a chemical equilibrium model, such as that presented in chapter four. Momentum diffusion, however, gives rise to shear stresses within the fluid, which in turn necessitate the inclusion of a viscous coefficient in the continuum derivation of the Navier-Stokes equations. Similarly, heat conduction terms arising from the diffusion of energy appear in the energy conservation equation through the inclusion of a coefficient of thermal conductivity. These two coefficients must be correctly modelled if translational nonequilibrium effects are to be represented.

The relaxation times associated with the translational and rotational excitation of diatomic gases at moderate temperatures are of the same order, with rotational excitation being slightly slower. The effects of rotational and translational relaxation are therefore almost indistinguishable. However, on a microscopic scale, the difference between the two relaxation times can become important, with rotational energy modes of the molecules requiring several more collisions to reach local equilibrium than translational modes. In this case, an additional coefficient, the bulk viscosity coefficient μ_B, must be introduced. Bulk viscosity is significant in analysing problems such as the structure of strong shocks at elevated temperatures in diatomic gas mixtures. The interest in this research has been in developing a model suitable for solving problems on the scale of space craft and artificial satellites at low Knudsen numbers, where the internal structure of flow features such as shock waves is of relatively low importance. Bulk viscosity effects are therefore neglected, and the Stokes relation:

$$3\lambda + 2\mu = 0 \tag{6.1}$$

is assumed to hold throughout the flow field, where:

$$\lambda = \mu_B - \frac{2}{3}\mu \, . \tag{6.2}$$

To represent the effects of translational and rotational nonequilibrium under the above assumptions, it is thus only necessary to develop models of the transport coefficients for momentum and energy.

6.2 CURVE FITS FOR THE TRANSPORT COEFFICIENTS.

The transport coefficients for a gas in chemical and vibrational equilibrium are functions only of the thermochemical state of the gas. Since the state of the gas can be fully defined by a set of curve fits in any two state variables, it follows that the transport coefficients can equally well be so defined. Providing the curve fits representing these coefficients are based on the same physical model as those representing the state equations, a consistent set of equations can be defined relating all the required variables in the conservation equations. Such an approach has been taken by Srinivasan et al. (1987b) to provide curve fits suitable for use with CFD applications. These curve fits are based on the Grabau transition functions discussed in section 4.1, and take the form:

$$\mu/\mu_0 = \phi_1(y,z) + \frac{\phi_2(y,z) - \phi_1(y,z)}{1 \pm \exp(\phi_3(y,z))} \tag{6.3}$$

and:

$$k/k_0 = \psi_1(y,z) + \frac{\psi_2(y,z) - \psi_1(y,z)}{1 \pm \exp(\psi_3(y,z))}, \tag{6.4}$$

where:

$$y = \log_{10}(\rho/\rho_0) \tag{6.5}$$

$$z = \log_{10}(e/e_0). \tag{6.6}$$

The interpolation and transition functions ϕ and ψ are based on bicubic expressions similar in form to Eqs. (4.21) to (4.26):

$$\phi_1(y,z) = c_1 + c_2z + c_3y + c_4yz + c_5z^2 + c_6y^2 + c_7z^2y + c_8zy^2 + c_9z^3 + c_{10}y^3 \tag{6.7}$$

$$\phi_2(y,z) - \phi_1(y,z) = c_{11} + c_{12}z + c_{13}y + c_{14}yz + c_{15}z^2 + c_{16}y^2 + c_{17}z^2y + c_{18}zy^2 + c_{19}z^3 + c_{20}y^3 \tag{6.8}$$

$$\phi_3(y,z) = c_{21} + c_{22}y + c_{23}z + c_{24}yz \tag{6.9}$$

$$\psi_1(y,z) = d_1 + d_2z + d_3y + d_4yz + d_5z^2 + d_6y^2 + d_7z^2y + d_8zy^2 + d_9z^3 + d_{10}y^3 \tag{6.10}$$

$$\psi_2(y,z) - \psi_1(y,z) = d_{11} + d_{12}z + d_{13}y + d_{14}yz + d_{15}z^2 + d_{16}y^2 + d_{17}z^2y + d_{18}zy^2 + d_{19}z^3 + d_{20}y^3 \tag{6.11}$$

$$\psi_3(y,z) = d_{21} + d_{22}y + d_{23}z + d_{24}yz \,. \qquad (6.12)$$

Table A3.5 in appendix three presents data for the coefficients c_1 to c_{24} and coefficients d_1 to d_{24} appear in Table A3.6. The functional forms of Eqs. (6.3) and (6.4) are illustrated in Figures 6.1 and 6.2 respectively. From Figure 6.1 it can be seen that the viscosity coefficient increases monotonically with respect to internal energy, until about 78.0 x 10^6 J kg^{-1}, at which point ionization causes the sudden appearance of large numbers of low mass particles and a consequent decrease in the diffusion of momentum. The simplicity of the form of these curves leads to an accurate representation of the viscosity coefficient using a minimal number of separate curves. The same is not true of the coefficient of thermal conductivity shown in Figure 6.2. Chemical changes within the gas cause fluctuations in the value of this coefficient over ratios more than ten times as great as for the coefficient of viscosity. A large number of separate curves is therefore required to represent the variation of this parameter.

The advantages and disadvantages of using curve fit models for the state equations were discussed in section 4.1. Similar arguments apply to modelling the transport coefficients this way, although it is less important to have smooth and continuous curves throughout the required range, because derivatives of these curves with respect to the independent variables are not required.

6.3 Transport Coefficients of the Component Species.

If a gas remains everywhere in chemical and vibrational equilibrium, its thermochemical properties can be expressed, in principle, as functions of any two state variables. For this reason, curve fits such as those presented in sections 4.2 and 6.2 can provide efficient methods for calculating mixture properties. However, if additional degrees of freedom are built into the gas model, such as vibrational relaxation or chemical nonequilibrium, the number of independent variables required to fix the state of the gas increases. The complexity of any curve fit required to represent the transport properties of such a gas then outweighs any advantage gained from the technique. Physically based methods must then be applied to provide the required versatility. The first step in any such method is to compute the transport properties of the component species, and the following sections outline how this problem may be approached.

Species	a_{μ_i}	b_{μ_i}	c_{μ_i}
O_2	0.044 929 0	-0.082 615 8	-11.504 533
N_2	0.026 814 2	0.317 783 8	-13.618 136
O	0.020 814 4	0.429 440 4	-13.905 725
NO	0.043 637 8	-0.033 551 1	-11.879 328
N	0.011 557 2	0.603 167 9	-14.735 335

Table 6.1 Curve Fit Coefficients for Species Viscosities.

6.3-a Curve Fitting Methods.

The results of molecular theory (Hirschfelder et al., 1954) show that viscosities and conductivities of pure gases at low pressures are functions only of temperature. It is therefore possible to use curve fits in one variable to determine these coefficients, in the same fashion as for the species thermodynamic properties in section 4.4. Such a technique is has been adopted by Blottner et al. (1971) and has been applied within CFD codes by Bhutta et al. (1985), Prabhu et al. (1987a and 1987b) and Bhutta and Lewis (1988). Similar curve fits for the species transport coefficients have been employed by Shuen (1992).

The Blottner et al. curve fits for the species viscosities take the form:

$$\mu_i = e^{c_{\mu_i} T^{(a_{\mu_i} \ln T + b_{\mu_i})}}, \tag{6.13}$$

where: μ_i = coefficient of viscosity for species i in kg m^{-1} s^{-1}

a_{μ_i}, b_{μ_i}, c_{μ_i} = curve fitting constants given in Table 6.1.

Figure 6.3b illustrates the species viscosity variation with temperature described by this equation. The Eucken relation is then used to compute the species thermal conductivities:

$$k_i = \frac{\mu_i}{\hat{M}_i}\left(\frac{\hat{c}_{v_i}}{\hat{R}} + 2.5\right)\hat{R}, \tag{6.14}$$

where: k_i = coefficient of thermal conductivity in J m^{-1} s^{-1} K^{-1}

$\hat{M}_i$ = molar mass in kg mol^{-1}

$\hat{c}_{v_i}$ = molar heat at constant volume in J mol^{-1} K^{-1}.

More accurate methods for calculating the species conductivities are discussed in section 6.3-c. Figure 6.4b illustrates the variation of species conductivities with temperature according to Eq. (6.14).

6.3-b Theoretical Techniques for Viscosity.

A rigorous application of kinetic theory to the calculation of viscosity leads to the expression:

$$\mu_i = 2.6693 \times 10^{-6} \frac{\sqrt{m_i T}}{\sigma_i^2 \, \Omega^{(2,2)^*}}, \tag{6.15}$$

where:
m_i = molecular weight in unified mass units
T = temperature in K
σ_i = collision cross section in Å
$\Omega^{(2,2)^*}$ = reduced collision integral.

The above expression is only a first approximation to the viscosity of a pure gas, but is shown by Hirschfelder et al. to provide close agreement with higher order approximations.

The reduced collision integral is a dimensionless function of reduced temperature T^*, and may be evaluated either from tabulated data, in the form of a look up table, or approximated by the expression:

$$\Omega^{(2,2)^*} = \frac{1.0}{0.697 \left(1.0 + 0.323 \ln T^*\right)}. \tag{6.16}$$

Comparisons between tabulated data and Eq. (6.16) are provided in Figure 6.5, from which it can be seen that some improvement in accuracy may be gained by developing a better curve fit than Eq. (6.16).

The reduced temperature is given by:

Species	σ (Å)	ε_0/k (K)	m (u)
O_2	3.467	106.7	31.999
N_2	3.798	71.4	28.013
O	3.050	106.7	15.9995
NO	3.492	116.7	30.006
N	3.298	71.4	14.0065
Ar	3.542	93.3	39.948

Table 6.2 Lennard-Jones (6-12) Potential Parameters for the Six Species Air Model.

$$T^* = \frac{kT}{\varepsilon_{0i}} \tag{6.17}$$

where k is the Boltzmann constant. The above expressions are based on the Lennard-Jones (6-12) model representing the potential energy of two interacting particles. The parameters associated with this potential, σ and ε_0, are taken from Svehla (1962) and given in Table 6.2, together with the species molecular weights. Figure 6.3a illustrates the variation of species viscosity based on Eq.(6.15) with the data given in Table 6.2. Comparing this result with Figures 6.3b highlights some differences in the two sets of data on which these plots are based. It is likely that the estimation techniques used by Svehla for the monatomic species data are less accurate than the information on which the curve fits are based, although further investigation into the original data sources for the curve fits is required in order to establish this.

6.3-c Theoretical Techniques for Thermal Conductivity.

Thermal conductivities are more difficult to estimate accurately than viscosities, mainly because of the numerous mechanisms available for exchanging energy between particles. For monatomic gases, rigorous kinetic theory, again based on the Lennard-Jones (6-12) potential, leads to the expression:

$$\frac{k_i \hat{M}_i}{\mu_i} = 2.5\, \hat{c}_{vi} \,. \tag{6.18}$$

This expression is valid where the only energy storage mode is translational. In the case of the diatomic species, a further extension of this equation is required. Several correlations have been proposed of the form:

$$\frac{k_i \hat{M}_i}{\mu_i} = f_{tr}\, \hat{c}_{tr} + f_{int}\, \hat{c}_{int} \,. \tag{6.19}$$

Of these, the most popular is the Eucken relation, Eq. (6.14). Reid and Sherwood (1966) describe additional empirically based models in this form, notably the modified Eucken model, the Stiel and Thodos model and the Brokaw model. However, none of these techniques are entirely satisfactory for diatomic gases over wide temperature ranges, in which case the Bromley model provides a greater accuracy. With this

Species	T_c (K)
O_2	154.8
N_2	126.2
NO	180.0

Table 6.3 Critical Temperatures for the Diatomic Species.

model, thermal conductivity is calculated from the expression:

$$\frac{k_i \hat{M}_i}{\mu_i} = 1.30\,\hat{c}_{v_i} + \left(1.75 - \frac{0.35}{T_{r_i}}\right)\hat{R}\,, \tag{6.20}$$

where: T_{r_i} = reduced temperature T/T_{c_i}

T_{c_i} = critical temperature in K.

The species specific heats appearing in Eqs. (6.18) and (6.20) may be calculated using the techniques of section 4.4. Critical temperatures for the three diatomic species are given in Table 6.3.

Figure 6.4a illustrates the application of Eq. (6.20). There is not good agreement between this data and the equivalent curve fit data in Figure 6.4b, primarily because of the differences between the viscosity calculations for the two techniques. Again, further investigation of the original data sources for the curve fit data are required before any conclusion can be drawn about the accuracy of either technique.

6.4 Transport Coefficients of the Gas Mixture.

Rigorous kinetic theory derivations of the transport coefficients for gas mixtures lead to an expression involving the determinants of matrices with elements dependent on the species properties, concentrations and various collision integrals. The resulting expression is complex and unwieldy, and not well suited to repeated evaluations within a CFD code. However, various estimation techniques have been developed which greatly simplify the problem, without introducing unacceptable approximations.

6.4-a Estimation of Mixture Viscosity.

The rigorous equation for mixture viscosities can be written in an approximate series form, and, by neglecting second order terms, reduced to:

$$\mu = \sum_{i=1}^{n} \frac{\mu_i}{1 + \sum\limits_{\substack{j=1 \\ j\neq i}}^{n} \phi_{ij} \frac{x_j}{x_i}}\,, \tag{6.21}$$

where: μ = mixture viscosity in kg m^{-1} s^{-1}

x_i = species mole fractions

ϕ_{ij} = viscosity parameter.

The accuracy of Eq (6.21) hinges on the expressions chosen to represent the viscosity parameter. Again, the equations for this parameter developed directly from kinetic

theory are too unwieldy for repeated use in CFD codes, since they rely on the evaluation of viscous and diffusion collision integrals and binary diffusion coefficients for each pair of species. The evaluation of Eq. (6.21) may be made more efficient if the Wilke estimation method for the viscosity parameter is employed. In this case ϕ_{ij} is given by:

$$\phi_{ij} = \frac{\left[1 + \left(\mu_i/\mu_j\right)^{1/2} \left(\hat{M}_j/\hat{M}_i\right)^{1/4} \right]^2}{\sqrt{8} \left[1 + \left(\hat{M}_i/\hat{M}_j\right) \right]^{1/2}} \tag{6.22}$$

$$\phi_{ji} = \left(\mu_i/\mu_j\right) \left(\hat{M}_j/\hat{M}_i\right) \phi_{ij} \, . \tag{6.23}$$

Since the species viscosities have been previously calculated, Eqs. (6.22) and (6.23) are easy to evaluate even for complex gas mixtures.

Mixture viscosity calculations are illustrated in Figure 6.6, based on the species curve fit data of Blottner et al. and the Wilke mixing formula. Excellent agreement can be observed with the curve fit data in Figure 6.1, up to energies of 25 x 10^6 J kg^{-1}. Above these energy levels, ionization becomes significant and the two gas models on which Figures 6.1 and 6.6 are based are no longer equivalent.

6.4-b Estimation of Mixture Thermal Conductivity.

Several techniques are available for estimating mixture conductivities based on expressions similar in form to Eq. (6.21). The most significant of these are discussed by Reid and Sherwood, who establish that the method developed by Cheung, Bromley and Wilke is most suitable for calculating the thermal conductivities of mixtures of monatomic gases with linear, non polar polyatomic gases. Since the gas model considered here consists of monatomic and diatomic, non polar species, this is the technique adopted. In this case, the conductivities of the pure components are broken into two parts, defined by:

$$k_i^{*} = \begin{cases} k_i & \text{monatomic species} \\ \dfrac{k_i}{1.0 + 0.35 \left(\hat{c}_{v_i}/\hat{R} - 1.0\right)} & \text{diatomic species} \end{cases} \tag{6.24}$$

$$k_i^{**} = k_i - k_i^{*}. \tag{6.25}$$

The mixture conductivity is then computed from the Wassiljewa expansion:

$$k = \sum_{i=1}^{n} \frac{k_i^*}{1 + \sum_{\substack{j=1 \\ j\neq i}}^{n} \left(\hat{M}_{ij}/\hat{M}_i\right)^{1/8} \phi_{ij} \frac{x_j}{x_i}} + \sum_{i=1}^{n} \frac{k_i^{**}}{1 + \sum_{\substack{j=1 \\ j\neq i}}^{n} \phi_{ij} \frac{x_j}{x_i}} \qquad (6.26)$$

where: $$\hat{M}_{ij} = \frac{1}{2}(\hat{M}_i + \hat{M}_j). \qquad (6.27)$$

Using the Wassiljewa expansion to compute mixture conductivity has the additional advantage in that the parameters ϕ_{ij} are already known from Eqs. (6.22) and (6.23) used in the computation of the mixture viscosity.

6.5 Recommendations on the Calculation of the Transport Coefficients.

For chemical equilibrium problems, most authors appear to prefer curve fits or look up tables directly for the transport properties of the gas mixture. For example, Thareja et al. (1983) implement simple curve fits for viscosity and neglect the pressure dependence of Prandtl number, expressing it only as a function of enthalpy so that:

$$k = \frac{\mu c_p}{Pr(h)}. \qquad (6.28)$$

The simplicity of their curve fits is unfortunately outweighed by their limited accuracy and validity. Prabhu and Tannehill (1986) also use curve fitting techniques and Tannehill et al. (1988) use the curve fits of Srinivasan et al. (1987b), as detailed in section 6.2.

The advantages of using physically based models for chemical equilibrium state equations, in terms of providing additional information about the flow, do not apply to such models for the transport coefficients. The fast execution of the curve fits therefore make this approach very attractive. However, the data presented in section 6.2 are based on a nine species air model, including ionization, and are therefore inconsistent with the six species air model developed in chapter four. The importance of this inconsistency is not likely to be significant at low temperatures, where little ionization is evident. However, at elevated temperatures the reduced viscosities and increased conductivities associated with ionization will produce inaccurate estimates of heat transfer rate and skin friction at solid surfaces. The most efficient technique consistent with the model developed in chapter four is therefore to use curve fits for species transport properties and use the estimation techniques of Wilke and Cheung et al. to compute mixture properties.

When considering extension to chemical or vibrational nonequilibrium, curve fitting for mixture properties is no longer a practical proposition. In this case, the most popular approach is to use species property curve fits such as those discussed in section 6.3-a, and one of the several mixture property estimation techniques available.

6.6 CHEMICAL NONEQUILIBRIUM.

Chemical and vibrational nonequilibrium phenomena have longer relaxation times than either translational or rotational processes, and are therefore treated somewhat differently. Vibrationally relaxing models have not been examined in the course of this work, but aspects of chemical relaxation have, and are therefore discussed here.

6.6-a Additional Chemical Reactions.

Park (1985) discusses an eleven species argon free air model, including ionization. This model includes thirty-three dissociation reactions, nine exchange reactions and five ionization reactions, and is therefore quite comprehensive, despite neglecting the presence of argon. The work presented here has neglected ionization on the understanding that care should be taken when assessing the accuracy of high temperature applications. Conversely, the inclusion of argon in the current model slightly improves the realism of low temperature solutions. In developing a chemically relaxing model consistent with the equilibrium model already presented, the Park model may be simplified and the reactions described by Eqs. (4.27) to (4.29) supplemented by the exchange reactions:

$$NO + O \leftrightarrow N + O_2 \qquad \Delta\hat{e}_R{}^0 = 133.364 \text{ kJ mol}^{-1} \quad (6.29)$$

$$N_2 + O \leftrightarrow N + NO \qquad \Delta\hat{e}_R{}^0 = 314.706 \text{ kJ mol}^{-1} \quad (6.30)$$

and the dissociation reactions:

$$NO + X \leftrightarrow N + O + X \qquad \Delta\hat{e}_R{}^0 = 626.930 \text{ kJ mol}^{-1}. \quad (6.31)$$

The dissociation reaction Eqs. (4.27) (4.29) and (6.31) each represent a set of six reactions with different catalytic bodies, and the overall model therefore represents a set of twenty one reactions.

The equilibrium constants for reaction Eqs. (4.27) to (4.29) have been described in section 4.5. For the above reactions, these constants may be computed from the equations:

$$K_4 = \frac{\eta_1\eta_5}{\eta_3\eta_4} = \left(\frac{K_3}{K_1K_2}\right)^{1/2} \tag{6.32}$$

$$K_5 = \frac{\eta_4\eta_5}{\eta_2\eta_3} = \left(\frac{K_2K_3}{K_1}\right)^{1/2} \tag{6.33}$$

$$K_6 = \frac{\eta_3\eta_5}{\eta_4} = \left(\frac{K_1K_3}{K_2}\right)^{1/2}. \tag{6.34}$$

Rakich et al. (1983) and Park (1985) use low order polynomial fits directly for the equilibrium coefficients in their models. Extending the Prabhu and Erickson method discussed in section 4.4-b to compute the equilibrium coefficients in Eqs. (4.47) to (4.49) and (6.32) to (6.34) should provide a more accurate and versatile technique, giving more detailed thermodynamic information at little additional computational expense.

6.6-b Modelling the Production Terms.

The species concentrations in a chemically relaxing gas are computed from the mass conservation equations discussed in chapter two. These relations require knowledge of the production rates for the six component gases. The production rates are in turn dependent on the forward and reverse reaction rates associated with the twenty one reactions. The forward reaction rates can be computed from the modified Arrhenius equation:

$$k_{f_r} = C_{f_r} T^{\eta_{f_r}} e^{-\theta_{f_r}/T} \qquad r = 1, 21 \tag{6.35}$$

and reverse reaction rates follow from the known equilibrium constants:

$$k_{b_r} = \frac{k_{f_r}}{K_r} \qquad r = 1, 21. \tag{6.36}$$

Table 6.4 summarizes the experimental data required to evaluate these rate constants.

The production rates required in Eqs. (2.13) are now given by:

$$\dot{\omega}_s = \sum_{r=1}^{26} \left(\nu''_{sr} - \nu'_{sr}\right) k_{f_r} \left\{ \prod_{s=1}^{6} \left(\rho\eta_s\right)^{\nu'_{sr}} - \frac{1}{K_r} \prod_{s=1}^{6} \left(\rho\eta_s\right)^{\nu''_{sr}} \right\} \tag{6.37}$$

where the ν'_{sr} and ν''_{sr} are the stoichiometric coefficients for each species s appearing on the left and right sides respectively of each reaction r:

r	Reaction	K	C_f	η_f	θ_f	ref.
1	$2O_2 \leftrightarrow 2O + O_2$	Eq. (4.47)	2.750×10^{19}	-1.0	59 500	c.
2	$O_2 + N_2 \leftrightarrow 2O + N_2$	"	2.750×10^{19}	"	"	c.
3	$O_2 + O \leftrightarrow 3O$	"	8.250×10^{19}	"	"	c.
4	$O_2 + NO \leftrightarrow 2O + NO$	"	2.750×10^{19}	"	"	c.
5	$O_2 + N \leftrightarrow 2O + N$	"	8.250×10^{19}	"	"	c.
6	$O_2 + Ar \leftrightarrow 2O + Ar$	"	3.628×10^{18}	"	"	a.
7	$N_2 + O_2 \leftrightarrow 2N + O_2$	Eq. (4.49)	3.700×10^{21}	-1.6	113 200	c.
8	$2N_2 \leftrightarrow 2N + N_2$	"	3.700×10^{21}	"	"	c.
9	$N_2 + O \leftrightarrow 2N + O$	"	1.110×10^{22}	"	"	c.
10	$N_2 + NO \leftrightarrow 2N + NO$	"	3.700×10^{21}	"	"	c.
11	$N_2 + N \leftrightarrow 3N$	"	1.110×10^{22}	"	"	c.
12	$N_2 + Ar \leftrightarrow 2N + Ar$	"	1.924×10^{17}	-0.5	"	a.
13	$NO + O_2 \leftrightarrow N + O + O_2$	Eq. (6.32)	2.300×10^{17}	-0.5	75 500	c.
14	$NO + N_2 \leftrightarrow N + O + N_2$	"	2.300×10^{17}	"	"	c.
15	$NO + O \leftrightarrow N + 2O$	"	4.600×10^{17}	"	"	c.
16	$2NO \leftrightarrow N + O + NO$	"	2.300×10^{17}	"	"	c.
17	$NO + N \leftrightarrow 2N + O$	"	4.600×10^{17}	"	"	c.
18	$NO + Ar \leftrightarrow N + O + Ar$	"	3.990×10^{20}	-1.5	"	a.
19	$N_2 + O_2 \leftrightarrow 2NO$	Eq. (4.48)	4.600×10^{24}	-2.5	64 600	b.
20	$NO + O \leftrightarrow N + O_2$	Eq. (6.30)	2.160×10^{8}	1.290	19 220	c.
21	$N_2 + O \leftrightarrow N + NO$	Eq. (6.31)	3.180×10^{13}	0.1	37 700	c.

Table 6.4 Forward Rate Constants for the Twenty One Reaction Air Model.
a. Wray (1962), b. Vincenti & Kruger (1965), c. Park (1985).

$$\sum_{s=1}^{6} \nu'_{sr} X_s \leftrightarrow \sum_{s=1}^{6} \nu''_{sr} X_s \,. \tag{6.38}$$

Two problems can be identified when computing species mole fractions from the above expressions. Firstly, the equilibrium constant K may tend to zero in some circumstances. From Eq (6.37), this will result in an infinite production rate. In such a case, the species mass conservation equations are redundant, and the concentrations may be computed using the equilibrium techniques of chapters four and five. A similar problem arises when the production rates are close to zero. This represents frozen flow, where again the species conservation equations are redundant.

The numerical problems associated with areas of equilibrium or frozen flow embedded in an otherwise nonequilibrium flow are not insubstantial. Further research is required in this area, in order to establish the viability of using Eq. (6.37) directly in the form given. One solution to this problem is to rewrite Eq. (6.37) in terms of the backward rate constant, using Eq. (6.36). Curve fits for both forward and backward rate constants in a modified Arrhenius form can then be used, so avoiding numerical overflow errors (Prabhu et al., 1987a).

The second problem linked to the species mass conservation equations is associated with cumulative numerical errors. In order to conserve mass globally, one species conservation equation must be dropped and the respective concentration found from the global continuity equation. However, if the species dropped is not a dominant one, numerical errors can force its concentration to become negative. This problem is exaggerated for inviscid flows, where nuclear conservation must also be satisfied. The solution to this problem is fully discussed by Park (1985 and 1990).

6.7 Solution Techniques for the Chemical Nonequilibrium Equations.

A number of techniques have been developed for integrating the equations of motion for finite rate chemically reacting flows. The most logical of these rely on simultaneously integrating the conservation equations for the fluid and chemical variables. Many of the schemes available for integrating viscous and inviscid perfect gas equations can be extended to solve chemical relaxation problems if this approach is adopted. This technique is favoured by Prabhu at al (1987a and 1987b) and Shuen (1992). However, the numerous unknowns associated with any but the simplest air model and the restrictive time step imposed by stiff chemical equations can render this approach impractical (Bhutta and Lewis, 1988).

Fortunately in many problems the coupling between the fluid variables and chemical variables is not strong, and some form of loosely coupled integrating scheme can be devised (Park, 1990). In this case, the overall problem is broken into two parts: a fluid mechanics problem and a chemistry problem. These two problems are then solved separately but iteratively, thereby greatly reducing the complexity of the algorithms required. Furthermore, existing perfect gas integration schemes can be modified to deal with the fluid mechanics problem with less effort than if the chemical equations are solved simultaneously. Loosely coupled integration schemes are favoured by many authors, notably Rakich et al. (1983), Bhutta et al. (1985), Sinha et al. (1987), York et al. (1988) and Bhutta and Lewis (1988).

Chapter Seven

CONCLUSIONS AND FUTURE RESEARCH

Chapters four and five presented the development and implementation of a state equation model for equilibrium air. Chapter six continued by discussing the techniques available for modelling the transport coefficients for air. This chapter completes the dissertation by drawing conclusions from previous results and putting forward recommendations for future research.

7.1 CONCLUSIONS.

The conclusions drawn from this research can be summarized as follows.

7.1-a Curve Fitting Techniques for Equilibrium Mixture Properties.

Curve fitting techniques are the easiest equilibrium gas models to implement within the CFD environment. They require little understanding of the basic physics of high temperature air, and they do not require the computation of the chemical composition of air. They are therefore the fastest techniques for calculating the equilibrium state of air, providing few state variables are required. Curve fits can be formulated directly in terms of either conserved or primitive variables, thereby precluding the need for any inversion of the state equations.

The lack of a physical foundation for these techniques can, however, be considered a disadvantage. Separate curves are necessary for each different thermodynamic variable required during the solution of the equations of motion, and the computing time when several such variables are required becomes excessive. Furthermore, it is not possible to form one continuous curve throughout the necessary temperature range. While careful choice of coefficients can to a large extent preserve continuity in any thermodynamic variable across boundaries between curves, thermodynamic derivatives inevitably exhibit discontinuous behaviour. Some degree of accuracy must therefore be sacrificed if parameters such as sonic speed, specific heats or derivatives χ and κ are to be evaluated from curve fit data for the basic thermodynamic properties.

7.1-b Physically Based Techniques for the Equilibrium Mixture Properties.

The technique developed in chapter four for computing the mixture properties provides improved versatility over any curve fitting method. In particular, the gas composition can easily be varied to represent different proportions of oxygen and nitrogen in the upper reaches of the stratosphere. Furthermore, the technique may be extended to include additional species, or to model ionization, with a minimal amount of work. As this technique relies on computing the chemical composition of the gas, very little extra calculation is required for additional state variables. The smoothness provided by using physically based techniques is greatly improved over any curve fitting method, and is particularly evident in sonic speed calculations.

The greatest disadvantage of physically based techniques is the need to use temperature as a fundamental variable. This does not fit in well with numerical algorithms for solving the equations of motion, which require the state variables either as functions of density and internal energy, or of density and pressure. Iterative schemes for computing temperature as a function of density and internal energy have therefore been investigated and it is concluded that Newton-Raphson schemes provide the best compromise between convergence rate and computation time.

The additional information provided by physically based techniques, particularly the data on the chemical composition of air, is not always needed directly by algorithms for solving the flow equations. Therefore if time accuracy is not required during the solution process, these techniques are unnecessarily slow when iterating to reach a steady state.

7.1-c Transport Coefficients.

For equilibrium calculations, transport coefficients must be calculated using curve fit data unless the chemical composition and species specific heats are known. However, if chemical data are available from a physically based state equation model, it is more efficient to combine this with an empirically based mixing rule such as the Wilke estimation method discussed in section 6.4. It is noted that species viscosities can be more quickly evaluated using curve fits, rather than relying on complex theoretical expressions.

In the case of chemical nonequilibrium calculations, mixing rules must be used because the composition of the gas is no longer a unique function of two state variables.

7.1-d Recommendations.

For steady state calculations derived using a time dependent approach, it is observed that computational speed is initially of greater importance than accuracy of the state equation model. Curve fitting techniques are therefore preferred in the initial stages of the solution process, and a switch to using physical methods made once the solution has almost converged. Furthermore, it is recommended that a converged perfect gas solution should be used as the initial condition for an equilibrium solution, in an effort to further reduce the required computing times.

It has been found that species property curve fits can provide a better compromise between accuracy and speed than equivalent expressions developed from molecular theories. For the air state calculations considered here, there is no sacrifice of versatility made by the adoption of this approach. It is therefore recommended that any extension of the techniques presented here should be made using such curve fits.

For time accurate solutions, it is desirable to always use physically based equilibrium models in order to provide the required accuracy, particularly for sonic speed calculations. Such an approach also provides more data at each time step and therefore facilitates more detailed analysis of the results.

Curve fitting for mixture properties becomes impractical for chemical nonequilibrium problems. It is envisaged that the most appropriate technique in this case is to again use species property curve fits and combine these using the results of section 4.8, with the chemical compositions computed from the solutions of production rate equations.

7.2 Future Research.

Future research in the field of hypersonic aerodynamics can be divided broadly into two categories; physical aspects and numerical aspects.

7.2-a Physical Aspects.

The most immediate extension of the work presented here is the implementation of the viscosity and thermal conductivity models within a CFD code. The state equation model discussed in chapters four and five can be included directly within a solution algorithm for the viscous equations, along with the transport coefficient models discussed in chapter six. However, the one dimensional nozzle problem is not well suited to testing viscous models, and more representative test problems should be designed, such as locally conical or parabolized Navier-Stokes problems or two

dimensional full Navier-Stokes problems. These test cases introduce additional complications with generating grids and performing grid transformations before solving the equations of motion.

A second straightforward expansion of this work is to extend the equilibrium routines to include ionization at high temperatures.

Some preliminary work has been laid down regarding the development of algorithms for the solution of chemical nonequilibrium problems. Further research is required in this area, particularly in establishing the best methods for modelling the production rate terms appearing in the equations of motion and in overcoming the stiffness problems associated with fast reactions. For inviscid chemical nonequilibrium problems, the one dimensional nozzle problem is an ideal test case, because equilibrium, frozen and nonequilibrium chemistry can be identified at various points along a subsonic-supersonic expansion nozzle. In addition, stationary discontinuities can be set up within the nozzle to demonstrate the ability of numerical algorithms to cope with the relaxation zone behind a shock.

Two aspects of nonequilibrium research which have not been addressed within this dissertation are vibrationally relaxing flows, where the internal energy of the individual species is considered to be out of equilibrium, and viscous chemically relaxing flows. In modelling vibrational relaxation, a unique temperature for the gas cannot be identified, and an additional thermodynamic variable, the vibrational temperature, must therefore be introduced. In order to describe the behaviour of this temperature, an additional relaxation equation must be introduced. A further refinement of this model would be to separate the vibrational temperatures for all diatomic species in the mixture and treat each one independently. Such an approach, while providing a very high potential for the accurate physical representation of air, would require detailed information on the vibrational behaviour of the component species.

Modelling viscous chemically relaxing flows introduces the requirement for mass diffusion coefficients for the species present in the mixture. These may be evaluated using mixing rules similar to those for viscosity and conductivity.

7.2-b Numerical Aspects.

It was mentioned at the beginning of chapter five that the scheme used to discretize the equations of motion was chosen for its numerical simplicity. The trapezoidal time differencing used provides the implicit scheme required for stiff, nonequilibrium problems, but the central space differencing is not considered adequate to resolve the relaxation zones behind shock waves in nonequilibrium air. Close to shock waves, discretization errors tend to swamp any physical refinements made to the equations of

motion. Modern high resolution schemes, however, can potentially capture shock waves with only one interior point and it is therefore highly desirable that these should be extended to deal with both equilibrium air problems and chemically relaxing problems.

Adaptive grid generation techniques are likely to be very useful in chemically relaxing flows, as grids can be refined in regions of high chemical activity, so improving the resolution of the solution and at the same time relieving some of the stiffness problems associated with fast reactions.

The execution times associated with the numerical solution of both equilibrium and nonequilibrium equations of motion are considerably longer than those for equivalent perfect gas cases. Clearly, it is desirable to extend available acceleration techniques for perfect gas algorithms, such as multi-grid acceleration, to deal with real gas algorithms.

REFERENCES

Abgrall, R. (1991) "An Extension of Roe's Upwind Scheme to Algebraic Equilibrium Real Gas Models", *Computers and Fluids*, Vol. 19, No. 2, pp 171-182.

Anderson, J. D., Jr. (1986) *Hypersonic and High Temperature Gas Dynamics*, McGraw-Hill Book Co.

Anderson, J. M. (1989) "Implementation of Equilibrium Air Models Within the Framework of an Existing Euler Code.", *GU Aero Report No. 8906*, Department of Aerospace Engineering, University of Glasgow.

Anderson, J. M. (1992) "A Fast Computational Module for the Calculation of Equilibrium State Variables and Sonic Speeds in Chemically Reacting Air, for Applications in CFD", *GU Aero Report No. 9206*, Department of Aerospace Engineering, University of Glasgow.

Anderson, W. K., Thomas, J. L. and van Leer, B. (1985) "A Comparison of Finite Volume Flux Vector Splittings for the Euler Equations", *AIAA paper 85-0122*, AIAA 23rd Aerospace Sciences Meeting.

Balakrishnan, A., Lombard, C. K. and Davy, W. C. (1983) "Real Gas Flowfields About Three Dimensional Configurations", *AIAA paper 83-0581*, AIAA 21st Aerospace Sciences Meeting.

Beam, R. M. and Warming, R. F. (1976) "An Implicit Finite-Difference Algorithm for Hyperbolic systems in Conservation-Law Form", *J. Computational Physics*, Vol. 22, pp 87-110.

Bhutta, B. A. and Lewis, C. H. (1988) "Three-Dimensional Hypersonic Nonequilibrium Flows at Large Angles of Attack", *AIAA paper 88-2568.*

Bhutta, B. A., Lewis, C. H. and Kautz, F. A. (1985) "A Fast Fully-Iterative Parabolized Navier-Stokes Scheme for Chemically-Reacting Reentry Flows", *AIAA paper 85-0926*, AIAA 20th Thermophysics Conference.

Blottner, F. G., Johnson, M. and Ellis, M. (1971) "Chemically Reacting Viscous Flow Program for Multi-Component Gas Mixtures", *Report no. SC-RR-70-754*, Sandia Laboratories, Albuquerque, New Mexico.

Erickson, W. D., Kemper, J. T. and Allison, D. O. (1966) "A Method for Computing Chemical-Equilibrium Compositions of Reacting-Gas Mixtures by Reduction to a Single Iteration Equation", *NASA Technical Note D-3488.*

Fröberg, C.-E. (1985) *Numerical Mathematics - Theory and Computer Applications*, Benjamin/Cummings Publishing Company.

Glaister, P. (1988) "An Approximate Linearised Riemann Solver for the Euler Equations for Real Gases", *J. Computational Physics*, Vol. 74, pp 382-408.

Gordon, S. and McBride, B. J. (1971) "Computer Program for Calculation of Complex Chemical Equilibrium Compositions, Rocket Performance, Incident and Reflected Shocks and Chapman-Jouget Detonations", *NASA SP-273 Interim Revision N78-17724.*

Grabau, M. (1959) "A Method of Forming Continuous Empirical Equations for the Thermodynamic Properties of Air from Ambient Temperatures to 15 000 K, with Applications", *AEDC-TN-59-102*, Arnold Engineering Development Centre.

Grossman, B. and Walters, R. W. (1989) "Analysis of Flux-Split Algorithms for Euler's Equations with Real Gases", *AIAA Journal*, Vol. 27, No. 5, pp 524-531.

Hilsenrath, J. and Klein, M. (1965) "Tables of Thermodynamic Properties of Air in Chemical Equilibrium Including Second Viral Corrections from 1500 to 15000 K", *AEDC-TR-65-68*, Arnold Engineering Development Centre.

Hirsch, C. (1989a) *Numerical Computation of Internal and External Flows*, Vol 1, John Wiley & Sons.

Hirsch, C. (1989b) *Numerical Computation of Internal and External Flows*, Vol 2, John Wiley & Sons.

Hirschfelder, J. O., Curtiss, C. F. and Bird, R. B. (1954) *Molecular Theory of Gases and Liquids* , John Wiley & Sons.

Jameson, A., Schmidt, W. and Turkel, E. (1981) "Numerical Solutions of the Euler Equations by Finite Volume Methods Using Runge-Kutta Time-Stepping Schemes", *AIAA paper 81-1259*, AIAA 14th Fluid and Plasma Dynamics Conference.

Kuo, K. K. (1986) *Principles of Combustion*, John Wiley & Sons.

Liepmann, H. W. and Roshko, A. (1957) *Elements of Gasdynamics*, John Wiley & Sons.

Liou, M.-S., van Leer, B. and Shuen, J.-S. (1990) "Splitting of Inviscid Fluxes for Real Gases", *J. Computational Physics*, Vol. 87, pp 1-24.

Lomax, H. and Inouye, M. (1964) "Numerical Analysis of Flow Properties About Blunt Bodies Moving at Supersonic Speeds in an Equilibrium Gas", *NASA Technical Report R-204.*

MacCormack, R. W. (1969) "The Effect of Viscosity in Hypervelocity Impact Cratering", *AIAA paper 69-354.*

Mansen, C. F. and Hodge, M. E. (1961) "Constant Entropy Properties for an Approximate Model of Equilibrium Air", *NASA Technical Note D-352.*

Maus, J. R., Griffith, B. J., Szema, K. Y. and Best, J. T. (1984) "Hypersonic Mach Number and Real Gas Effects on Space Shuttle Orbiter Aerodynamics.", *J. Spacecraft*, Vol. 21, No. 2, pp 136-141.

Mayer, J. E. and Mayer, M. G. (1940) *Statistical Mechanics*, John Wiley & Sons.

Moore, C. E. (1942, 1952, 1958) *Atomic Energy Levels as Derived from the Analysis of Optical Spectra*. U. S. National Bureau of Standards Circulars 467, Vols. 1, 2 and 3.

Oran, E. S. and Boris, J. P. (1987) *Numerical Simulation of Reactive Flow*, Elsevier Publishing Co.

Osher, S. and Chakravarthy, S. (1983) "Upwind Schemes and Boundary Conditions with Applications to Euler Equations in General Geometries", *J. Computational Physics*, Vol. 50, pp 447-481.

Osher, S. and Solomon, F. (1982) "Upwind Difference Schemes for Hyperbolic Systems of Conservation Laws", *Mathematics of Computation*, Vol. 38, No. 158, pp 339-374.

Park, C. (1985) "On Convergence of Computation of Chemically Reacting Flows", *AIAA paper 85-0247*, AIAA 23rd Aerospace Sciences Meeting.

Park, C. (1990) *Nonequilibrium Hypersonic Aerothermodynamics*, John Wiley & Sons.

Poll, D. I. A. and Hodgson, J. P. (1988) "The Development of an Equilibrium Gas Code Module for Aerodynamic Design of HOTOL-type Space Vehicles", *Report No. DIAP10-AML*, Department of Engineering, University of Manchester.

Prabhu, D. K., Tannehill, J. C. (1986) "Numerical Solution of Space Shuttle Orbiter Flowfield Including Real-Gas Effects", *J. Spacecraft*, Vol. 23, No. 3, pp 264-272.

Prabhu, D. K., Tannehill, J. C., and Marvin, J. G. (1987a) "A New PNS Code for Chemical Nonequilibrium Flows", *AIAA paper 87-0284*, AIAA 25th Aerospace Sciences Meeting.

Prabhu, D. K., Tannehill, J. C., and Marvin, J. G. (1987b) "A New PNS Code for Three-Dimensional Chemically Reacting Flows", *AIAA paper 87-1472*, AIAA 22nd Thermophysics Conference.

Prabhu, R. K. and Erickson, W. D. (1988) "A Rapid Method for the Computation of Equilibrium Chemical Composition of Air to 15 000 K", *NASA Technical Paper 2792*.

Qin, N. (1987) *Towards Numerical Simulation of Hypersonic Flow Around Space-Plane Shapes*, Ph. D. Thesis, University of Glasgow.

Rakich, J. V., Bailey, H. E. and Park, C. (1983) "Computation of Nonequilibrium, Supersonic Three-Dimensional Inviscid Flow over Blunt-Nosed Bodies", *AIAA Journal*, Vol. 21, No. 6, pp 834-841.

Reid, R. C. and Sherwood, T. K. (1966) *The Properties of Gases and Liquids*, McGraw-Hill Book Company.

Roe, P. L. (1981) "Approximate Riemann Solvers, Parameter Vectors and Difference Schemes", *J. Computational Physics*, Vol. 43, pp 357-372.

Royal Aeronautical Society (1962) *Mollier Chart of the Thermodynamic Properties of Argon-free Air in Dissociation Equilibrium*, R. Ae. S., 4 Hamilton Place, London.

Shuen, J.-S. (1992) "Upwind Differencing and LU Factorization for Chemical Non-equilibrium Navier-Stokes Equations", *J. Computational Physics*, Vol. 99, pp 233-250.

Sinha, N., Dash, S. M. and Krawczyk, W. J. (1987) "Inclusion of Chemical Kinetics into Beam-Warming Based PNS Model for Hypersonic Propulsion Applications", *AIAA paper 87-1898*, AIAA/SAE/ASME/ASEE 23rd Joint Propulsion Conference.

Srinivasan, S., Tannehill, J. C. and Weilmuenster, K. J. (1987a) "Simplified Curve Fits for the Thermodynamic Properties of Equilibrium Air", *NASA Reference Publication 1181*.

Srinivasan, S., Tannehill, J. C., and Weilmuenster, K. J. (1987b) "Simplified Curve Fits for the Transport Properties of Equilibrium Air", *ISU-ERI Report 88405*, Iowa State University, Engineering Research Institute, Ames, Iowa.

Suresh, A. and Liou, M.-S. (1991) "Osher's Scheme for Real Gases", *AIAA Journal*, Vol. 29, No. 6, pp 920-926.

Svehla, R. A. (1962) "Estimated Viscosities and Thermal Conductivities of Gases at High Temperatures", *NASA Technical Report R-132*.

Tannehill, J. C. and Mugge, P. H. (1974) "Improved Curve Fits for the Thermodynamic Properties of Equilibrium Air Suitable for Numerical Computation Using Time-Dependent or Shock-Capturing Methods", *NASA Contractor Report 2470*.

Tannehill, J. C., Ievalts, J. O. and Lawrence, S. L. (1988) "An Upwind Parabolized Navier-Stokes Code for Real Gas Flows", *AIAA paper 88-0713*, AIAA 26th Aerospace Sciences Meeting.

Thareja, R. R., Szema, K. Y. and Lewis, C. H. (1983) "Chemical Equilibrium Laminar or Turbulent Three-Dimensional Viscous Shock-Layer Flows", *J. Spacecraft*, Vol. 20, No. 5, pp. 454-460.

Vincenti, W. G. and Kruger, C. H. (1965) *Introduction to Physical Gas Dynamics*, Robert E. Krieger Publishing Co.

Vinokur, M. and Montagné, J.-L. (1990) "Generalized Flux-Vector Splitting and Roe Average for an Equilibrium Real Gas", *J. Computational Physics*, Vol. 89, pp 276-300.

Wang, Z. J. (1990) *Numerical Simulation of 3-D Hypersonic Flow Using High Resolution Schemes*, Ph. D. Thesis, University of Glasgow.

Wray, K. L. (1962) "Chemical Kinetics of High Temperature Air", *Progress in Astronautics and Rocketry*, Vol. 7, Academic Press, New York.

York, B. J., Sinha, N. and Dash, S. M. (1988) "Computational Models for Chemically-Reacting Hypersonic Flow", *AIAA paper 88-0509*, AIAA 26th Aerospace Sciences Meeting.

Young, J. C., Perez, L. F. Romere, P. O. and Kanipe, D. B. (1981) "Space Shuttle Entry Aerodynamic Comparisons of Flight 1 with Preflight Predictions", *AIAA paper 81-2476*, AIAA/SETP/SFTE/SAE/ITEA/IEEE 1st Flight Testing Conference.

APPENDIX ONE

The Jacobian matrix defined by Eq. (3.2) can be derived as follows. Writing the flux vector **F** in terms of the components of the solution vector **U** gives:

$$\mathbf{F} = \begin{bmatrix} m \\ \frac{m^2}{\rho} + p \\ \frac{m}{\rho}(E+p) \end{bmatrix} \tag{A1.1}$$

where:

$$m = \rho u \tag{A1.2}$$

$$E = \varepsilon + \frac{\rho u^2}{2} \tag{A1.3}$$

The components of **F** can be differentiated to form the Jacobian:

$$\frac{\partial \mathbf{F}}{\partial \mathbf{U}} = \begin{bmatrix} 0 & 1 & 0 \\ \left(\frac{\partial p}{\partial \rho}\right)_{m,E} - \frac{m^2}{\rho^2} & \left(\frac{\partial p}{\partial m}\right)_{\rho,E} + 2\frac{m}{\rho} & \left(\frac{\partial p}{\partial E}\right)_{\rho,m} \\ \frac{m}{\rho}\left(\frac{\partial p}{\partial \rho}\right)_{m,E} - (E+p)\frac{m}{\rho^2} & \frac{m}{\rho}\left(\frac{\partial p}{\partial m}\right)_{\rho,E} + \frac{E+p}{\rho} & \frac{m}{\rho}\left(\frac{\partial p}{\partial E}\right)_{\rho,m} + \frac{m}{\rho} \end{bmatrix} \tag{A1.4}$$

To evaluate the pressure derivatives in Eq. (A1.4), the chain rule for differentiation is applied to the generic form of the state equation, such that:

$$p = p(\rho, \varepsilon) \tag{A1.5}$$

$$\left(\frac{\partial p}{\partial \rho}\right)_{m,E} = \left(\frac{\partial p}{\partial \rho}\right)_{\varepsilon} + \left(\frac{\partial p}{\partial \varepsilon}\right)_{\rho}\left(\frac{\partial \varepsilon}{\partial \rho}\right)_{m,E} \tag{A1.6}$$

$$\left(\frac{\partial p}{\partial m}\right)_{\rho,E} = \left(\frac{\partial p}{\partial \varepsilon}\right)_{\rho}\left(\frac{\partial \varepsilon}{\partial m}\right)_{\rho,E} \tag{A1.7}$$

$$\left(\frac{\partial p}{\partial E}\right)_{\rho,m} = \left(\frac{\partial p}{\partial \varepsilon}\right)_{\rho}\left(\frac{\partial \varepsilon}{\partial E}\right)_{\rho,m} \tag{A1.8}$$

Internal energy density can be expressed from Eq. (A1.3) as:

$$\varepsilon = E - \frac{m^2}{2\rho} \tag{A1.9}$$

from which the required internal energy derivatives become:

$$\left(\frac{\partial \varepsilon}{\partial \rho}\right)_{m,E} = \frac{m^2}{2\rho^2} = \frac{u^2}{2} \tag{A1.10}$$

$$\left(\frac{\partial \varepsilon}{\partial m}\right)_{\rho,E} = -\frac{m}{\rho} = -u \tag{A1.11}$$

$$\left(\frac{\partial \varepsilon}{\partial E}\right)_{\rho,m} = 1 \tag{A1.12}$$

Defining the pressure derivatives χ and κ as:

$$\chi = \left(\frac{\partial p}{\partial \rho}\right)_{\varepsilon} \tag{A1.13}$$

$$\kappa = \left(\frac{\partial p}{\partial \varepsilon}\right)_{\rho} \tag{A1.14}$$

gives:

$$\left(\frac{\partial p}{\partial \rho}\right)_{m,E} = \chi + \kappa\frac{u^2}{2} \tag{A1.15}$$

$$\left(\frac{\partial p}{\partial m}\right)_{\rho,E} = -u\kappa \tag{A1.16}$$

$$\left(\frac{\partial p}{\partial E}\right)_{\rho,m} = \kappa \tag{A1.17}$$

Equation (A1.4) can now be expressed fully in terms of the primitive variables as:

$$A = \begin{bmatrix} 0 & 1 & 0 \\ \chi - (2-\kappa)\frac{u^2}{2} & (2-\kappa)u & \kappa \\ (\chi + \kappa\frac{u^2}{2} - \frac{\varepsilon+p}{\rho} - \frac{u^2}{2})u & \frac{\varepsilon+p}{\rho} + \frac{u^2}{2} - \kappa u^2 & (1+\kappa)u \end{bmatrix} \tag{A1.18}$$

The total specific enthalpy is identified by the grouping:

$$h_o = \frac{\varepsilon + p}{\rho} + \frac{u^2}{2} \tag{A1.19}$$

which reduces Eq. (A1.4) to:

$$A = \begin{bmatrix} 0 & 1 & 0 \\ \chi - (2-\kappa)\frac{u^2}{2} & (2-\kappa)u & \kappa \\ (\chi + \kappa\frac{u^2}{2} - h_o)u & h_o - \kappa u^2 & (1+\kappa)u \end{bmatrix} \tag{A1.20}$$

APPENDIX TWO

The exact equation for sonic speed derived from a generic thermal state equation in the form:

$$p = (\bar{\gamma} - 1)\,\rho\, e \tag{A2.1}$$

where:
$$\bar{\gamma} = \bar{\gamma}(\rho, e) \tag{A2.2}$$

is given as follows.

From the first and second laws of thermodynamics, the differential relationship between specific entropy, specific internal energy and mass density is:

$$T\,ds = de - \frac{p}{\rho^2}\,d\rho. \tag{A2.3}$$

The differential form of the state equation, Eq. (A2.1), is given by:

$$dp = e\left(\bar{\gamma} - 1 + \rho\left(\frac{\partial\bar{\gamma}}{\partial\rho}\right)_e\right)d\rho + \rho\left(\bar{\gamma} - 1 + e\left(\frac{\partial\bar{\gamma}}{\partial e}\right)_\rho\right)de. \tag{A2.4}$$

Combining Eqs. (A2.3) and (A2.4) and noting that $\frac{\partial}{\partial x} = \frac{1}{x}\frac{\partial}{\partial \ln x}$ gives:

$$\rho\left(\bar{\gamma}-1+\left(\frac{\partial\bar{\gamma}}{\partial \ln e}\right)_\rho\right)T ds = dp - \left[e\left(\bar{\gamma}-1+\left(\frac{\partial\bar{\gamma}}{\partial \ln \rho}\right)_e\right) + \frac{p}{\rho}\left(\bar{\gamma}-1+\left(\frac{\partial\bar{\gamma}}{\partial \ln e}\right)_\rho\right)\right]d\rho. \tag{A2.5}$$

Acoustic propagation speed is given by the thermodynamic derivative $\left(\frac{\partial p}{\partial \rho}\right)_s$, which can be written in terms of $\bar{\gamma}$ by setting ds in Eq (A2.5) to zero, representing a constant entropy process:

$$\left(\frac{\partial p}{\partial \rho}\right)_s = e\left(\bar{\gamma} - 1 + \left(\frac{\partial\bar{\gamma}}{\partial \ln \rho}\right)_e\right) + \frac{p}{\rho}\left(\bar{\gamma} - 1 + \left(\frac{\partial\bar{\gamma}}{\partial \ln e}\right)_\rho\right). \tag{A2.6}$$

Finally, the state equation may be applied to Eq. (A2.6) to reproduce the result given in Srinivasan et al. (1987):

$$c_e^2 = e\left[(\bar{\gamma} - 1)\left(\bar{\gamma} + \left(\frac{\partial\bar{\gamma}}{\partial \ln e}\right)_\rho\right) + \left(\frac{\partial\bar{\gamma}}{\partial \ln \rho}\right)_e\right]. \tag{A2.7}$$

APPENDIX THREE

This appendix contains the curve fit data used to represent the thermodynamic properties of both equilibrium air and the component species of air. The sources of these data are:

Tables A3.1 and A3.2	Tannehill and Mugge (1974).
Tables A3.3 and A3.4	Srinivasan et al. (1987a).
Tables A3.5 and A3.6	Srinivasan et al. (1987b).
Table A3.7	Prabhu and Erickson (1988).

Notes:

1) In Table A3.1,
$y = \log_{10}(\rho/1.292)$
$z = \log_{10}(e/78\ 408.4)$.

2) In Table A3.2,
$x = \log_{10}(p/1.013\ 4 \times 10^5)$
$y = \log_{10}(\rho/1.225)$
$z = x - y$
$T_0 = 288.16$ K
For small z, $T = p(\rho, e)/\rho R$.

3) In Table A3.3,
$y = \log_{10}(\rho/1.292)$
$z = \log_{10}(e/78\ 410.4)$.

4) In Table A3.4,
$x = \log_{10}(p/1.013\ 25 \times 10^5)$
$y = \log_{10}(\rho/1.292)$
$z = x - y$
$T_0 = 273.15$ K
For small z, $T = p(\rho, e)/\rho R$.

5) In Tables A3.5 and A3.6,
$y = \log_{10}(\rho/1.243)$
$z = \log_{10}(e/78\ 408.4)$
$\mu_0 = 1.748\ 583 \times 10^{-5}$ kg m^{-1} s^{-1}
$k_0 = 1.879\ 15 \times 10^{-2}$ J m^{-1} s^{-1} K^{-1}.

6) In all cases, dimensional variables are in S. I. units (see nomenclature).

	$z \leq 0.65$	$0.65 < z \leq 1.5$	$1.5 < z \leq 2.2$	$2.2 < z \leq 3.05$	$3.05 < z \leq 3.38$	$3.38 < z$
a_1	1.3999996e+00	1.4654303e+00	2.0263596e+00	1.6080399e+00	1.2567196e+00	-8.4032700e+01
a_2	0.0000000e+00	7.6249987e-03	5.8493000e-02	3.4791000e-02	7.0730001e-03	-8.3176100e-01
a_3	0.0000000e+00	-2.5449997e-01	-4.5488602e-01	-1.8890601e-01	-3.9228000e-02	7.2206604e+01
a_4	0.0000000e+00	-1.7244000e-02	-2.7433001e-02	-1.0926999e-02	4.9100001e-04	4.9191397e-01
a_5	0.0000000e+00	2.9199990e-04	0.0000000e+00	0.0000000e+00	0.0000000e+00	1.1529999e-03
a_6	0.0000000e+00	3.5590702e-01	0.0000000e+00	0.0000000e+00	0.0000000e+00	-2.0355896e+01
a_7	0.0000000e+00	1.5422001e-02	0.0000000e+00	0.0000000e+00	0.0000000e+00	-7.0617020e-02
a_8	0.0000000e+00	-1.6323501e-01	0.0000000e+00	0.0000000e+00	0.0000000e+00	1.9097900e+00
a_9	0.0000000e+00	0.0000000e+00	-1.6526502e-01	-1.2411702e-01	7.2179800e-01	0.0000000e+00
a_{10}	0.0000000e+00	0.0000000e+00	-1.4274999e-02	-7.2770007e-03	7.3752999e-02	0.0000000e+00
a_{11}	0.0000000e+00	0.0000000e+00	1.3668501e-01	6.9839001e-02	-1.9894201e-01	0.0000000e+00
a_{12}	0.0000000e+00	0.0000000e+00	1.0070998e-02	3.9849989e-03	-2.1538999e-02	0.0000000e+00
a_{13}	0.0000000e+00	0.0000000e+00	-3.0000000e+01	-3.0000000e+01	-5.0000000e+01	0.0000000e+00
a_{14}	0.0000000e+00	0.0000000e+00	0.0000000e+00	0.0000000e+00	0.0000000e+00	0.0000000e+00
a_{15}	0.0000000e+00	0.0000000e+00	-9.5000006e-03	-6.9999993e-03	-8.4999986e-03	0.0000000e+00
a_{16}	0.0000000e+00	0.0000000e+00	-1.9469995e+00	-2.6910000e+00	-3.3339996e+00	0.0000000e+00
K_1	0.0000000e+00	-9.5400000e-04	8.7360000e-03	1.7884000e-02	2.3790000e-03	6.5720000e-03
K_2	0.0000000e+00	1.7118700e-01	1.8484200e-01	1.5367200e-01	2.1795900e-01	1.8339600e-01
K_3	0.0000000e+00	4.5670000e-03	-3.0244100e-01	-9.3022400e-01	5.9430000e-03	-1.3596000e-01

Table A3.1 Sixteen Coefficient Curve Fits for $p = p(\rho, e)$: $-7.0 \leq y \leq -4.5$

	$z \leq 0.65$	$0.65 < z \leq 1.54$	$1.54 < z \leq 2.22$	$2.22 < z \leq 2.9$	$2.9 < z$
a_1	1.3999996e+00	1.4481297e+00	1.7315798e+00	1.5935001e+00	1.1268797e+00
a_2	0.0000000e+00	1.2920001e-03	3.9019999e-03	7.5323999e-02	-2.5957000e-02
a_3	0.0000000e+00	-7.3509991e-02	-2.7284598e-01	-1.7618603e-01	1.3602000e-02
a_4	0.0000000e+00	-1.9479999e-03	6.2370002e-03	-2.6071999e-02	1.3772000e-02
a_5	0.0000000e+00	0.0000000e+00	0.0000000e+00	0.0000000e+00	0.0000000e+00
a_6	0.0000000e+00	0.0000000e+00	0.0000000e+00	0.0000000e+00	0.0000000e+00
a_7	0.0000000e+00	0.0000000e+00	0.0000000e+00	0.0000000e+00	0.0000000e+00
a_8	0.0000000e+00	0.0000000e+00	0.0000000e+00	0.0000000e+00	0.0000000e+00
a_9	0.0000000e+00	5.4745000e-02	4.1418999e-02	-2.0083803e-01	-1.2773699e-01
a_{10}	0.0000000e+00	-1.3705000e-02	3.7475001e-02	-5.8536001e-02	-8.7942004e-02
a_{11}	0.0000000e+00	-5.5473000e-02	1.6984001e-02	9.9686980e-02	4.3104000e-02
a_{12}	0.0000000e+00	2.1873999e-02	-1.8038001e-02	2.5286999e-02	2.3547001e-02
a_{13}	0.0000000e+00	-1.0000000e+01	-1.0000000e+01	-1.0000000e+01	-2.0000000e+01
a_{14}	0.0000000e+00	0.0000000e+00	3.0000000e+00	5.0000000e+00	4.0000000e+00
a_{15}	0.0000000e+00	0.0000000e+00	-2.4999999e-02	0.0000000e+00	0.0000000e+00
a_{16}	0.0000000e+00	-1.4200001e+00	-2.0249996e+00	-2.6999998e+00	-3.3000002e+00
K_1	0.0000000e+00	-1.9730000e-03	-1.3027000e-02	4.3420000e-03	6.3480000e-03
K_2	0.0000000e+00	1.8523300e-01	7.4270000e-02	2.1219200e-01	2.0971600e-01
K_3	0.0000000e+00	-5.9952000e-02	1.2889000e-02	-1.2930000e-03	-6.001000e-03

Table A3.1 (continued) Sixteen Coefficient Curve Fits for $p = p(\rho, e)$: $-4.5 < y \leq -0.5$

	$z \leq 0.65$	$0.65 < z \leq 1.68$	$1.68 < z \leq 2.46$	$2.46 < z$
a_1	1.3999996e+00	1.4551001e+00	1.5960798e+00	1.5436296e+00
a_2	0.0000000e+00	-1.0200001e-04	-4.2426001e-02	-4.9070999e-02
a_3	0.0000000e+00	-8.1537008e-02	-1.9283998e-01	-1.5356201e-01
a_4	0.0000000e+00	1.6600000e-04	2.9353000e-02	2.9208999e-02
a_5	0.0000000e+00	0.0000000e+00	0.0000000e+00	0.0000000e+00
a_6	0.0000000e+00	0.0000000e+00	0.0000000e+00	0.0000000e+00
a_7	0.0000000e+00	0.0000000e+00	0.0000000e+00	0.0000000e+00
a_8	0.0000000e+00	0.0000000e+00	0.0000000e+00	0.0000000e+00
a_9	0.0000000e+00	1.2864703e-01	-1.9430000e-02	-3.2490700e-01
a_{10}	0.0000000e+00	-4.9454000e-02	5.9540011e-03	-7.7598989e-02
a_{11}	0.0000000e+00	-1.0103601e-01	2.6097000e-02	1.4240801e-01
a_{12}	0.0000000e+00	3.3518001e-02	-6.1639994e-03	2.2071000e-02
a_{13}	0.0000000e+00	-1.5000000e+01	-1.5000000e+01	-1.0000000e+01
a_{14}	0.0000000e+00	0.0000000e+00	0.0000000e+00	0.0000000e+00
a_{15}	0.0000000e+00	0.0000000e+00	0.0000000e+00	0.0000000e+00
a_{16}	0.0000000e+00	-1.4200001e+00	-2.0500002e+00	-2.7080002e+00
K_1	0.0000000e+00	4.5000000e-04	-6.6609000e-03	-8.1000000e-05
K_2	0.0000000e+00	2.0389200e-01	1.2763700e-01	2.2660100e-01
K_3	0.0000000e+00	1.0179700e-01	2.9703700e-01	1.7092200e-01

Table A3.1 (concluded) Sixteen Coefficient Curve Fits for $p = p(\rho, e)$: $-0.5 < y$

	$z \leq 0.3$	$0.3 < z \leq 1.0$	$1.0 < z \leq 1.35$	$1.35 < z \leq 1.79$	$1.79 < z \leq 2.47$	$2.47 < z$
b_1	See Note 2	2.7179998e-01	1.3992500e+00	1.1140099e+00	1.0172195e+00	-4.5087097e+01
b_2		7.4000005e-04	1.6777998e-01	2.2209999e-03	-1.7918002e-02	-9.0050402e+00
b_3		9.9013603e-01	-1.4316797e-01	3.5187501e-01	4.7352302e-01	3.5868500e+01
b_4		-4.9469993e-03	-1.5923399e-01	1.7246000e-02	2.5456000e-02	6.7922201e+00
b_5		0.0000000e+00	0.0000000e+00	0.0000000e+00	0.0000000e+00	-6.7769899e+00
b_6		0.0000000e+00	0.0000000e+00	0.0000000e+00	0.0000000e+00	-6.4705014e-02
b_7		0.0000000e+00	0.0000000e+00	0.0000000e+00	0.0000000e+00	2.5325000e-02
b_8		0.0000000e+00	0.0000000e+00	0.0000000e+00	0.0000000e+00	-1.2736998e+00
b_9		9.9071699e-01	-2.7947001e-02	-1.1509895e+00	-2.1797800e+00	0.0000000e+00
b_{10}		1.7519403e-01	-9.0761006e-02	-1.7355502e-01	-3.3471602e-01	0.0000000e+00
b_{11}		-9.8240697e-01	3.0703598e-01	6.7334199e-01	8.9861900e-01	0.0000000e+00
b_{12}		-1.5923202e-01	1.2162101e-01	8.8398993e-02	1.2738597e-01	0.0000000e+00
b_{13}		0.0000000e+00	0.0000000e+00	0.0000000e+00	0.0000000e+00	0.0000000e+00
b_{14}		0.0000000e+00	0.0000000e+00	0.0000000e+00	0.0000000e+00	0.0000000e+00
b_{15}		-2.0000000e+01	-2.0000000e+01	-2.0000000e+01	-2.0000000e+01	0.0000000e+00
b_{16}		-8.8000000e-01	-1.1700001e+00	-1.5600004e+00	-2.2200003e+00	0.0000000e+00

Table A3.2 Sixteen Coefficient Curve Fits for $T = T(\rho, e)$: $-7.0 \leq y \leq -4.5$

	$z \leq 0.48$	$0.48 < z \leq 0.9165$	$0.9165 < z \leq 1.478$	$1.478 < z \leq 2.176$	$2.176 < z$
b_1	See Note 2	2.8431201e-01	5.0207102e-01	1.0229397e+00	1.4754000e+00
b_2		1.6439999e-03	-1.2990002e-02	2.1535002e-02	1.2962002e-01
b_3		9.8791200e-01	7.7481800e-01	4.2721200e-01	2.5415403e-01
b_4		0.0000000e+00	2.5396999e-02	6.9000013e-03	-4.6411000e-02
b_5		0.0000000e+00	0.0000000e+00	0.0000000e+00	0.0000000e+00
b_6		0.0000000e+00	0.0000000e+00	0.0000000e+00	0.0000000e+00
b_7		0.0000000e+00	0.0000000e+00	0.0000000e+00	0.0000000e+00
b_8		0.0000000e+00	0.0000000e+00	0.0000000e+00	0.0000000e+00
b_9		0.0000000e+00	9.9119991e-03	-4.2782301e-01	-2.2122902e-01
b_{10}		0.0000000e+00	-1.5052700e-01	-2.1199101e-01	-5.7077002e-02
b_{11}		0.0000000e+00	-3.8499990e-04	2.5709599e-01	1.5811598e-01
b_{12}		0.0000000e+00	1.0573399e-01	1.0119200e-01	3.0430000e-02
b_{13}		0.0000000e+00	0.0000000e+00	0.0000000e+00	0.0000000e+00
b_{14}		0.0000000e+00	0.0000000e+00	0.0000000e+00	5.0000000e+00
b_{15}		0.0000000e+00	-1.5000000e+01	-1.2000000e+01	0.0000000e+00
b_{16}		0.0000000e+00	-1.2799997e+00	-1.7779999e+00	-2.3999996e+00

Table A3.2 (continued) Sixteen Coefficient Curve Fits for $T = T(\rho, e)$: $-4.5 < y \leq -0.5$

	$z \leq 0.48$	$0.48 < z \leq 1.07$	$1.07 < z$
b_1	See Note 2	2.7926803e-01	2.3326099e-01
b_2		0.0000000e+00	-5.6382999e-02
b_3		9.9217200e-01	1.1978302e+00
b_4		0.0000000e+00	6.3121021e-02
b_5		0.0000000e+00	-1.6598499e-01
b_6		0.0000000e+00	0.0000000e+00
b_7		0.0000000e+00	0.0000000e+00
b_8		0.0000000e+00	0.0000000e+00
b_9		0.0000000e+00	-8.1453502e-01
b_{10}		0.0000000e+00	9.9232972e-02
b_{11}		0.0000000e+00	6.0238498e-01
b_{12}		0.0000000e+00	-6.7427993e-02
b_{13}		0.0000000e+00	-9.3990982e-02
b_{14}		0.0000000e+00	5.0000000e+00
b_{15}		0.0000000e+00	-2.0000000e+01
b_{16}		0.0000000e+00	-1.7799997e+00

Table A3.2 (concluded) Sixteen Coefficient Curve Fits for $T = T(\rho, e)$: $-0.5 < y$

	$z \leq 0.65$	$0.65 < z \leq 1.5$	$1.5 < z \leq 2.2$	$2.2 < z \leq 3.05$	$3.05 < z \leq 3.4$	$3.4 < z$
a_1	1.3964996e+00	1.5279198e+00	-1.7033295e+01	2.2437401e+00	-2.0807007e+01	-5.2295105e+01
a_2	0.0000000e+00	-1.2695301e-02	-5.0854498e-01	1.0307300e-01	4.0197003e-01	-4.0001100e-01
a_3	0.0000000e+00	-6.1351401e-01	2.4629898e+01	-5.3223801e-01	2.2591003e+01	4.5643906e+01
a_4	0.0000000e+00	-5.0826199e-02	4.4561702e-01	-5.5985201e-02	-2.5660002e-01	2.2448403e-01
a_5	0.0000000e+00	-5.4938383e-03	-8.9529790e-03	3.5648399e-03	-9.5833000e-04	-3.7377500e-03
a_6	0.0000000e+00	6.3183498e-01	-1.1020400e+01	-4.8015598e-02	-7.7173996e+00	-1.2975600e+01
a_7	0.0000000e+00	4.7512003e-05	2.2961800e-03	-1.0135899e-04	2.3966001e-03	2.4316099e-03
a_8	0.0000000e+00	3.3401199e-02	-9.8972678e-02	1.0679401e-02	4.6060000e-02	-2.7951699e-02
a_9	0.0000000e+00	-3.1846808e-04	-2.8918590e-04	1.5912700e-04	3.3670990e-04	2.2475500e-04
a_{10}	0.0000000e+00	-2.1992099e-01	1.6290302e+00	3.6603499e-02	8.7800002e-01	1.2299805e+00
a_{11}	0.0000000e+00	-4.9628601e+01	1.8679703e+01	-5.7037802e+00	-2.1737000e+02	0.0000000e+00
a_{12}	0.0000000e+00	-1.1793200e+01	5.1966202e-01	-3.1005597e-01	-4.6927004e+00	0.0000000e+00
a_{13}	0.0000000e+00	6.9102798e+01	-2.4133804e+01	5.0109396e+00	1.8100999e+02	0.0000000e+00
a_{14}	0.0000000e+00	4.4040497e+01	-4.3483698e-01	1.8041098e-01	2.6620998e+00	0.0000000e+00
a_{15}	0.0000000e+00	5.0924902e+00	9.1608912e-03	-9.4936118e-03	-3.4759000e-02	0.0000000e+00
a_{16}	0.0000000e+00	1.3730800e+01	1.0203500e+01	-1.4033098e+00	-5.0018997e+01	0.0000000e+00
a_{17}	0.0000000e+00	-1.4032602e+00	-1.5208200e-03	1.9483899e-03	6.4680986e-03	0.0000000e+00
a_{18}	0.0000000e+00	-1.7872604e+01	9.7076178e-02	-2.7971800e-02	-3.8380998e-01	0.0000000e+00
a_{19}	0.0000000e+00	2.0898801e-01	3.4648203e-04	-2.2490800e-04	-7.0390990e-04	0.0000000e+00
a_{20}	0.0000000e+00	-1.8694305e+01	-1.3945999e+00	1.2027800e-01	4.5795002e+00	0.0000000e+00
a_{21}	0.0000000e+00	2.4604523e+01	-1.4276199e+02	1.1397549e+02	4.5443726e+02	0.0000000e+00
a_{22}	0.0000000e+00	-2.0000000e+00	-1.6470881e+00	-4.9854670e+00	1.2501330e+01	0.0000000e+00
a_{23}	0.0000000e+00	-2.0930222e+01	7.6603119e+01	-4.2238327e+01	-1.3760010e+02	0.0000000e+00
a_{24}	0.0000000e+00	0.0000000e+00	8.2593459e-01	2.0097055e+00	-3.6417742e+00	0.0000000e+00
sign	+	-	+	+	+	+

Table A3.3 Twenty Four Coefficient Curve Fits for $p = p(\rho, e)$: $-7.0 \leq y \leq -4.5$

	$z \leq 0.65$	$0.65 < z \leq 1.5$	$1.5 < z \leq 2.22$	$2.22 < z \leq 2.95$	$2.95 < z$
a_1	1.3979998e+00	1.3912296e+00	-1.2078400e+00	-2.2645998e+00	-1.6690399e+01
a_2	0.0000000e+00	-4.0832087e-03	-2.5790900e-01	-7.8226328e-02	-2.5831801e-01
a_3	0.0000000e+00	1.4254499e-02	5.0230703e+00	4.9049702e+00	1.7835007e+01
a_4	0.0000000e+00	1.4176901e-02	2.8720099e-01	7.1809590e-02	1.5489799e-01
a_5	0.0000000e+00	2.5722501e-04	-9.9557713e-03	-3.0644301e-03	-9.7126290e-03
a_6	0.0000000e+00	6.2555015e-02	-3.2061901e+00	-2.2475004e+00	-5.9410801e+00
a_7	0.0000000e+00	6.5291207e-04	5.2352399e-03	1.7420901e-03	3.9773993e-03
a_8	0.0000000e+00	-7.8363717e-03	-7.5040519e-02	-1.3164099e-02	-2.0133499e-02
a_9	0.0000000e+00	8.4691201e-05	-1.4557400e-04	2.8421404e-05	9.0429996e-05
a_{10}	0.0000000e+00	-9.7872019e-02	6.5156400e-01	3.3365798e-01	6.6043198e-01
a_{11}	0.0000000e+00	5.8095503e+00	-6.6284103e+00	-1.4790400e+01	8.5468994e+01
a_{12}	0.0000000e+00	-1.8230200e-01	2.7711201e-02	-1.7662698e-01	1.1755400e+01
a_{13}	0.0000000e+00	-9.6239595e+00	7.3076200e+00	1.3503600e+01	-7.2175995e+01
a_{14}	0.0000000e+00	1.7961901e-01	-7.6822996e-02	8.7728024e-02	-7.1572304e+00
a_{15}	0.0000000e+00	-2.3051798e-02	7.1942098e-03	-2.1332700e-03	-4.1615002e-02
a_{16}	0.0000000e+00	5.2704697e+00	-2.3316097e+00	-3.9537201e+00	2.0175797e+01
a_{17}	0.0000000e+00	1.1872001e-02	-3.6246299e-03	7.1548694e-04	1.3814699e-02
a_{18}	0.0000000e+00	-3.6550701e-02	3.0476701e-02	-8.9615099e-03	1.0899000e+00
a_{19}	0.0000000e+00	-3.3549895e-04	1.6277700e-04	7.3092800e-05	5.4518390e-04
a_{20}	0.0000000e+00	-9.1989702e-01	1.6685599e-01	3.6322898e-01	-1.8643799e+00
a_{21}	0.0000000e+00	1.4200000e+01	1.2553239e+02	1.7885420e+02	2.8832617e+02
a_{22}	0.0000000e+00	0.0000000e+00	2.0153351e+00	6.3178940e+00	1.2485360e+01
a_{23}	0.0000000e+00	-1.0000000e+01	-6.3907471e+01	-6.7567413e+01	-8.8169846e+01
a_{24}	0.0000000e+00	0.0000000e+00	-6.5152252e-01	-2.4600601e+00	-3.7203093e+00
sign	+	+	+	+	+

Table A3.3 (continued) Twenty Four Coefficient Curve Fits for $p = p(\rho, e)$: $-4.5 < y \leq -0.5$

	$z \leq 0.65$	$0.65 < z \leq 1.7$	$1.7 < z \leq 2.35$	$2.35 < z$
a_1	1.3987999e+00	1.3706198e+00	3.4384601e-02	-1.7063303e+00
a_2	0.0000000e+00	1.2967300e-02	-2.3358399e-01	-1.4840299e-01
a_3	0.0000000e+00	1.1141801e-01	2.8557396e+00	4.2310400e+00
a_4	0.0000000e+00	-3.2691199e-02	2.5978702e-01	1.3729000e-01
a_5	0.0000000e+00	1.0686901e-03	-1.0899272e-02	-9.1093406e-03
a_6	0.0000000e+00	-1.0613298e-01	-1.9478502e+00	-1.9729204e+00
a_7	0.0000000e+00	-2.0028600e-03	4.2365901e-03	3.8570701e-03
a_8	0.0000000e+00	1.9025099e-02	-6.7386508e-02	-2.8182998e-02
a_9	0.0000000e+00	2.3830500e-04	3.8571190e-04	2.6902603e-04
a_{10}	0.0000000e+00	3.0221001e-03	4.0851802e-01	2.9588199e-01
a_{11}	0.0000000e+00	0.0000000e+00	-4.2056904e+00	3.4158005e+01
a_{12}	0.0000000e+00	0.0000000e+00	1.3313901e-01	-1.8997192e+01
a_{13}	0.0000000e+00	0.0000000e+00	4.5123596e+00	-4.0858002e+01
a_{14}	0.0000000e+00	0.0000000e+00	-1.6634101e-01	1.3032100e+01
a_{15}	0.0000000e+00	0.0000000e+00	1.6778701e-03	-8.0127198e-01
a_{16}	0.0000000e+00	0.0000000e+00	-1.3551598e+00	1.6082596e+01
a_{17}	0.0000000e+00	0.0000000e+00	-1.1002200e-03	2.7512097e-01
a_{18}	0.0000000e+00	0.0000000e+00	4.9171600e-02	-2.2338600e+00
a_{19}	0.0000000e+00	0.0000000e+00	3.0667591e-04	-1.7796901e-04
a_{20}	0.0000000e+00	0.0000000e+00	7.5250924e-02	-2.0885296e+00
a_{21}	0.0000000e+00	0.0000000e+00	1.7570419e+02	2.5613232e+02
a_{22}	0.0000000e+00	0.0000000e+00	-2.1632776e+00	1.7370889e+02
a_{23}	0.0000000e+00	0.0000000e+00	-8.8337021e+01	-9.0588898e+01
a_{24}	0.0000000e+00	0.0000000e+00	1.8975430e+00	-5.8388031e+01
sign	+	+	+	+

Table A3.3 (concluded) Twenty Four Coefficient Curve Fits for $p = p(\rho, e)$: $-0.5 < y \leq 3.0$

	$z \leq 0.25$	$0.25 < z \leq 0.95$	$0.95 < z \leq 1.4$	$1.4 < z \leq 1.95$	$1.95 < z$
b_1	See Note 4	1.4482403e-01	-9.3249998e+00	-1.9308197e+01	-2.5972107e+01
b_2		1.3674401e-02	-9.3201703e-01	-1.5455704e+00	-1.7741899e+00
b_3		1.1709899e-01	2.5717606e+01	3.6903503e+01	3.6249496e+01
b_4		-8.2229912e-02	1.6129198e+00	1.9221401e+00	1.5538301e+00
b_5		-6.7530293e-04	-3.0024201e-02	-3.5902701e-02	-4.5135900e-02
b_6		1.3936996e+00	-2.1662003e+01	-2.2044006e+01	-1.5998800e+01
b_7		-1.4731400e-03	2.6295900e-02	2.3182701e-02	2.4364799e-02
b_8		6.8306625e-02	-6.8143100e-01	-5.8093500e-01	-3.1780702e-01
b_9		-7.9085105e-05	-2.7765101e-04	-2.0132700e-04	1.2804000e-04
b_{10}		-6.6567302e-01	6.2696199e+00	4.4336700e+00	2.4058399e+00
b_{11}		0.0000000e+00	-3.3853397e+00	-3.8306904e+00	-1.8143295e+01
b_{12}		0.0000000e+00	1.8259400e-01	1.3286400e-01	1.5489602e-01
b_{13}		0.0000000e+00	1.8492800e-01	-3.9190197e+00	1.2658200e+01
b_{14}		0.0000000e+00	-7.0110899e-01	-6.7956400e-01	-3.6625201e-01
b_{15}		0.0000000e+00	1.1015002e-02	6.0634105e-04	3.2449599e-02
b_{16}		0.0000000e+00	5.4701996e+00	7.2463198e+00	-1.4175901e+00
b_{17}		0.0000000e+00	-1.6057000e-02	-8.1299692e-03	-1.6638499e-02
b_{18}		0.0000000e+00	4.1162401e-01	3.1546098e-01	1.1124098e-01
b_{19}		0.0000000e+00	1.5770100e-05	-1.6101199e-04	3.0217692e-04
b_{20}		0.0000000e+00	-2.8149796e+00	-2.1787901e+00	-3.1098300e-01
b_{21}		0.0000000e+00	-3.8870148e+01	2.0800003e+01	1.1158839e+02
b_{22}		0.0000000e+00	-2.9082275e+01	-2.5600006e+01	-6.4526062e+00
b_{23}		0.0000000e+00	4.0705566e+01	1.0000000e+00	-5.3378632e+01
b_{24}		0.0000000e+00	2.6823471e+01	1.8000000e+01	2.0269861e+00

Table A3.4 Twenty Four Coefficient Curve Fits for $T = T(\rho, e)$: $-7.0 \leq y \leq -4.5$

	$z \leq 0.25$	$0.25 < z \leq 0.95$	$0.95 < z \leq 1.4$	$1.4 < z \leq 2.0$	$2.0 < z$
b_1	See Note 4	2.9499602e-02	-5.5332403e+00	-1.2377900e+01	-1.7607895e+01
b_2		7.2499700e-03	-3.5374898e-01	-1.1472797e+00	-1.2657900e+00
b_3		7.8178298e-01	1.6363800e+01	2.4138199e+01	2.4854401e+01
b_4		-3.2740202e-02	5.8754700e-01	1.3895702e+00	1.0944204e+00
b_5		3.2335706e-04	-1.1608101e-02	-3.6369301e-02	-3.6553401e-02
b_6		3.9519799e-01	-1.4123900e+01	-1.4284400e+01	-1.0816600e+01
b_7		-9.6998899e-04	7.9957098e-03	2.2426501e-02	1.5434600e-02
b_8		2.9292598e-02	-2.3514599e-01	-4.0655297e-01	-2.2780299e-01
b_9		-8.9324003e-06	-2.7931598e-04	-3.2388791e-04	-4.5982189e-04
b_{10}		-2.1218199e-01	4.2889099e+00	2.8761997e+00	1.6064100e+00
b_{11}		0.0000000e+00	9.0797901e+00	4.4078197e+00	2.6066895e+01
b_{12}		0.0000000e+00	1.0130796e+00	1.3304596e+00	2.3179102e+00
b_{13}		0.0000000e+00	-2.2942795e+01	-1.1540500e+01	-3.2243301e+01
b_{14}		0.0000000e+00	-1.5212202e+00	-1.5989199e+00	-1.8264503e+00
b_{15}		0.0000000e+00	3.7838999e-02	5.3057998e-02	4.9462099e-02
b_{16}		0.0000000e+00	1.9565704e+01	8.5730896e+00	1.3382900e+01
b_{17}		0.0000000e+00	-2.6311502e-02	-3.1037599e-02	-1.8554199e-02
b_{18}		0.0000000e+00	5.7383901e-01	4.7127402e-01	3.5974401e-01
b_{19}		0.0000000e+00	5.4640207e-04	4.7764997e-04	5.0481502e-04
b_{20}		0.0000000e+00	-5.6305704e+00	-1.9623299e+00	-1.8651695e+00
b_{21}		0.0000000e+00	7.6198029e+01	1.4075000e+02	3.0937549e+02
b_{22}		0.0000000e+00	-1.5011550e+01	-6.4999924e+00	1.8750183e+01
b_{23}		0.0000000e+00	-6.7708450e+01	-7.7500000e+01	-1.3750040e+02
b_{24}		0.0000000e+00	1.2731470e+01	5.0000000e+00	-8.3334179e+00

Table A3.4 (continued) Twenty Four Coefficient Curve Fits for $T = T(\rho, e)$: $-4.5 < y \leq -0.5$

	$z \leq 0.25$	$0.25 < z \leq 0.95$	$0.95 < z \leq 1.45$	$1.45 < z$
b_1	See Note 4	-2.9408101e-03	1.3239603e+00	-1.6064301e+00
b_2		5.7391496e-04	8.5277081e-02	-5.0736800e-02
b_3		9.8888302e-01	-3.2425699e+00	3.9587202e+00
b_4		-3.7121400e-03	-2.0093697e-01	3.6938298e-02
b_5		1.1238700e-04	5.6814589e-03	-1.5937800e-03
b_6		2.8665598e-02	4.5382299e+00	-1.7120104e+00
b_7		-3.7652790e-04	-6.8585612e-03	1.0605699e-03
b_8		4.5605898e-03	1.1812299e-01	9.2512406e-03
b_9		1.7619197e-05	1.9836600e-04	6.5327797e-05
b_{10}		-1.9949801e-02	-1.6246004e+00	2.7103901e-01
b_{11}		0.0000000e+00	-5.2667302e-01	1.8047607e+01
b_{12}		0.0000000e+00	-1.5869099e-01	1.6296396e+00
b_{13}		0.0000000e+00	2.6160002e+00	-2.7312393e+01
b_{14}		0.0000000e+00	3.1635600e-01	-1.5742998e+00
b_{15}		0.0000000e+00	-1.9075502e-02	5.8527701e-02
b_{16}		0.0000000e+00	-3.3793001e+00	1.3634200e+01
b_{17}		0.0000000e+00	1.7012399e-02	-2.7731299e-02
b_{18}		0.0000000e+00	-1.5221202e-01	3.7071401e-01
b_{19}		0.0000000e+00	-5.5839797e-04	1.1614601e-03
b_{20}		0.0000000e+00	1.3075705e+00	-2.2378702e+00
b_{21}		0.0000000e+00	1.4422060e+02	1.2925150e+02
b_{22}		0.0000000e+00	-2.5447266e+01	1.3605518e+00
b_{23}		0.0000000e+00	-1.2770551e+02	-7.0748199e+01
b_{24}		0.0000000e+00	2.2366470e+01	1.3605318e+00

Table A3.4 (concluded) Twenty Four Coefficient Curve Fits for $T = T(\rho, e)$: $-0.5 < y \leq 3.0$

	$z \leq 0.67$	$0.67 < z \leq 1.75$	$1.75 < z \leq 2.5$	$2.5 < z \leq 2.85$	$2.85 < z \leq 3.15$	$3.15 < z \leq 3.19$	$3.19 < z$
c_1	4.8454702e-01	-3.7166595e+01	-1.6514700e+02	-7.0927383e+03	-1.2774800e+03	4.5591914e+03	-4.4179199e+02
c_2	4.6713501e-01	6.6788300e+01	2.1102800e+02	7.1364805e+03	1.2940000e+03	-4.2105703e+03	9.7985983e-02
c_3	5.7120505e-04	-2.4399796e+00	-4.7094803e+00	-2.4601401e+02	-3.6072403e+01	1.0300100e+01	-3.0314795e+02
c_4	-1.4362901e-03	2.1230898e+00	2.7825804e+00	1.6582600e+02	2.6319397e+01	-2.6347794e+01	7.6064989e-03
c_5	2.5510998e+00	-3.6925903e+01	-8.7830795e+01	-2.3795200e+03	-4.2295801e+02	1.2906899e+03	-5.5711003e-05
c_6	2.5341590e-04	-1.4644599e-01	-3.1986701e-01	-3.4974403e+00	-4.7442502e-01	-8.2813702e+00	-7.5610001e+01
c_7	-2.3347200e-04	-3.0842602e-01	-1.2867099e-01	-2.7548706e+01	-4.3822803e+00	6.5958700e+00	-3.5283601e-06
c_8	-4.7237496e-04	7.5442314e-02	1.7317897e-01	1.2864103e+00	2.8968400e-01	1.9827003e+00	-4.7681597e-04
c_9	-1.4410200e+00	7.3648596e+00	1.2763900e+01	2.6346509e+02	4.5057098e+01	-1.3141299e+02	8.8614804e-09
c_{10}	1.8689898e-05	-2.9146399e-03	3.8610599e-03	-3.1371100e-03	1.6404800e-02	-1.7286998e-01	-6.4885902e+00
c_{11}	0.0000000e+00	3.6175705e+01	2.3040700e+02	5.2615781e+03	0.0000000e+00	0.0000000e+00	6.7238687e+04
c_{12}	0.0000000e+00	-6.1110199e+01	-2.9805493e+02	-4.9670117e+03	0.0000000e+00	0.0000000e+00	3.2839804e+00
c_{13}	0.0000000e+00	2.4053097e+00	-6.1830702e+00	2.0313800e+02	0.0000000e+00	0.0000000e+00	3.5500898e+04
c_{14}	0.0000000e+00	-2.0591402e+00	8.4459496e+00	-1.3298399e+02	0.0000000e+00	0.0000000e+00	2.7261600e+00
c_{15}	0.0000000e+00	3.2391098e+01	1.2693300e+02	1.5242400e+03	0.0000000e+00	0.0000000e+00	2.1371399e-03
c_{16}	0.0000000e+00	1.3791603e-01	-2.3022901e-02	3.3243198e+00	0.0000000e+00	0.0000000e+00	6.5088594e+03
c_{17}	0.0000000e+00	2.7914900e-01	-2.6167097e+00	2.1508102e+01	0.0000000e+00	0.0000000e+00	3.4237700e-04
c_{18}	0.0000000e+00	-6.7204118e-02	2.2545800e-02	-1.1599703e+00	0.0000000e+00	0.0000000e+00	3.8055998e-01
c_{19}	0.0000000e+00	-5.0763998e+00	-1.7725693e+01	-1.5045000e+02	0.0000000e+00	0.0000000e+00	-6.8489726e-08
c_{20}	0.0000000e+00	2.6198700e-03	-4.4107214e-03	1.1486199e-02	0.0000000e+00	0.0000000e+00	4.1411597e+02
c_{21}	0.0000000e+00	-3.4330002e+01	-6.8820007e+01	-3.5939990e+02	0.0000000e+00	0.0000000e+00	2.9779999e+01
c_{22}	0.0000000e+00	-1.8230000e+00	8.8240004e+00	-3.7630005e+01	0.0000000e+00	0.0000000e+00	5.4150000e+00
c_{23}	0.0000000e+00	2.4990005e+01	3.2029999e+01	1.3189999e+02	0.0000000e+00	0.0000000e+00	1.7130000e-03
c_{24}	0.0000000e+00	6.5030003e-01	-5.3590002e+00	1.3480000e+01	0.0000000e+00	0.0000000e+00	3.1149993e-04

Table A3.5 Curve Fit Coefficients for $\mu = \mu(\rho, e)$: $y \leq -3.8$

	$z \leq 0.67$	$0.67 < z \leq 1.75$	$1.75 < z \leq 2.5$	$2.5 < z \leq 2.85$	$2.85 < z \leq 3.15$	$3.15 < z$
c_1	4.8454702e-01	-3.7166595e+01	-1.6514700e+02	-7.0927383e+03	-1.2774800e+03	-6.4028984e+03
c_2	4.6713501e-01	6.6788300e+01	2.1102800e+02	7.1364805e+03	1.2940000e+03	6.2425391e+03
c_3	5.7120505e-04	-2.4399796e+00	-4.7094803e+00	-2.4601401e+02	-3.6072403e+01	1.0327901e+02
c_4	-1.4362901e-03	2.1230898e+00	2.7825804e+00	1.6582600e+02	2.6319397e+01	-8.7318100e+01
c_5	2.5510998e+00	-3.6925903e+01	-8.7830795e+01	-2.3795200e+03	-4.2295801e+02	-2.0286499e+03
c_6	2.5341590e-04	-1.4644599e-01	-3.1986701e-01	-3.4974403e+00	-4.7442502e-01	-1.2239700e+01
c_7	-2.3347200e-04	-3.0842602e-01	-1.2867099e-01	-2.7548706e+01	-4.3822803e+00	1.7187805e+01
c_8	-4.7237496e-04	7.5442314e-02	1.7317897e-01	1.2864103e+00	2.8968400e-01	3.5783005e+00
c_9	-1.4410200e+00	7.3648596e+00	1.2763900e+01	2.6346509e+02	4.5057098e+01	2.1990700e+02
c_{10}	1.8689898e-05	-2.9146399e-03	3.8610599e-03	-3.1371100e-03	1.6404800e-02	-1.2795299e-01
c_{11}	0.0000000e+00	3.6175705e+01	2.3040700e+02	5.2615781e+03	0.0000000e+00	0.0000000e+00
c_{12}	0.0000000e+00	-6.1110199e+01	-2.9805493e+02	-4.9670117e+03	0.0000000e+00	0.0000000e+00
c_{13}	0.0000000e+00	2.4053097e+00	-6.1830702e+00	2.0313800e+02	0.0000000e+00	0.0000000e+00
c_{14}	0.0000000e+00	-2.0591402e+00	8.4459496e+00	-1.3298399e+02	0.0000000e+00	0.0000000e+00
c_{15}	0.0000000e+00	3.2391098e+01	1.2693300e+02	1.5242400e+03	0.0000000e+00	0.0000000e+00
c_{16}	0.0000000e+00	1.3791603e-01	-2.3022901e-02	3.3243198e+00	0.0000000e+00	0.0000000e+00
c_{17}	0.0000000e+00	2.7914900e-01	-2.6167097e+00	2.1508102e+01	0.0000000e+00	0.0000000e+00
c_{18}	0.0000000e+00	-6.7204118e-02	2.2545800e-02	-1.1599703e+00	0.0000000e+00	0.0000000e+00
c_{19}	0.0000000e+00	-5.0763998e+00	-1.7725693e+01	-1.5045000e+02	0.0000000e+00	0.0000000e+00
c_{20}	0.0000000e+00	2.6198700e-03	-4.4107214e-03	1.1486199e-02	0.0000000e+00	0.0000000e+00
c_{21}	0.0000000e+00	-3.4330002e+01	-6.8820007e+01	-3.5939990e+02	0.0000000e+00	0.0000000e+00
c_{22}	0.0000000e+00	-1.8230000e+00	8.8240004e+00	-3.7630005e+01	0.0000000e+00	0.0000000e+00
c_{23}	0.0000000e+00	2.4990005e+01	3.2029999e+01	1.3189999e+02	0.0000000e+00	0.0000000e+00
c_{24}	0.0000000e+00	6.5030003e-01	-5.3590002e+00	1.3480000e+01	0.0000000e+00	0.0000000e+00

Table A3.5 (concluded) Curve Fit Coefficients for $\mu = \mu(\rho, e)$: $-3.8 < y$

	$z \leq 0.65$	$0.65 < z \leq 1.25$	$1.25 < z \leq 1.775$	$1.775 < z \leq 1.93$	$1.93 < z \leq 2.60$	$2.60 < z \leq 2.69$	$2.69 < z$
d_1	1.8100369e-01	-1.0593500e+04	3.7937500e+03	2.0665187e+05	7.1572625e+04	1.1456830e+06	-8.5499625e+04
d_2	4.8126802e+00	2.3147000e+04	-7.4035117e+03	-3.1656450e+05	-9.2471625e+04	-1.2375250e+06	1.1739656e+05
d_3	-2.7231116e-02	-7.4129395e+02	3.2969800e+02	-3.0732202e+02	1.9646323e+03	1.4024508e+04	6.4563168e+04
d_4	1.2691337e-01	1.2172400e+03	-3.5591602e+02	4.5703638e+02	-2.0280527e+03	-9.3467227e+03	-3.9551203e+04
d_5	-8.9913034e+00	-1.6760102e+04	4.7712187e+03	1.6182494e+05	3.9446105e+04	4.4593056e+05	-4.8170254e+04
d_6	-4.7198236e-03	1.3510500e+01	1.9706100e+01	1.9226027e+00	-9.2131958e+01	2.8485107e+02	2.3473167e-01
d_7	-1.2624085e-01	-4.4318408e+02	1.0024100e+02	-1.5550845e+02	4.5673853e+02	1.5330740e+03	6.0816055e+03
d_8	9.2328079e-03	4.9491396e+00	-8.4255400e+00	-2.2478809e+00	1.2724541e+01	-1.0968916e+02	1.8871567e+01
d_9	8.9649105e+00	4.0663101e+03	-1.0074900e+03	-2.7603957e+04	-5.5728672e+03	-5.3608352e+04	6.2052031e+03
d_{10}	-2.9488327e-04	1.5538597e+00	4.8040003e-01	-3.0622602e-01	-5.0568476e+00	-1.0955791e+00	4.0757723e+00
d_{11}	0.0000000e+00	1.0603199e+04	-4.5360312e+03	-2.0656431e+05	-3.2910781e+04	-1.7520870e+06	5.8546887e+04
d_{12}	0.0000000e+00	-2.3156000e+04	9.0560508e+03	3.1819131e+05	4.2551211e+04	1.7967500e+06	-9.4634875e+04
d_{13}	0.0000000e+00	7.4695093e+02	-4.9587012e+02	2.1754229e+03	1.4566331e+03	-1.3278737e+05	-6.6513812e+04
d_{14}	0.0000000e+00	-1.2246499e+03	6.3356299e+02	-2.4667078e+03	-2.2653745e+03	9.8215562e+04	4.0899945e+04
d_{15}	0.0000000e+00	1.6760398e+04	-5.9531719e+03	-1.6359706e+05	-1.9476277e+04	-6.0791744e+05	4.2127227e+04
d_{16}	0.0000000e+00	-1.2861500e+01	-2.0008698e+01	3.3952682e+01	-1.3324594e+02	-1.3384084e+03	-1.0260344e+00
d_{17}	0.0000000e+00	4.4591895e+02	-2.0544200e+02	7.1675317e+02	8.4370288e+02	-1.8119430e+04	-6.3717305e+03
d_{18}	0.0000000e+00	-5.3239803e+00	1.1885100e+01	-7.5384665e+00	1.0591533e+02	5.2707324e+02	-5.3432770e+01
d_{19}	0.0000000e+00	-4.0625801e+03	1.2894500e+03	2.8092637e+04	3.2389702e+03	6.7709875e+04	-5.7495195e+03
d_{20}	0.0000000e+00	-1.5295601e+00	-1.7173499e-01	1.9121437e+00	5.8639469e+00	2.5904894e+00	-1.1017392e+01
d_{21}	0.0000000e+00	-4.2190002e+01	-3.3179993e+01	-3.9239990e+02	4.9169998e+01	-1.7980000e+02	5.4110003e+00
d_{22}	0.0000000e+00	-4.6870003e+00	3.1580001e-01	-5.2059998e+01	2.4149994e+01	7.3710003e+00	1.1620000e+01
d_{23}	0.0000000e+00	2.8119995e+01	1.8630005e+01	2.0539999e+02	-2.4550003e+01	6.7309998e+01	-1.0819998e+00
d_{24}	0.0000000e+00	3.1250000e+00	-1.0349998e+00	2.6789993e+01	-1.1810000e+01	-3.2049999e+00	-3.3909998e+00

Table A3.6 Curve Fit Coefficients for $k = k(\rho, e)$: $y \leq -3.0$

	$z \leq 0.65$	$0.65 < z \leq 1.29$	$1.29 < z \leq 1.85$	$1.85 < z \leq 2.0$	$2.0 < z \leq 2.58$	$2.58 < z \leq 2.73$	$2.73 < z$
d_1	1.8100369e-01	-1.2249301e+04	3.1806001e+03	5.1402398e+04	5.1131824e+04	1.0088046e+06	-9.6638500e+04
d_2	4.8126802e+00	2.4107102e+04	-6.6966406e+03	-7.5273312e+04	-6.6648750e+04	-1.0863210e+06	1.3206488e+04
d_3	-2.7231116e-02	-1.6182900e+03	4.3338196e+01	-3.3088892e+02	2.0217100e+03	1.3844801e+04	-4.7458105e+04
d_4	1.2691337e-01	2.2253501e+03	-2.1464900e+02	3.1155005e+02	-1.9306292e+03	-9.7268516e+03	2.3596875e+04
d_5	-8.9913034e+00	-1.5926102e+04	4.4137695e+03	3.6653898e+04	2.8762395e+04	3.8985325e+05	1.8602773e+04
d_6	-4.7198236e-03	1.9802599e+00	-3.6218994e+01	-4.8416397e+01	-8.4970047e+01	1.4840726e+02	-5.3564258e+03
d_7	-1.2624085e-01	-7.5321289e+02	9.4135895e+01	-7.4122696e+01	4.3353467e+02	1.7091665e+03	-2.3068020e+03
d_8	9.2328079e-03	5.1848297e+00	1.1553800e+01	2.2313293e+01	1.7925919e+01	-5.2645004e+01	2.2433904e+03
d_9	8.9649105e+00	3.5337600e+03	-9.2975806e+02	-5.9301484e+03	-4.1064609e+03	-4.6621066e+04	-4.0413552e+03
d_{10}	-2.9488327e-04	1.4785099e+00	-2.1462097e+00	-9.1911799e-01	-6.2576542e+00	-1.5477133e-01	2.5188145e+02
d_{11}	0.0000000e+00	1.2248602e+04	-5.9876406e+03	-1.8089800e+05	-6.2768156e+04	-1.0733510e+06	1.0962581e+05
d_{12}	0.0000000e+00	-2.4102301e+04	1.2924301e+04	2.8253200e+05	8.6015875e+04	1.1457100e+06	-2.9901160e+04
d_{13}	0.0000000e+00	1.6181001e+03	-2.7226099e+02	-1.0105300e+03	-1.0002036e+03	-1.9343957e+04	4.7883496e+04
d_{14}	0.0000000e+00	-2.2257100e+03	5.4237793e+02	9.7557593e+02	6.2537280e+02	1.3366211e+04	-2.3785383e+04
d_{15}	0.0000000e+00	1.5923500e+04	-9.0329297e+03	-1.4722000e+05	-3.9578270e+04	-4.0670987e+05	-1.1753969e+04
d_{16}	0.0000000e+00	-2.1548204e+00	2.7417892e+01	3.2868099e+00	-1.0591702e+02	-4.1016724e+02	5.4734180e+03
d_{17}	0.0000000e+00	7.5374609e+02	-2.1178700e+02	-2.3363100e+02	-3.8467377e+01	-2.2955198e+03	2.2905522e+03
d_{18}	0.0000000e+00	-5.0511503e+00	-5.6857796e+00	-1.7658796e+00	7.6361420e+01	1.4994148e+02	-2.3208018e+03
d_{19}	0.0000000e+00	-3.5316799e+03	2.0783101e+03	2.5594000e+04	6.1295312e+03	4.7999871e+04	3.1304399e+03
d_{20}	0.0000000e+00	-1.4879503e+00	1.9121704e+00	-1.5496200e-01	5.9388590e+00	-1.9779787e+00	-2.6570068e+02
d_{21}	0.0000000e+00	-3.1110001e+01	-1.8539993e+01	-4.1039993e+01	-3.9010000e+00	-1.0260001e+02	-3.1070007e+01
d_{22}	0.0000000e+00	-4.4440002e+00	7.1099997e+00	6.5070007e+01	2.4179993e+01	6.3020004e+01	1.0820000e+01
d_{23}	0.0000000e+00	1.9440002e+01	1.0680000e+01	2.0830002e+01	1.3739996e+00	3.8190002e+01	1.0470000e+01
d_{24}	0.0000000e+00	2.7779999e+00	-5.4490004e+00	-3.4720001e+01	-1.1450000e+01	-2.4309998e+01	-3.0469999e+00

Table A3.6 (continued) Curve Fit Coefficients for $k = k(\rho, e)$: $-3.0 < y \leq -1.0$

	$z \leq 0.65$	$0.65 < z \leq 1.40$	$1.40 < z \leq 1.91$	$1.91 < z \leq 2.05$	$2.05 < z \leq 2.57$	$2.57 < z \leq 2.75$	$2.75 < z$
d_1	1.8100369e-01	-1.5838601e+03	7.8925488e+02	3.5869102e+04	3.1899562e+04	7.0838087e+05	3.1855037e+05
d_2	4.8126802e+00	3.4922300e+03	-1.9174299e+03	-5.1685199e+04	-4.2186664e+04	-7.5619919e+05	-3.3041156e+05
d_3	-2.7231116e-02	-8.3983398e+02	3.5922705e+02	-6.3018896e+02	2.3055603e+03	3.9503091e+03	2.2983352e+04
d_4	1.2691337e-01	1.0956499e+03	-4.4407007e+02	6.6331396e+02	-1.9897017e+03	-2.7381802e+03	-1.6623461e+04
d_5	-8.9913034e+00	-2.5617500e+03	1.3946299e+03	2.4747102e+04	1.8499980e+04	2.6888181e+05	1.1384800e+05
d_6	-4.7198236e-03	-1.2240700e+01	1.9068100e+01	-4.2387100e+01	-1.6195114e+01	-1.2532251e+02	-1.8599039e+02
d_7	-1.2624085e-01	-3.5619702e+02	1.3408299e+02	-1.7353799e+02	4.2561816e+02	4.7728687e+02	3.0098223e+03
d_8	9.2328079e-03	7.6563396e+00	-1.0928500e+01	2.0804794e+01	5.8640623e+00	4.7734787e+01	6.9840683e+01
d_9	8.9649105e+00	6.2514502e+02	-3.1344604e+02	-3.9316699e+03	-2.6808696e+03	-3.1838160e+04	-1.3020133e+04
d_{10}	-2.9488327e-04	2.5823498e-01	4.2493299e-02	-1.0551205e+00	-3.6172504e+00	-4.0148029e+00	-7.7371645e+00
d_{11}	0.0000000e+00	1.5802500e+03	-1.3140100e+03	-1.1052200e+05	-5.7594039e+04	-2.5216325e+05	0.0000000e+00
d_{12}	0.0000000e+00	-3.4766399e+03	3.1313401e+03	1.6759100e+05	7.9328437e+04	2.1727769e+05	0.0000000e+00
d_{13}	0.0000000e+00	8.3958789e+02	-5.1875488e+02	4.6187695e+03	-1.9275989e+03	9.2882383e+03	0.0000000e+00
d_{14}	0.0000000e+00	-1.0948999e+03	6.8026807e+02	-4.9493008e+03	1.6730544e+03	-7.7809180e+03	0.0000000e+00
d_{15}	0.0000000e+00	2.5468201e+03	-2.3249299e+03	-8.4655812e+04	-3.6473008e+04	-5.6539297e+04	0.0000000e+00
d_{16}	0.0000000e+00	1.2084300e+01	-3.3200104e+01	2.2506500e+01	-7.9208084e+01	1.8537296e+02	0.0000000e+00
d_{17}	0.0000000e+00	3.5567407e+02	-2.2139301e+02	1.3244099e+03	-3.6100732e+02	1.6120212e+03	0.0000000e+00
d_{18}	0.0000000e+00	-7.4485703e+00	2.1181900e+01	-1.1031600e+01	4.0542084e+01	-7.1010757e+01	0.0000000e+00
d_{19}	0.0000000e+00	-6.1850391e+02	5.5256299e+02	1.4243801e+04	5.5975430e+03	3.9419248e+03	0.0000000e+00
d_{20}	0.0000000e+00	-2.9120201e-01	-4.7516298e-01	9.6288699e-01	2.1495867e+00	1.1307096e+00	0.0000000e+00
d_{21}	0.0000000e+00	-2.1710007e+01	-5.0250000e+01	-1.6810001e+02	-5.7330002e+01	-1.7860001e+02	0.0000000e+00
d_{22}	0.0000000e+00	-4.3420000e+00	-8.4119997e+00	7.0630005e+01	2.0880005e+01	2.1799999e-01	0.0000000e+00
d_{23}	0.0000000e+00	1.3160000e+01	2.9820007e+01	8.7500000e+01	2.5919998e+01	6.7139999e+01	0.0000000e+00
d_{24}	0.0000000e+00	2.6320000e+00	3.5089998e+00	-3.7500000e+01	-9.7930002e+00	-4.7390002e-01	0.0000000e+00

Table A3.6 (concluded) Curve Fit Coefficients for $k = k(\rho, e)$: $-1.0 < y$

	200 ≤ T < 800	800 ≤ T < 3 000	3 000 ≤ T < 6 000	6 000 ≤ T < 10 000	10 000 ≤ T < 15 000
	Diatomic Oxygen				
a_1	3.7703733e+00	2.8969173e+00	2.8421116e+00	5.6821089e+00	-2.7258968e-01
a_2	-2.8952206e-03	2.3736544e-03	1.3320560e-03	-7.5300597e-04	2.0115140e-03
a_3	9.5332234e-06	-1.4917096e-06	-3.3915853e-07	2.2980078e-07	-2.4547717e-07
a_4	-9.2469925e-09	4.6603388e-10	4.4652185e-11	-2.3955921e-11	1.2025200e-11
a_5	3.0191908e-12	-5.3945167e-14	-2.2914825e-15	8.0048468e-16	-2.1389860e-16
a_6	-1.8859756e+01	8.2240433e+01	5.8350391e+02	-2.4700371e+03	7.6117734e+03
a_7	3.6933498e+00	7.5019388e+00	8.6255035e+00	-9.8740053e+00	3.1631744e+01
	Diatomic Nitrogen				
a_1	3.4622650e+00	2.7022400e+00	3.9143505e+00	1.2657471e+00	2.7715942e+01
a_2	5.8202352e-04	1.9443934e-03	3.1537097e-04	1.8269790e-03	-7.4173473e-03
a_3	-3.0525453e-06	-8.9300045e-07	-5.6481042e-08	-3.7583897e-07	8.2395968e-07
a_4	6.2280066e-09	1.9739206e-10	3.6012296e-12	3.3033715e-11	-3.5285302e-11
a_5	-3.3755958e-12	-1.6967811e-14	5.2359434e-17	-9.3651118e-16	4.9671198e-16
a_6	8.7951738e-01	2.0180222e+02	-5.3551953e+02	3.1426960e+03	-5.6942691e+04
a_7	3.2192650e+00	7.2040844e+00	2.1671999e-02	1.7943298e+01	-1.7402873e+02
	Monatomic Oxygen				
a_1	3.2167139e+00	2.6045370e+00	2.8101683e+00	1.9209270e+00	1.9209270e+00
a_2	-3.7822688e-03	-1.7235464e-04	-2.9039918e-04	2.1776554e-04	2.1776554e-04
a_3	8.4746789e-06	1.1574139e-07	9.0833339e-08	-1.8288404e-08	-1.8288404e-08
a_4	-8.8658254e-09	-3.6417855e-11	-9.9427818e-12	4.9050960e-13	4.9050960e-13
a_5	3.5365599e-12	4.6011541e-15	3.7704359e-16	2.8507299e-18	2.8507299e-18
a_6	2.9640461e+04	2.9728961e+04	2.9536613e+04	3.0783422e+04	3.0783422e+04
a_7	1.8526411e+00	4.5865259e+00	3.2536469e+00	9.2748632e+00	9.2748632e+00

Table A3.7 Species Property Curve Fit Coefficients.

	200 ≤ T < 800	800 ≤ T < 3 000	3 000 ≤ T < 6 000	6 000 ≤ T < 10 000	10 000 ≤ T < 15 000
	Nitric Oxide				
a_1	4.2064362e+00	2.7543774e+00	3.8015413e+00	4.9133167e+00	2.0456650e+01
a_2	-4.5098364e-03	2.3093284e-03	4.9857539e-04	6.1755264e-07	-6.1498061e-03
a_3	1.0557385e-05	-1.2823357e-06	-1.2531319e-07	-5.5222383e-08	8.6914275e-07
a_4	-8.5919396e-09	3.4043524e-10	1.4093893e-11	1.1686489e-11	-5.0877511e-11
a_5	2.4047101e-12	-3.4807545e-14	-4.4820198e-16	-5.4642498e-16	1.0624156e-15
a_6	1.0888965e+04	1.1134324e+04	1.0666566e+04	8.8453789e+03	-2.2955242e+04
a_7	2.3137932e+00	9.0789671e+00	3.1619387e+00	-4.5786896e+00	-1.1561955e+02
	Monatomic Nitrogen				
a_1	2.5000000e+00	2.5075111e+00	2.6376047e+00	3.3720617e+00	-1.0205642e+01
a_2	0.0000000e+00	-2.4797875e-05	-8.7373319e-06	-8.8554644e-04	4.2931363e-03
a_3	0.0000000e+00	2.9641516e-08	-6.4772678e-08	2.5293269e-07	-4.9310665e-07
a_4	0.0000000e+00	-1.5288104e-11	2.3473432e-11	-2.3187896e-11	2.4951069e-11
a_5	0.0000000e+00	2.8913713e-15	-1.7396164e-15	7.0471426e-16	-4.6969946e-16
a_6	5.6626707e+04	5.6624949e+04	5.6452266e+04	5.6270152e+04	8.4933750e+04
a_7	4.1807280e+00	4.1431866e+00	3.2232103e+00	-1.0563974e+00	9.6403748e+01
	Argon				
a_1	2.5000000e+00	2.5000000e+00	2.5000000e+00	2.6303549e+00	-9.1423988e+00
a_2	0.0000000e+00	0.0000000e+00	0.0000000e+00	-7.7393444e-05	3.8508170e-03
a_3	0.0000000e+00	0.0000000e+00	0.0000000e+00	1.7219730e-08	-4.6800437e-07
a_4	0.0000000e+00	0.0000000e+00	0.0000000e+00	-1.7028228e-12	2.4506924e-11
a_5	0.0000000e+00	0.0000000e+00	0.0000000e+00	6.3198849e-17	-4.5646902e-16
a_6	-4.2498957e-02	-4.2498957e-02	-4.2498957e-02	-1.7548010e+02	2.7751914e+04
a_7	4.3664980e+00	4.3664980e+00	4.3664980e+00	3.4890099e+00	8.9461761e+01

Table A3.7 (concluded) Species Property Curve Fit Coefficients.

APPENDIX FOUR

Expressions for χ and κ, based on the enthalpy derivatives $(h)_T$ and $(h)_{\eta_i}$ and the chemical derivatives $(\eta_i)_T$ and $(\eta_i)_\rho$ defined in section 4.9 are required. These expressions can be developed from the thermal state equation:

$$p = \hat{R}\sum_i \eta_i \rho T \tag{A4.1}$$

combined with a generalized caloric state equation in the form:

$$h = h\,(T, \eta_i(\rho, T)). \tag{A4.2}$$

The differential forms of these equations are:

$$dp = \hat{R}\rho\left[\eta + T\sum_i (\eta_i)_T\right]dT + \hat{R}T\left[\eta + \rho\sum_i (\eta_i)_\rho\right]d\rho \tag{A4.3}$$

$$dh = \left[(h)_T + \sum_i (h)_{\eta_i}(\eta_i)_T\right]dT + \left[\sum_i (h)_{\eta_i}(\eta_i)_\rho\right]d\rho \tag{A4.4}$$

where $\eta = \sum\eta_i$. By definition, specific enthalpy and internal energy density are related by:

$$h = \frac{\varepsilon + p}{\rho} \tag{A4.5}$$

which can also be expressed in differential form as:

$$\rho\,dh = d\varepsilon + dp - h\,d\rho. \tag{A4.6}$$

Eliminating dT from Eqs. (A4.3) and (A4.4), then further eliminating dh using Eq. (A4.6) gives the result:

$$\left\{\left[(h)_T + \sum_i (h)_{\eta_i}(\eta_i)_T\right] - \hat{R}\left[\eta + T\sum_i (\eta_i)_T\right]\right\} dp$$

$$= \hat{R}\left[\eta + T\sum_i (\eta_i)_T\right] d\varepsilon$$

$$+ \left\{\hat{R}T\left[(h)_T + \sum_i (h)_{\eta_i}(\eta_i)_T\right]\left[\eta + \rho\sum_i (\eta_i)_\rho\right]\right.$$

$$\left. - \hat{R}\left[h + \rho\sum_i (h)_{\eta_i}(\eta_i)_\rho\right]\left[\eta + T\sum_i (\eta_i)_T\right]\right\} d\rho\,. \tag{A4.7}$$

Alternately setting dε then dρ to zero in Eq. (A4.7) gives the derivatives required in section 5.2:

$$\kappa = \frac{\hat{R}\left[\eta + T\sum_i (\eta_i)_T\right]}{\left[(h)_T + \sum_i (h)_{\eta_i}(\eta_i)_T\right] - \hat{R}\left[\eta + T\sum_i (\eta_i)_T\right]} \qquad \text{(A4.8)}$$

$$\chi = \frac{\hat{R}T\left[(h)_T + \sum_i (h)_{\eta_i}(\eta_i)_T\right]\left[\eta + \rho\sum_i (\eta_i)_\rho\right]}{\left[(h)_T + \sum_i (h)_{\eta_i}(\eta_i)_T\right] - \hat{R}\left[\eta + T\sum_i (\eta_i)_T\right]} -$$

$$\frac{\hat{R}\left[h + \rho\sum_i (h)_{\eta_i}(\eta_i)_\rho\right]\left[\eta + T\sum_i (\eta_i)_T\right]}{\left[(h)_T + \sum_i (h)_{\eta_i}(\eta_i)_T\right] - \hat{R}\left[\eta + T\sum_i (\eta_i)_T\right]} . \qquad \text{(A4.9)}$$

APPENDIX FIVE

The quasi-one-dimensional equations of motion are given by:

$$\frac{\partial U}{\partial t} + \frac{\partial F}{\partial x} = \Omega + \frac{\partial}{\partial x}\left(\nu_N \frac{\partial U}{\partial x}\right) \tag{A5.1}$$

The source term Ω represents area changes through a nozzle and ν_N is an artificial viscosity term. Trapezoidal time differencing takes the form:

$$\frac{\Delta U}{\Delta t} = \frac{1}{2}\left(\frac{\partial U^n}{\partial t} + \frac{\partial U^{n+1}}{\partial t}\right) \tag{A5.2}$$

Using Eq. (A5.1) to replace the time derivatives in Eq. (A5.2) gives:

$$\frac{\Delta U}{\Delta t} = \frac{1}{2}\left(-\frac{\partial F^n}{\partial x} + \Omega^n + \frac{\partial}{\partial x}\left(\nu_N \frac{\partial U}{\partial x}\right)^n - \frac{\partial F^{n+1}}{\partial x} + \Omega^{n+1} + \frac{\partial}{\partial x}\left(\nu_N \frac{\partial U}{\partial x}\right)^{n+1}\right) \tag{A5.3}$$

Terms evaluated at time $t = (n+1)\Delta t$ can be expanded in a Taylor series as:

$$\frac{\partial F^{n+1}}{\partial x} = \frac{\partial F^n}{\partial x} + \Delta t \frac{\partial}{\partial t}\frac{\partial F^n}{\partial x} + O(\Delta t^2)$$

$$= \frac{\partial F^n}{\partial x} + \Delta t \frac{\partial}{\partial x}\left(\frac{\partial F}{\partial U}\frac{\partial U}{\partial t}\right)^n + O(\Delta t^2)$$

$$= \frac{\partial F^n}{\partial x} + \frac{\partial}{\partial x}\left(\frac{\partial F}{\partial U}\Delta U\right)^n + O(\Delta t^2)\,. \tag{A5.4}$$

Similarly

$$\Omega^{n+1} = \Omega^n + \left(\frac{\partial \Omega}{\partial U}\Delta U\right)^n + O(\Delta t^2) \tag{A5.5}$$

$$\frac{\partial}{\partial x}\left(\nu_N \frac{\partial U}{\partial x}\right)^{n+1} = \frac{\partial}{\partial x}\left(\nu_N \frac{\partial U}{\partial x}\right)^n + \frac{\partial^2}{\partial x^2}(\nu_N \Delta U)^n + O(\Delta t^2) \tag{A5.6}$$

Replacing the time derivatives at $t = (n+1)\Delta t$ in Eq. (A5.3) then gives:

$$\frac{\Delta U}{\Delta t} = \left(-\frac{\partial F}{\partial x} + \Omega + \frac{\partial}{\partial x}\left(\nu_N \frac{\partial U}{\partial x}\right)\right)^n - \frac{1}{2}\frac{\partial}{\partial x}\left(\frac{\partial F}{\partial U}\Delta U\right)^n + \frac{1}{2}\left(\frac{\partial \Omega}{\partial U}\Delta U\right)^n + \frac{1}{2}\frac{\partial^2}{\partial x^2}(\nu_N \Delta U)^n \tag{A5.7}$$

Finally, collecting $\Delta\mathbf{U}$ terms on the left hand side gives:

$$\left[\frac{\mathbf{I}}{\Delta t} - \frac{1}{2}\frac{\partial \Omega}{\partial \mathbf{U}} + \frac{1}{2}\frac{\partial}{\partial x}\frac{\partial \mathbf{F}}{\partial \mathbf{U}} \bullet - \frac{\mathbf{I}}{2}\frac{\partial^2}{\partial x^2}\nu_N \bullet\right]^n \Delta\mathbf{U}$$

$$= \left[- \frac{\partial \mathbf{F}}{\partial x} + \Omega + \frac{\partial}{\partial x}\left(\nu_N \frac{\partial \mathbf{U}}{\partial x}\right)\right]^n + O(\Delta t^2) \qquad \text{(A5.8)}$$

where the following notation has been adopted:

$$\left[\frac{\partial}{\partial x}\frac{\partial \mathbf{F}}{\partial \mathbf{U}} \bullet\right]\Delta\mathbf{U} = \frac{\partial}{\partial x}\left(\frac{\partial \mathbf{F}}{\partial \mathbf{U}}\Delta\mathbf{U}\right) \qquad \text{(A5.9)}$$

APPENDIX SIX

The flux vector appearing in the Euler equations is an homogeneous function of degree one in the conserved variables, providing the fluid obeys a prefect gas state relation. That is to say, for some constant λ:

$$\mathbf{F}(\lambda \mathbf{U}) = \lambda \mathbf{F}(\mathbf{U}) \, . \tag{A6.1}$$

This property leads to the important relation (Beam and Warming, 1976):

$$\mathbf{F}(\mathbf{U}) = \left(\frac{\partial \mathbf{F}}{\partial \mathbf{U}} \right) \mathbf{U} . \tag{A6.2}$$

The validity of this equation for a general gas must be established before it can be applied to the numerical solution of equilibrium gas problems.

The flux vector is given in terms of the conserved variables by:

$$\mathbf{F}(\mathbf{U}) = \begin{bmatrix} m \\ \dfrac{m^2}{\rho} + p(\mathbf{U}) \\ \dfrac{m}{\rho} \left(E + p(\mathbf{U}) \right) \end{bmatrix} . \tag{A6.3}$$

The generic form of the state equation may be written:

$$p\,(\mathbf{U}) = p\left(\rho, \frac{E}{\rho} - \frac{m^2}{2\rho^2} \right) \tag{A6.4}$$

so that:

$$p\,(\lambda \mathbf{U}) = p\,(\lambda \rho, e). \tag{A6.5}$$

Thus, Eq. (A6.1) is satisfied providing:

$$\mathbf{F}(\lambda \mathbf{U}) = \lambda \begin{bmatrix} m \\ \dfrac{m^2}{\rho} + \dfrac{p(\lambda \mathbf{U})}{\lambda} \\ \dfrac{m}{\rho} \left(E + \dfrac{p(\lambda \mathbf{U})}{\lambda} \right) \end{bmatrix} . \tag{A6.6}$$

and so in order to make use of Eq. (A6.2), the state equation must satisfy:

$$p\,(\rho, e) = \frac{p\,(\lambda \rho, e)}{\lambda} \, . \tag{A6.7}$$

Equation (A6.7) is satisfied if the gas is calorically or thermally perfect, but not in general.

APPENDIX SEVEN

The one dimensional nozzle test problems presented in chapter five are based on nozzle geometries of the following form:

$$A(x) = \exp(c_3x^3 + c_2x^2 + c_1x + c_0) \tag{A7.1}$$

The coefficients c_i are chosen to satisfy certain constraints on the shape of the nozzle. In particular, if the position of the throat and the exhaust relative to the inlet are defined by x_t and x_e respectively and the nozzle cross sectional areas are specified at throat and exhaust as A_t and A_e, then the c_i will be given by the solution of the following linear equations:

$$\begin{bmatrix} x_e^3 & x_e^2 & x_e & 1 \\ x_t^3 & x_t^2 & x_t & 1 \\ 3x_e^2 & 2x_e & 1 & 0 \\ 3x_t^2 & 2x_t & 1 & 0 \end{bmatrix} \begin{bmatrix} c_3 \\ c_2 \\ c_1 \\ c_0 \end{bmatrix} = \begin{bmatrix} \ln A_e \\ \ln A_t \\ 0 \\ 0 \end{bmatrix} \tag{A7.2}$$

The first derivative of A(x) in Eq. (A7.1) has been set to zero at the exhaust to prevent rapid changes in the source terms appearing in the Euler equations at this boundary. Equations (A7.2) can easily be solved to give the coefficients c_i:

$$c_0 = \frac{x_e^2(x_e - 3x_t)}{(x_e - x_t)^3} \ln (A_t/A_e) + \ln A_e \tag{A7.3}$$

$$c_1 = 6 \frac{x_t x_e}{(x_e - x_t)^3} \ln (A_t/A_e) \tag{A7.4}$$

$$c_2 = -3 \frac{(x_e + x_t)}{(x_e - x_t)^3} \ln (A_t/A_e) \tag{A7.5}$$

$$c_3 = \frac{2}{(x_e - x_t)^3} \ln (A_t/A_e) \tag{A7.6}$$

Cubic expressions of the form of Eq. (A7.1) have two turning points, and these are constrained to locate at the throat and at the exhaust. For test cases with non-zero area derivitive at the exhaust, the same expressions are used but the nozzle length is truncated between the throat and the exhaust. This does not permit accurate control over the absolute value of the exhaust area, but does ensure there can be no turning point between the throat and the exhaust, which would give an invalid nozzle shape.

FIGURES

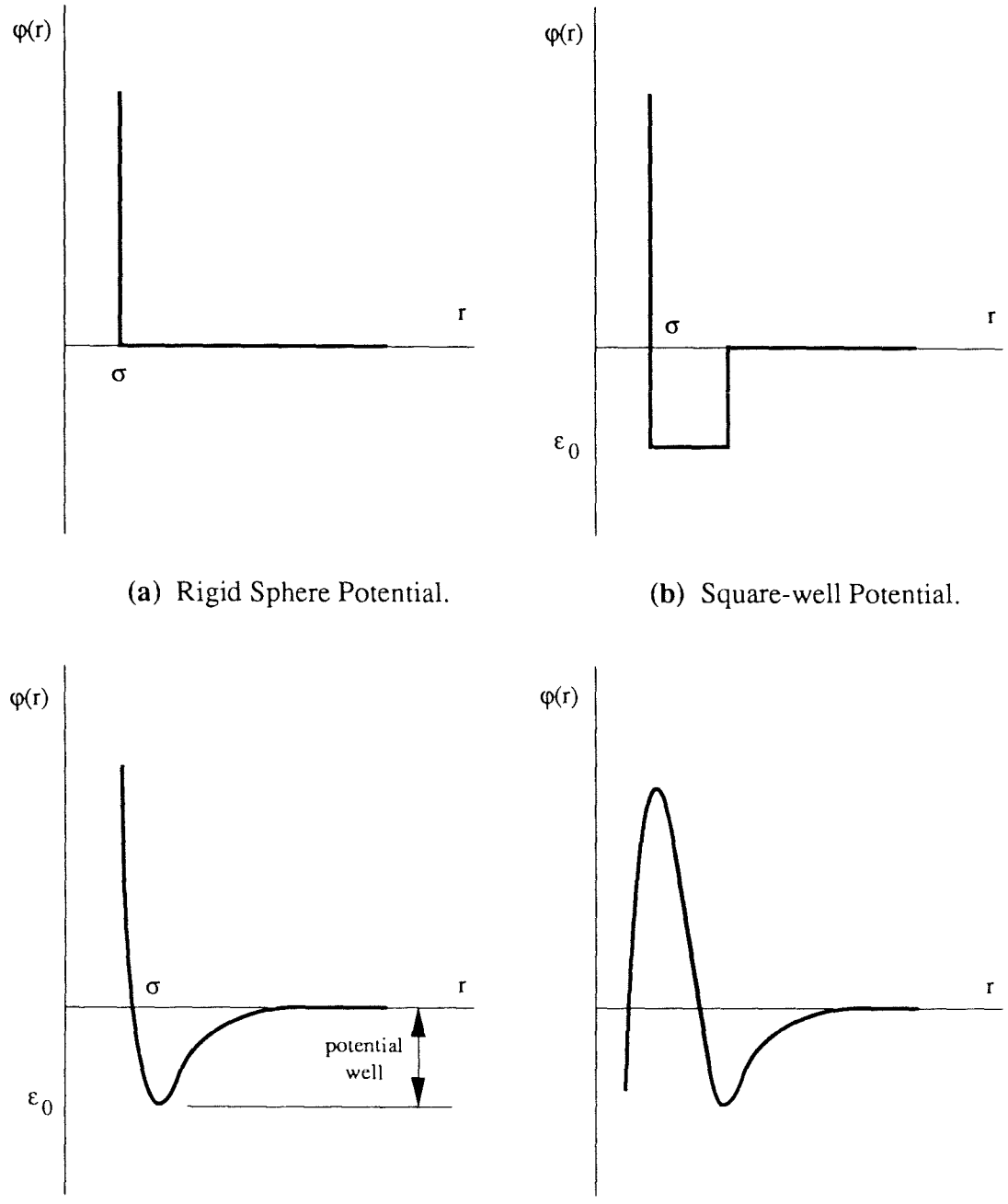

(a) Rigid Sphere Potential.

(b) Square-well Potential.

(c) Lennard-Jones Potential.

(d) Buckingham Potential.

Figure 2.1 Spherically Symmetrical Intermolecular Potential Functions.
φ(r) = Intermolecular Potential
r = Internuclear Separation

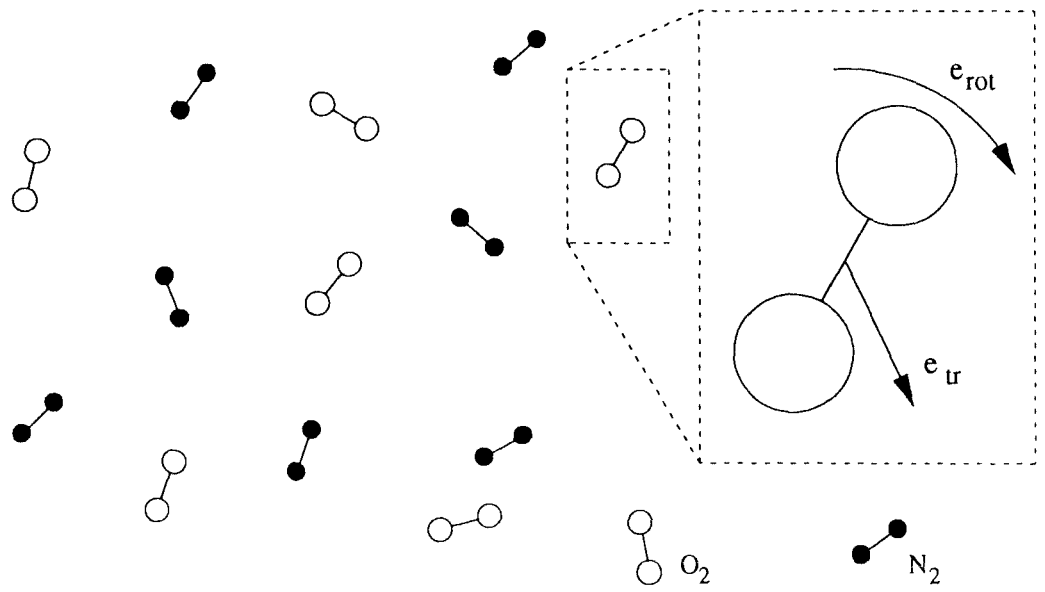

(a) Perfect Gas Molecular Model.

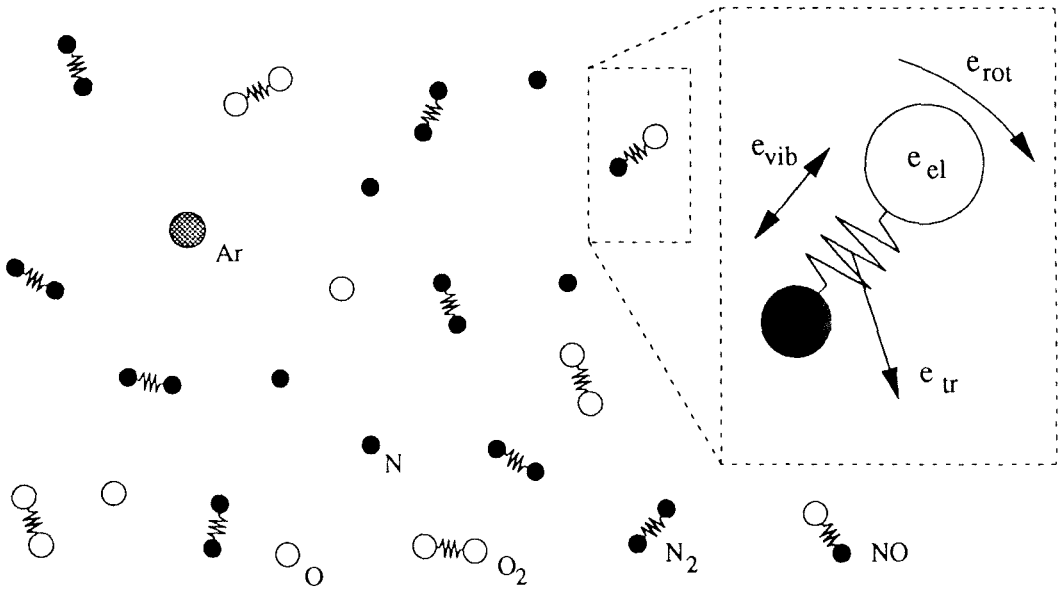

(b) Real Gas Molecular Model.

Figure 2.2 Molecular Representations for Perfect and Imperfect Air.

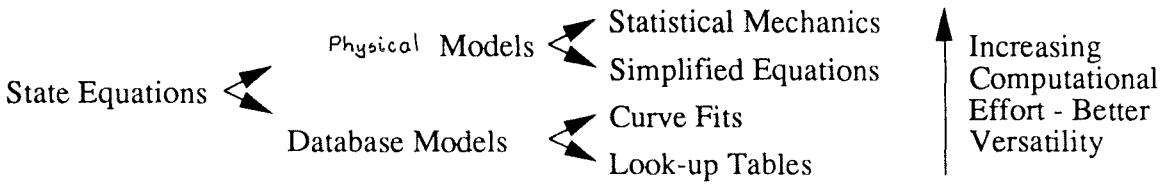

Figure 4.1 Hierarchy of Models for Equilibrium State Equations.

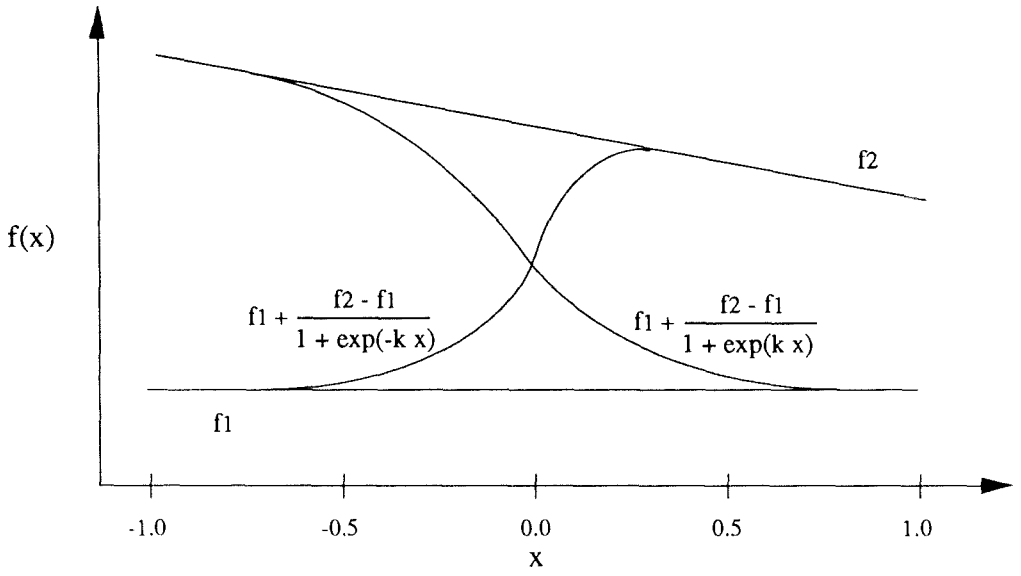

(a) Odd Transition Function.

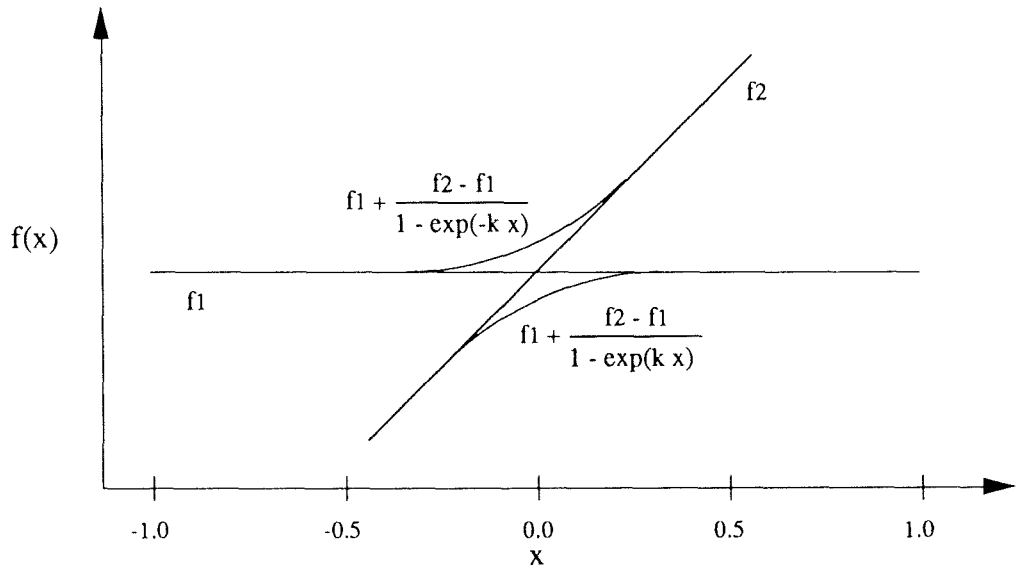

(b) Even Transition Function.

Figure 4.2 Grabau Type Transition Functions in One Dimension.

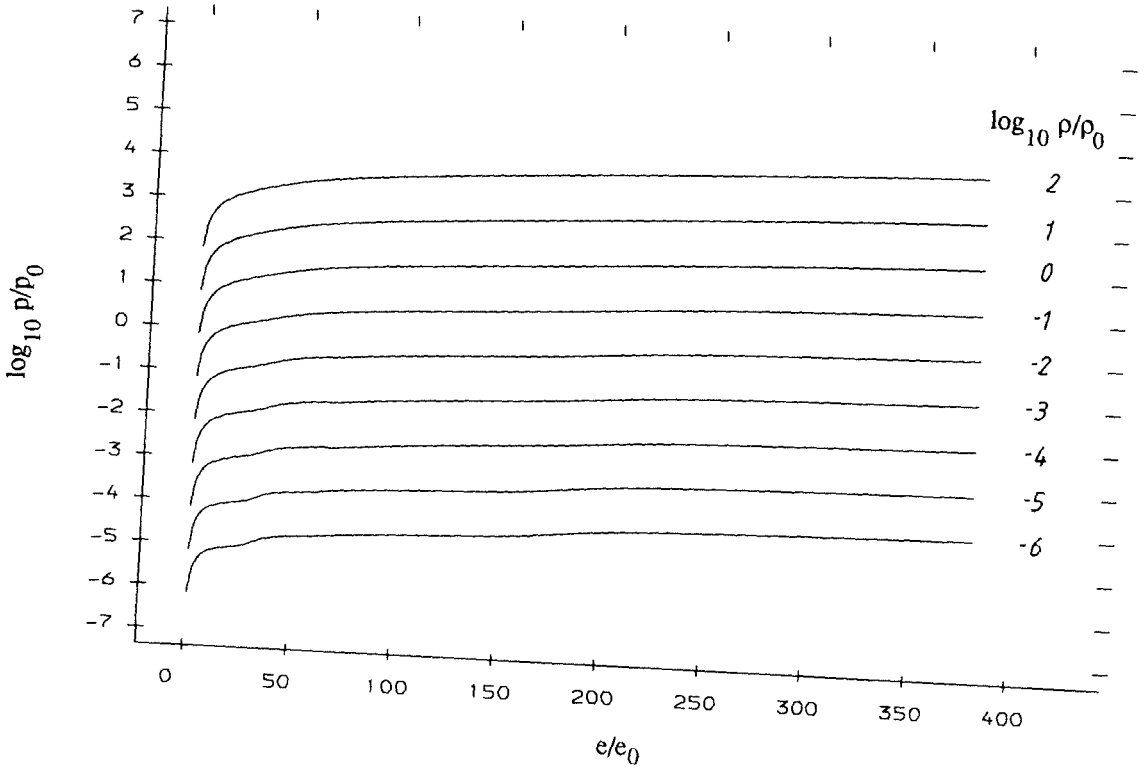

(a) Sixteen Coefficient Curve Fits.

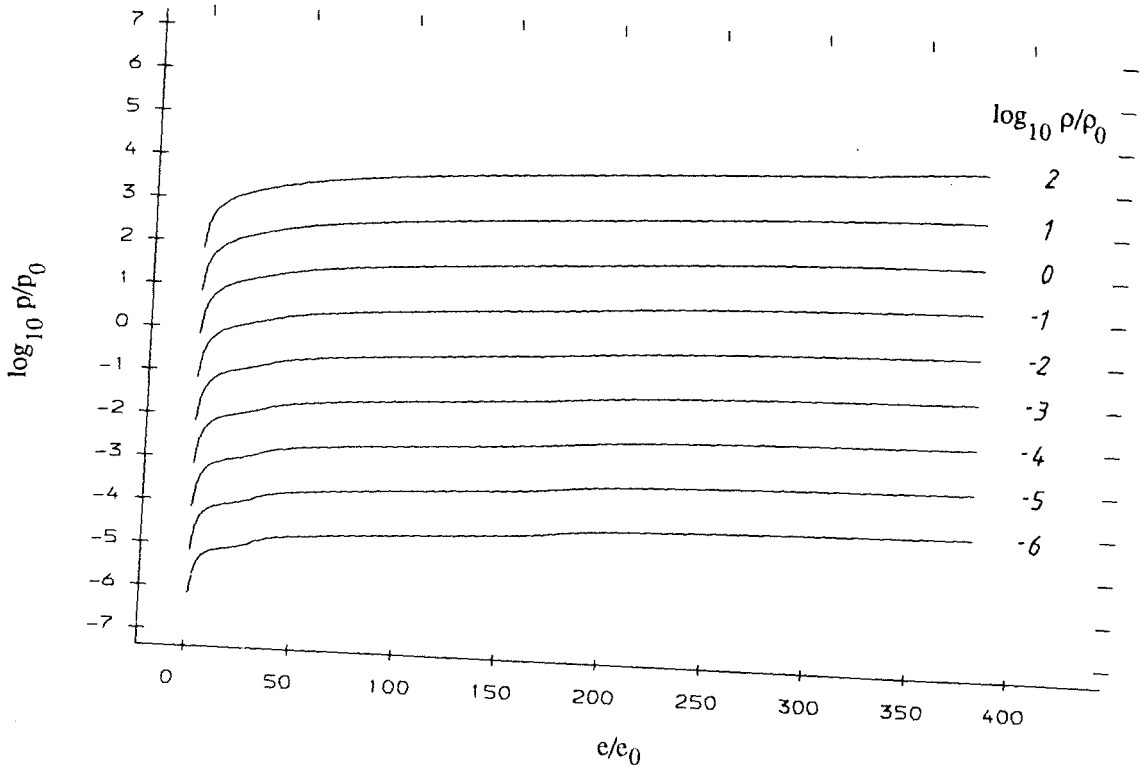

(b) Twenty Four Coefficient Curve Fits.

Figure 4.3 Curve Fits for Pressure in the Form $p = p(\rho, e)$.

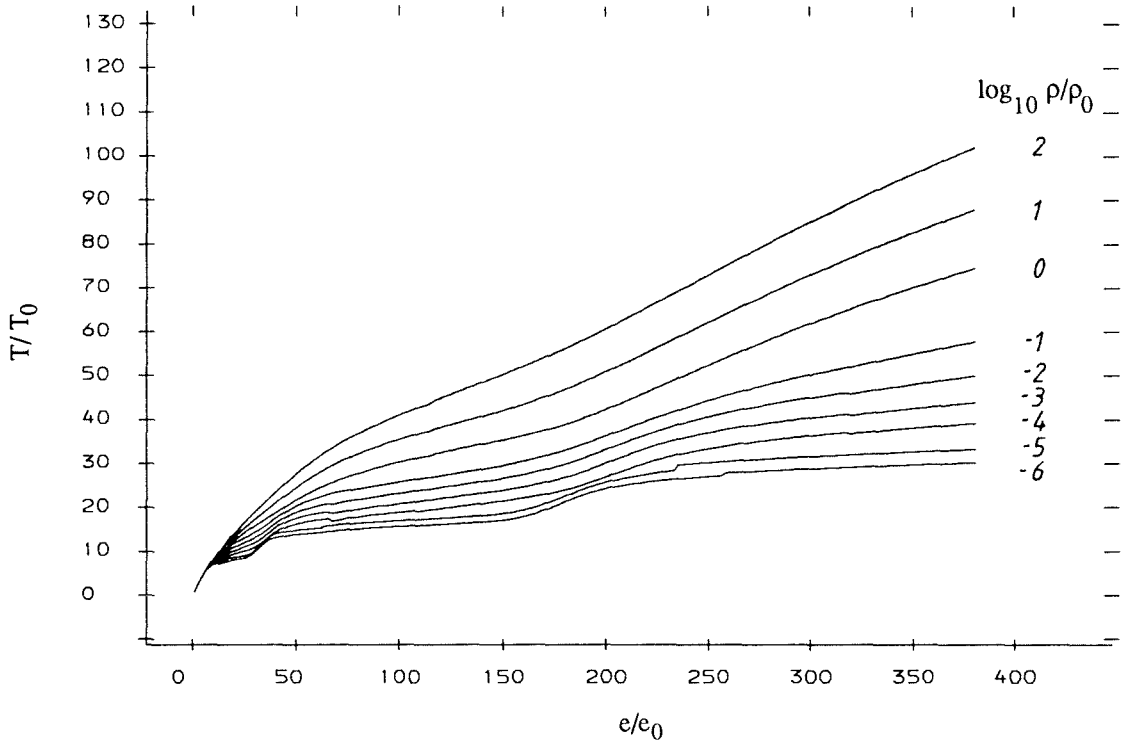

(a) Sixteen Coefficient Curve Fits.

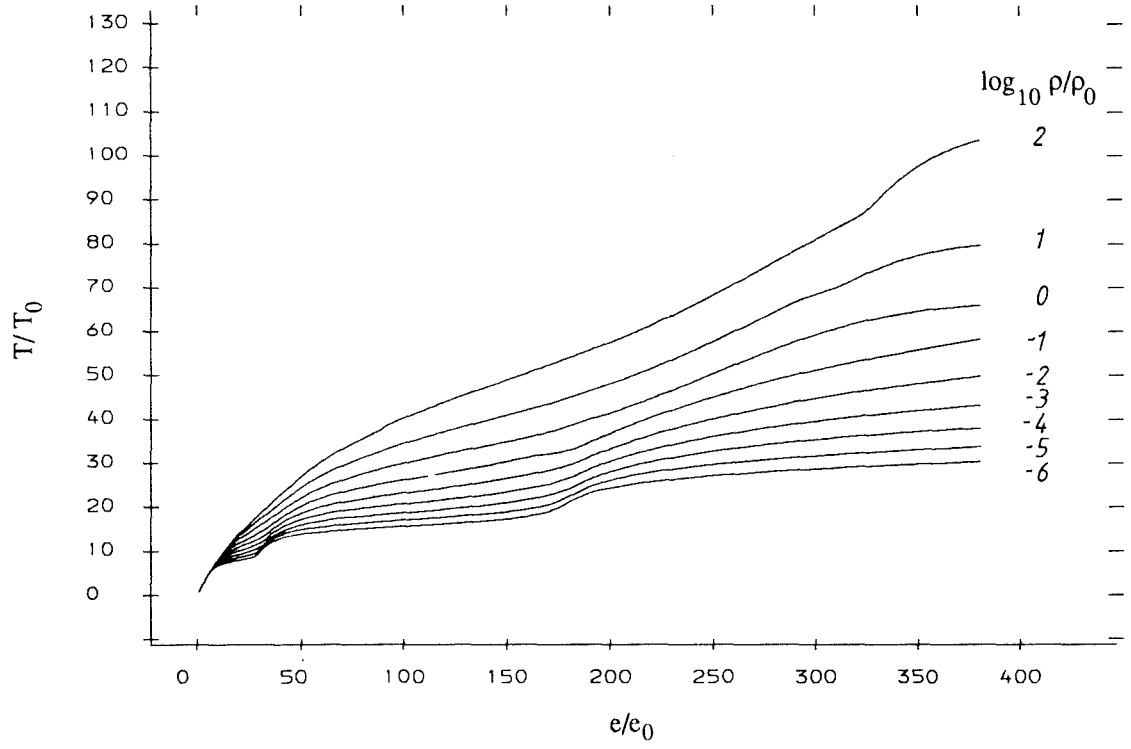

(b) Twenty Four Coefficient Curve Fits.

Figure 4.4 Curve Fits for Temperature in the Form $T = T(\rho, e)$.

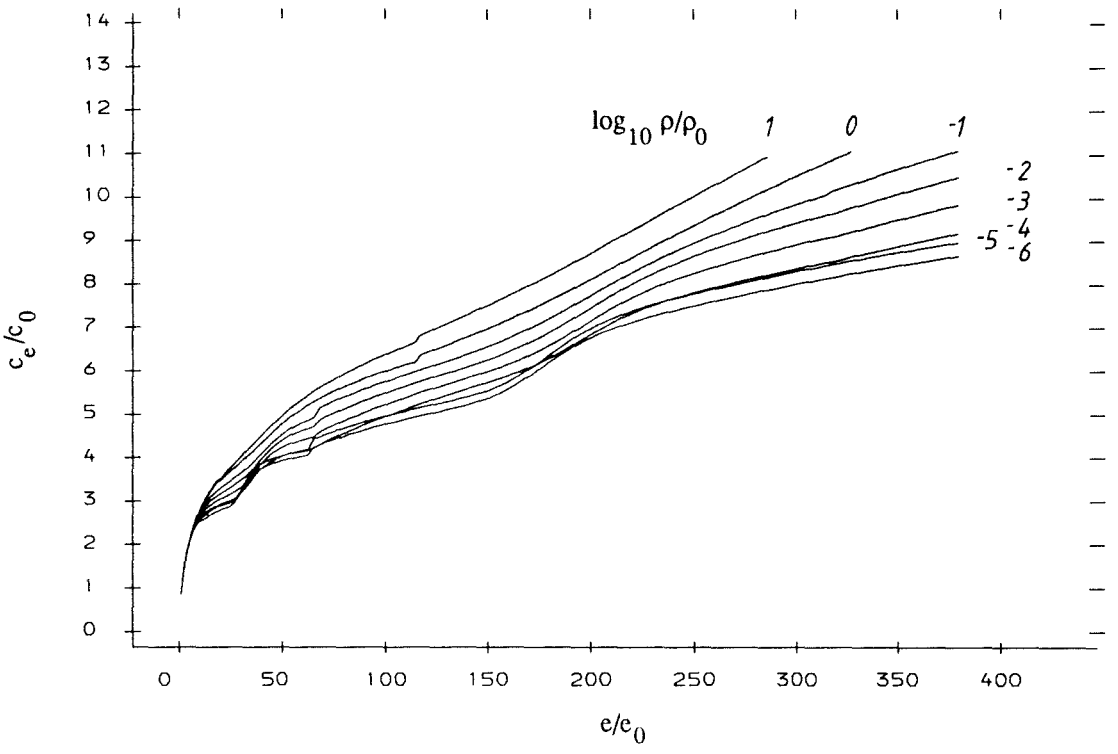

(a) Sixteen Coefficient Curve Fits.

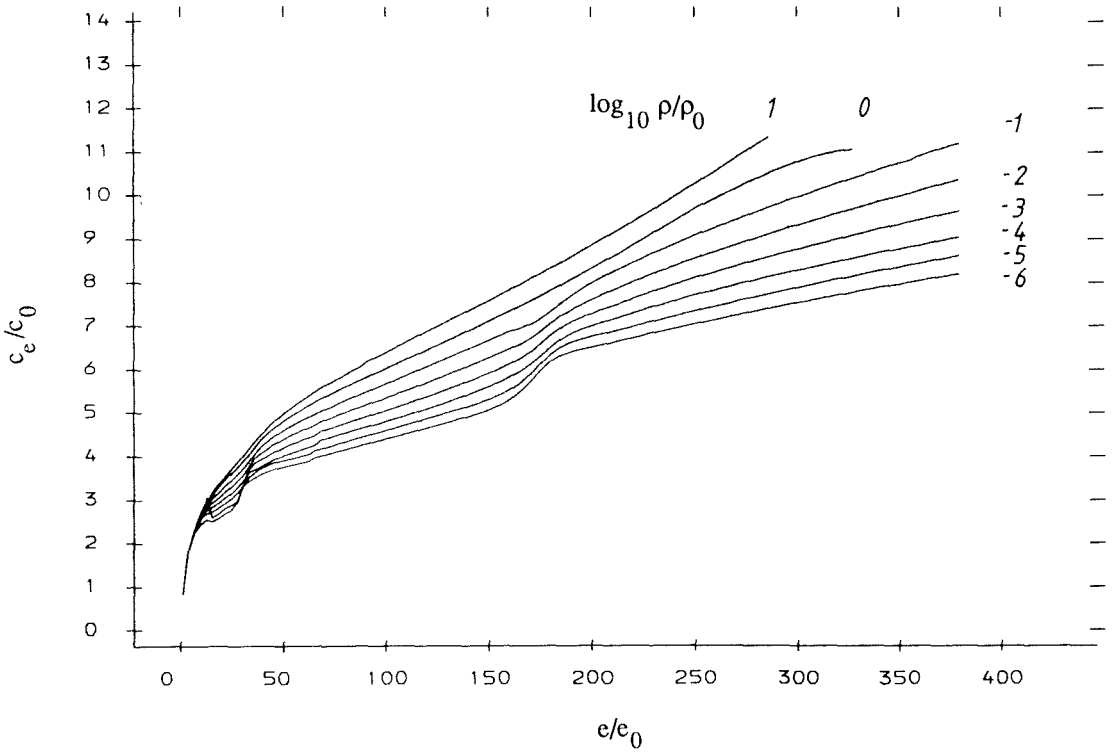

(b) Twenty Four Coefficient Curve Fits.

Figure 4.5 Curve Fits for Equilibrium Sonic Speed in the Form $c_e = c_e(\rho, e)$.

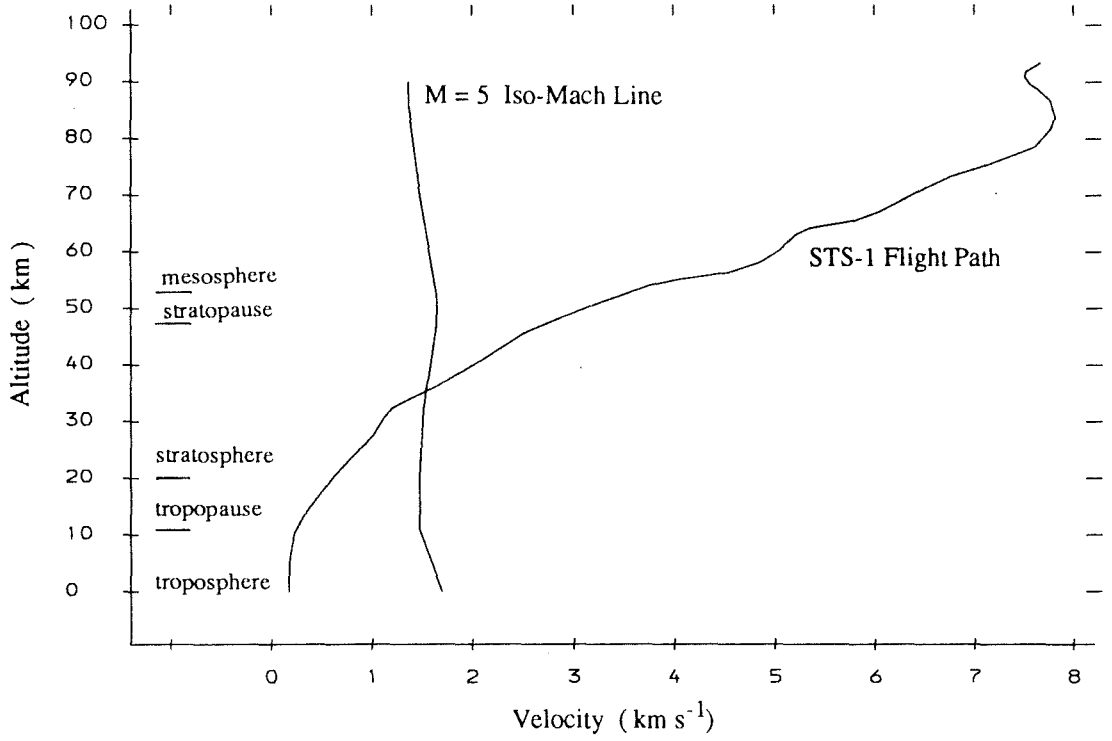

Figure 4.6 Space Shuttle STS-1 Reentry Trajectory.

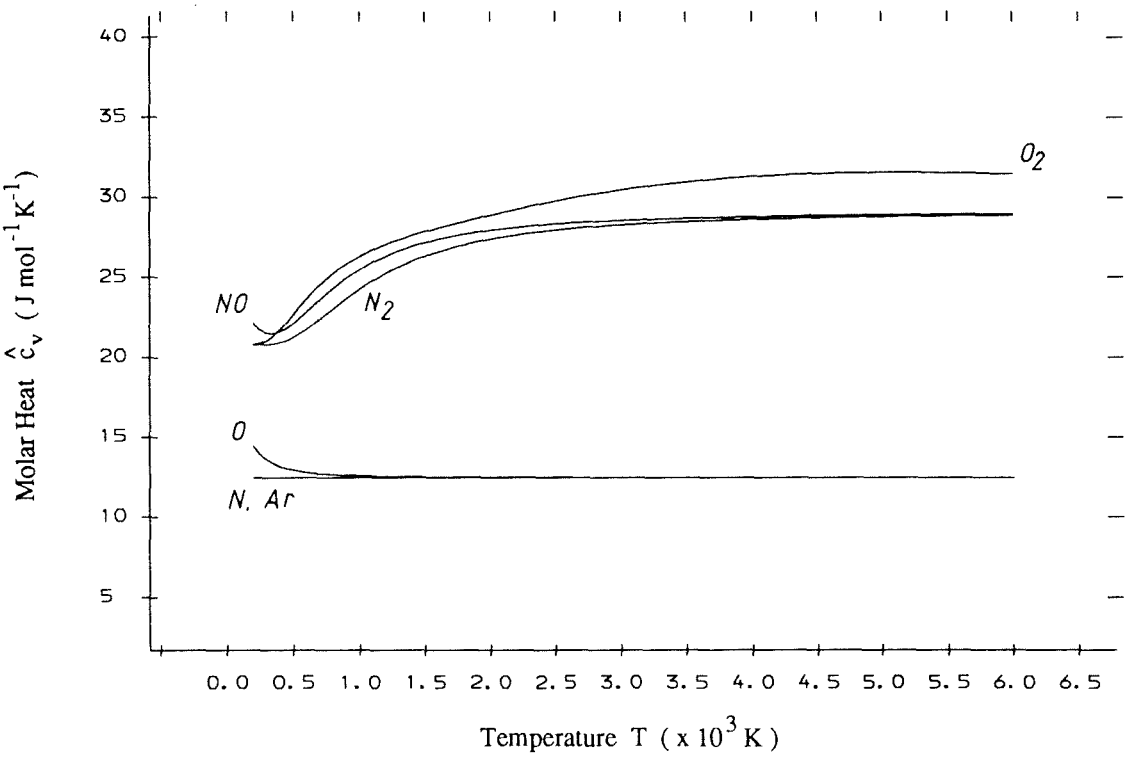

(a) Theoretical Calculation.

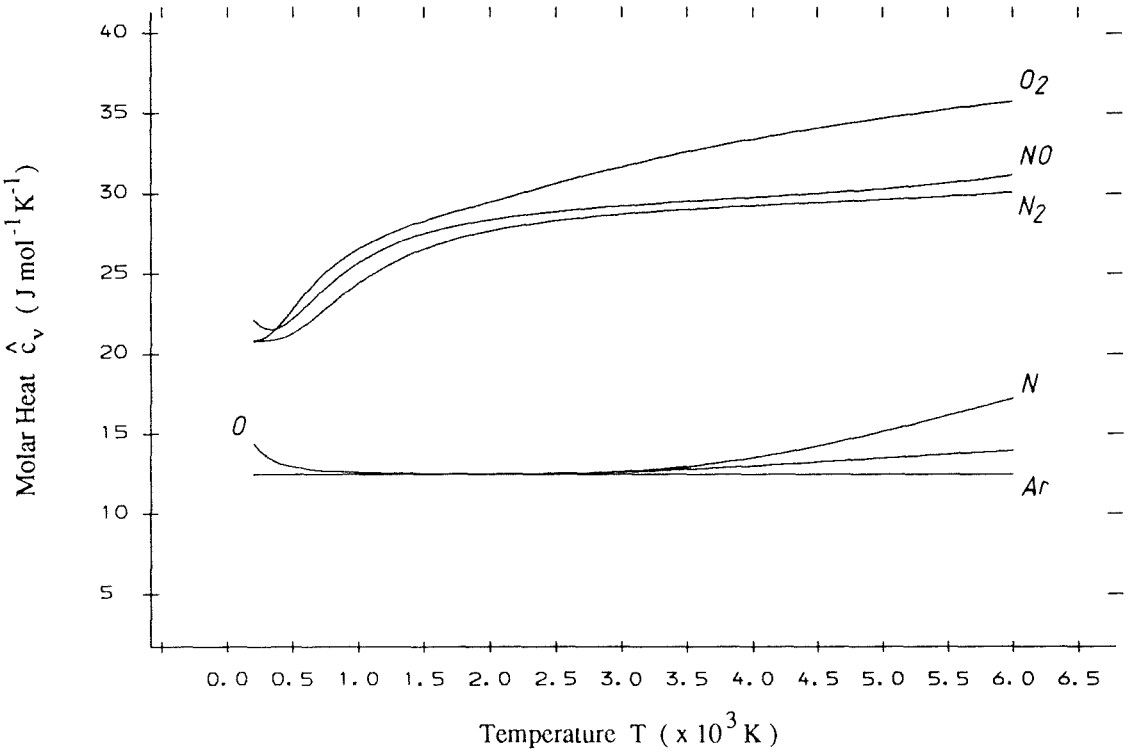

(b) Curve Fit Calculation.

Figure 4.7 Variation of Species Molar Heats at Constant Volume.

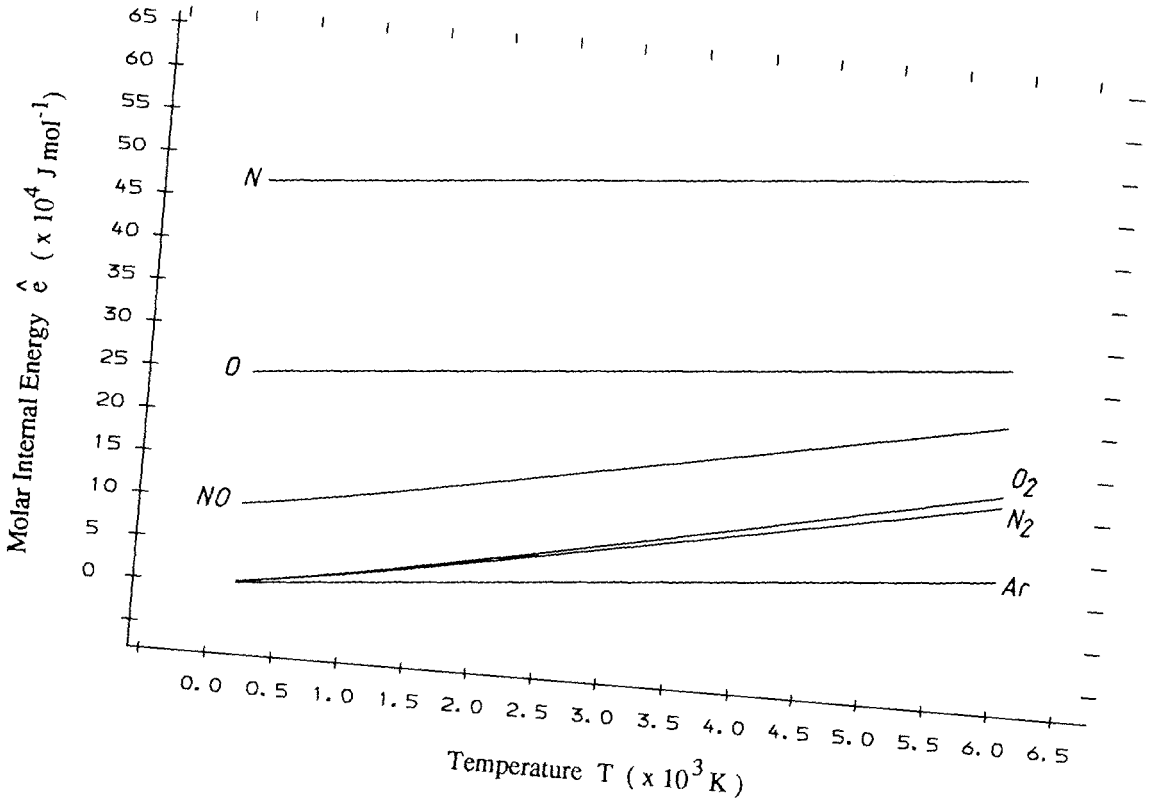

(a) Theoretical Calculation.

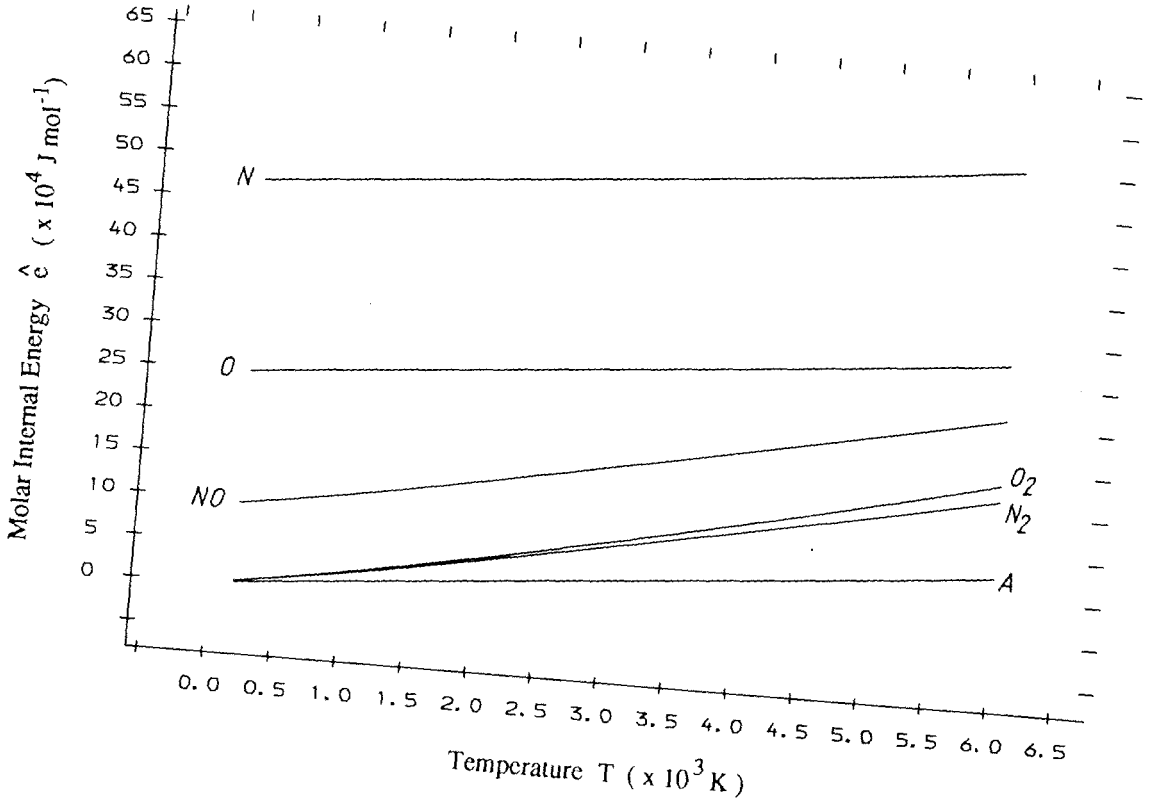

(b) Curve Fit Calculation.

Figure 4.8 Variation of Species Molar Internal Energies.

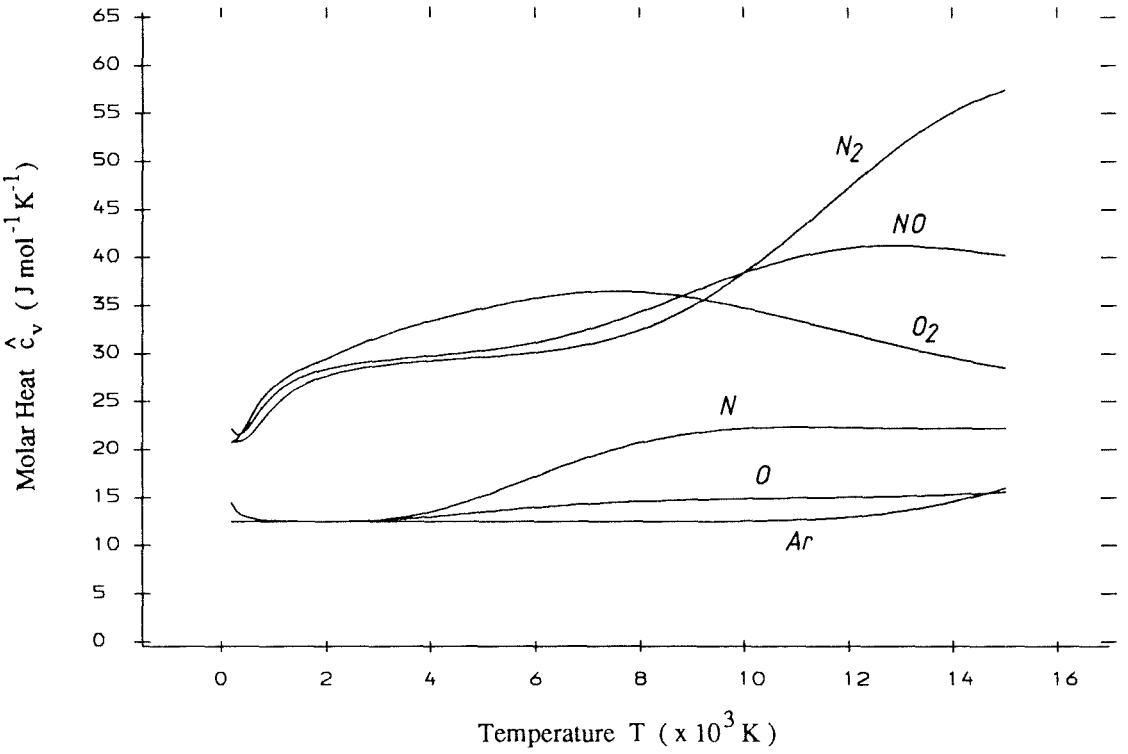

Figure 4.9 Variation of Species Molar Heat with Temperature Between 200 K and 15 000 K, from Curve Fit Data.

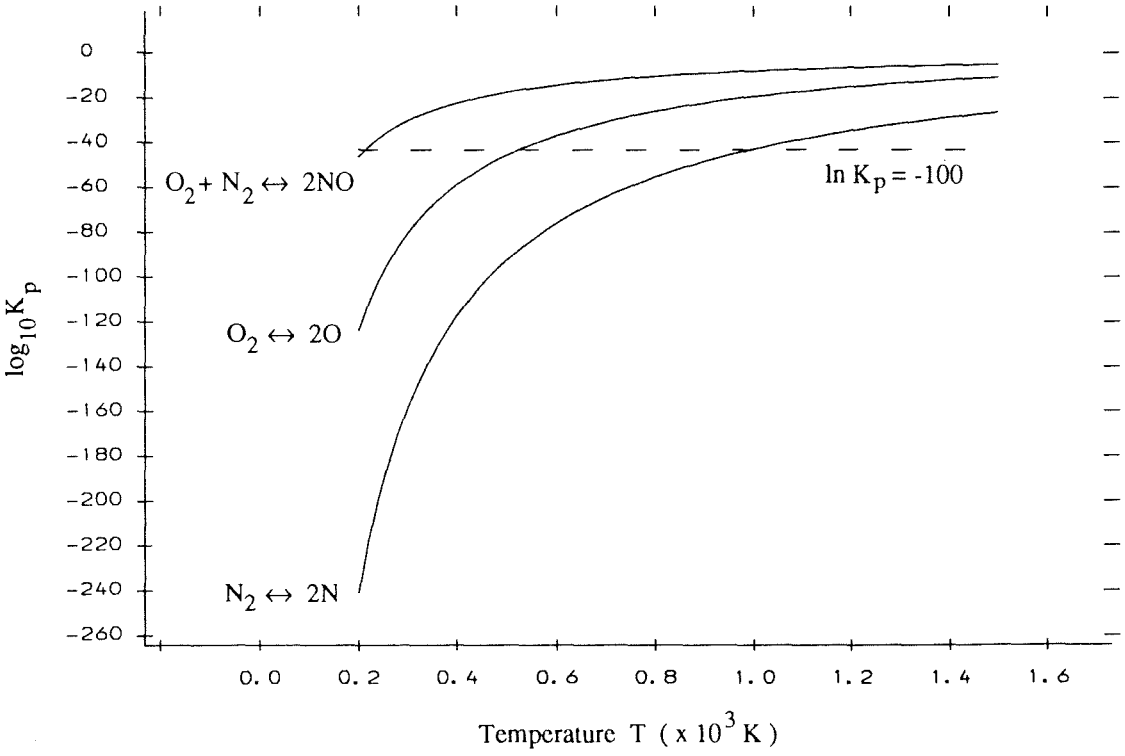

Figure 4.10 Equilibrium Constants in Terms of Partial Pressures.

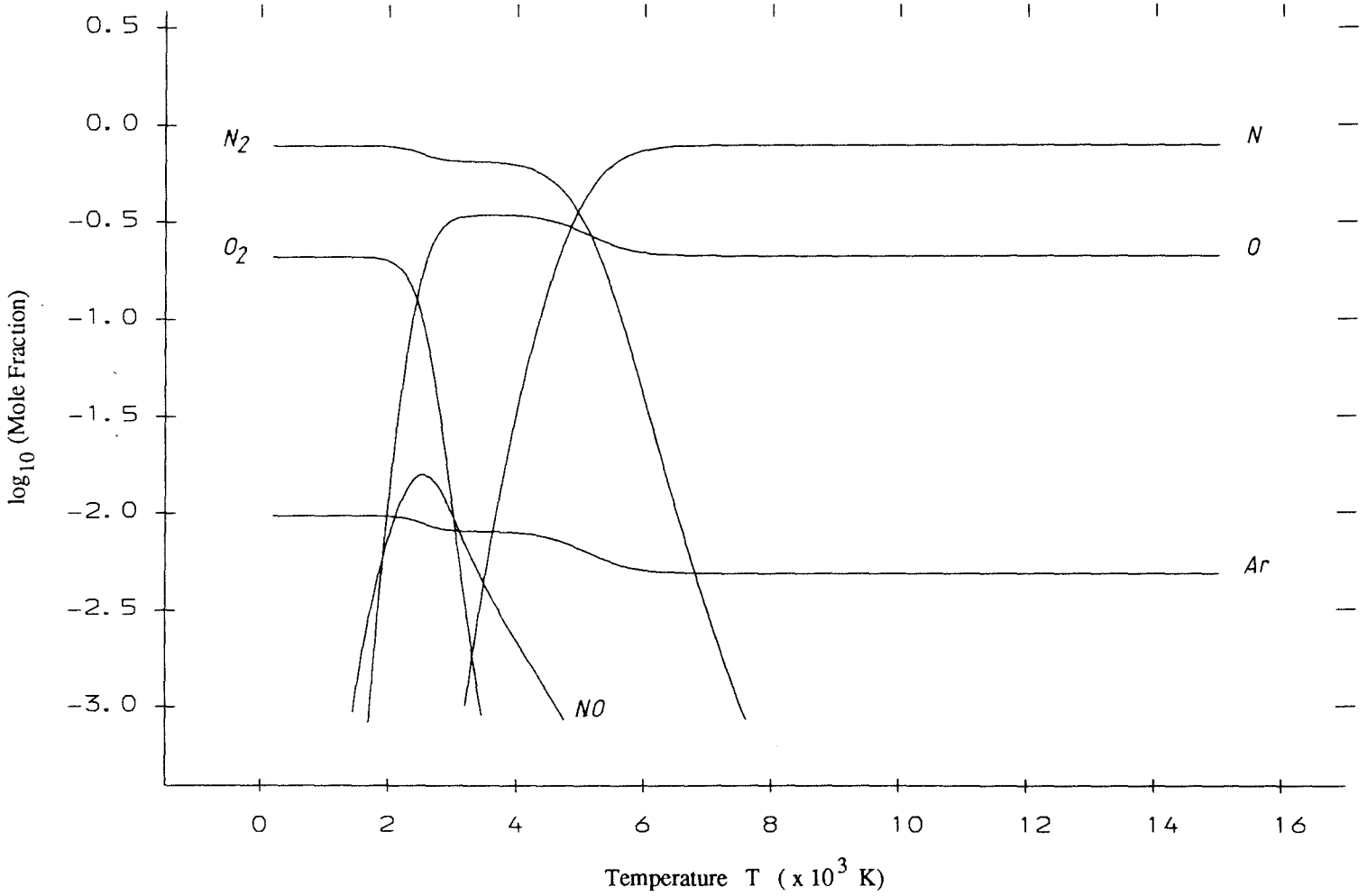

(a) Density $\rho = 1.225 \times 10^{-4}$ kg m^{-3}.

Figure 4.11 Chemical Composition of Equilibrium Air.

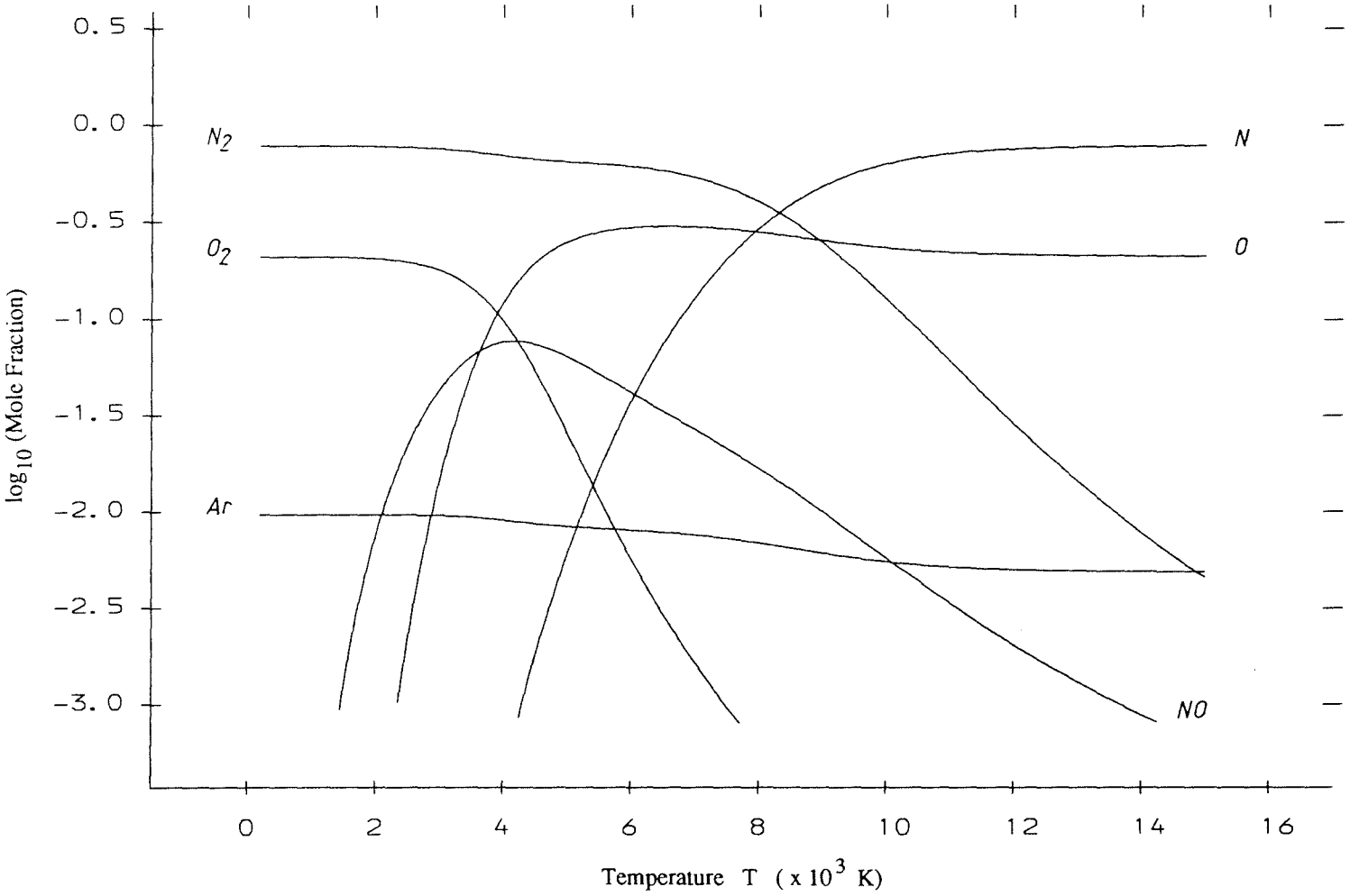

(b) Density $\rho = 1.225$ kg m^{-3}.

Figure 4.11 (continued)

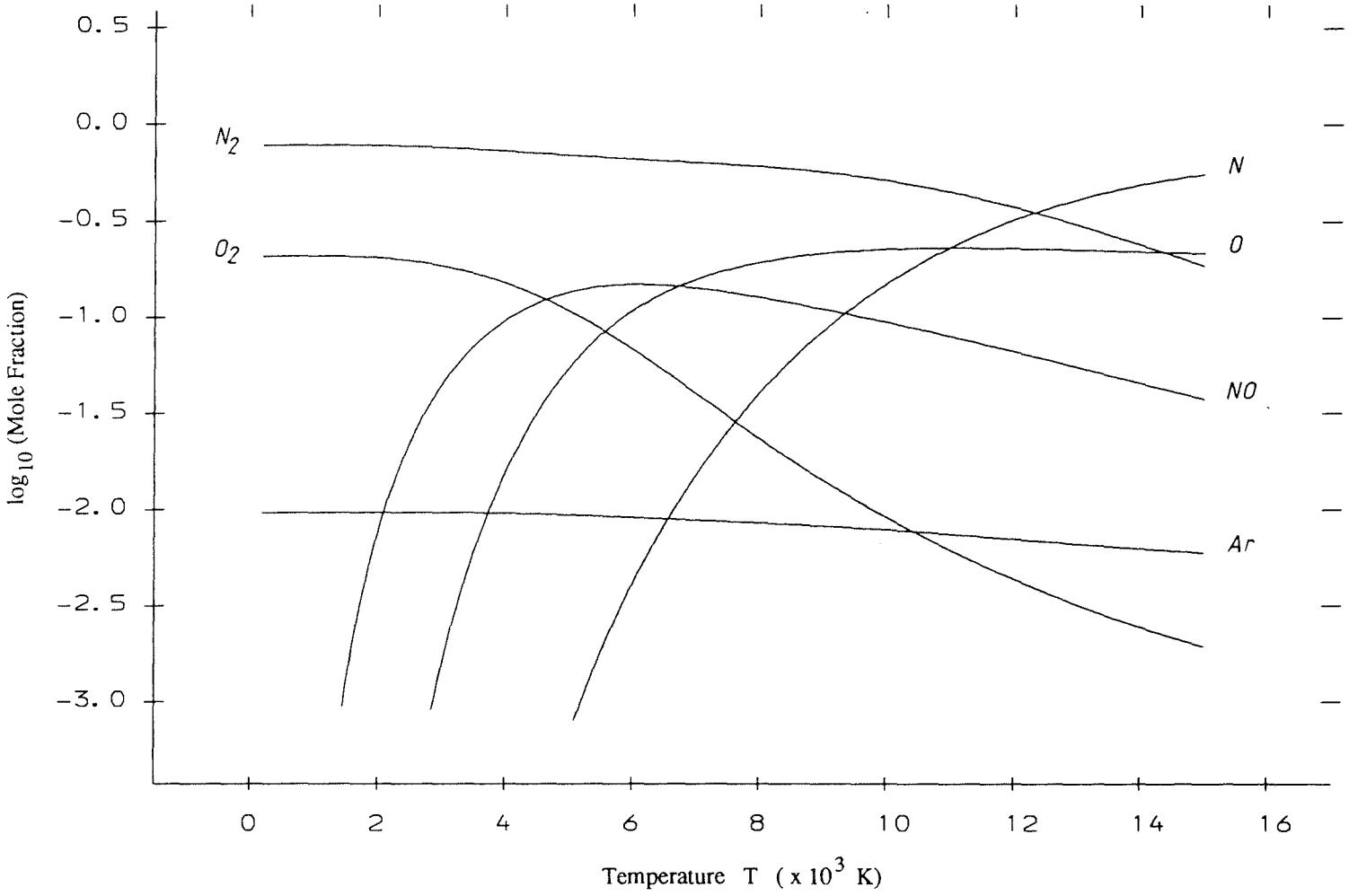

(c) Density $\rho = 122.5$ kg m^{-3}.

Figure 4.11 (continued)

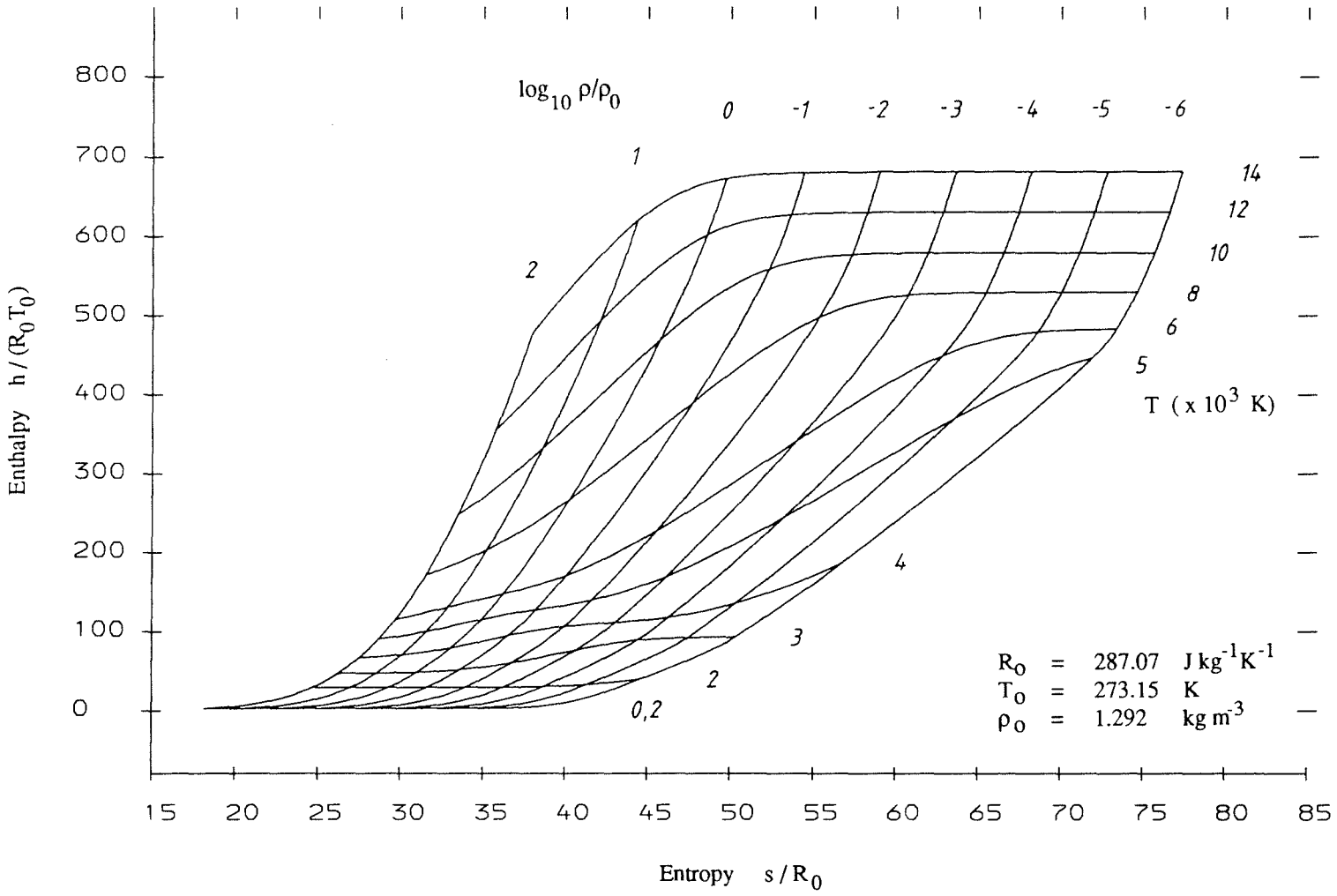

Figure 4.12 Constant Density and Constant Temperature Lines on an Enthalpy-Entropy Chart.

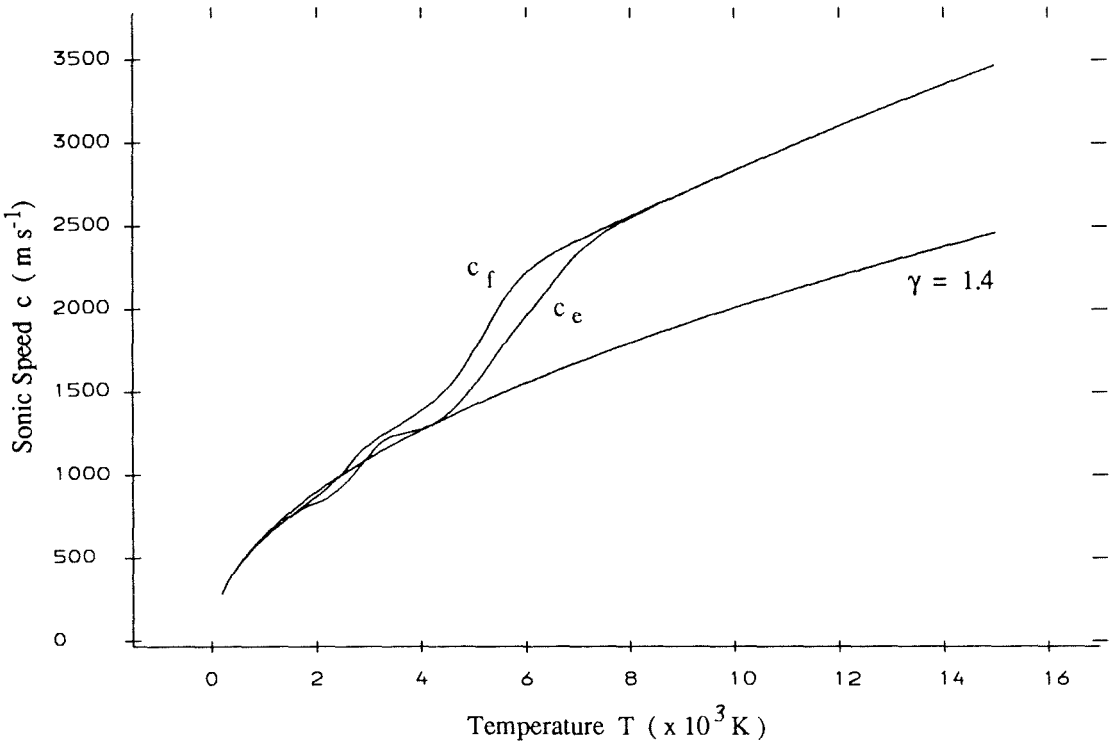

(a) Density $\rho = 1.225 \times 10^{-4}$ kg m^{-3}.

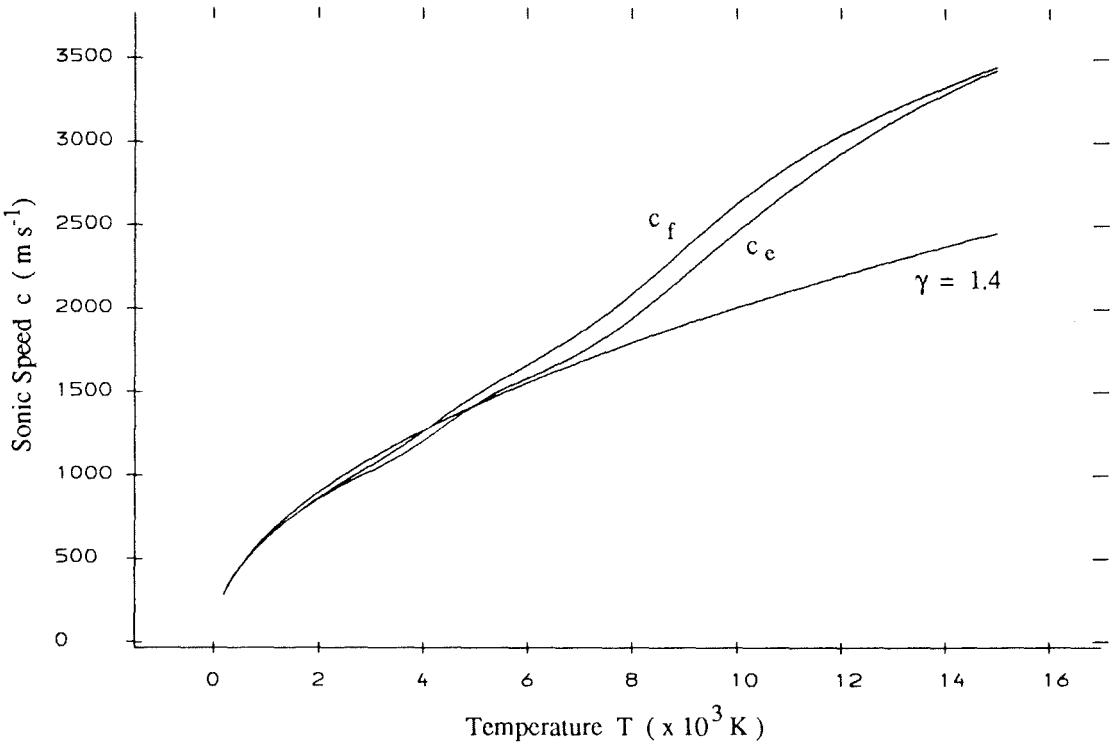

(b) Density $\rho = 1.225$ kg m^{-3}.

Figure 4.13 Perfect, Frozen and Equilibrium Speeds of Sound.

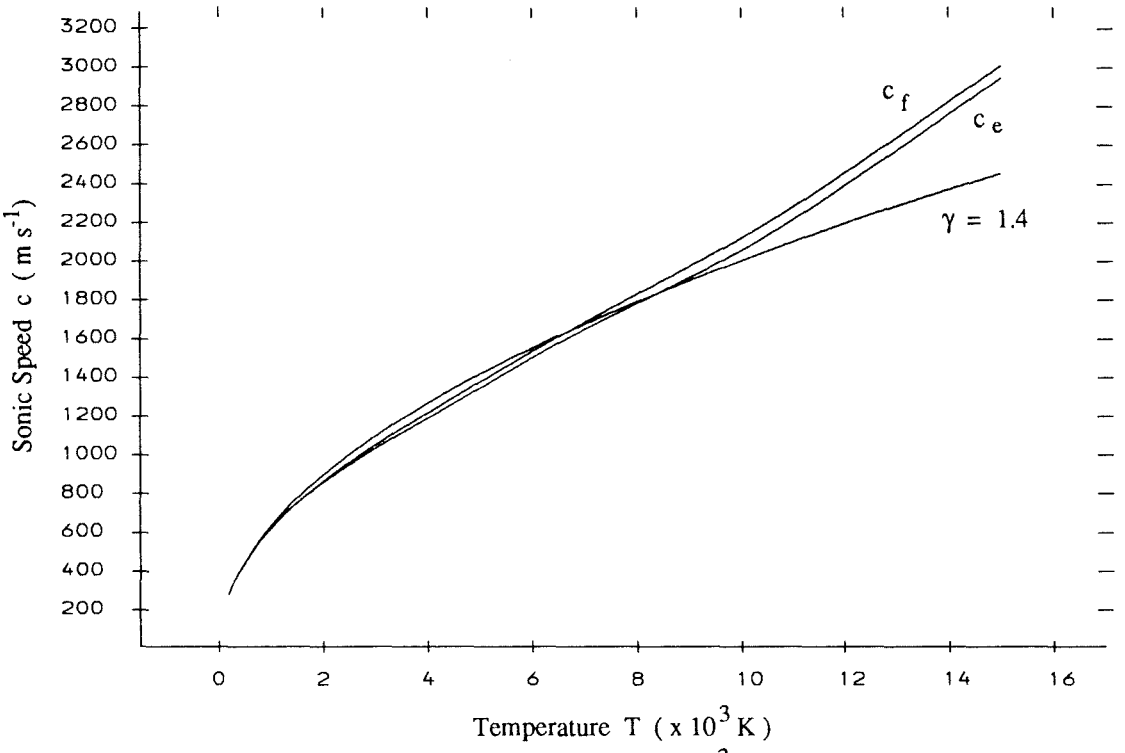

(c) Density $\rho = 122.5$ kg m^{-3}.

Figure 4.13 (continued)

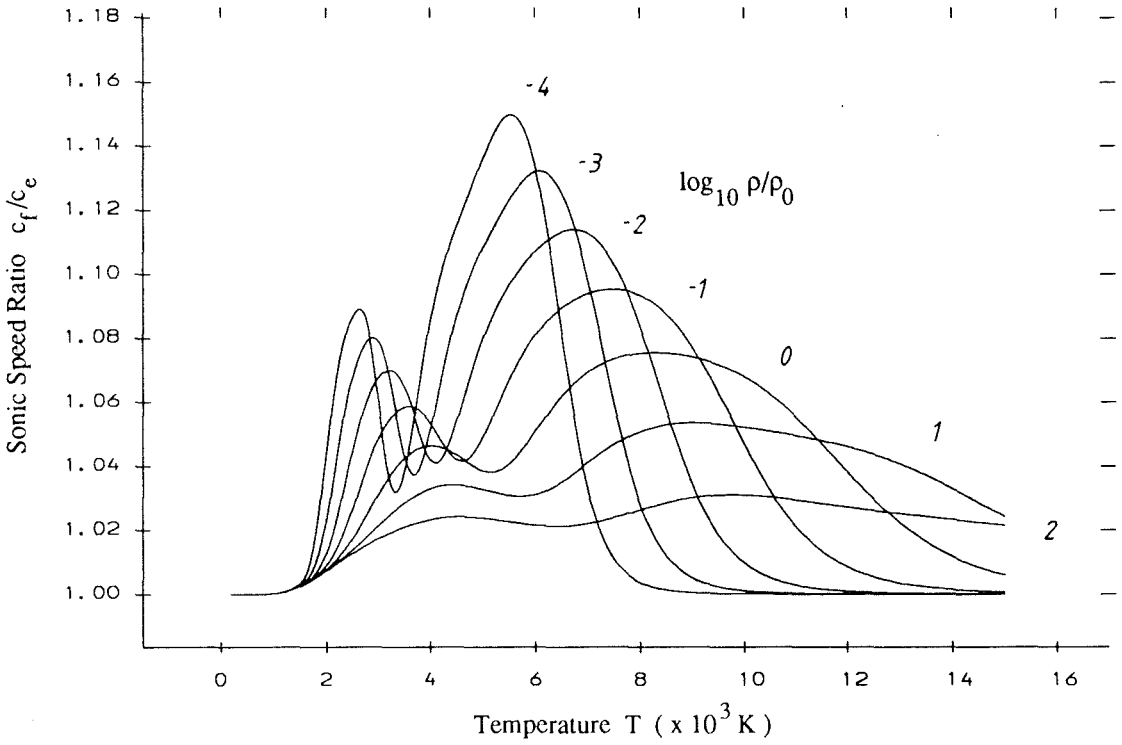

Figure 4.14 Ratio of Frozen to Equilibrium Speed of Sound.

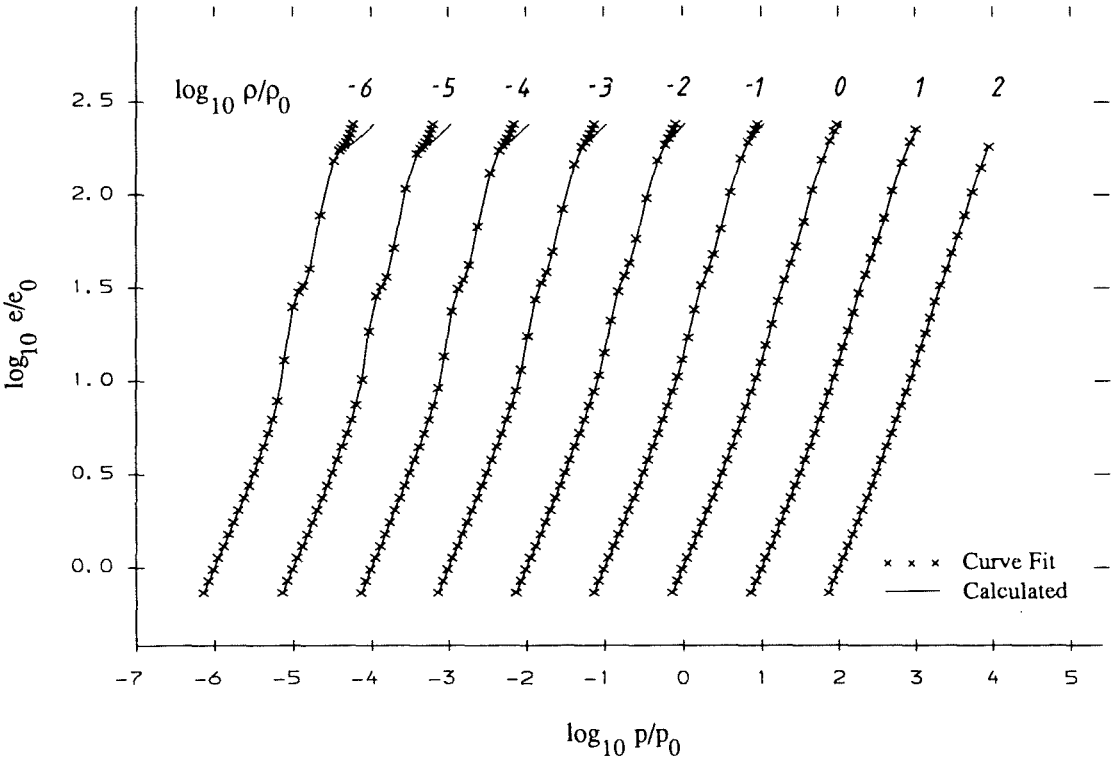

Figure 4.15 Comparison Between Curve Fit Data and Calculated Data for Specific Internal Energy Variation with Pressure.

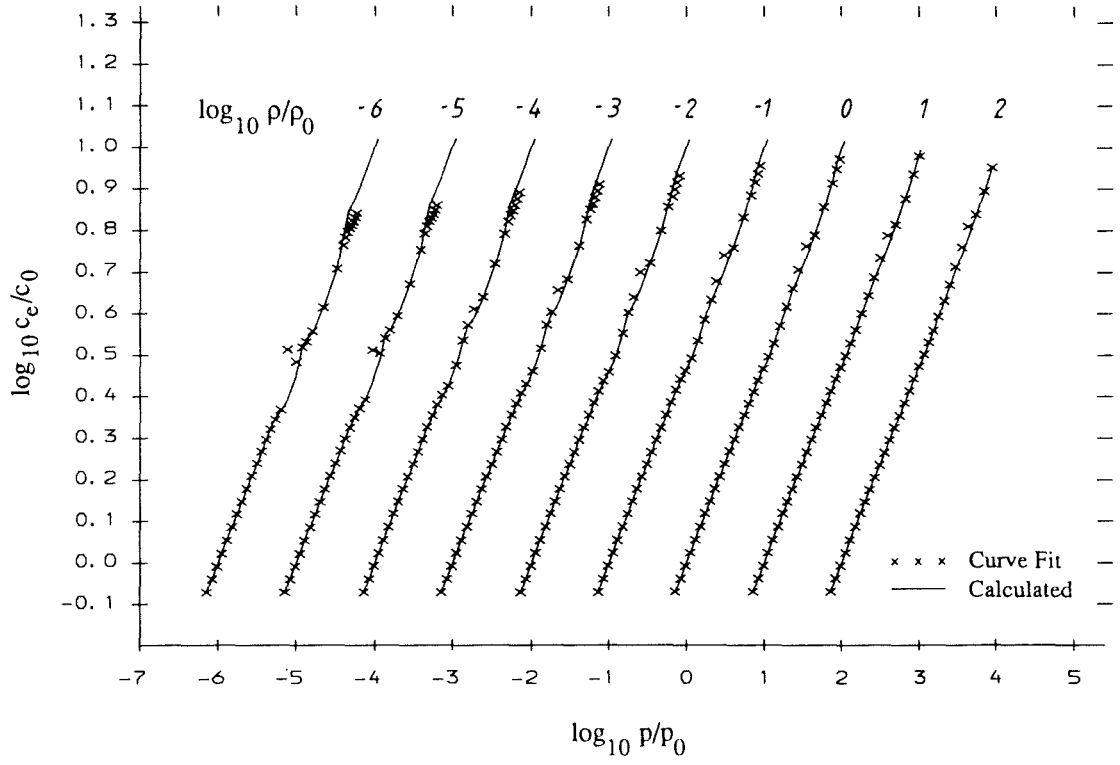

Figure 4.16 Comparison Between Curve Fit Data and Calculated Data for Equilibrium Sonic Speed Variation with Pressure.

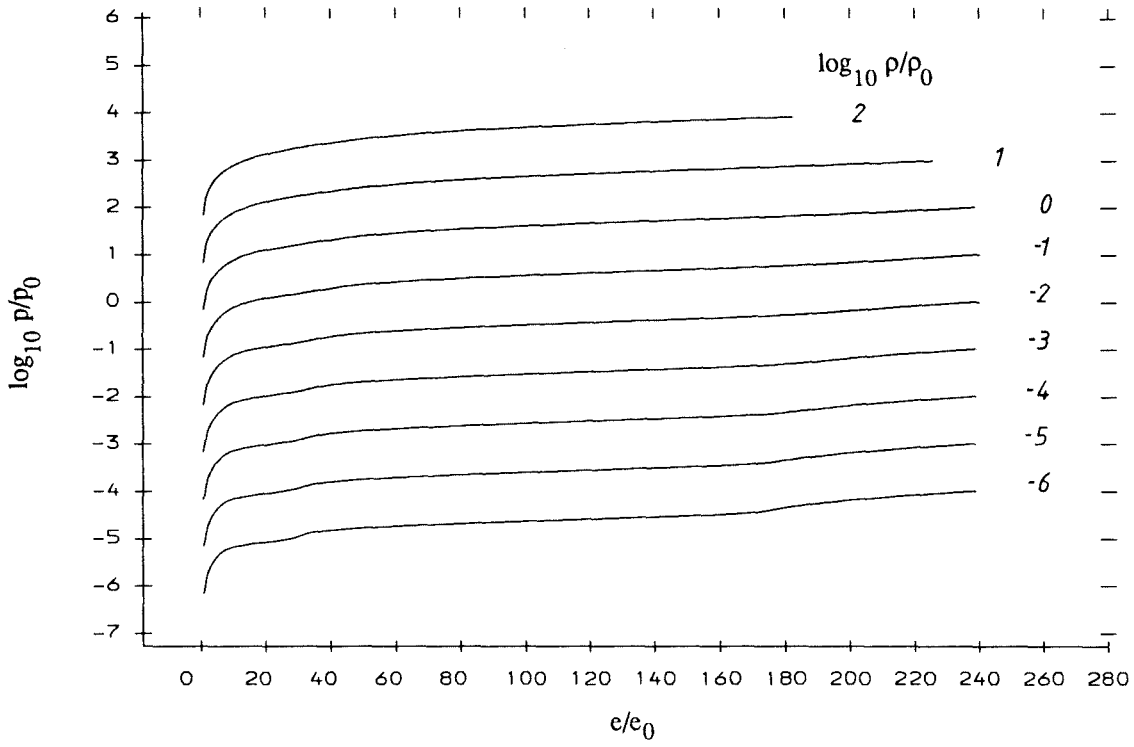

Figure 5.1 Pressure as a Function of Internal Energy at Constant Density.

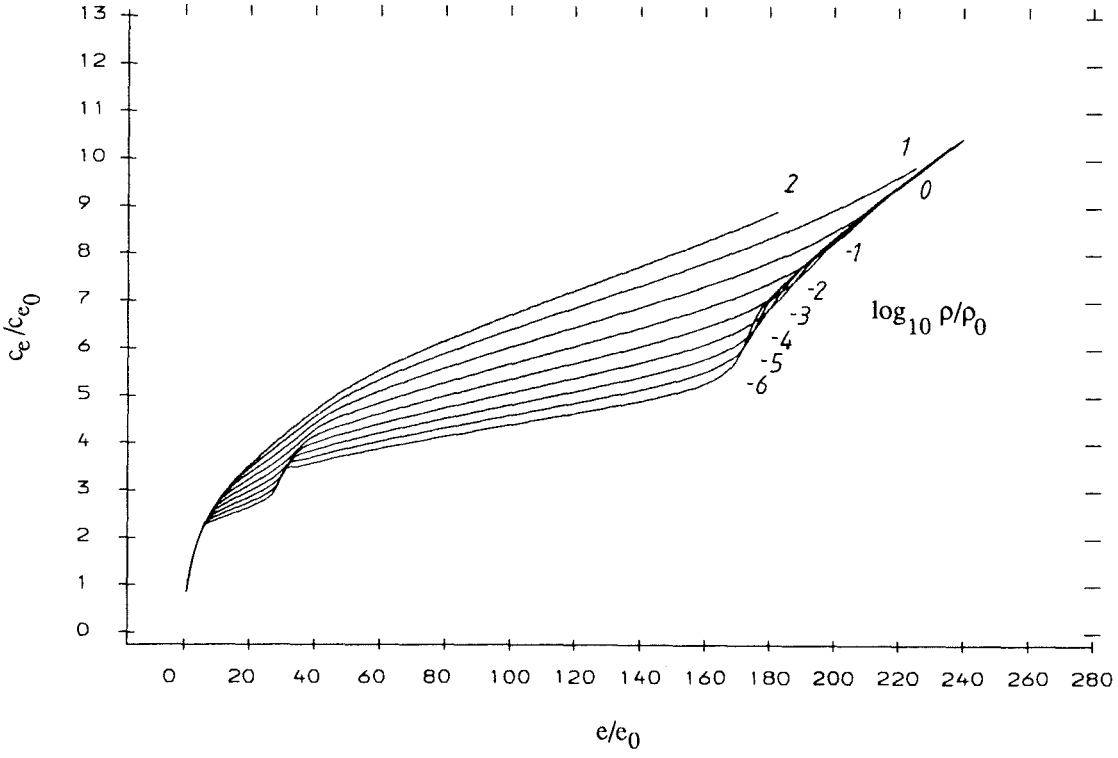

Figure 5.2 Equilibrium Speed of Sound as a Function of Internal Energy at Constant Density.

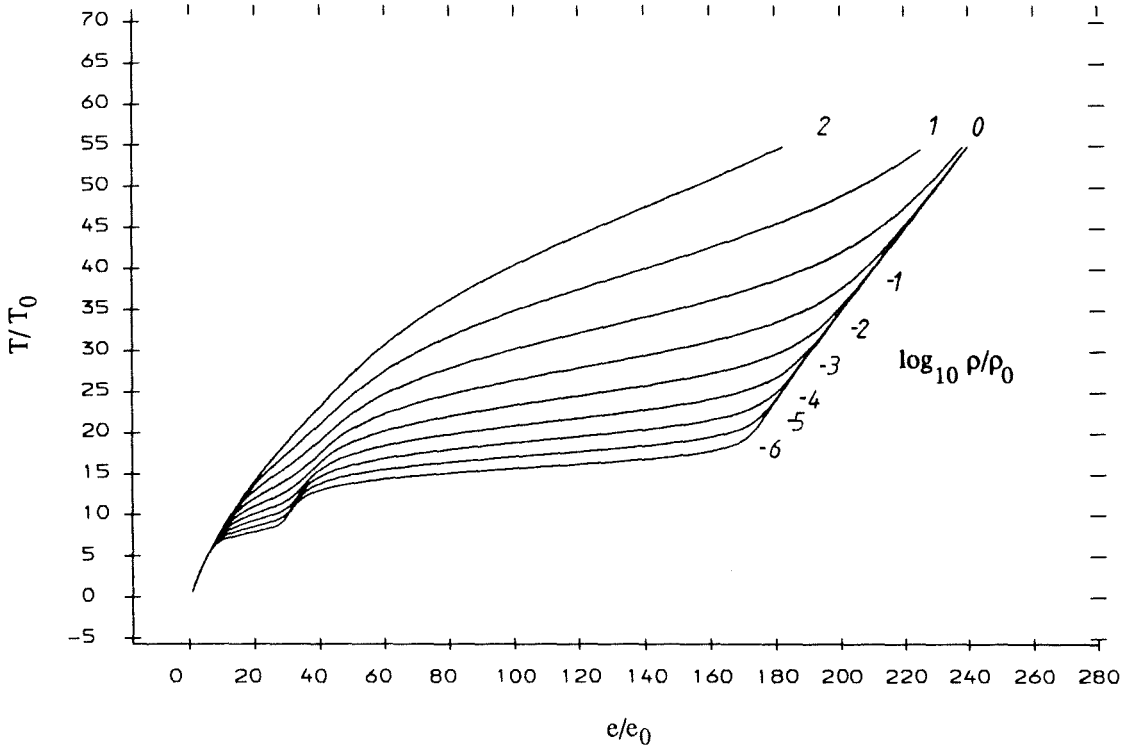

Figure 5.3 Temperature as a Function of Internal Energy at Constant Density

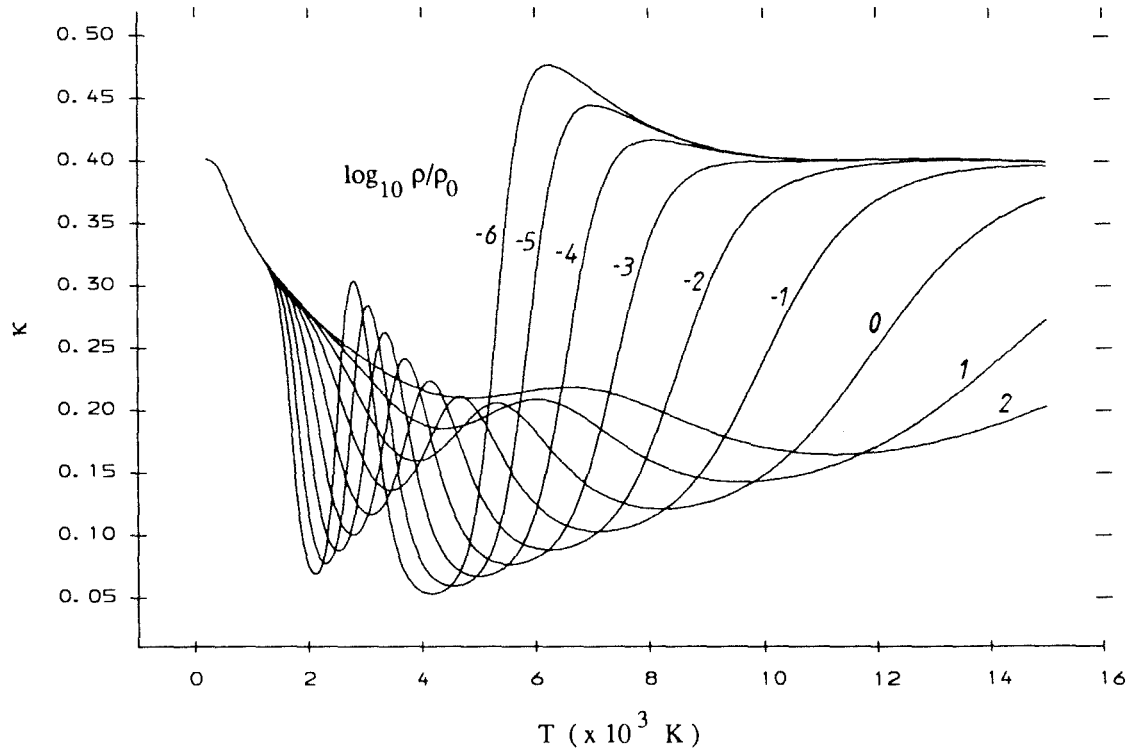

(a) $\kappa = (\partial p/\partial \varepsilon)_\rho$

Figure 5.4 Temperature Dependence of the Thermodynamic Derivatives.

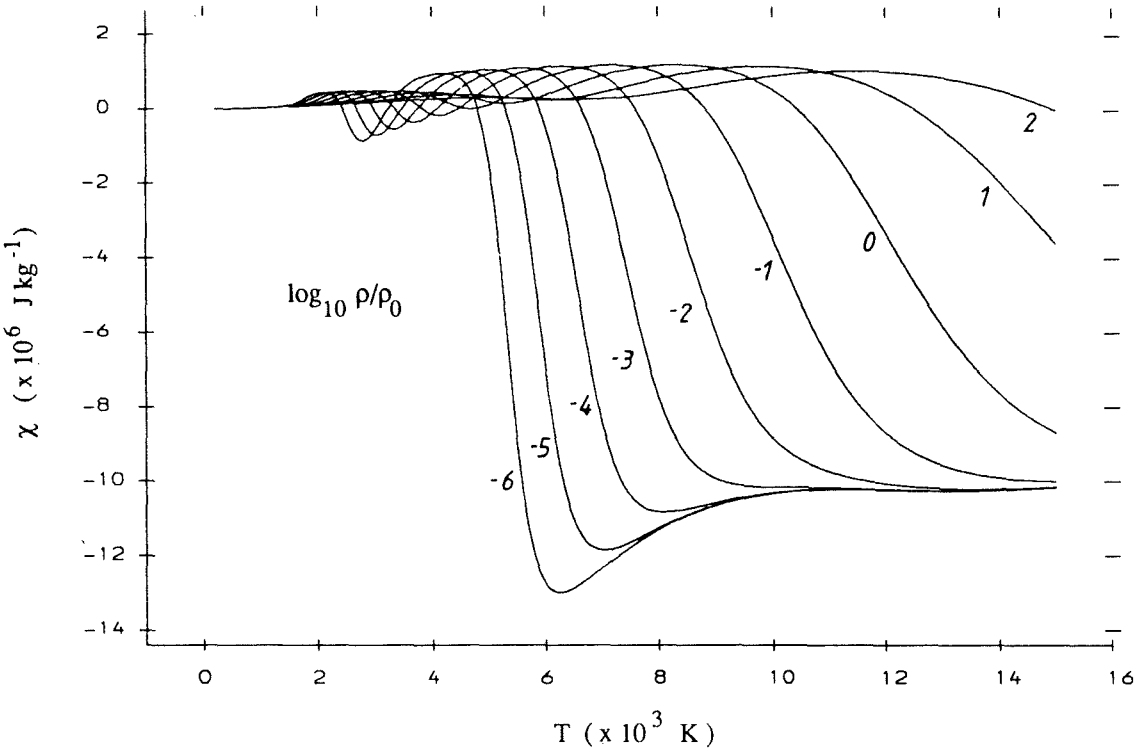

(b) $\chi = (\partial p/\partial \rho)_{\varepsilon}$

Figure 5.4 (continued)

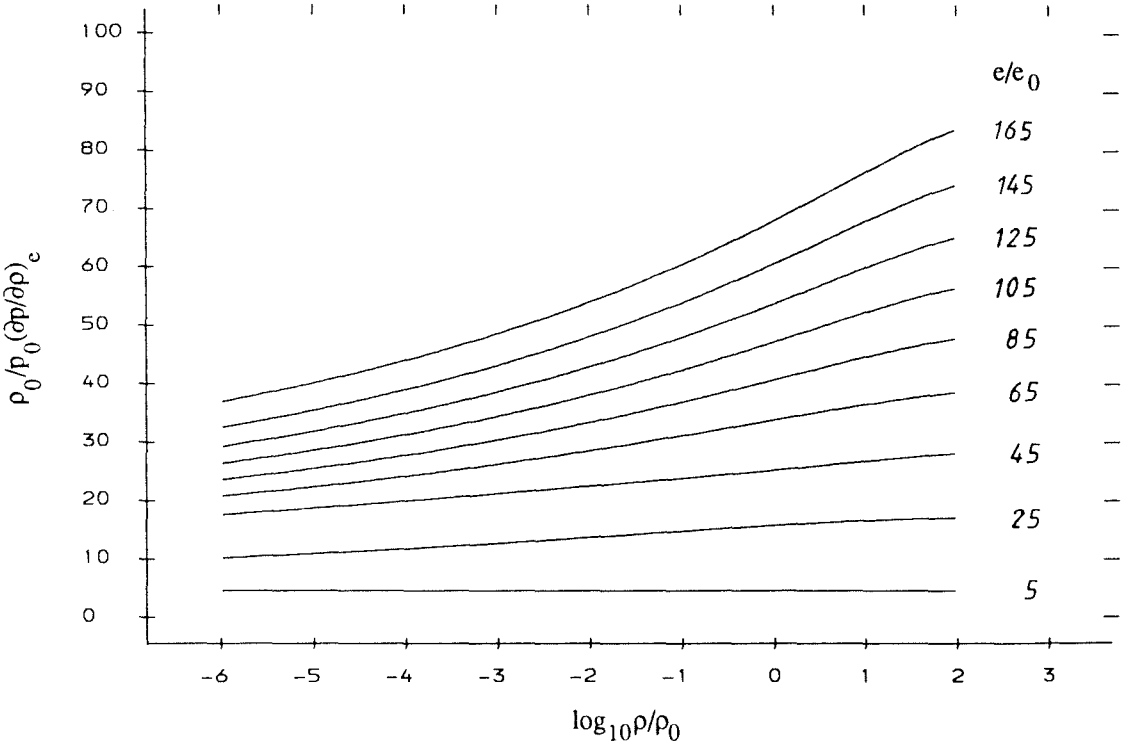

Figure 5.5 Constant Internal Energy Derivatives of Pressure with respect to Density.

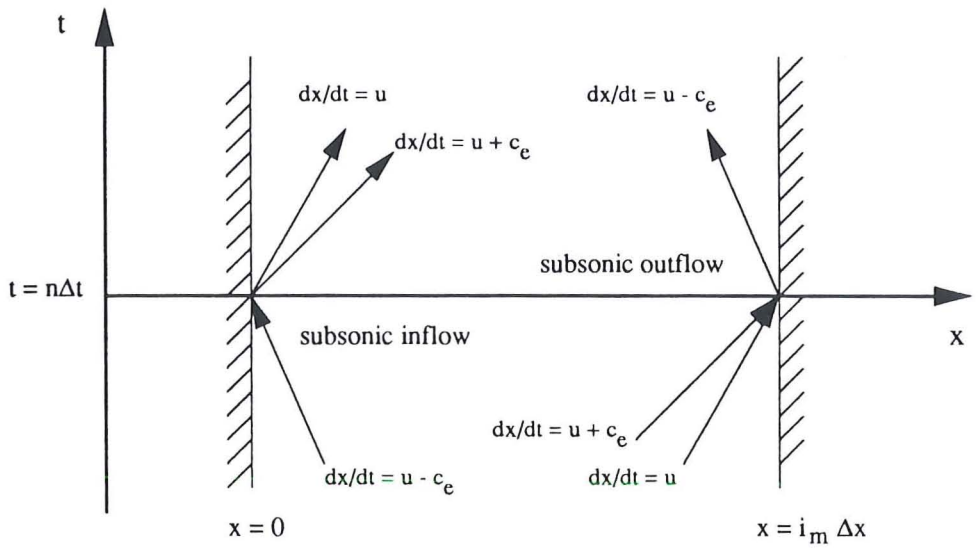

(a) Characteristic Behaviour at Subsonic Boundaries.

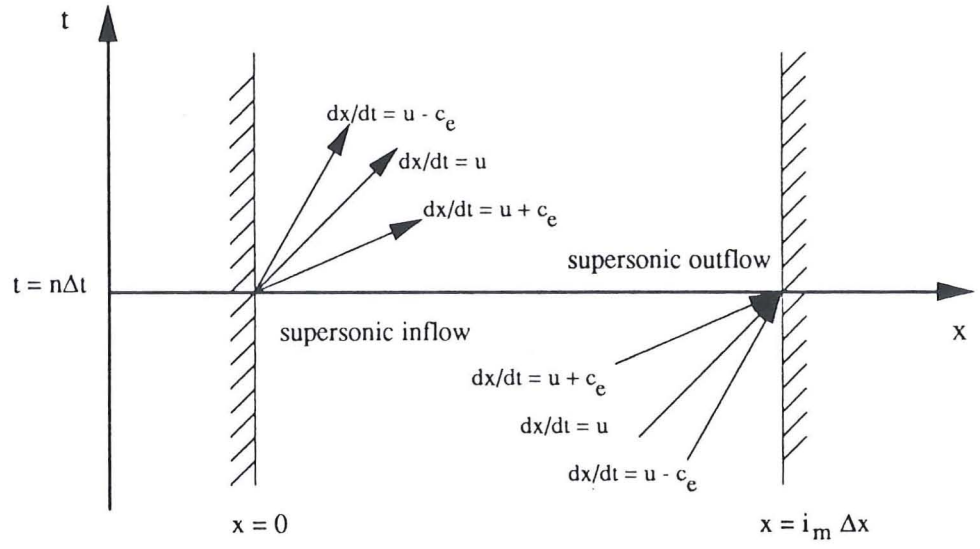

(b) Characteristic Behaviour at Supersonic Boundaries.

Figure 5.6 Propagation Directions for Information at Inflow and Outflow Boundaries for Subsonic and Supersonic Boundary Conditions.

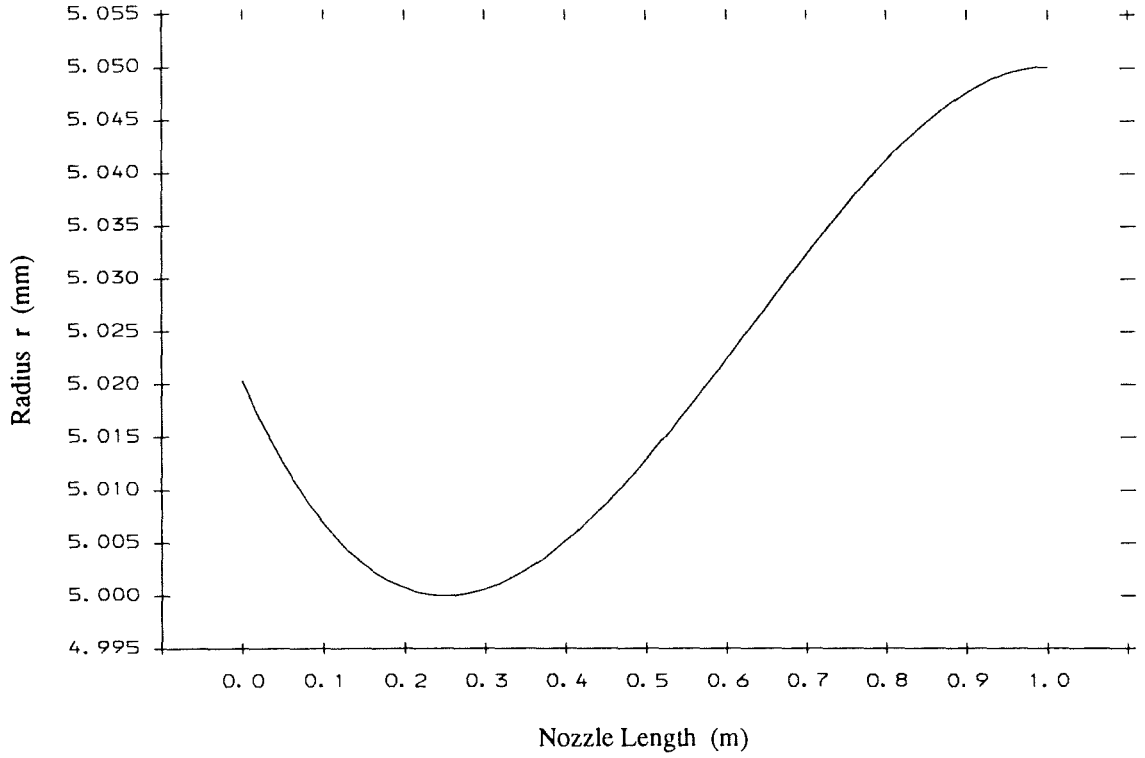

Figure 5.7 Low Speed Calorically Imprefect Gas Test Case: Nozzle Geometry.

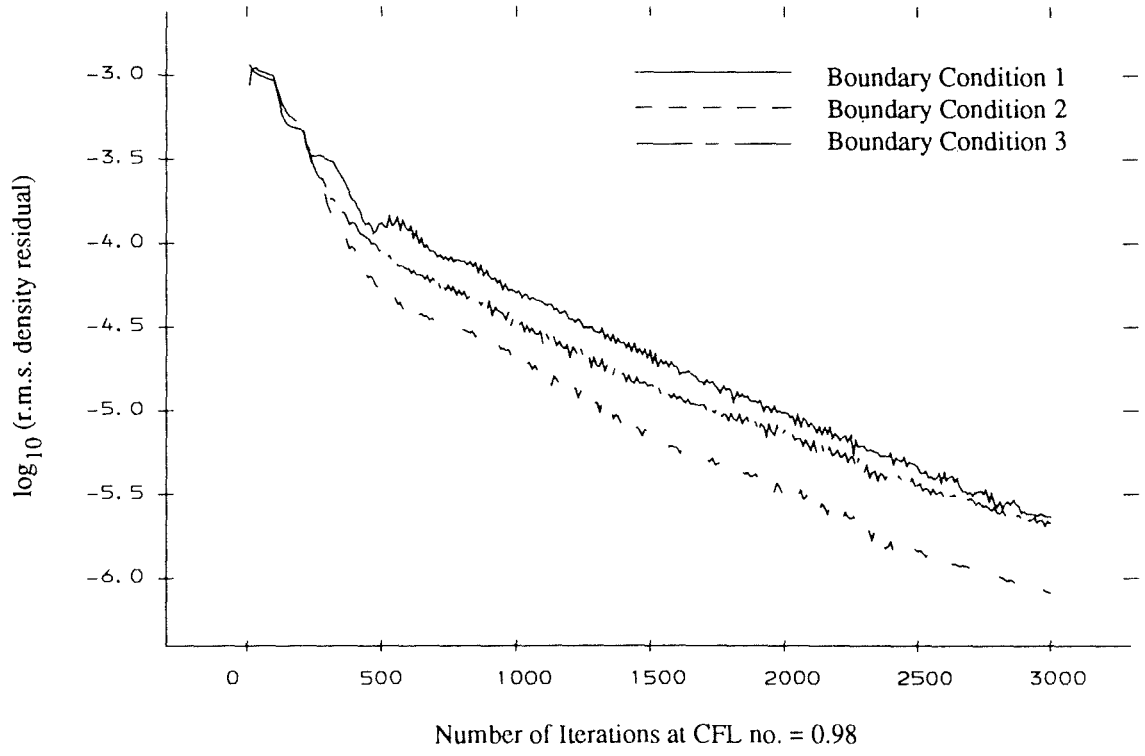

Figure 5.8 Low Speed Calorically Imperfect Gas Test Case: Convergence History for Supersonic Exhaust Case.

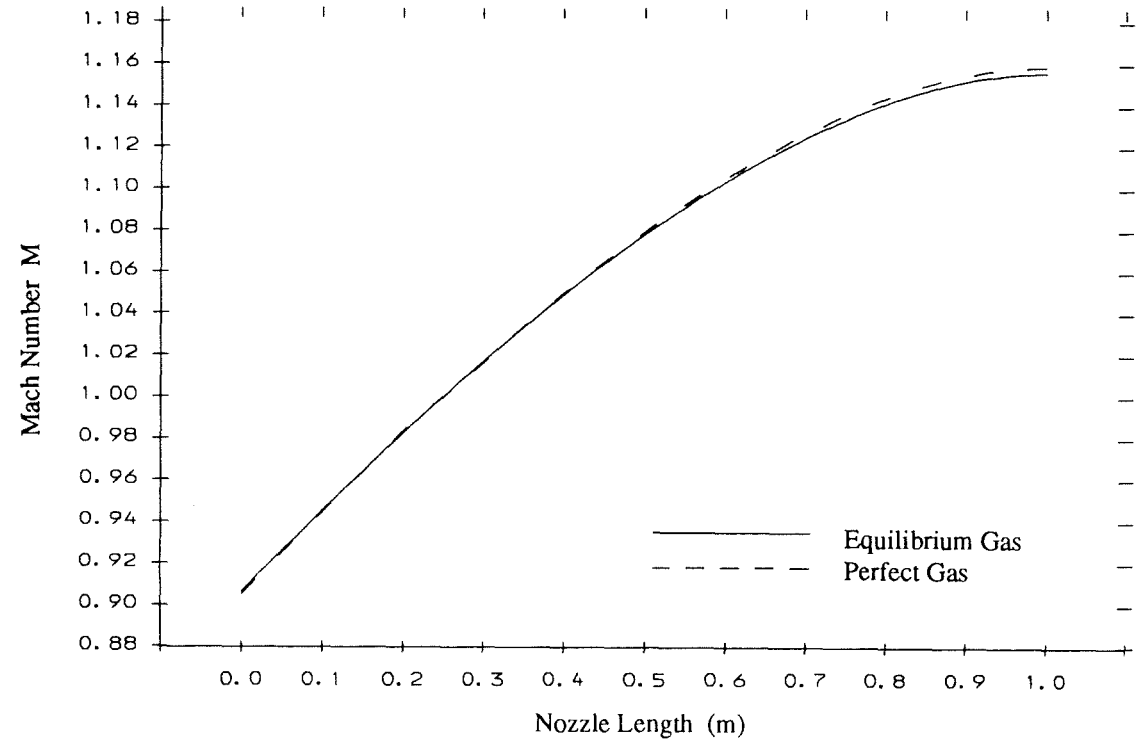

(a) Mach Number Variation.

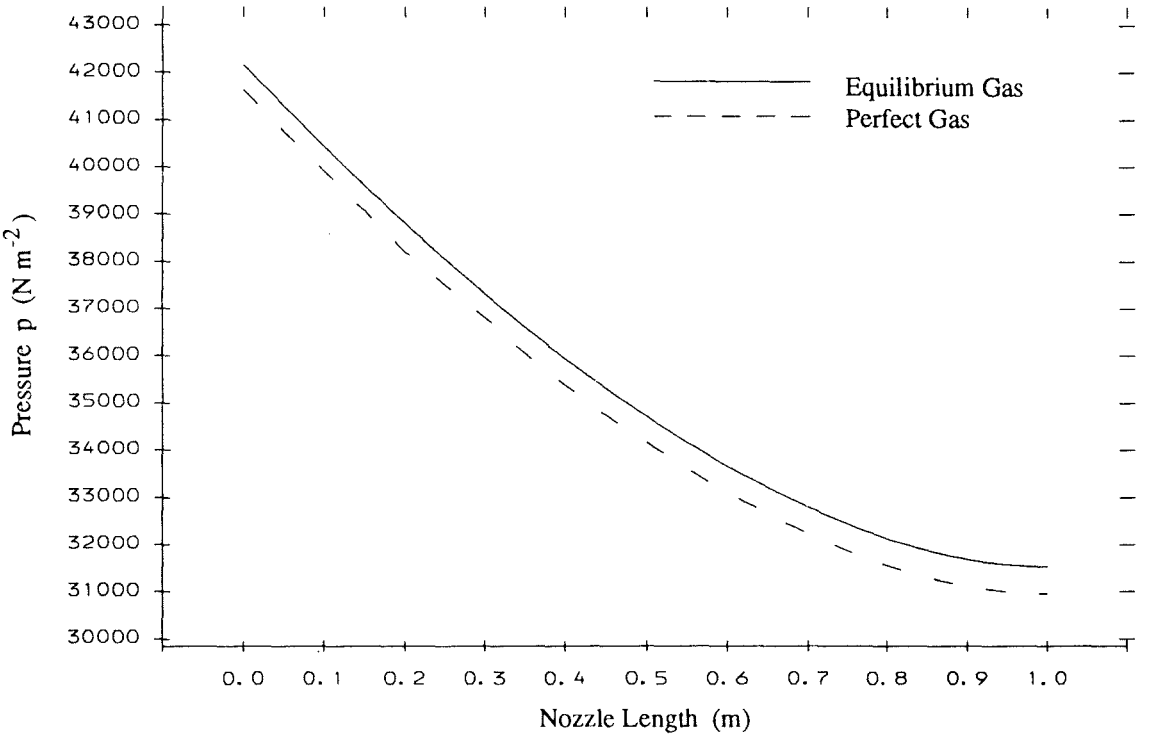

(b) Pressure Variation.

Figure 5.9 Variation of the Thermodynamic Properties of Calorically Imperfect Air Through a Low Speed Expansion Nozzle with Supersonic Exhaust.

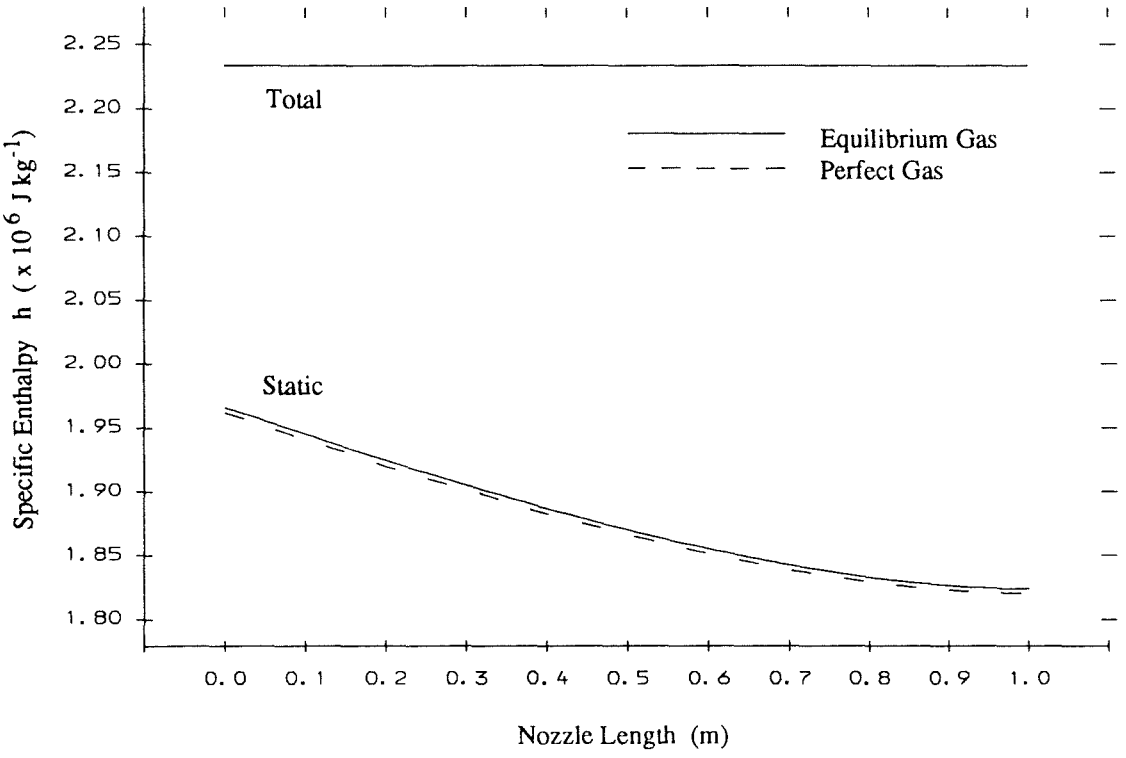

(c) Enthalpy Variation.

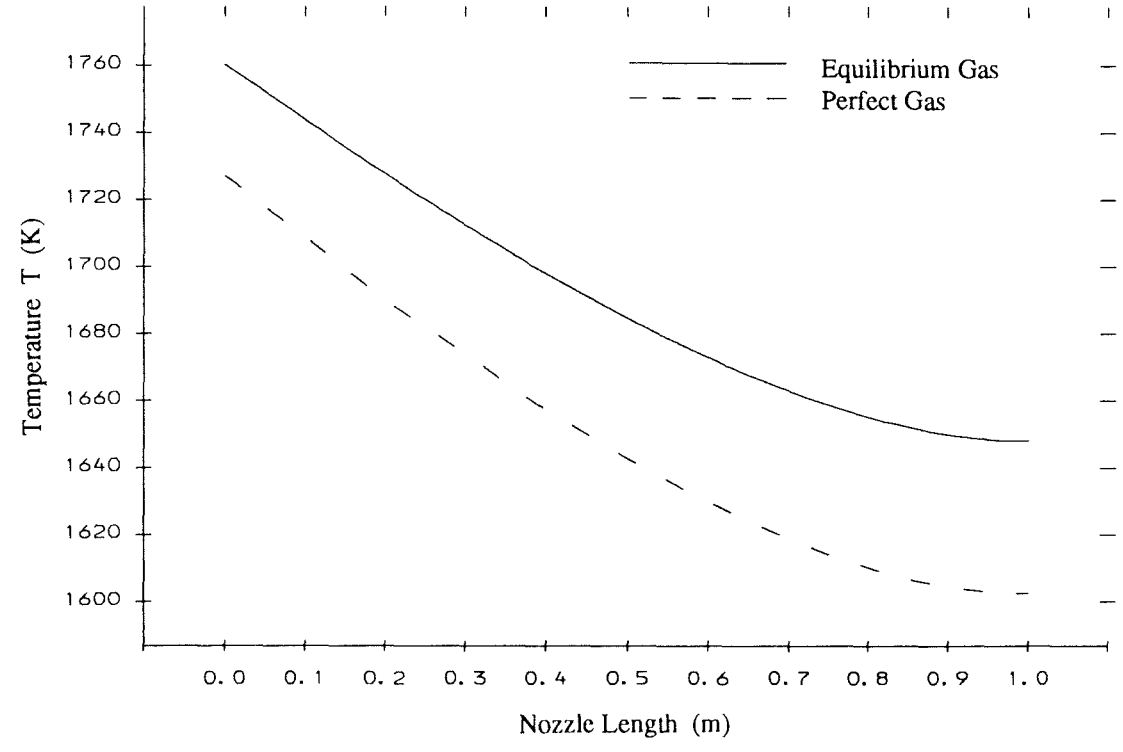

(d) Temperature Variation.

Figure 5.9 (continued)

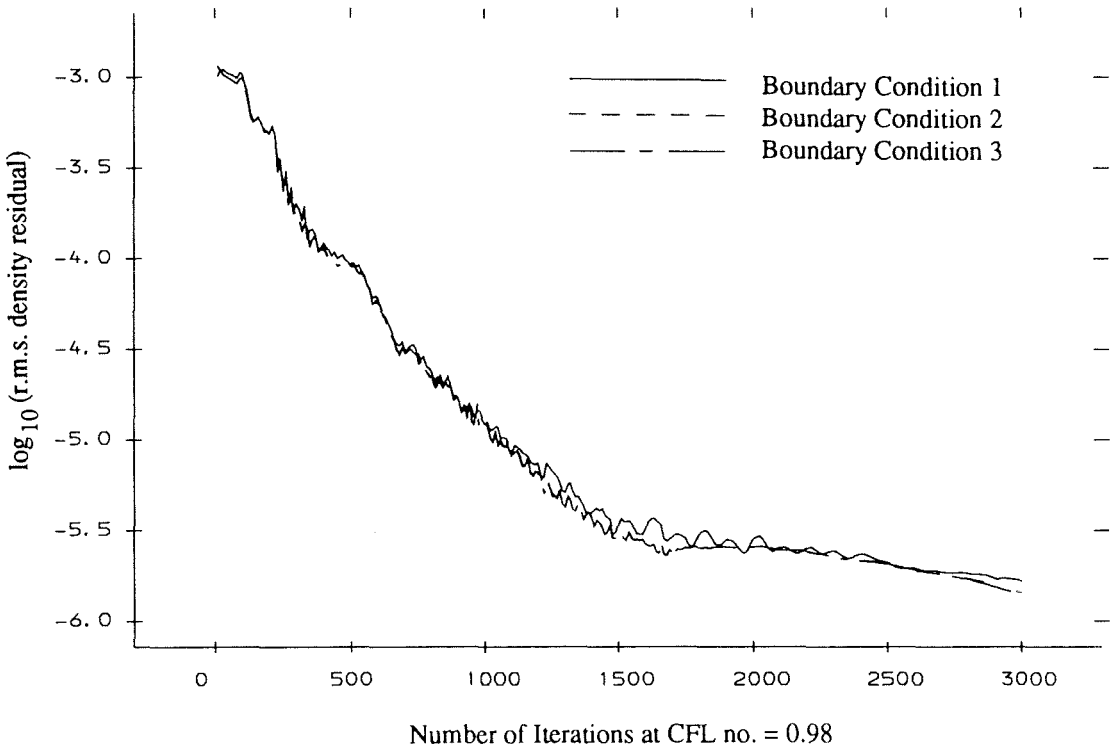

Figure 5.10 Low Speed Calorically Imperfect Gas Test Case: Convergence History for Subsonic Exhaust Case.

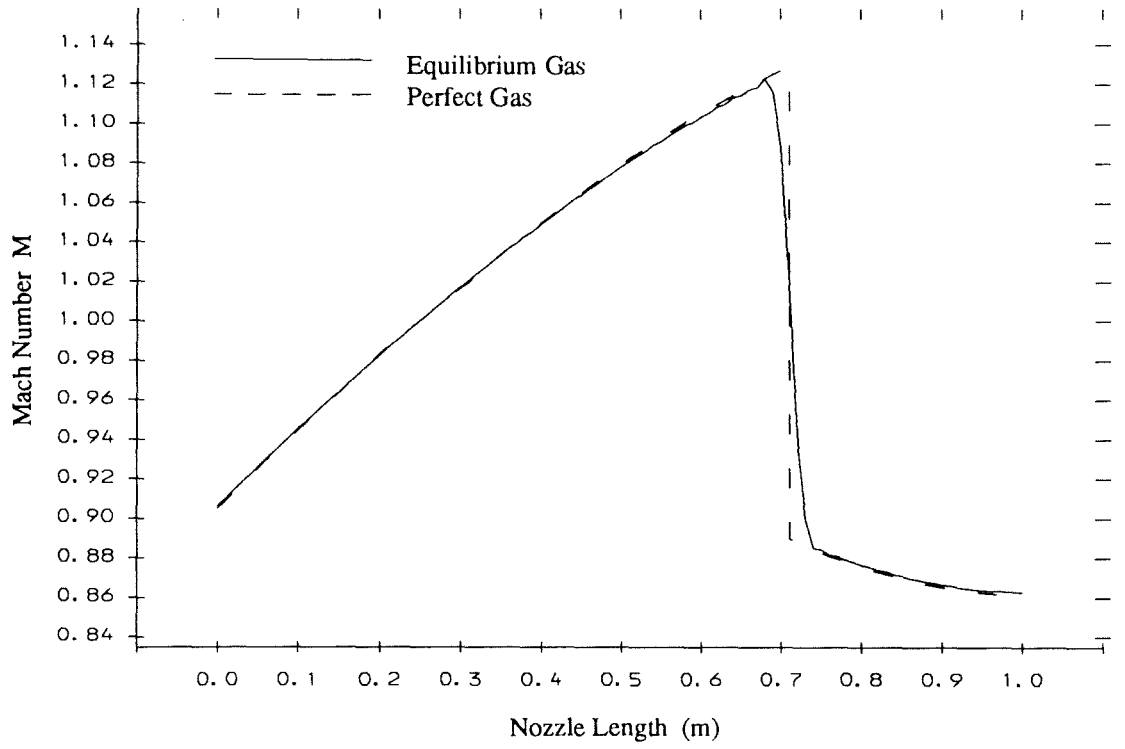

(a) Mach Number Variation.

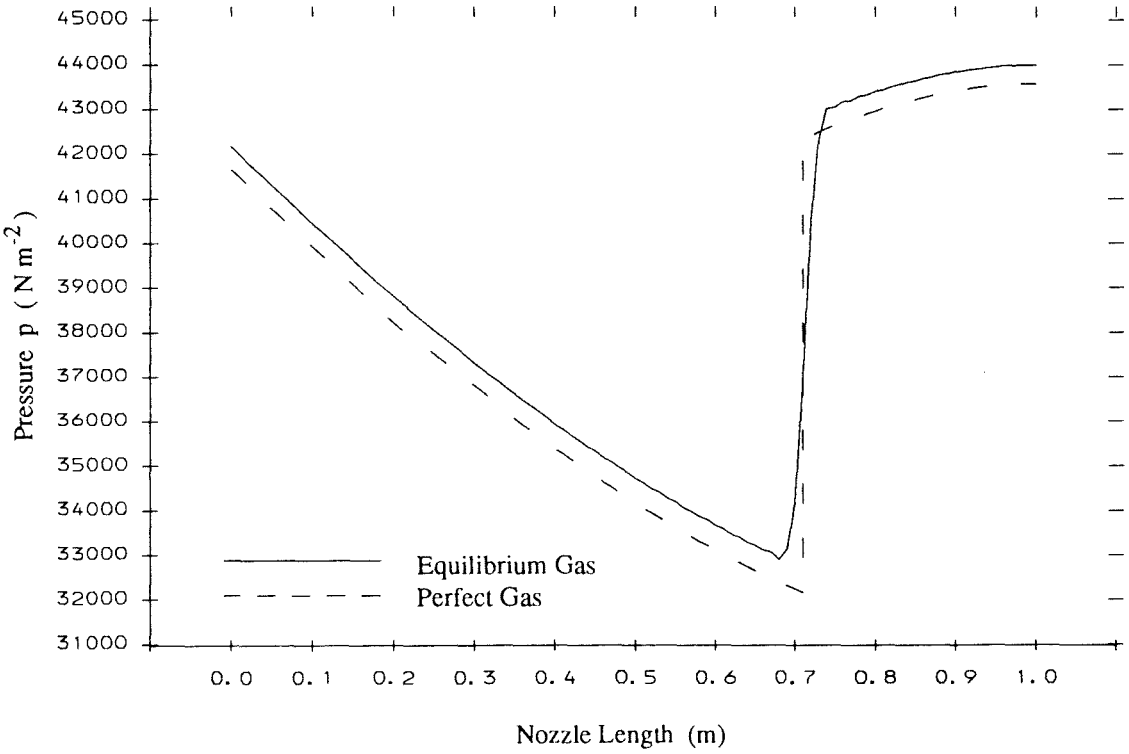

(b) Pressure Variation.

Figure 5.11 Variation of the Thermodynamic Properties of Calorically Imperfect Air Through a Low Speed Expansion Nozzle with Subsonic Exhaust.

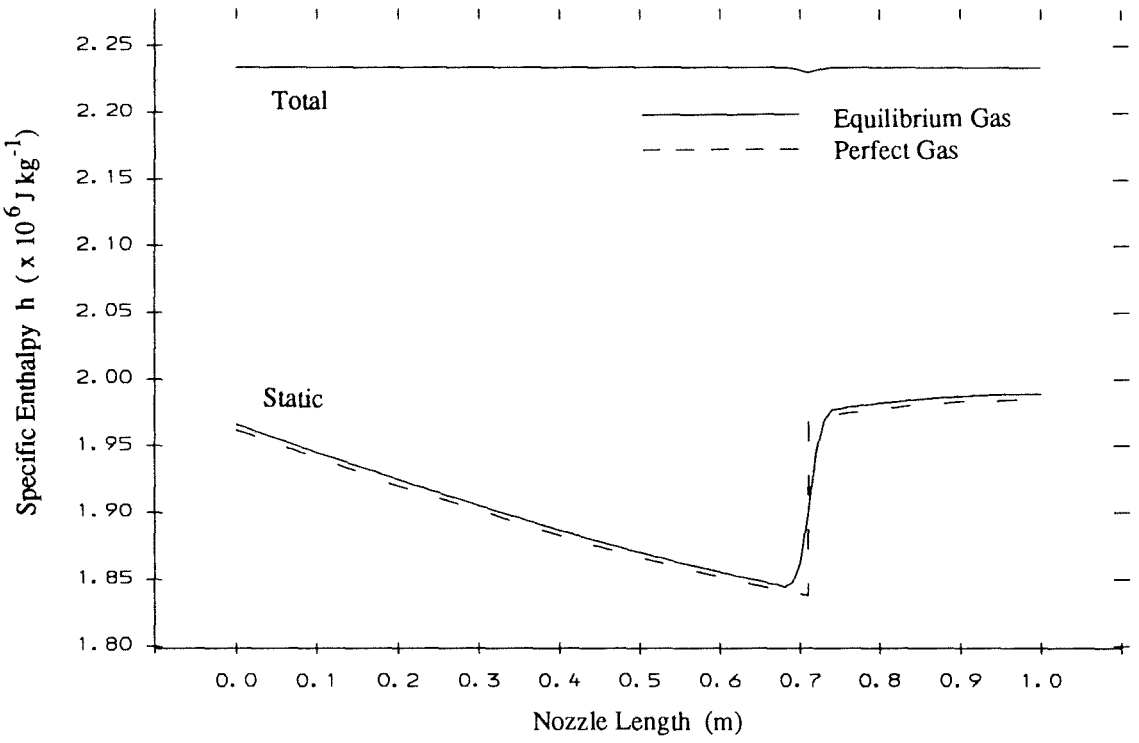

(c) Enthalpy Variation.

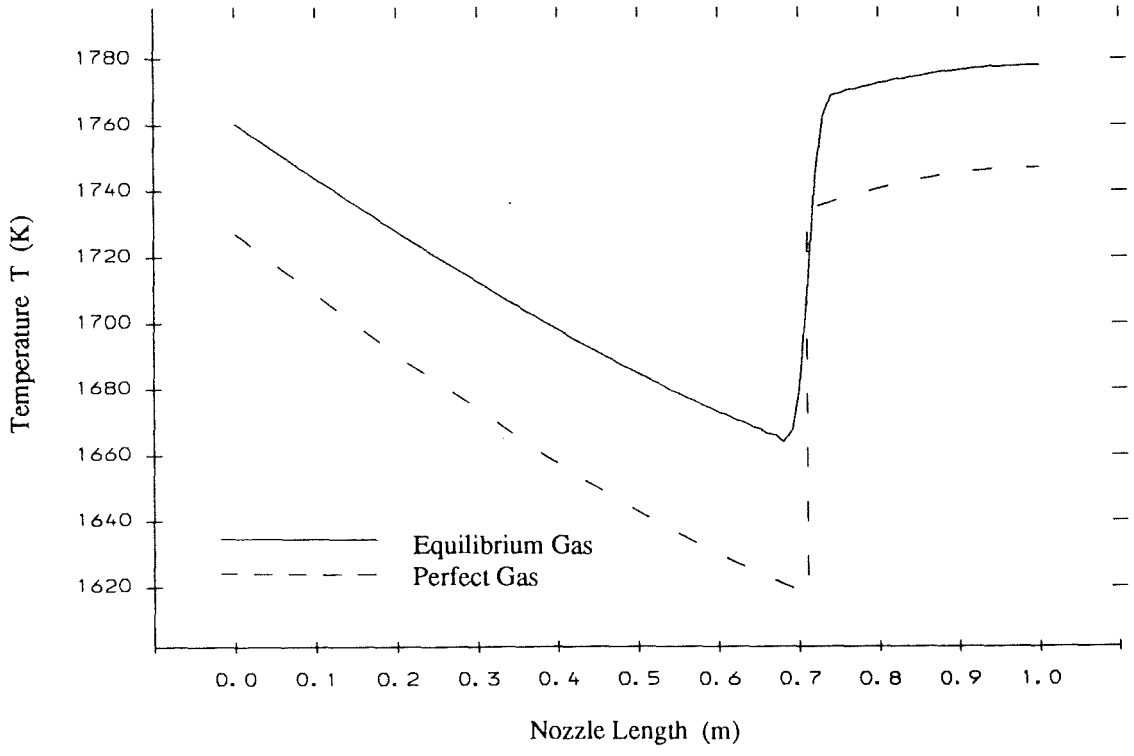

(d) Temperature Variation.

Figure 5.11 (continued)

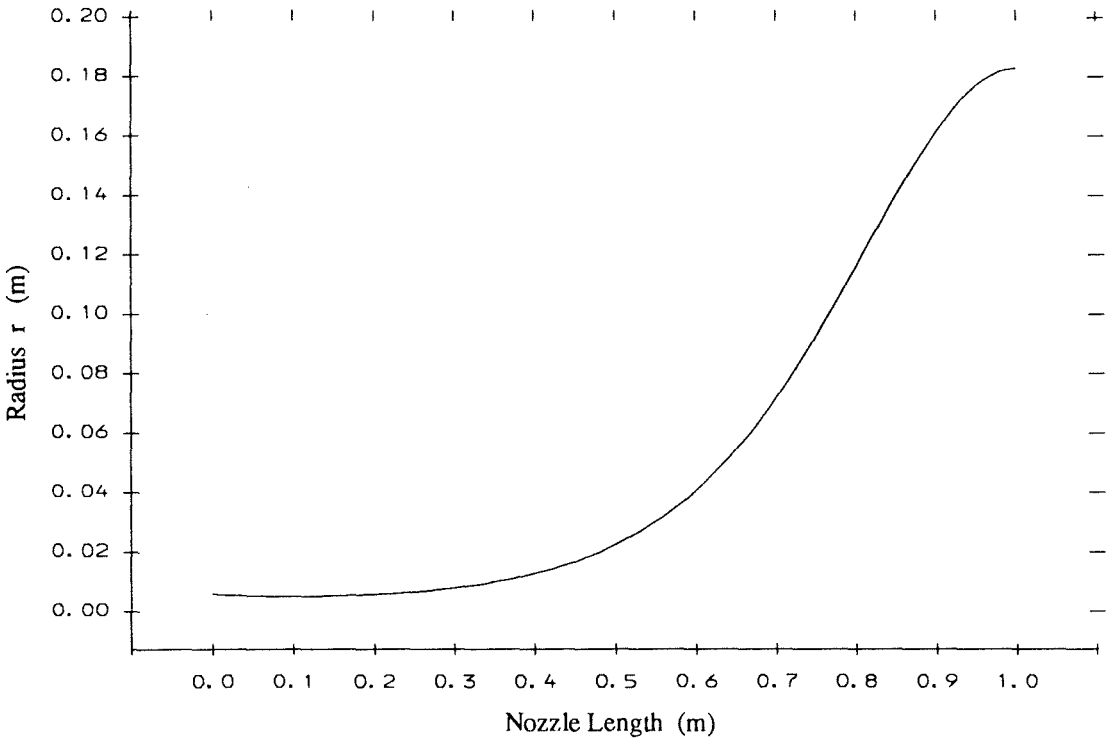

Figure 5.12 Hypersonic Thermally Imperfect Gas Test Case: Nozzle Geometry.

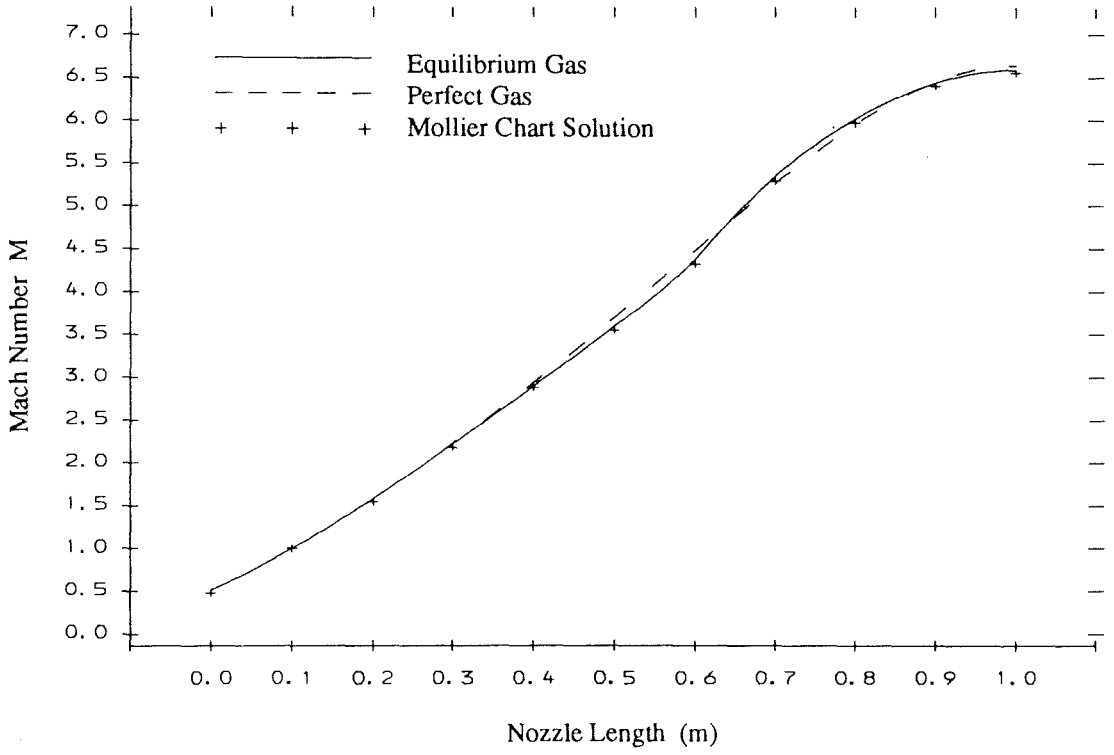

(a) Mach Number Variation.

Figure 5.13 Variation of the Thermodynamic Properties of Thermally Imperfect Air Through an Hypersonic Expansion Nozzle with Supersionc Exhaust.

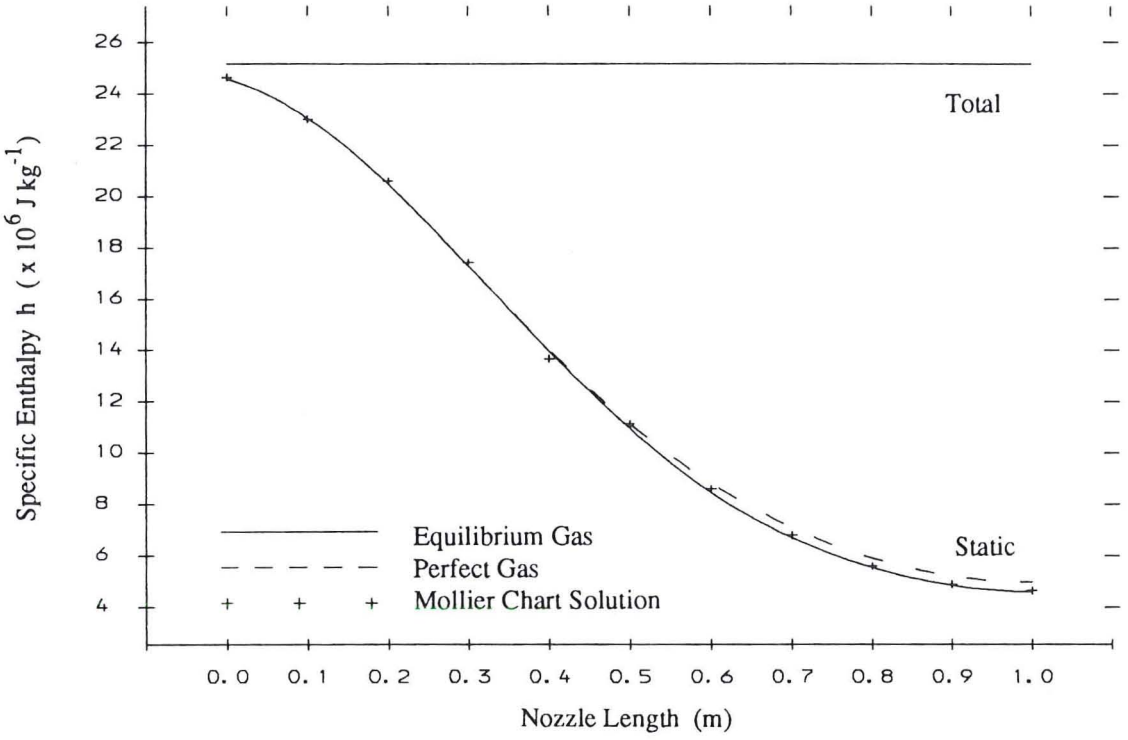

(b) Enthalpy Variation.

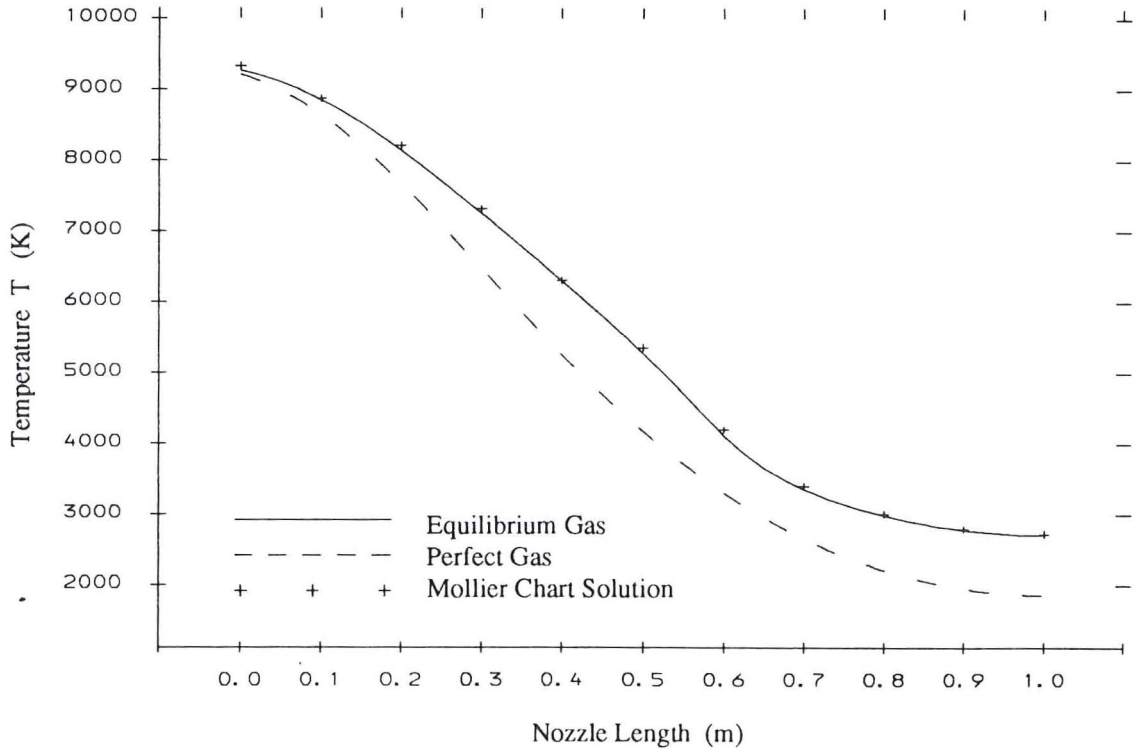

(c) Temperature Variation.

Figure 5.13 (continued)

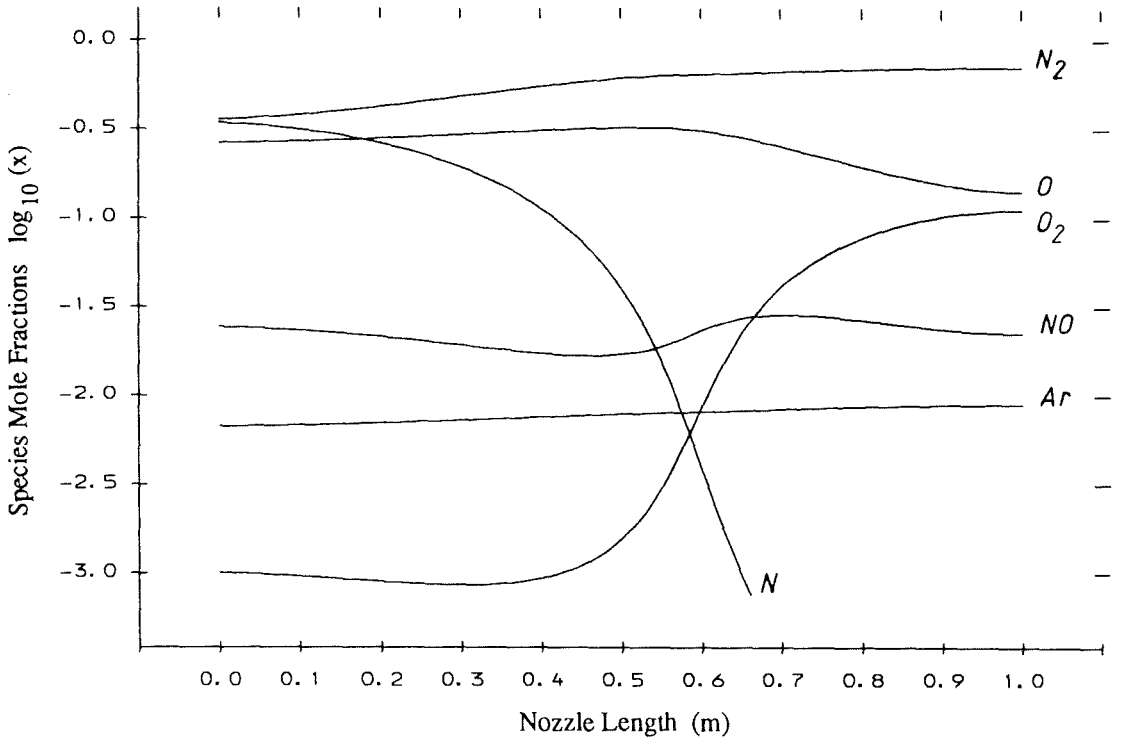

(a) Gas Chemical Composition.

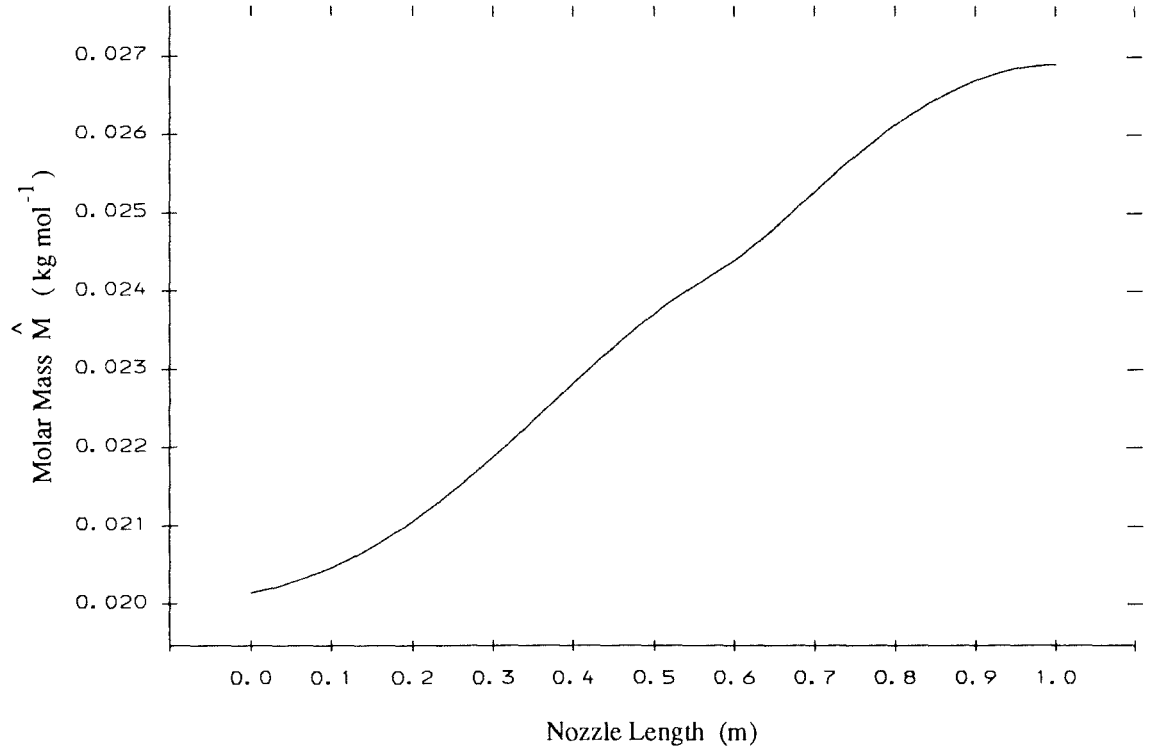

(b) Mixture Molar Mass.

Figure 5.14 Thermochemical Properties of Equilibrium Air in an Hypersonic Expansion Nozzle.

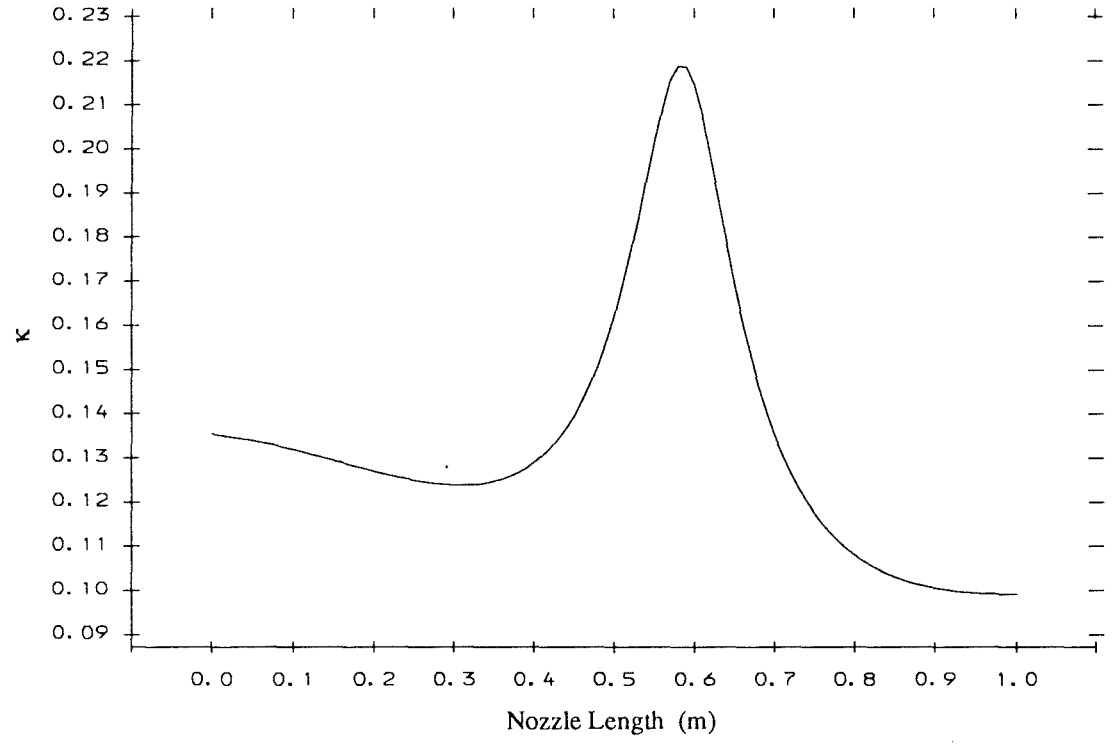

(c) Thermodynamic Derivative $\kappa = (\partial p/\partial \varepsilon)_\rho$

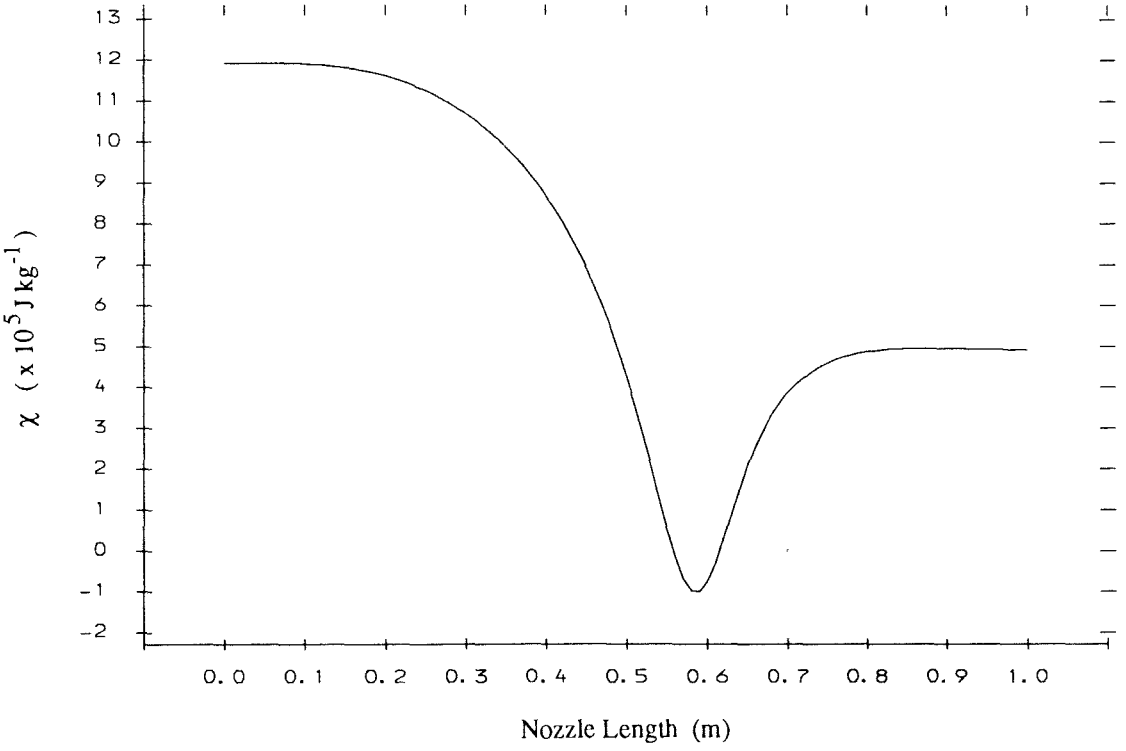

(d) Thermodynamic Derivative $\chi = (\partial p/\partial \rho)_\varepsilon$

Figure 5.14 (continued)

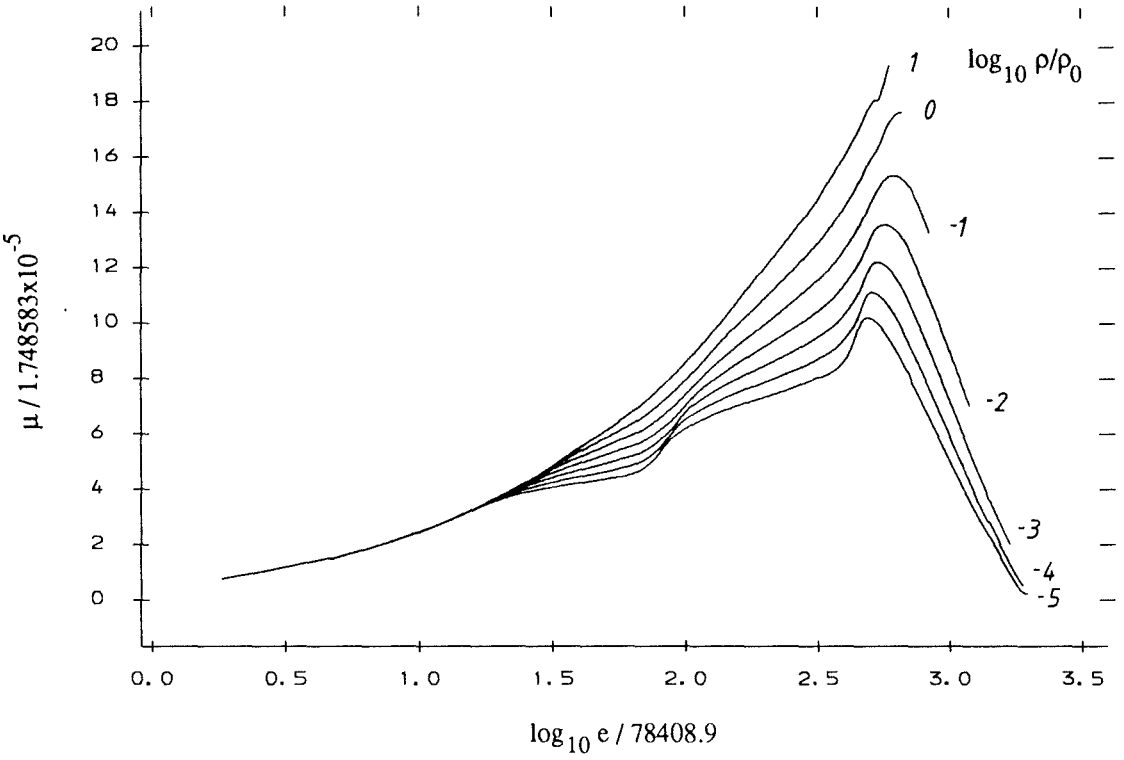

Figure 6.1 Curve Fits for Viscosity in the Form $\mu = \mu(\rho, e)$.

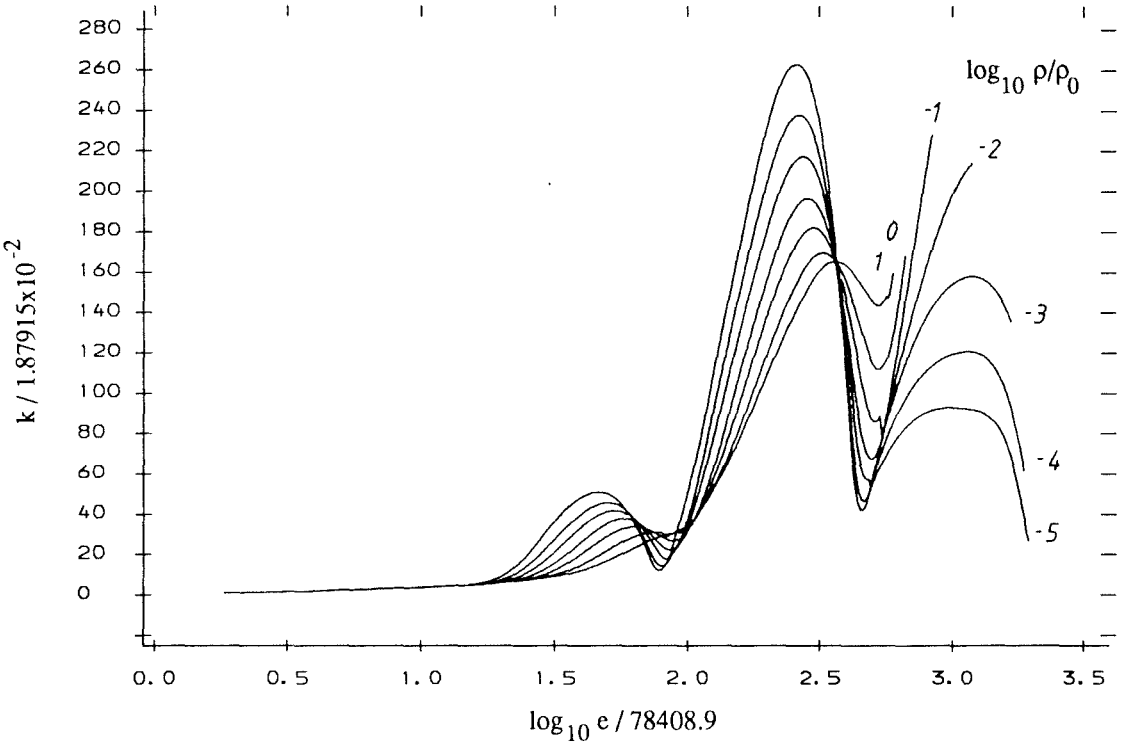

Figure 6.2 Curve Fits for Thermal Conductivity in the Form $k = k(\rho, e)$.

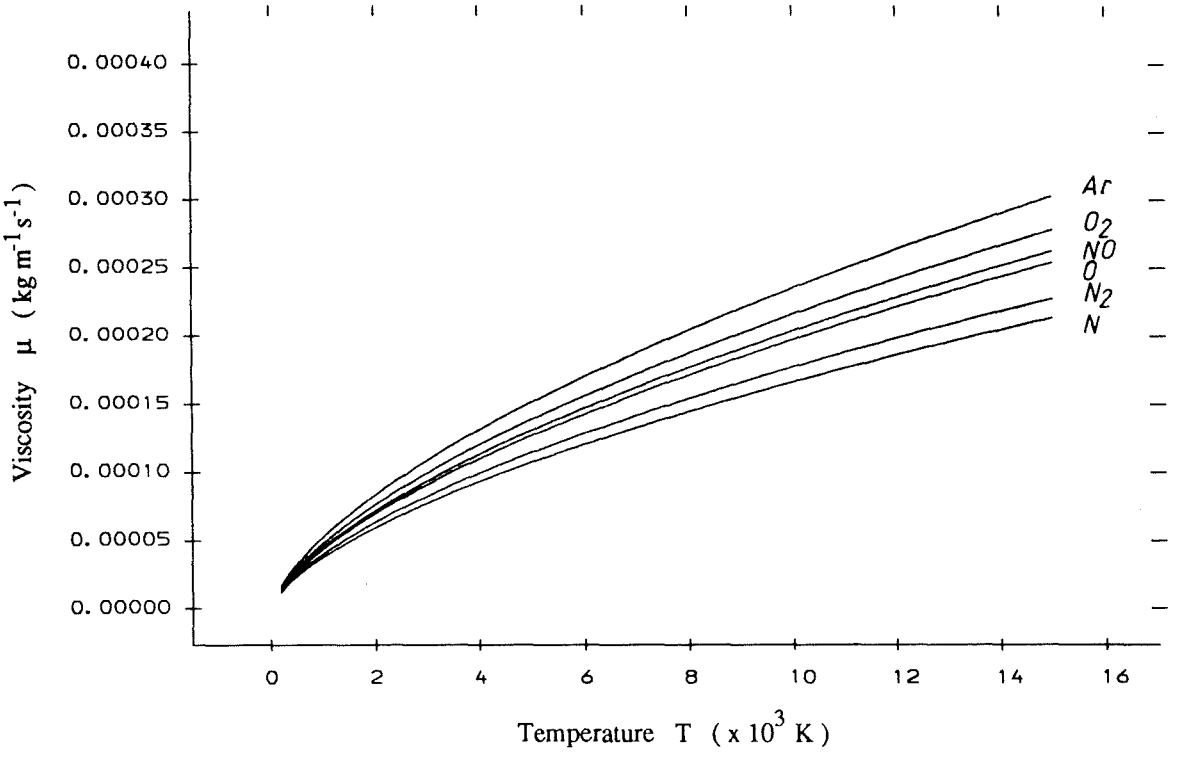

(a) Theoretical Calculation.

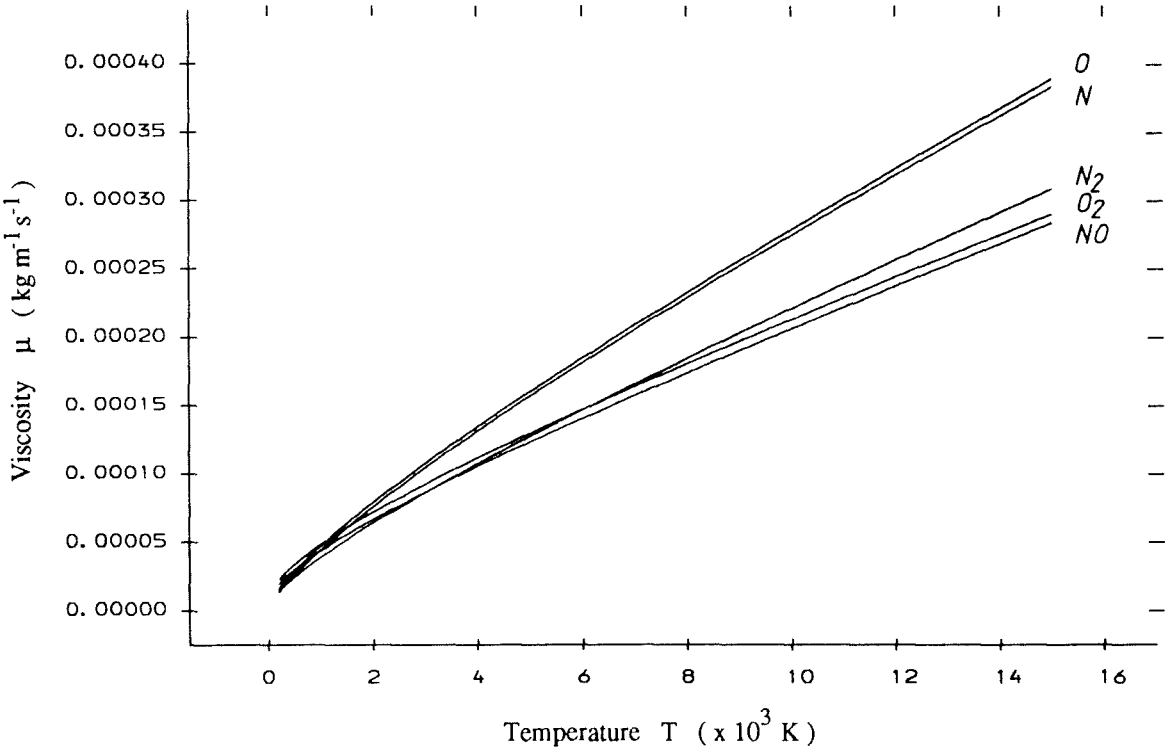

(b) Curve Fit Calculation.

Figure 6.3 Species Viscosity Variation with Temperature.

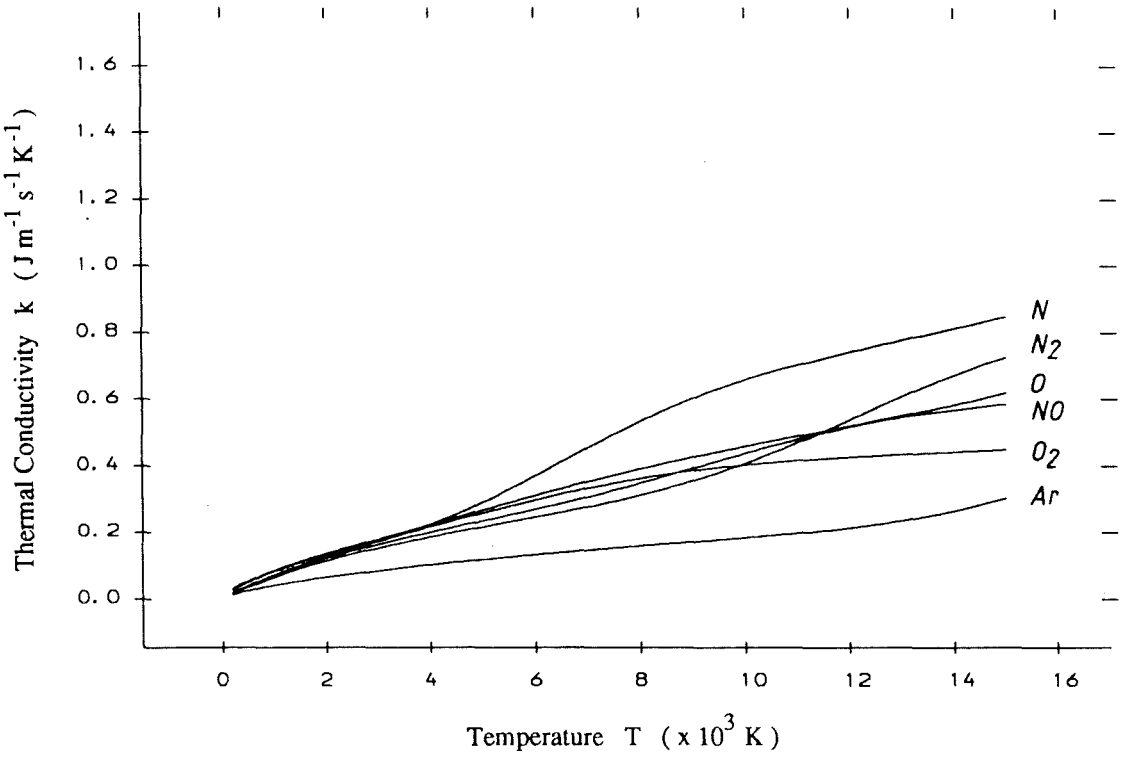

(a) Theoretical Calculation.

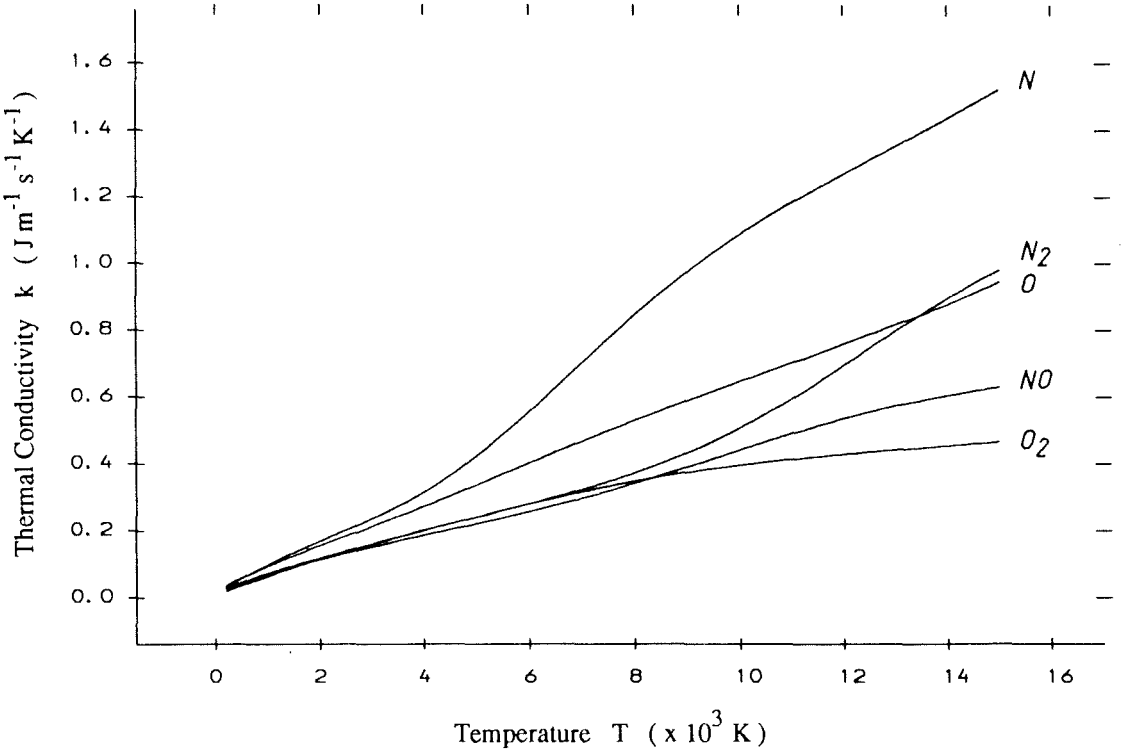

(b) Curve Fit Calculation.

Figure 6.4 Species Thermal Conductivity Variation with Temperature.

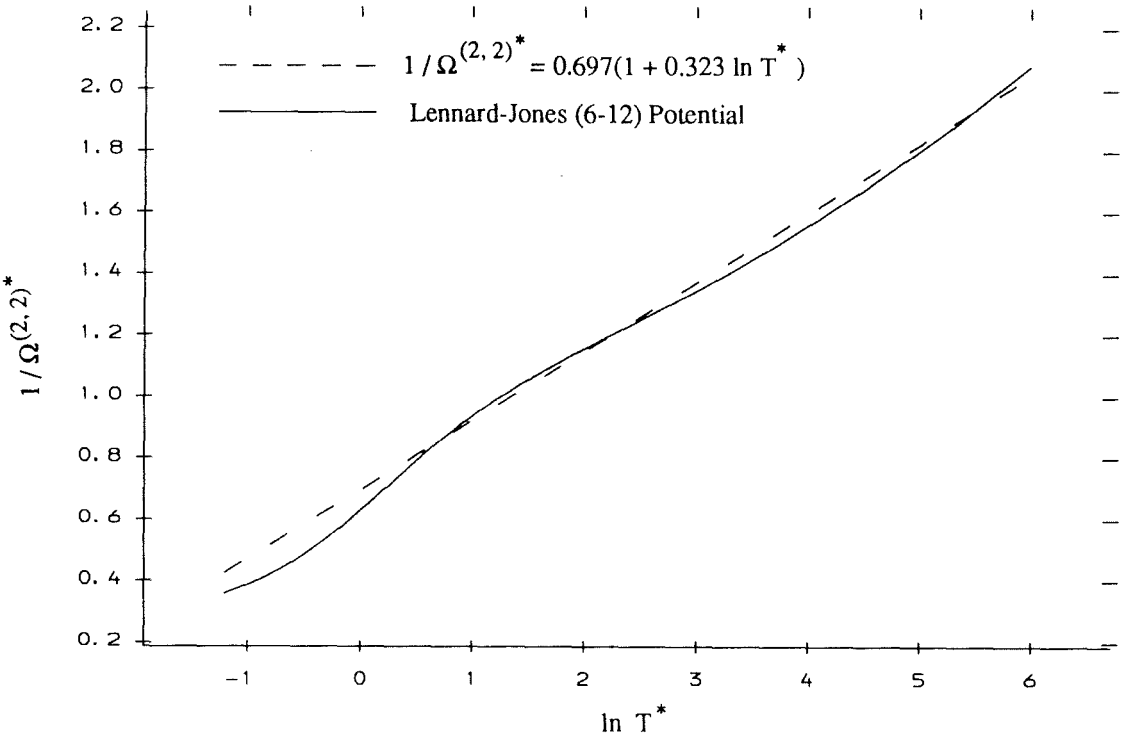

Figure 6.5 Reduced Collision Integral for Viscosity Calculations.

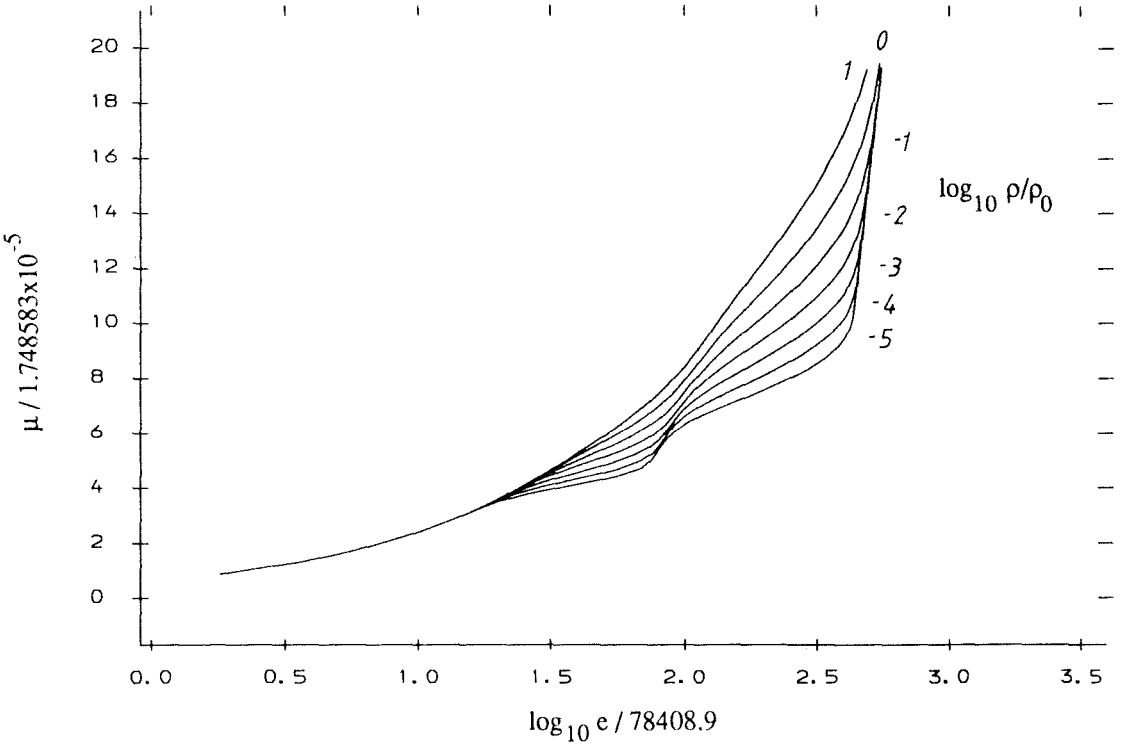

Figure 6.6 Calculated Mixture Viscosity.